

Preface

Dielectric functions can be used to describe the interaction of charged particles with matter. Dielectric functions are generally not known, and one relies on approximations. Chapidif is a program that can help with developing a proper model dielectric function, checking the sum rule compliance of the dielectric function, and calculating a large number of observables, based on the dielectric function. It is written in Python, but the computational-intensive part is taken care of by a provided library written in C++.

This document describes the Chapidif program. The first chapter is a more traditional manual, followed by several chapters that describe part of the underlying physics and applications.

Chapter 2 introduces the dielectric functions that can be used in Chapidif as a basis for the model dielectric function and highlights the differences in stopping ('shell effects') between the models.

Chapter 3 describes the various ways the RPA dielectric functions are calculated.

Chapter 4 is a case study for aluminium, and compares a range of phenomena with calculations based on a relatively simple model dielectric function.

Chapter 5 describes our implementation of the Kaneko dielectric function in some detail, as it differs somewhat from the original version.

Chapter 6 describes a number of simple analytical expressions for the inelastic mean free path, stopping and straggling for electrons and protons, similar to the ones derived by Nguyen-Truong, for electrons. These approximations are available in Chapidif and can be compared with the results with the full calculation.

The aim of the program is not only to get the 'right answer', but also to show how the answer varies as different approximations are made. For example, the user can choose to use dispersion consistent with relativistic or non-relativistic dispersion, apply the Mermin correction to the Lindhard dielectric function or not, Mott cross section versus Coulomb cross section, optional inclusion of (simplified) exchange effects for electrons etc.

Only two types of particles are implemented: electrons and protons. Positrons will differ at very low energy due to absence of exchange effects, and at relativistic energies due to differences in cross section, but behave very similar to electrons at intermediate energies. For heavier nuclei, charge state effects add a level of complexity that is not implemented.

We hope that the program is useful for your research. For questions and bug reports, don't hesitate to contact us (maarten.vos@anu.edu.au)

Maarten Vos
Pedro Grande

Contents

1	Manual	1
1.1	Installation	1
1.2	Running Chapidif	1
1.3	Tab 1: Define dielectric function	1
1.3.1	GOS	2
1.3.2	Belkacem-Sigmund	3
1.3.3	Kaneko	3
1.3.4	RPA options	3
1.3.5	Dispersion	3
1.4	Tab 2: Perform calculations	4
1.4.1	plot dielectric function	4
1.4.2	color plot $\text{Im}[-1/\epsilon(\omega, q)]$	5
1.4.3	n, k	5
1.4.4	Kramers-Kronig tests	5
1.4.5	oscillator strength	5
1.4.6	dynamical structure factor	5
1.4.7	sum rules	5
1.4.8	inertial sum rules	5
1.4.9	$S(q, \omega)$ sum rule	5
1.4.10	mean ionization energy	5
1.4.11	Compton profile	6
1.4.12	Local density approximation: pseudo charge density	6
1.4.13	Local density approximation: radial pseudo charge density	6
1.4.14	Local density approximation: $\omega_p(r), \lambda(r)$ etc.	6
1.4.15	DIIMFP	7
1.4.16	Energy dependence IMFP, stopping and straggling	7
1.4.17	L (stopping number)	7
1.4.18	partial DIIMFP	7
1.4.19	double differential cross section at energy ω : $d\sigma/d\omega d\Omega$	7
1.4.20	differential cross section in angle: $d\sigma/d\Omega$	8
1.4.21	double differential cross section at angle Θ : $d\sigma/d\omega d\Omega$	8
1.4.22	differential cross section: $d\sigma/d\Omega$	8
1.4.23	2D-distributions $d\sigma/d\omega d\Omega$ with and without retardation	8
1.4.24	electron-specific: SELF, DSEP	8
1.4.25	electron-specific: color plot SELF	8
1.4.26	electron-specific: (R)EELS spectrum	8
1.4.27	Second Column	9
1.4.28	Third Column	9
1.4.29	Mott Correction	9
1.4.30	exchange correction	9
1.4.31	Third Column: DF transformations	10

1.4.32 DF from OOS	10
1.4.33 ‘Penn’	11
1.4.34 DL/Mermin to MLL	11
1.4.35 DL/Mermin to Kaneko	12
1.5 Defaults Tab	12
2 Model dielectric functions for ion stopping	14
2.1 Abstract	14
2.2 Introduction	14
2.2.1 Stopping in the linear regime	15
2.2.2 Physical observable quantities	16
2.2.3 Sum rules, Kramers-Kronig relations and mean excitation energy	17
2.3 Model Dielectric Functions (DF)	18
2.3.1 Ad-hoc DF	18
2.3.2 Examples of Classical Dielectric functions	19
2.3.3 Examples of quantum-physics based dielectric functions	22
2.4 Compton profiles	27
2.5 Multiple oscillators	30
2.6 Shell corrections in stopping	33
2.7 Conclusion	36
2.A Appendix: Stopping formulae and shell corrections for simple dispersion relations	40
2.B Appendix: Straggling formula for Ad-hoc and Drude-Lindhard DF	41
3 RPA Dielectric Functions: Streamlined Approach to Relaxation Effects, Binding and High Momentum Dispersion	43
3.1 abstract	43
3.2 Introduction	43
3.3 Classical Drude dielectric function	44
3.4 RPA based dielectric functions	46
3.4.1 RPA dielectric function for a free electron gas	48
3.4.2 Relativistic dispersion	48
3.4.3 RPA for Gaussian occupancy	48
3.4.4 Mermin Correction	49
3.4.5 Inclusion of ‘binding energy’ or ‘band gap’ effects	49
3.5 Alternative definition of ω_c	51
3.6 Proton stopping	53
3.7 Conclusion	53
3.A Appendix: Python Library DF_complex_lib	56
3.B Appendix: Sum Rules, Kramers-Kronig Relations	58
4 Dielectric functions, their properties and their relation to observables: investigations using the Chapidif program for the case of aluminum	62
4.1 abstract	62
4.2 Introduction	63
4.3 Model Dielectric Function	63
4.3.1 Drude-Lindhard model	64
4.3.2 Quantum physics-based models	65
4.3.3 Sum rules	65
4.3.4 Model used for Aluminum	66
4.4 Results from Chapidif Calculations	67
4.4.1 Visualizing the DF and checking sum rules	67
4.4.2 Density effect for valence band	70

4.4.3	Compton profiles	72
4.4.4	Measurement of the loss function at specific momentum transfers	72
4.4.5	Differential cross sections and scattering angles	73
4.4.6	Differential inelastic inverse mean-free-path	78
4.4.7	IMFP, stopping and straggling	78
4.4.8	Pseudo Charge-Density	82
4.4.9	Consequences of the assumptions for dispersion and exchange	84
4.4.10	Using tabulated oscillator strength as input	86
4.4.11	Electron energy loss spectra	86
4.5	Some Numerical Details	91
4.6	Conclusion and Outlook	92
4.7	Acknowledgement	93
4.A	Appendix: Installation	99
4.B	Appendix: Relativistic Kinematics	99
5	Extensions of Kaneko's wave-packet model for non-zero angular momentum orbitals	102
5.1	abstract	102
5.2	Introduction	102
5.3	Modifications and extensions of Kaneko's model	104
5.3.1	$l = 0$ states	104
5.3.2	extension for $l \neq 0$	105
5.3.3	using Gaussian basis sets	106
5.3.4	introducing a minimum excitation energy	106
5.3.5	changing the reference density	106
5.3.6	local approximation	106
5.4	Comparing model dielectric functions	107
5.5	Comparing with experiment	109
5.6	Real materials	110
5.6.1	homogeneous Kaneko approach	110
5.6.2	Local Kaneko approach	113
5.7	Discussion and conclusion	115
5.A	Appendix: Kaneko theory based on subshell density	119
5.A.1	Subshell density	119
5.A.2	The relation between dielectric function and sub-shell densities	119
5.A.3	Evaluation of dielectric function for $l=0$	120
5.B	Appendix: Use of Gaussian basis sets	121
5.C	Appendix: Derive Kaneko-type dielectric function from optical ELF	122
6	A unified approach to the inelastic mean free path,stopping and straggling of electrons and protons using a simple analytical-solvable model	124
6.1	Introduction	124
6.2	Dielectric theory	126
6.2.1	Stopping, single oscillator	127
6.2.2	IMFP, single oscillator	129
6.2.3	Straggling: single oscillator	130
6.2.4	Summary single oscillator results	131
6.3	Multiple Components	131
6.3.1	Stopping, multiple components	134
6.3.2	IMFP: multiple components	135
6.3.3	Straggling: multiple components	136
6.4	Deriving parameters for the core levels from appropriate GOS calculations	136

6.5 Comparing with experiment	138
6.5.1 IMFP	138
6.5.2 Stopping	142
6.5.3 Straggling	143
6.6 Conclusion	144

Chapter 1

Manual

1.1 Installation

- unzip the archive containing the chapidif program at a location of your choice
- In lib-source directory contains both the epslib.cpp source file and the Faddeeva.cc source file, the latter containing an open-source implementation of the Faddeeva function. There are batch files for compiling the source files for your operating system:

```
script_epslib.bat: windows 32 bit (not tested)
script_epslib_64.bat: windows 64 bit
script_epslib.sh: linux
script_epslib_mac.sh : mac
```

Execute the appropriate script, and the library should be created in the lib subfolder.
(requires gcc)

- Then execute chapidif.py in the usual way you execute a python3 file. (It requires that the following (widely-used) python packages are installed: matplotlib, tkinter, numpy)

1.2 Running Chapidif

The user interface consists of 3 tabs, the first tab defines the dielectric function that describes the material, the second tab selects the desired calculation, and the third tab allows for changing some of the default parameters, for the calculation and the plot appearance.

In the chapter we link the different items of the user interface with description of the underlying features in the following chapters.

1.3 Tab 1: Define dielectric function

The dielectric function consists of one (or more) of the following components: valence band Oscillator, a Hydrogenic GOS, Belkacem-Sigmund harmonic oscillator or a Kaneko Oscillator

Valence band model Oscillators

The model oscillator are usually used to describe the valence band and can be either:

-Extended Drude type, see section 2.3.2 (a)

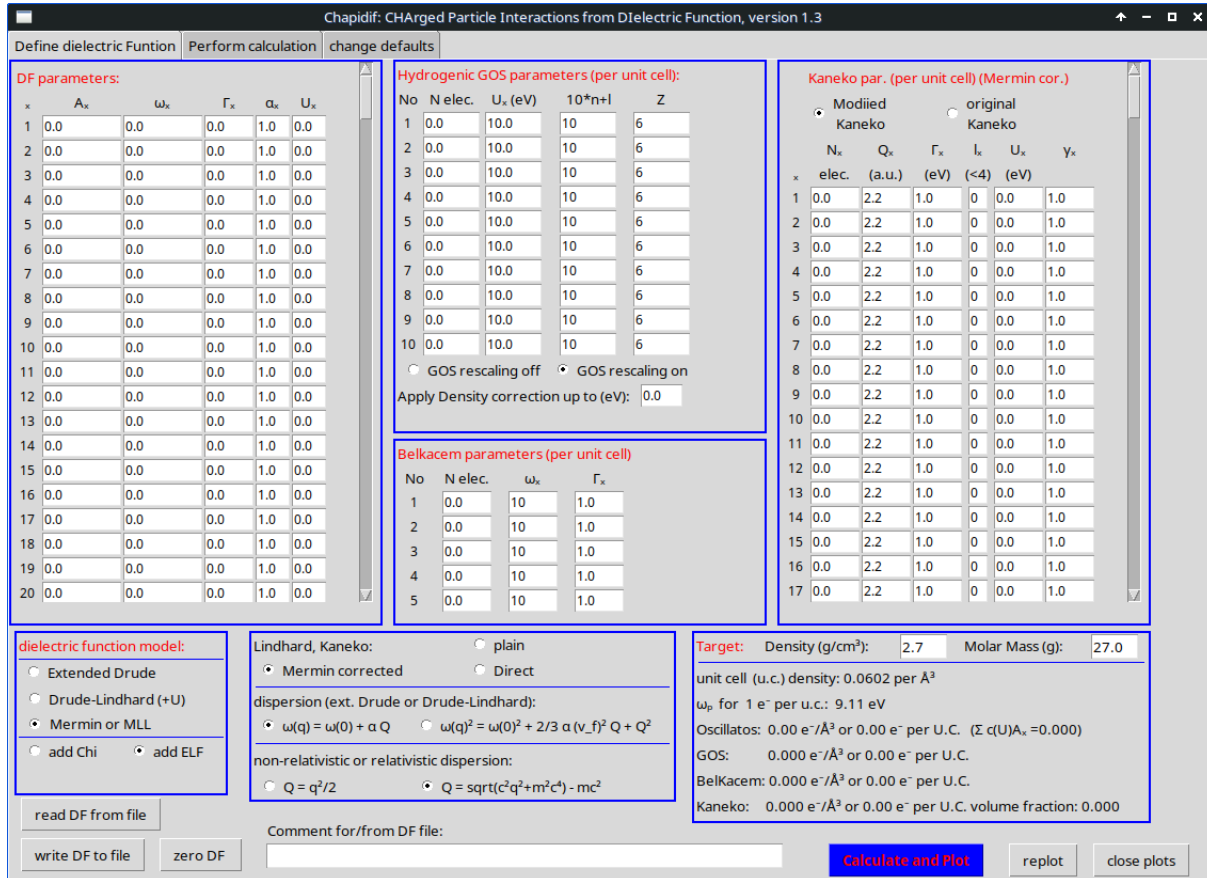


Figure 1.1: the tab defining the dielectric function

-Drude-Lindhard type, see section 2.3.2 (b)

-Mermin or Levine-Louie type, see section 2.3.3

The type of oscillator used depends on the choice of the radiobutton in the lower left box. If more than one oscillator is present then either the energy loss function (ELF) is added or the Chi's are added, as discussed in section. 2.5. These model oscillators are defined per unit volume. If the correct density and molecular mass is used for input in the lower right box, then the lower right box also displays the number of electrons associated with all model oscillators per unit cell. If this output turns red, then non-physical input is used (in particular for Drude-Lindhard or Mermin: $\sum_i A_i > 1$), see figure 4.1 and associated text. All other contributions are per unit cell. How they are added depends thus also on the input parameters: Target density and Molar mass.

1.3.1 GOS

GOS (generalized oscillator strength) contributions, based on hydrogenic wave functions, are available for the orbitals in the K, L and M shells. see section 2.3.3. It is most useful describing deeper core levels. To ensure the same contribution at any q value, the GOS rescaling button should be checked. Without density correction one has for the GOS: $\text{Im}[-1/\epsilon(\omega, q)] = \text{Im}\epsilon(\omega, q)$, a reasonable approximation for deep core levels or low-density matter (gas) but not for shallow core levels, see fig. 2.10 and associated text. Density correction is calculated up to energy loss value given here. It slows down the calculation a lot, and has minor influence for stopping etc. but is important if one wants to accurately check the sum rules, see section 4.4.1.

1.3.2 Belkacem-Sigmund

This model dielectric function for electrons bound in a harmonic potential. It is one of the few quantum systems for which a dielectric function is readily calculated. See section 2.3.3 for details. It is not expected that this approach can be directly applied to ‘real materials’.

1.3.3 Kaneko

This is another approach of describing the contribution of deeper levels to the dielectric function. It differs from a free-electron approach, where levels are occupied up to the Fermi level, and mimics the more gradual decrease of momentum densities seen for core levels. See section 2.3.3 and chapter 5 for more extensive discussions and the meaning of the parameters.

1.3.4 RPA options

Lindhard and Kaneko gave expressions that were intended to be used in the limit of $\Gamma \rightarrow 0$. The ‘plain’ option uses these expressions with the Γ values of the dielectric function. The Mermin-corrected option fixes issues in the RPA solution of Lindhard with finite Γ values. Without the Mermin correction the dielectric function is called ‘Lindhard’. If checked, the Mermin correction is also applied to the Kaneko oscillators. Alternatively a ‘direct method’ can be used, which calculates the dielectric functions with the same limiting properties of the Mermin one, as explained in chapter 3.

1.3.5 Dispersion

For the classical models ‘extended Drude’ or ‘Drude Lindhard’ one can choose either ‘simple quadratic dispersion’ (eq. 2.16) or ‘full dispersion’ (eq. 2.17). If the energy transfer to the target electron is non-negligible compared to its rest mass (511 keV) then dispersion is affected by relativistic effects. For all contributions relativistic dispersion is used when the relativistic dispersion box is ticked.

Files

Once a dielectric function has been defined it can be written to file for later retrieval. The comment description is added to the file, for convenience. The default extension is CPD but a DAT extension has also been used for literature dielectric function. If the result of a calculation is saved (see next tab) then the definition of the dielectric function is the file header. So the dielectric function can also be recovered by reading a result file.

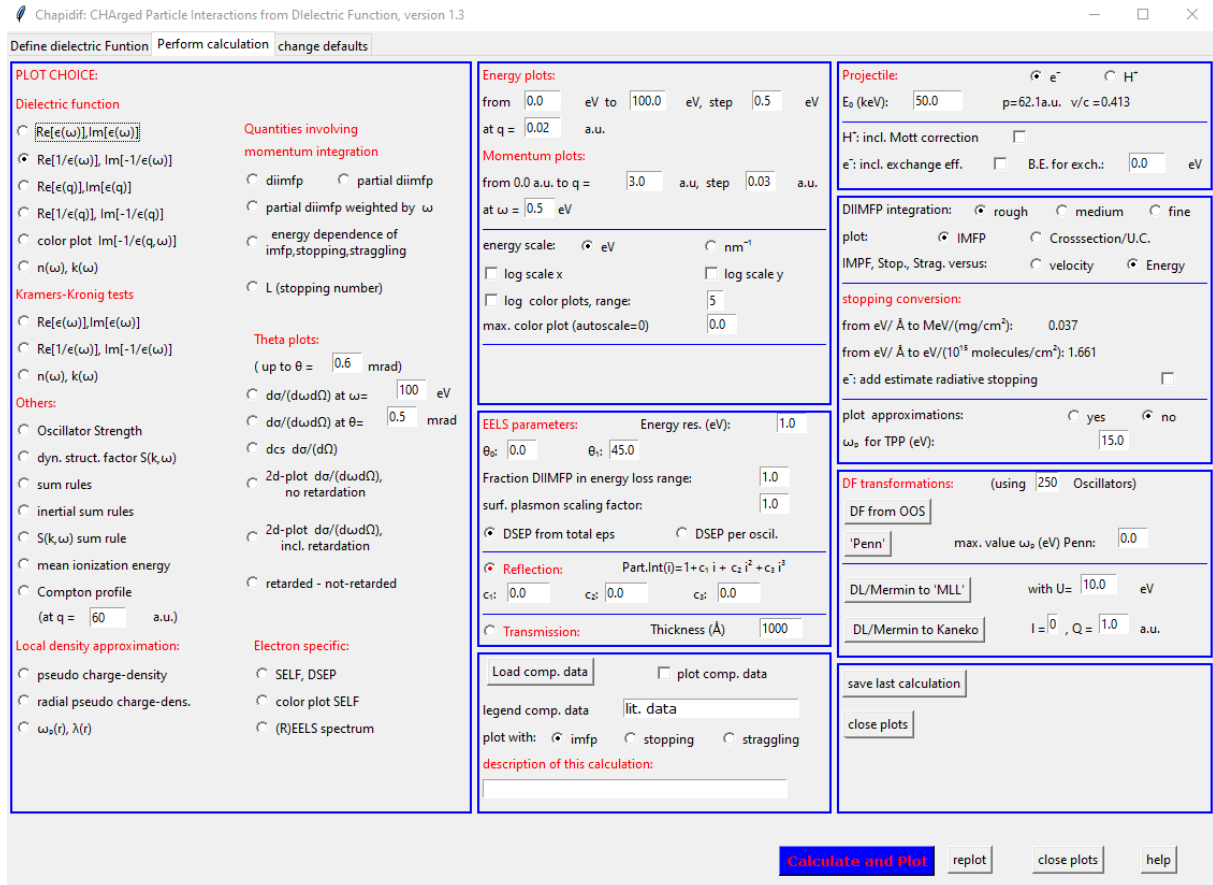


Figure 1.2: the tab defining what to calculate and plot. Left panel determines what is calculated. Center and right panel define the parameters being used and plot options.

1.4 Tab 2: Perform calculations

The calculations tab consists of 3 column. The left column determines what is calculated and plotted. The central and right panel determine parameters for the calculation and plotting.

Many calculations are done for a specific energy loss ω or a specific momentum transfer q . ω or q as their x -axis. Which energy loss and momentum transfer is determined by the top central box, which also sets the range of the plot, as well as the step size. For Mermin and Kaneko calculations at $q = 0$ would result in an error and for very small q the equivalent Drude-Lindhard dielectric function is used instead.

It is often worthwhile, if the calculation depends on the energy or momentum step size used, to repeat it with a smaller step size, or larger range. The step size in energy loss should be smaller than the sharpest feature in the loss distribution.

In the following we mention the quantities that can be calculated and refer to examples of its use, mainly in chapter 4, where additional details can be found.

1.4.1 plot dielectric function

The first 4 calculation options plot the dielectric function either $\epsilon(\omega, q)$ or $1/\epsilon(\omega, q)$ as a function of either the momentum transfer q or energy loss ω .

1.4.2 color plot $\text{Im}[-1/\epsilon(\omega, q)]$

Plot the loss function as a two-dimensional (2D) false color plot, see e.g. fig 4.3. The color plot can either be linear or based on the log of the loss intensity, as set by the parameters in the central column. Here also the maximum value displayed in the 2D-distribution can be set manually.

In addition, the boundary of the ω, q -space that can be excited by the current projectile is shown as a red line. The current projectile (either electron or proton) and its energy, for which this boundary applies, is set in the top-right box of the calculations tab. If the energy of the projectile is set to 0, then the red line is suppressed.

1.4.3 n, k

Plot the refractive index and extinction coefficient as a function of ω at the current q value, see e.g. fig. 4.20, right panels. The energy scale can be either in eV or nm^{-1} , as set by the check box in the central column.

1.4.4 Kramers-Kronig tests

This plots either the $\epsilon(\omega, q)$ or $1/\epsilon(\omega, q)$ or $n(\omega, q)$, $k(\omega, q)$ distribution at a specific q just as the previous options but in addition calculates the real part from the imaginary part and vice versa via the Kramers-Kronig transformation. As an example, see fig. 4.1.

1.4.5 oscillator strength

Plots the (generalized) oscillator strength (loss function weighted by ω) at the current q value as a function of ω . At $q = 0$ this quantity is often referred to as the optical oscillator strength (OOS).

1.4.6 dynamical structure factor

This is another quantity, closely related to the loss function, see fig. 4.6. Requires $q > 0$.

1.4.7 sum rules

Plot the Bethe, F and k sum rules for the current dielectric function at the present q value. For this to work properly, the range of the energy plot should start at 0, and the step size in ω should be sufficiently small. See fig. 4.1, right panels.

1.4.8 inertial sum rules

More sum rules, these often require small step sizes and converge only at large energy losses, see fig. 4.2, first 3 panels.

1.4.9 $S(q, \omega)$ sum rule

Sum rule for the dynamical structure factor, see fig. 4.2 last panel.

1.4.10 mean ionization energy

This option calculates the mean ionization energy I from the integral:

$$\ln I = \frac{\int_0^\infty \omega' \log \omega' \text{Im}[-1/\epsilon(\omega', 0)] d\omega'}{\int_0^\omega \omega' \text{Im}[-1/\epsilon(\omega', 0)] d\omega'}. \quad (1.1)$$

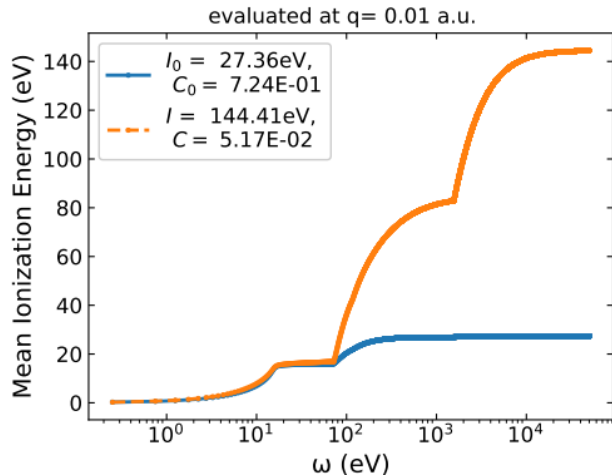


Figure 1.3: Result of the integrals 1.2 and 1.1 for a model dielectric function of Aluminum

This is a slowly converging integral and for obtaining the right value of the mean ionization energy the ω range has to extend to large values. The mean ionization energy is central to the Bethe theory of stopping and determines the stopping behaviour for high projectile energies.

A similar integral can be derived for the IMFP (I_0):

$$\ln I_0 = \frac{\int_0^\infty \log \omega' \text{Im}[-1/\epsilon(\omega', 0)] d\omega'}{\int_0^\omega \omega' \text{Im}[-1/\epsilon(\omega', 0)] d\omega'}. \quad (1.2)$$

Figure 1.3 shows these integrals for the standard model dielectric function for aluminum of chapter 4 (see table 4.1).

The behaviour for IMFP (stopping) in the limit of high-energy is the same of a single, narrow Drude-Lindhard oscillator at energy I_0 (I) and amplitude C_0 (C), see chapter 6 for details.

1.4.11 Compton profile

This calculates a Compton profile at the specified q value. For smaller q -values the Compton profile is somewhat asymmetric and changes with q . For high-enough q values the profile becomes symmetric and does not change if q is increased further. Then it relates to the momentum density of the target electrons, see fig. 4.5

1.4.12 Local density approximation: pseudo charge density

In the local density approximation the intensity of the ELF at energy loss ω at $q = 0$ is related to a part of the unit cell that is filled with an electron gas with density such that $\omega_p = \omega$. It is thus possible to retrieve this charge density from the ELF, see fig. 4.13, top left panel. This (and the next 2) items first calculate the ELF at $q \approx 0$, and it depends thus on the range set for the energy plots in the middle column.

1.4.13 Local density approximation: radial pseudo charge density

If there is only one atom per unit cell, and one approximates the unit cell by a sphere with the same volume (Muffin Tin approximation) then the pseudo charge density, calculated in the previous item, can be transformed to a radial charge density, see fig. 4.13, top right panel.

1.4.14 Local density approximation: $\omega_p(r)$, $\lambda(r)$ etc.

This plots (based on the radial pseudo charge density) as a function of r the plasmon energy ω_p , IMFP stopping and straggling that are characteristic for a free electron gas with the density that

is present at r , as calculated in the previous item. The approximate formulae for Drude-Lindhard oscillators are used here, see chapter 6.

1.4.15 DIIMFP

Note This, and the next 4 quantities, involve integration over $\omega - q$ space. The precision required (and the time consumed) depend on the quality settings for DIIMFP integration in the 3rd column

The DIIMFP option calculates the differential inverse inelastic mean free path, considering the energy range of the energy plots as boundaries, but extending over all q . The energy step of the integration is constant, and the same as the energy step of the energy plots. It displays a plot of the DIIMFP and gives the IMFP, stopping and straggling based on the energy range considered. It obviously depends on the energy and particle type (electron/proton) set in the top of the right column. See fig. 4.10 top panel, for an example.

1.4.16 Energy dependence IMPF, stopping and straggling

This calculates the IMFP, stopping and straggling for the current projectile. Integration extends over all q values and energy losses (as far as practical). For electrons the inclusion of "exchange" (right column) influences the result, for protons the choice of cross section ('Mott correction' or 'Coulomb') influences the result at relativistic energies.

For this option the smallest step used in the energy integration is the step size of the energy plots (central column). To speed up this calculation this step size increases with energy loss by a factor set in Tab3 ('energy increment factor').

Plots can be made as a function of projectile energy (keV) or as function of projectile velocity (a.u.), as set in the right column. An example is given in the lower panels of fig. 4.12.

Instead of the IMFP it is also possible to plot the cross section per unit cell (i.e. per atom if there is only a single atom in the unit cell), as controlled by a 'tick box' in the right column.

The number of projectile energies calculated and energy increment factor can be varied by parameters in the default tab. Using the standard parameters values calculated for protons and electrons are at the same velocity.

It is possible to plot the approximate results as derived in chapter 6 as well, by ticking the 'plot approximation' check box (again right column). For the TPP (Tanuma-Powell-Penn) approximation of the IMFP one has to manually add the correct plasmon energy for the TPP theory (right column)

1.4.17 L (stopping number)

The stopping is usually written as a product of two factors: $(-\frac{dE}{dx}) = \frac{4\pi n}{v^2} L$, with n the electron density and v the projectile velocity). Often L is plotted, rather than the stopping itself, see the top panels of fig. 4.12 for an example.

1.4.18 partial DIIMFP

Here we take the maximum (q_{\max}) of the range of the momentum plots (top second column) and divide the momentum range of the DIIMFP integration into 10 segments with width $q_{\max}/10$, and perform the DIIMFP integration for each momentum segment only. It gives an impression how the contribution to the DIIMFP depends on q . See fig. 4.10, lower panel.

1.4.19 double differential cross section at energy ω : $d\sigma/d\omega d\Omega$

In the following we describe some cross sections that can be obtained from the dielectric function for either electrons or protons. The maximum scattering angle considered is θ_{\max} variable for

the "Theta plots".

The double differential cross section (DDCS: $d\sigma/d\omega d\Omega$, scattering cross section per unit energy (ω) and unit solid angle (Ω) can be calculated for electrons at a chosen energy loss, either with or without relativistic corrections (retardation), see fig. 4.7 top panels.

1.4.20 differential cross section in angle: $d\sigma/d\Omega$

Integrating the DDCS over all possible energy losses ω one obtains the DCS ($d\sigma/d\Omega$), see e.g. the lower panel of fig. 4.7.

1.4.21 double differential cross section at angle Θ : $d\sigma/d\omega d\Omega$

Rather than plotting the DDCS at a specific energy as a function of angle , one can plot the DDCS at a particular angle as a function of energy. For scattering angle of $\theta = 0$ this is proportional to the loss function at the red line of fig. 4.3 and is given in fig. 4.9 for the case of proton scattering from aluminum.

1.4.22 differential cross section: $d\sigma/d\Omega$

Integrating the DDCS over all possible energy losses ω one obtains the DCS ($d\sigma/d\Omega$), see e.g. the lower panel of fig. 4.7.

1.4.23 2D-distributions $d\sigma/d\omega d\Omega$ with and without retardation

For an example of the 2d-distribution of the DDCS for protons from an electron gas see fig. 4.8 at non-relativistic speeds. Due to the large mass difference between a proton and an electron there is only a limited range of scattering angles and a limited range of energy losses possible.

At relativistic speeds retardation effects become significant. It is possible to make a false color plot of the DDCS either with or without retardation. This is particularly of interest for insulators where Cerenkov radiation can be produced if the projectile's speed exceeds the speed of light in the medium. An example for a dielectric function that resembles the one of GaP is shown in figure 1.4. It shows the DDCS distribution for 100 keV electrons without retardation (A), with retardation (B), their difference (C) as well as a plot of the DDCS with retardation over a larger angular range. For the background see section 4.4.5.

1.4.24 electron-specific: SELF, DSEP

For electrons as projectile surface plasmons can be created when the electron moves from the vacuum into the material and vice-versa. Associated with this are the Surface Energy Loss Function (SELF) and the Differential Surface Excitation Parameter (DSEP), as shown in fig. 4.18, top panel.

1.4.25 electron-specific: color plot SELF

A false color plot of the Surface Energy Loss Function, see 4.18, lower panel.

1.4.26 electron-specific: (R)EELS spectrum

It is possible to generate a (R)EELS ((reflection) electron energy loss spectroscopy) spectrum from the current dielectric function. Parameters are defined in the second box of the central column. Either a transmission spectrum (then it is EELS) or a spectrum in a reflection geometry (i.e. REELS) can be calculated. In the latter case one can change the partial intensities by the parameters c_1 , c_2 and c_3 (take values much magnitude smaller than 1 for these parameters). For details see fig. 4.19 and fig. 4.20 and their discussion.

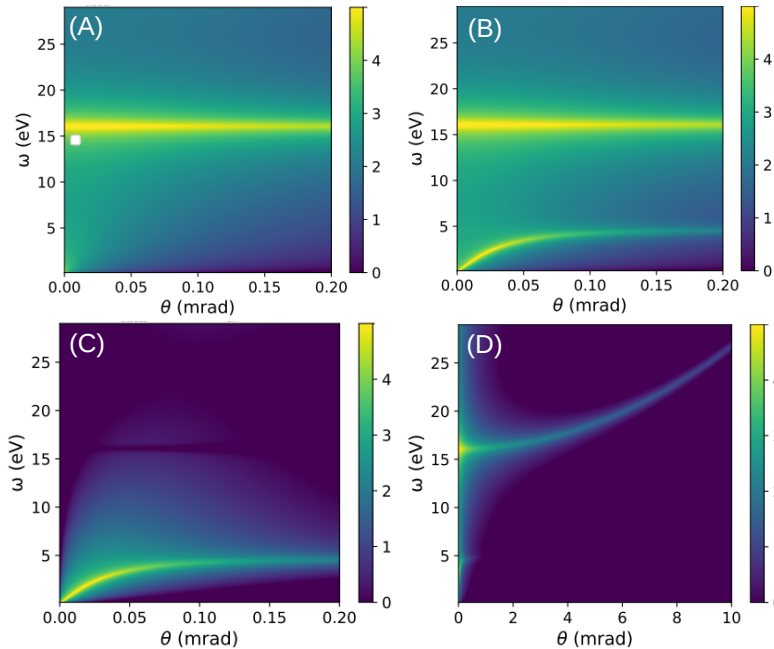


Figure 1.4: The DDGS of 100keV electrons for a dielectric function resembling that of GaP. The log of the DDGS distribution for 100 keV electrons is plotted without retardation (A), with retardation (B), their difference (C), representing the Cerenkov losses as well as a plot of the DDGS with retardation over a larger energy range (D).

1.4.27 Second Column

These items affect what is calculated and how it is plotted. Most of it will be self-explanatory. We discuss here the last item.

It is possible to display an additional curve ('comparison data') in the $x = y$ plots. In this way one can compare the result of the calculation easily with e.g. experimental results or estimates obtained from the literature etc.

One has to read this curve from a simple ascii file. The first line is comment, then the program expects (many) lines with two numbers, the x,y coordinates for each data points. A string can be added that is treated as the legend of the comparison data. The comparison data will only be plotted if the corresponding box is ticked.

1.4.28 Third Column

Most items will be self-explanatory, or have been discussed in the context of the relevant calculation. Here, only the description of the non-trivial items

1.4.29 Mott Correction

For protons at relativistic speed the interaction between nuclei deviates from the Coulomb one. An approximate correction is calculated based on correction factor eq. 16 of Salvat PRA 106 032809

1.4.30 exchange correction

A simple estimate of the exchange effects on the IMFP stopping and straggling can be included for electrons, but only when the dielectric function is due to a single level with binding energy E_b as specified here. It is assumed that the energy loss is due to a collision with a target electron that creates a secondary electron. The secondary electron has an kinetic energy of $\omega - E_b$. Then a projectile electron with energy loss of ω has the same kinetic energy ($E_0 - \omega$) as the secondary electron created after a collision with energy loss $\omega' = E_0 - \omega + E_b$. These electrons are indistinguishable and can 'interfere'. Thus one has to take these two contributions together as described by e.g. Ashley, J. Electron Spectroscopy 46 199 (1988). The DIIMFP (including

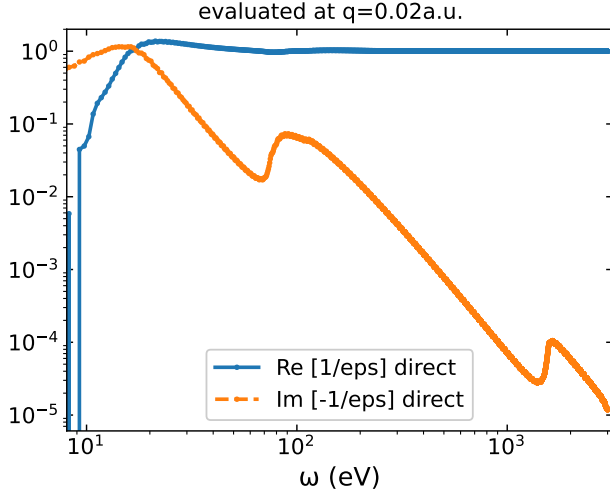


Figure 1.5: The ELF as obtained from the fit of the OOS file of a cBethe run with 250 DL oscillators.

exchange) at energy loss ω for an electron with binding energy U is then given by:

$$W_b^{\text{exch}}(\omega) = W_b(\omega) + W_b(E_0 - \omega + U) - \sqrt{W_b(\omega)W_b(E_0 - \omega + U)} \quad (1.3)$$

where the 3rd term is a quantum effect. The largest possible energy loss is $0.5(E_0 + U)$. Applying this to the valence band (with $E_b = 0$) will overestimate the exchange correction as plasmon excitation does not correspond to a secondary electron that is indistinguishable from the primary electron after energy loss.

Alternatively exchange effects can be included, in a way similar to what is done in SBethe [1] by restricting the range of possible energy losses ω to values smaller than $0.5E_0$ and replacing the Rutherford cross section by the Møller one, i.e scaling the DIIMFP by a factor

$$F_{\text{Møller}} = 1 + \left(\frac{\omega}{\omega - E_0} \right)^2 - \frac{(1-b)\omega}{E_0 - \omega} + b \frac{\omega^2}{E_0^2}, \quad (1.4)$$

with $b = \left(\frac{\gamma-1}{\gamma} \right)^2$. This approximation should work well for large E_0 values.

Which approximation is used is determined by a tick box in the ‘change defaults’ panel

1.4.31 Third Column: DF transformations

The first two options calculate dielectric function based on DL or Mermin oscillators that describe a certain ELF. It uses only the ELF in the current energy range of the plot. The number of oscillators used can be chosen (up to a maximum of 250).

1.4.32 DF from OOS

Often one want to use the ELF in the optical limit as a starting point. The program cBethe by Salvat (F. Salvat, Phys. Rev. A 106, 032809, 2022) is available in the supplementary material of that paper and gives state-of-the-art way of calculating stopping power of charged particles. Running this program gives a file that contains the optical oscillator strength (OOS) with extension ‘.mat’. Chapidif can read this file and generate a set of Drude-Lindhard (or Mermin) oscillators that has approximately the same OOS. It can be used as a starting point for Chapidif-based calculations. An example of the obtained ELF from cBethe for the case of aluminum is given in fig. 1.5.

The program extract an dielectric function based on the current energy range of the energy plots. This allows for the selection of a certain energy window.

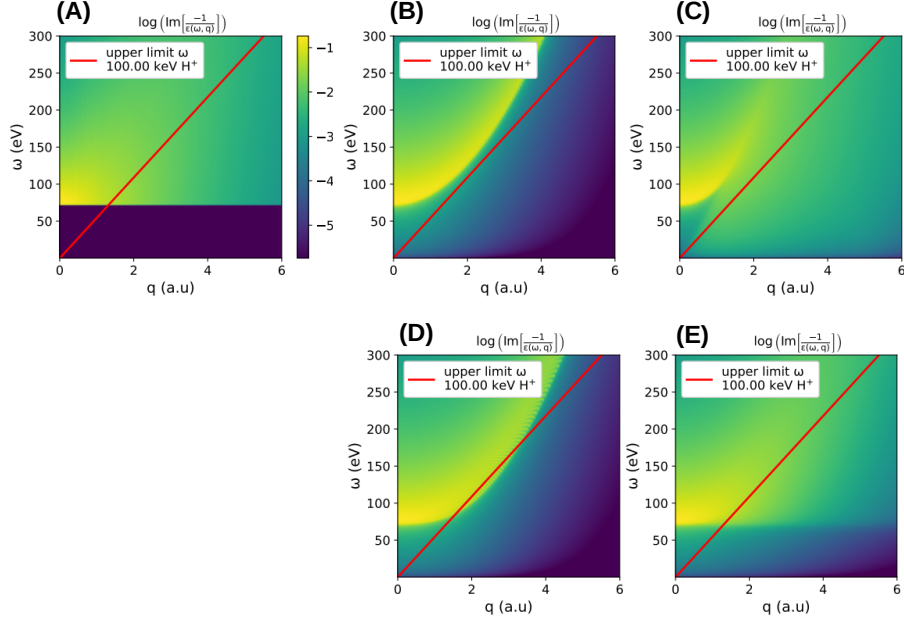


Figure 1.6: The loss function as calculated from the Al 2p GOS (A) and that obtained after fitting the GOS ELF at $q = 0$ with 250 oscillators, interpreted as Drude-Lindhard oscillators (B), or Mermin oscillators (C). In (B) and (C) the U parameter was set to 0 eV. In (D) and (E) we show again the results for Drude-Lindhard oscillators and Mermin oscillators respectively, but now with $U = 70$ eV. For 100 keV H^+ excitations are only possible for ω, q combinations below the red line.

1.4.33 ‘Penn’

This option fits the ELF corresponding to the currently defined dielectric function with a number of DL or Mermin oscillators. For example one can calculate the ELF (at $q = 0$) from a GOS, and obtain a set of oscillators that describe approximately this ELF. As the dispersion of DL and GOS is different one can study in this way to what extend two dielectric functions with the same optical ELF can have different stopping. Under normal operation the Penn procedure leaves the U parameter at zero, but a constant U value can be added afterwards with the ‘DL/Mermin to MLL’ button. Fitting is accomplished by varying the amplitude of regularly spaced (in ω oscillators, and with width of the order of the oscillator spacing.

The description above is when the ‘max value ω_p ’ parameter is set to zero. If this parameter is set to other values then the procedure does not change for oscillators with ω_p less than this value. For larger losses the ELF is fitted by putting ω_p to the maximum value but adding a (varying) U value for oscillators describing higher losses. The idea is to describe valence electrons with a free electron like approach and assume that binding (i.e. U) is important for core electrons.

1.4.34 DL/Mermin to MLL

Calculates the parameters of a MLL dielectric function (with the U value chosen by the user) that has the same optical ELF as the current set of DL or Mermin oscillators. If other contributions to the ELF are present, first fit them with the ‘Penn’ option. Oscillators with energy less than U will not be considered. This can be used to study how, e.g. the stopping varies when a U parameter is introduced. In fig 1.6 we show the loss function as a false color plot for the Al 2p GOS and the loss function obtained after the ‘Penn’ procedure, with U parameter of either 0 or 70 eV and the oscillators interpreted as either Mermin or Drude-Lindhard.

1.4.35 DL/Mermin to Kaneko

Calculates a set of Kaneko oscillators that have the same ELF as the current set of DL (or Mermin) oscillators. If an U value was present then this will apply to the Kaneko DF as well. The Kaneko oscillators have a Q and l value as defined by the user. Fitting of the ELF is accomplished by adjusting the γ parameter as defined by Archubi and Arista (Phys. Rev. A 96, 062701 (2017))

1.5 Defaults Tab

This should be mostly self-explanatory.

Bibliography

- [1] F. Salvat, P. Andreo, Sbethe: Stopping powers of materials for swift charged particles from the corrected Bethe formula, Comput. Phys. Commun. 287. doi:10.1016/j.cpc.2023.108697.

Chapter 2

Model dielectric functions for ion stopping : the relation between their shell corrections, plasmon dispersion and Compton profiles.¹

2.1 Abstract

We describe a set of energy (ω) and momentum (q) dependent dielectric functions with the same shape of the loss function ($\text{Im}[-1/\epsilon(\omega, q)]$) in the optical limit ($q = 0$) and thus the same mean ionization energy I but different behavior away from $q = 0$. The corresponding proton stopping values differ especially at lower energies. Within the Bethe formula the stopping only depends on the mean excitation energy I . These models display thus different shell corrections, defined as the deviation from the stopping from the Bethe values. Shell-correction contributions originate equally from collisions with low momentum transfer and with high momentum transfer. Intermediate q collisions do not contribute to the shell corrections. At high q the shell corrections are related to the width of the loss function at these q values. (which is proportional to the momentum distribution of the electrons ('Compton profiles')) or, for classical models, from a shift in position. The low- q contribution is related to the plasmon dispersion.

2.2 Introduction

The interaction of fast, charged particles with matter has been a central topic of research for a long time. Bohr used it to test his emerging understanding of the quantum nature of matter [1], Bethe derived a first description, fully consistent with modern quantum physics [2], and further refinements were due to Lindhard [3], to name only the major players. Besides its fundamental interest the topic is studied for its importance in technological fields like ion beam analysis and ion beam modification of materials. More recently, it has attracted attention within the context of ion-beam based cancer therapy. It is also used to calculate the excitation spectra after interacting with hypothetical dark matter [4]. The field has been thoroughly reviewed by Sigmund [5] and is described in the context of materials science by Nastasi *et al* [6], and in medical physics by Nikjoo *et al* [7]. In medical physics the dielectric function is used in track simulation of protons and electrons for charged particle dosimetry see e.g. [8, 9].

In the first Born approximation (FBA) the interaction between projectile and target is considered weak. This is the case when the charge of the projectile is small and its velocity is large. Then one is in the linear regime and first order perturbation theory should suffice. The projectile

¹Updated version of M. Vos and P.L. Grande Advances in Quantum Chemistry Volume 85, 2022, Pages 267-301

can then be described as a plane wave and cross sections are proportional to the square of its charge. Under these conditions ion stopping can then be described in terms of the momentum (q) and energy (ω)-dependent dielectric function $\epsilon(\omega, q)$ [5, 10]. Within this framework obtaining the right stopping values requires knowledge of $\epsilon(\omega, q)$ (or equivalently knowledge of $\text{Im}[-1/\epsilon(\omega, q)]$), but generally, there are no experimental data or ab-initio calculations of this quantity, especially away from $q = 0$. Therefore, model dielectric functions are often employed.

An overview of a variety of model dielectric functions used in the literature was given by Nikjoo *et al* [10] and within the context of proton stopping in water by Emfietzoglou *et al* [11]. The effect of calculating the dielectric function beyond the random phase approximation (RPA) is discussed in ref. [12]. Novel approaches of including the q -dependence to the dielectric function were discussed by Chantler and Bourke [13, 14] will not be considered here.

We want to study how ion stopping depends on the extension scheme used for the dielectric function away from $q = 0$ in particular how the stopping of different models differ from the Bethe value. The dielectric functions are either based on classical physics (Drude-Lindhard and extended Drude) or formulated in terms of the RPA and based on either:

- plane waves with occupied states up to k_f (Lindhard [3], Mermin [15])
- plane waves with a Gaussian dependence of the occupation number (Kaneko [16])
- hydrogenic wave functions (then, in the dilute limit the loss function can be expressed in terms of the generalised oscillator strength (GOS))
- eigenfunctions of the harmonic potential [17, 18].

These models can be modified for the presence of a band gap U as demonstrated by Levine and Louie for the Lindhard dielectric function. This modification was not strictly derived but its merits is that the obtained dielectric function resembles that of a semiconductor/insulator and adheres to sum rules and Kramers Kronig relations. All models converge to the Bethe stopping values at high proton energies, but the rate of convergence differ greatly i.e. they have different shell corrections.

We aim to keep the discussion as simple as possible, suitable as an introduction to the topic, and will only consider proton stopping, to avoid largely the problems due to different charge states, and assume that the projectile velocity is low enough for relativistic effects to be neglected. Unless otherwise stated we use atomic units ($\hbar = 1$, $m_e = 1$, $\frac{e^2}{4\pi\varepsilon_0} = 1$).

Calculations were done with the Chapidif python/C++ code which is available on request from one of the authors (M. Vos).

2.2.1 Stopping in the linear regime

The relation between stopping and the dielectric function can be derived using purely classical physics arguments, or based on quantum physics.

Within the classical picture the potential due to the fast projectile causes a change in potential varying in space and time. This can be decomposed in different Fourier components, and then the induced charge redistribution in the target is described by $\epsilon(\omega, q)$. The redistributed charge causes an electrostatic field at the projectile position (the wake field) which causes a decelerating force. The stopping is then just the magnitude of the projectile charge times this induced field (see Abril *et al* [19] for details).

Within quantum physics one calculates, based on perturbation theory, the probability that the projectile with energy E_0 loses ω energy and changes momentum by q per unit length travelled. This is the double differential inverse inelastic mean free path $\frac{d\Lambda}{d\omega dq}$: It is given by [7]:

$$\frac{d\Lambda}{d\omega dq} = \frac{2Z^2}{\pi v^2} \frac{1}{q} \text{Im} \left[\frac{-1}{\epsilon(\omega, q)} \right]. \quad (2.1)$$

where the Z and v are the charge and velocity of the projectile and $\text{Im} \left[\frac{-1}{\epsilon(\omega, q)} \right]$, often called the energy loss function (ELF) is a target property. The fact that $\frac{d\Lambda}{d\omega dq}$ can be written as a product

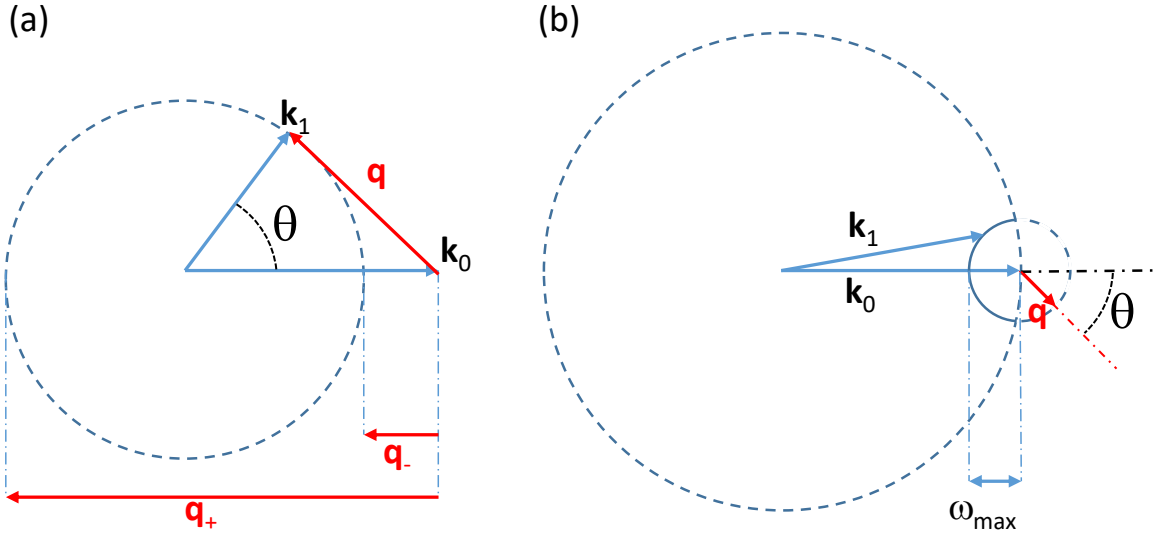


Figure 2.1: In (a) we show the kinematics at constant energy loss ω . The transferred momentum q is the difference in momentum particle before ($|k_0| = \sqrt{2ME_0}$) and after ($|k_1| = \sqrt{2M(E_0 - \omega)}$) the energy loss event and varies from $q_- = |k_0| - |k_1|$ for $\theta = 0^\circ$ to $q_+ = |k_0| + |k_1|$ for $\theta = 180^\circ$. In (b) we show the kinematics at constant magnitude of \mathbf{q} . The largest energy loss is now (for $\theta = 180^\circ$) $\omega_{\max} = k_0^2/2M - (k_0 - q)^2/2M \simeq qv_0$. The dashed part of the small circle corresponds to energy gain, and can not be accessed.

of two factors, one describing the projectile and one describing the target, is a general property of the first Born approximation. Note that the quantum description also describes the deflections due to the projectile-target interactions, which are particularly important for light projectiles (electrons), but were absent in the classical approach sketched before. Also, as we will see, the quantum description makes it possible to calculate other properties such as the inelastic mean free path and straggling, that do not easily follow from the classical description. See the book by Nikjoo *et al* [7] for a more complete introduction to the dielectric theory within quantum physics.

2.2.2 Physical observable quantities

In the context of describing the charged particle interaction with matter there are 3 quantities that are often used to characterize this interaction: the mean-free-path (usually calculated when the charged particle is an electron) and the stopping and straggling (calculated both for electrons and ions). As we will see these quantities are obtained by integrating the loss function ($\text{Im}[-1/\epsilon(\omega, q)]$) suitably weighted over the accessible $q-\omega$ space. However, one can also measure the dielectric function directly e.g the dielectric function at $q = 0$ by optical means by measuring absorption and/or reflection as a function of the energy of a photon [20]. Alternatively, using thin samples the loss function can be obtained at $q \simeq 0$ by measuring in the forward direction the energy of a transmitted high-energy electron beam [21]. The experimental knowledge of the dielectric function away from $q = 0$ is much more limited. It can be obtained by moving the detector in a transmission electron microscope away from the forward direction ($\theta_{\text{scat}} \neq 0$ (see e.g. [22] for the case of Al) or it can be obtained from inelastic X-ray scattering experiments as was done e.g. for the case of water by Hayashi *et al* [23]. In the high- q limit such an experiment is often referred to as Compton spectroscopy [24] and here more data are available.

The mean free path λ for an ion with charge Z is given by:

$$\begin{aligned}\frac{1}{\lambda} &= \int \frac{d\Lambda}{d\omega dq} d\omega dq \\ &= \frac{2Z^2}{\pi v^2} \int_0^{E_0} d\omega \int_{q_-}^{q_+} \frac{dq}{q} \text{Im} \left[\frac{-1}{\epsilon(\omega, q)} \right].\end{aligned}\quad (2.2)$$

If the integration is only over q then the obtained quantity is the differential inverse inelastic mean free path (DIIMFP). For a given energy loss value the limit of integration over momentum (q_\pm) in eq. 2.3 depends on ω , see fig. 2.1(a).

In order to obtain the stopping one weights the integral over the loss function by ω

$$\begin{aligned}\frac{dE}{dx} &= \int \omega \frac{d\Lambda}{d\omega dq} d\omega dq \\ &= \frac{2Z^2}{\pi v^2} \int_0^{E_0} \omega d\omega \int_{q_-}^{q_+} \frac{dq}{q} \text{Im} \left[\frac{-1}{\epsilon(\omega, q)} \right].\end{aligned}\quad (2.3)$$

Now it is customary to interchange the order of integration. Then the limits of the accessible energy losses will depend on q , as explained in Fig. 2.1(b), and extends from 0 to qv .

$$\frac{dE}{dx} = \frac{2Z^2}{\pi v^2} \int_0^\infty \frac{dq}{q} \int_0^{qv} \omega d\omega \text{Im} \left[\frac{-1}{\epsilon(\omega, q)} \right] \quad (2.4)$$

This is the usual equation for ion stopping in terms of the dielectric function. Thus for a given q the maximum value of ω contributing to the stopping is qv .

For the straggling the weighting factor in the DIIMFP is ω^2 :

$$\begin{aligned}\frac{d\Omega^2}{dx} &= \int \omega^2 \frac{d\Lambda}{d\omega dq} d\omega dq \\ &= \frac{2Z^2}{\pi v^2} \int_0^{E_0} \omega^2 d\omega \int_{q_-}^{q_+} \frac{dq}{q} \text{Im} \left[\frac{-1}{\epsilon(\omega, q)} \right].\end{aligned}\quad (2.5)$$

Weighting the integral over the double differential inverse inelastic mean free path by ω and even more so by ω^2 changes the range of ω values that has to be considered for the integration. A reasonable estimate of λ can usually be obtained from an integration up to 100 eV. For stopping values contributions up to $\omega = 1$ keV are significant, whereas for straggling contributions up to a few times the binding energy of the inner shell have to be considered.

2.2.3 Sum rules, Kramers-Kronig relations and mean excitation energy

There are sum rules that should apply to any dielectric function. These are nicely summarised in ref. [25]. For example, there is the f-sum rule:

$$\frac{1}{2\pi^2} \int_0^\infty \omega' \text{Im} [\epsilon(\omega', q)] d\omega' = n, \quad (2.6)$$

which should be fulfilled at any q . Here n is the electron density of the system described by the dielectric function. Similarly the Bethe sum rule:

$$\frac{1}{2\pi^2} \int_0^\infty \omega' \text{Im} \left[\frac{-1}{\epsilon(\omega', q)} \right] d\omega' = n, \quad (2.7)$$

Causality implies that the real and imaginary part of $\epsilon(\omega, q)$ are linked via Kramers-Kronig relations:

$$\text{Re} [\epsilon(\omega, q)] - 1 = \frac{2}{\pi} \mathcal{P} \int_0^\infty \frac{\omega' \text{Im} [\epsilon(\omega', q)]}{(\omega')^2 - \omega^2} d\omega' \quad (2.8)$$

with \mathcal{P} the Cauchy principal value (this relation should again apply for any q). and similarly:

$$\operatorname{Re} \left[\frac{1}{\epsilon(\omega, q)} \right] - 1 = \frac{2}{\pi} \mathcal{P} \int_0^\infty \frac{\omega' \operatorname{Im} \left[\frac{1}{\epsilon(\omega', q)} \right]}{(\omega')^2 - \omega^2} d\omega' \quad (2.9)$$

The real and imaginary parts of $\operatorname{Im}[1/\epsilon(\omega, q)]$ are thus Kramers-Kronig pairs as well. All dielectric function used fulfills all these sum rules for any q with the electron density n being the actual electron density of the system (either the valence electron density if only low losses are considered or the total electron density if the integration of eq. 2.7 and eq. 2.6 extends over all energies.)

For very large momentum transfer it is generally accepted that one has binary collisions with a single electron. This implies that the energy transfer should be centered around $q^2/2$. All dielectric functions considered here will have for their loss functions centered near $q^2/2$ for large q values .

For each dielectric function one can calculate the mean excitation energy I , as introduced by Bethe. It is obtained from the ELF in the optical limit ($q = 0$) and given by:

$$I = \exp \left[\frac{\int_0^\infty \omega' \ln \omega' \operatorname{Im} \left[\frac{-1}{\epsilon(\omega', 0)} \right] d\omega'}{\int_0^\infty \omega' \operatorname{Im} \left[\frac{-1}{\epsilon(\omega', 0)} \right] d\omega'} \right] \quad (2.10)$$

This quantity is sufficient to describe the stopping at very high projectile energies.

2.3 Model Dielectric Functions (DF)

2.3.1 Ad-hoc DF

Before we describe the more traditional dielectric functions let us first define a rather ad-hoc (AH) dielectric function

$$\operatorname{Im} \left[\frac{-1}{\epsilon(\omega, q)} \right] = \frac{A_{\text{AH}} \delta(\omega - \omega_p(q))}{\omega_p(q)} \quad (2.11)$$

with $\omega_p(q) = \max(\omega_{\text{AH}}, \frac{q^2}{2})$. We refer to this q dependence as ‘Bethe dispersion’.

Collisions with q values such that $q^2/2 < \omega_{\text{AH}}$ are considered ‘soft’ collisions, otherwise they are considered ‘hard’ (billiard ball-type) collisions. From eq. 2.7 it is clear that this dielectric function has indeed for any q the same Bethe sum and the electron density of this system is given by $n = A_{\text{AH}}/(2\pi^2)$. Using Kramers-Kronig (eq. 2.9) one can show that $\operatorname{Re} \left[\frac{1}{\epsilon(0, 0)} \right] = 0$, as required for a metal, if $\omega_{\text{AH}}^2 = 4\pi n$ and $\operatorname{Re} \left[\frac{1}{\epsilon(0, 0)} \right] > 0$ for $\omega_{\text{AH}}^2 > 4\pi n$ values. Densities for which $\omega_{\text{AH}}^2 < 4\pi n$ would result in negative values of $\operatorname{Re} \left[\frac{1}{\epsilon(0, 0)} \right]$ and these densities are considered non-physical.

The ad-hoc dielectric function obeys the sum rules and corresponds at large q values to scattering from stationary electrons. Moreover, it can be shown, see 2.A, that calculating the stopping by evaluating eq. 2.3 one obtains the famous Bethe stopping equation:

$$-\frac{dE}{dx} = \frac{4\pi n Z^2}{v^2} \ln \left(\frac{2v^2}{\omega_p(0)} \right) = \frac{4\pi n Z^2}{v^2} \ln \left(\frac{2v^2}{I} \right). \quad (2.12)$$

Thus by comparing a model loss functions with this ad-hoc loss function one can understand why the stopping at a certain ion energy for this model loss function is larger or smaller than the Bethe value. Sigmund defines the shell effects as the difference of the actual stopping from the Bethe value. (ref. [5] eq. 6.100). We will use this ad-hoc dielectric function as a reference, when we introduce other dielectric function.

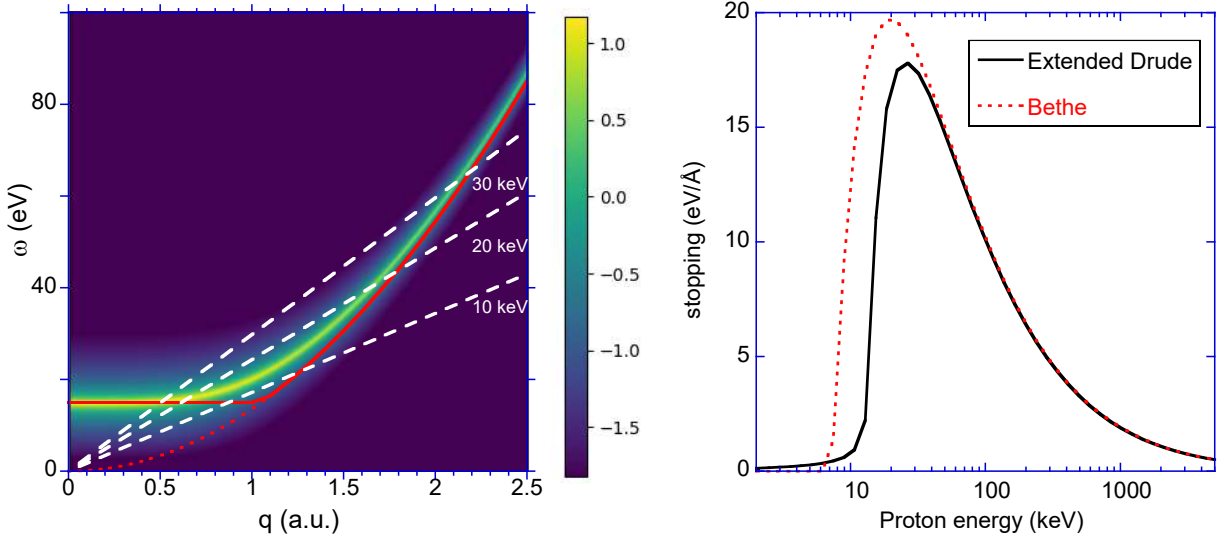


Figure 2.2: In the left panel we show the log of the loss function $\text{Im}[-1/\epsilon(\omega, q)]$ for the extended Drude dielectric function with $\omega_p = 15$ eV and as a solid red line the Bethe dispersion. The dotted line is the energy transfer to a stationary electron ($q^2/2$) and the white dashed lines are the qv lines at the energy as indicated. Only the loss function below the qv line contributes to the stopping at that energy. The Drude dispersion follows the Bethe dispersion closely. Hence the stopping (right panel) corresponding to this Drude dielectric function is quite similar to the Bethe one.

2.3.2 Examples of Classical Dielectric functions

Classical dielectric functions are quite simple and convenient since all other, more advanced, DF converge to them in giving limits, generally high frequencies ω or small moment transfer q (optical limit). They were derived in different contexts in classical physics for long wavelengths and can be written as

$$\epsilon(\omega) = 1 - \frac{\omega_p^2}{(\omega(\omega + i\Gamma) - \omega_0^2)} \quad (2.13)$$

where ω_p is the plasmon frequency (also Langmuir frequency) for free electron oscillations determined from the electron density n ($\omega_p^2 = 4\pi n$) and ω_0 is the harmonic oscillator frequency representing bound electron oscillations. $\text{Re}[\epsilon(\omega)] = 0$ at $\omega = \sqrt{\omega_p^2 + \omega_0^2}$ for vanishing damping constant Γ . This causes a maximum in the corresponding ELF.

(a) Extended Drude

Here we present briefly the model dielectric functions we will be using. Most of them have been described extensively in the literature before, e.g. see ref. [10, 21, 26, 27, 28] and the first two (Extended Drude and Drude-Lindhard) can be seen as simple extensions of Eq.(2.13) to finite q values.

The Extended Drude dielectric function $\epsilon^{\text{ED}}(\omega, q)$:

$$\begin{aligned} \text{Re} [\epsilon^{\text{ED}}(\omega, q)] &= 1 - \frac{A_1(\omega^2 - \omega_1(q)^2 - U_1^2)}{(\omega^2 - \omega_1(q)^2 - U_1^2)^2 + \Gamma_1^2 \omega^2} \\ \text{Im} [\epsilon^{\text{ED}}(\omega, q)] &= \frac{A_1 \Gamma_1 \omega}{(\omega^2 - \omega_1(q)^2 - U_1^2)^2 + \Gamma_1^2 \omega^2} \end{aligned} \quad (2.14)$$

is obtained (for $U_1 = 0$) from Eq.(2.13) after associating $A_1 = \omega_p^2$ and $\omega_1(0) = \omega_0$. Therefore, A_1 (in units of (energy)²) relates to the density of electrons and $\omega_1(q)$ is the excitation energy of this oscillator at momentum q . Γ_1 determines the width of the excitation. In this work we will

use for the dispersion: $\omega_1(q) = \omega_1(0) + q^2/2$. For a free electron metal $\omega_1(0) = 0$, $U_1 = 0$ and then the original Drude model is retrieved.

Note that the refractive index n is given by:

$$n^2 = \text{Re}[\epsilon(0, 0)] = 1 + \frac{A_1}{\omega_1(0)^2}, \quad (2.15)$$

and the maximum of the loss function at $q = 0$ is at $\sqrt{A_1 + \omega_1^2}$. For $\omega_1(0) = 0$ (i.e. the material consist of free electron) $\text{Re}[\epsilon(0, 0)]$ is indeed infinite, as a DC field is completely screened in a metal.

The energy of oscillator 1 can depend on q (dispersion). This dependence will be assumed here to have a simple form (using atomic units):

$$\omega_1(q) = \omega_1 + \alpha_1 \frac{q^2}{2} \quad (2.16)$$

but more complex dependencies (e.g. full dispersion [29]) could be used as well. The maximum in the loss function will then be at

$$\omega_1(q) = \sqrt{\omega_p^2 + (\omega_1 + \alpha_1 q^2/2)^2 + U_1^2} \quad (2.17)$$

Only for $\alpha_1 = 1$ does the peak position of the loss function approaches the free electron value ($q^2/2$) at large q .

An example of the extended Drude dielectric function is compared with the ad-hoc dielectric function in fig. 2.2. A_1 was chosen to be 225 eV² (corresponding to a plasmon energy of 15 eV), $\omega_1 = 0$ eV and $\alpha_1 = 1$ and $U_1 = 0$. These values are chosen to mimic the behaviour of the valence band of Al. The dispersion is very close to the Bethe dispersion with $\omega_{\text{AH}} = 15$ eV and an electron density n such that $\omega_{\text{AH}}^2 = 4\pi n$, and the proton stopping follows the Bethe stopping below closely, with differences appearing at relative low energy (40 keV).

The dielectric function described above corresponds to a metal. One can use the extended Drude model as well to describe an insulator by choosing $\omega_1 \neq 0$. E.g. by taking $A_1 = 112.5$ eV² and $\omega_1 = 10.6$ eV, $U_1 = 0$ eV one obtains again a loss function with a peak at 15 eV, but now only half its height. Dispersion (for $\alpha_1 = 1$) would then follow $\sqrt{A_1 + (\omega_1 + q^2/2)^2 + U_1^2}$. The U_1 parameter can be used to control when the dispersion ‘kicks in’. If one can takes ω_1 smaller and increases U_1 in such a way that $\sqrt{\omega_1^2 + U_1^2}$ remains constant, then the ELF at $q = 0$ remains unchanged. However dispersion only becomes noticeable when $(\omega_1 + q^2/2)^2$ is not small compared to $\omega_p^2 + U_1^2$.

(b) Drude-Lindhard

A second model, but closely related model is often referred to as the Drude-Lindhard (DL) model [30]. Here ϵ^{DL} is defined in terms of $1/\epsilon(\omega, q)$ rather than $\epsilon(\omega, q)$ itself:

$$\text{Im} \left[\frac{-1}{\epsilon^{\text{DL}}(\omega, q)} \right] = C_1 \frac{\omega \Gamma_i \omega_1(0)^2}{(\omega^2 - \omega_1(q)^2 - U_1^2)^2 + \omega^2 \Gamma_1^2} \quad (2.18)$$

and for the real part:

$$\text{Re} \left[\frac{1}{\epsilon^{\text{DL}}(\omega, q)} \right] = 1 + C_1 \frac{(\omega^2 - \omega_1(q)^2 - U_1^2) \omega_1(0)^2}{(\omega^2 - \omega_1(q)^2 - U_1^2)^2 + \omega^2 \Gamma_1^2} \quad (2.19)$$

For a free electron metal the DL dielectric function is at $q = 0$ equivalent to the Drude dielectric function if $C_1 = 1$ and $\omega_1^{\text{DL}} = \sqrt{A_1}$, but even then, away from $q = 0$, when using again eq. 2.16 their effective dispersion will differ. Fur $U_1 = 0$, the maximum of the loss function is now simply at $\omega_1 + \alpha_1 q^2/2$. Again the U_1 parameter, usually omitted (and taken to be 0 in the rest of this

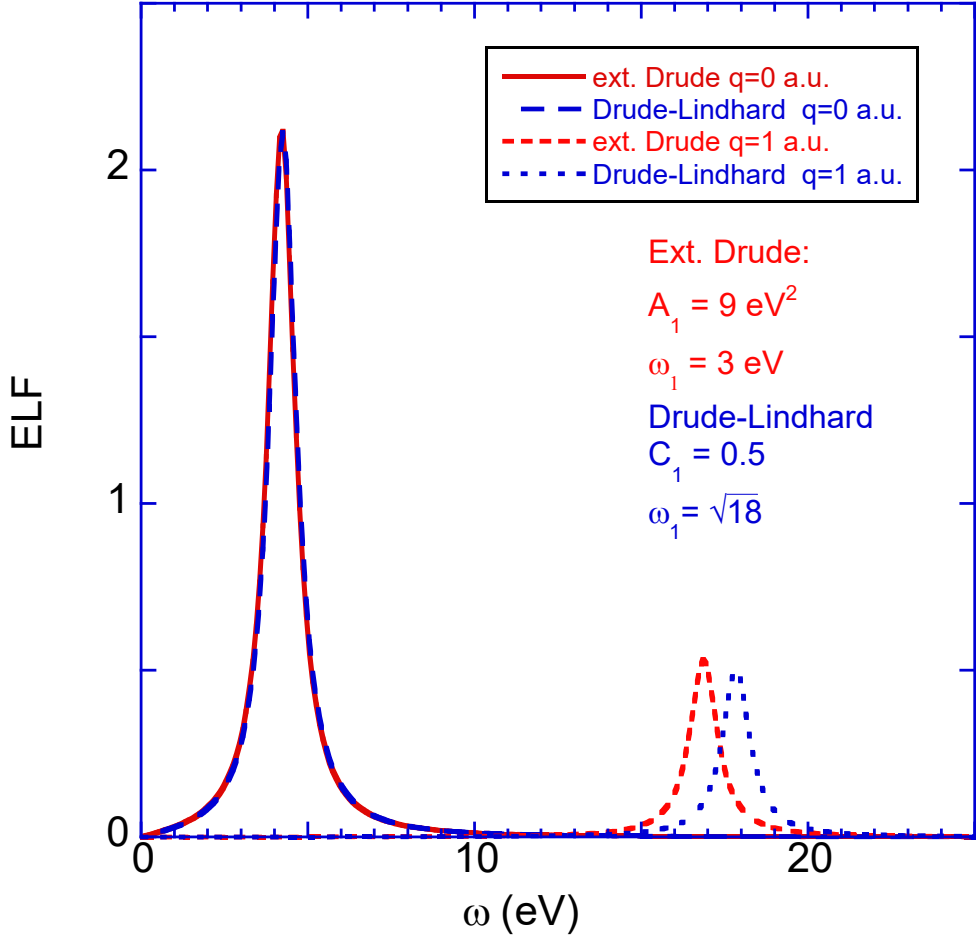


Figure 2.3: The loss function at $q = 0$ and $q = 1$ for the extended Drude and Drude-Lindhard models for the parameters as indicated. In both cases $\alpha_1 = 1$ and $\Gamma = 1 \text{ eV}$) The ELF at $q = 0$ are identical, but not at $q = 1 \text{ a.u.}$.

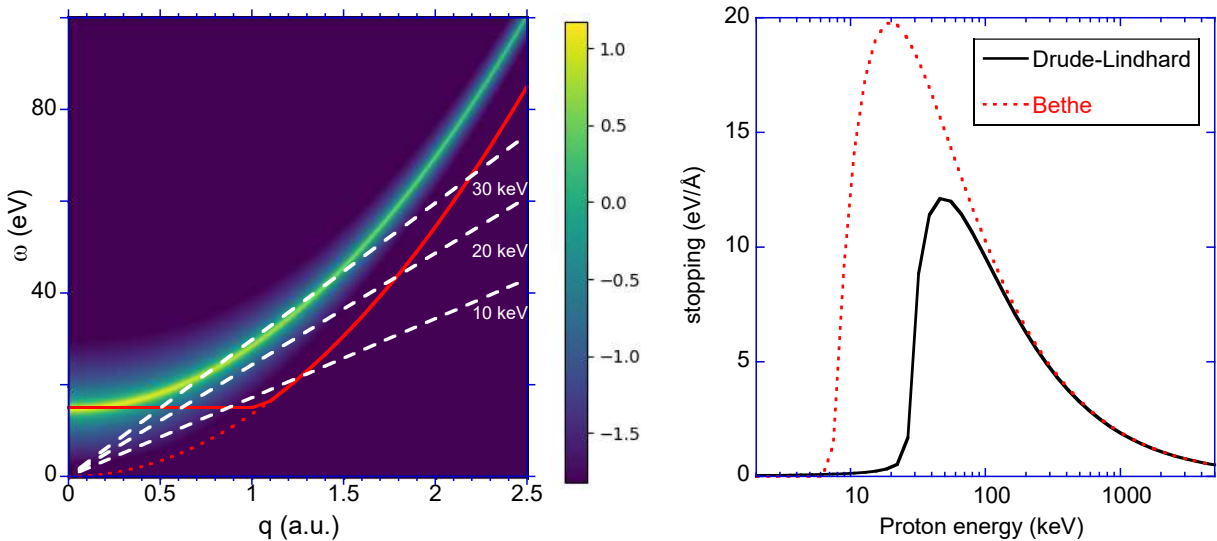


Figure 2.4: Same as fig. 2.2 but now for the Drude-Lindhard dielectric function. The electron density (and hence the plasmon energy at $q = 0$) is the same. The dispersion is now faster, and hence the stopping is more severely reduced, compared to the Bethe stopping

section) can be used to control details of the dispersion near $q = 0$, while retaining convergence to the Bethe ridge for large q (when $\alpha_1 = 1$).

For $0 < C_1 < 1$, one obtains $1/n^2 = \text{Re}[1/\epsilon(0,0)] = 1 - C_1$ and the model describes an insulator. C_1 values > 1 result in negative values for $\text{Re}[\epsilon(0,0)]$ and are again considered non-physical. At $q = 0$ one get thus the equivalent extended Drude ELF if one uses in addition of $\omega_1^{\text{DL}} = \sqrt{A_1 + \omega_1^{\text{ED}}}$ also $1/(1 - C_1) = n^2 = 1 + A_1/\omega_1^{\text{ED}}$. E.g. extended Drude with $A_1 = 9$ eV², $\omega_1^{\text{ED}} = 3$ eV and $\Gamma_1 = 1$ eV is at $q = 0$ equivalent to the Drude-Lindhard model with parameters: $C_1 = 0.5$, $\omega_1^{\text{DL}} = \sqrt{18}$ eV and $\Gamma_1 = 1$ eV. This is illustrated in fig. 2.3

In fig. 2.4 we compare again the loss function and associated proton stopping with the ad-hoc dielectric function with the same n and I values. Now the dispersion at small q values is stronger than in the extended Drude case. As a consequence the stopping drops off more quickly at low projectile energies. One could change this by adopting another dispersion relation for Drude-Lindhard:

$$\omega_1(q) = \sqrt{\omega_1(0)^2 + (\alpha_1 \frac{q^2}{2})^2}. \quad (2.20)$$

Then both approaches would give again the same result.

2.3.3 Examples of quantum-physics based dielectric functions

For an isotropic medium made of independent atoms (or molecules) with electron density n the longitudinal dielectric function in the framework of RPA. For simplicity we restrict ourselves to the RPA here, for fully-quantitative description extension beyond the RPA are required see e.g. [31, 32]. In the non-relativistic approximation the RPA is given by [5] :

$$\epsilon(\omega, q) = 1 + \omega_p^2/q^2 \sum_j |F_{j0}(q)|^2 \left(\frac{1}{\omega_{j0} - \omega - i\Gamma} + \frac{1}{\omega_{j0} + \omega + i\Gamma} \right), \quad (2.21)$$

where $\omega_p^2 = 4\pi n$, ω_{j0} is the transition energy from the ground-state ($j = 0$) to an excited state j .

$F_{j0}(q)$ is the form factor, it should be evaluated for the appropriate basis set. This has been done for plane waves (leading to the Lindhard dielectric function), harmonic oscillator eigenstates (leading to the Belkacem-Sigmund dielectric function) and here we do it as well based on hydrogenic wavefunctions. We will discuss theses cases briefly.

Lindhard and Mermin dielectric function

The loss functions described so far have their roots in classical physics. LinOi JOdhard derived, based on quantum physics, a dielectric function for a free electron gas $\epsilon^L(\omega, q)$ [3] (see appendix A for details). Here the loss function consists of a delta function (describing collective excitations, or ‘plasmons’) and a continuous part (describing single-particle excitations). Mermin added relaxation time to the Lindhard dielectric function which transforms the delta function to a peak with finite width [15]:

$$\epsilon^M(\omega, q) = 1 + \frac{(1 + i\Gamma/\omega)(\epsilon^L(\omega + i\Gamma, q) - 1)}{1 + i\Gamma/\omega [\epsilon^L(\omega + i\Gamma, q) - 1] / [\epsilon^L(0, q) - 1]} \quad (2.22)$$

It is instructive to see the effect of the Mermin correction on the Lindhard dielectric function with finite Γ in some detail. For this we take parameters as are suitable for Al, but an exaggerated width of $\Gamma = 6$ eV. $\text{Re}[\epsilon(0,0)]$ of the Lindhard dielectric function does not go to infinity as expected for a metal, after the Mermin correction it does. The ELF at $q = 0$ is wider than 6 eV in the Lindhard case, but the 6 eV width is recovered after the Mermin correction. Both dielectric functions fulfill the F and Bethe sum rules (eq. 2.6,2.7) with the same number of electrons per

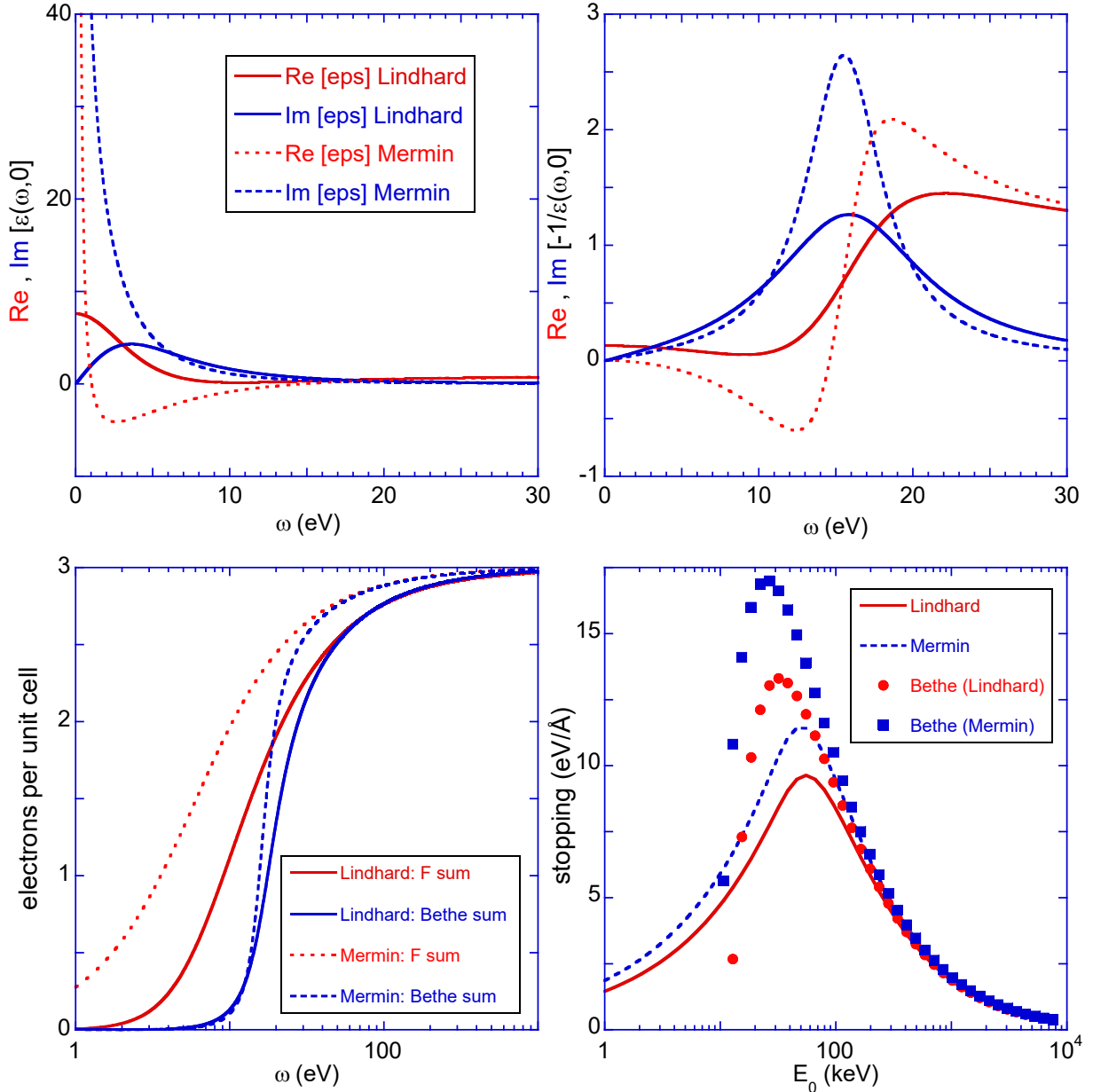


Figure 2.5: A comparison of $\text{Re}[\epsilon(\omega, 0)]$ and $\text{Im}[\epsilon(\omega, 0)]$ of the Lindhard dielectric function with a large Γ value (6 eV) with and without the Mermin correction. All other parameters are taken as applies to the aluminum valence band (top left panel). The same comparison but for $\text{Re}[1/\epsilon(\omega, 0)]$ and $\text{Im}[-1/\epsilon(\omega, 0)]$ is given in the top right panel. The lower left panel shows the sum rule integrals (eq. 2.7 and eq. 2.6) as a function of ω as the upper limit of the integral. The lower right panel shows their stopping values as well as the Bethe stopping for the corresponding I values. The differences are discussed in the main text.

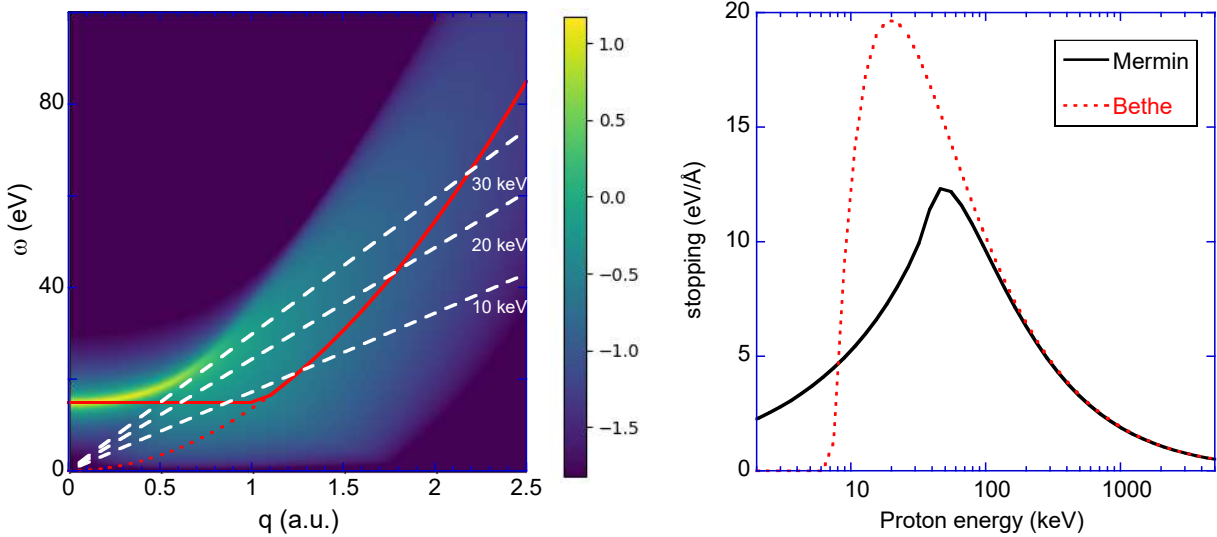


Figure 2.6: Same as fig. 2.2 but now for the Mermin dielectric function. The electron density is again the same. The dispersion of the plasmon is similar to Drude-Lindhard but now there is a second broad low-intensity branch due to electron-hole excitations that extends below the qv line, even at low energies. As a consequence the stopping is larger at low energies.

unit volume. The Lindhard dielectric function has a larger I value (as it is broader) and has thus somewhat smaller stopping compared to that obtained after the Mermin correction. This is all illustrated in fig. 2.5. Clearly the Mermin dielectric function is to be preferred over the Lindhard one, for finite Γ values, since the latter does not yield the correct dc conductivity and Thomas-Fermi static screening [33]. The Lindhard dielectric function with finite Γ thus fails to describe a free electron gas but is still a ‘valid’ dielectric function in the sense that it adheres to sum rules and the real and imaginary part are related by Kramers-Kronig relations.

The Mermin loss function, again compared to our ‘ad-hoc’ loss function is shown in fig. 2.6. Compared to Drude-Lindhard there is now a broad low-intensity structure visible covering at $\omega = 0$ the region between $k = 0$ and $2k_f$. In the stopping curve this has the effect of significant stopping, even at 1 keV, as the qv line always intersect with the electron-hole pair excitation region.

Levine-Louie dielectric function for insulators

The derivation of the Lindhard loss function (and hence the Mermin one) assumes a free electron gas, and its use to describe an insulator is thus highly questionable. Levine and Louie derived a loss function based on quantum physics for an insulator (ϵ^{LL}) by transforming the energy scale according to $\omega \rightarrow \sqrt{(\omega^2 + U^2)}$ with U a parameter that is related to the band gap [34] (see chapter 3 for more information). It reverts to the Lindhard function for $U \rightarrow 0$. Archubi and Arista studied the effect of the U parameter on the stopping, inelastic mean free path and straggling for electrons, positrons and protons using the ϵ^L (or equivalently, ϵ^{LL} with $U = 0$) and ϵ^{LL} dielectric function with $U \neq 0$ [35]. Here we add a relaxation time to this function by replacing ϵ^L in eq. 2.22 by ϵ^{LL} and refer to the resulting dielectric function as ϵ^{MLL} (Mermin-Levine-Louie). Using this approach one has $\sum_i C_i^{MLL} = 1$ as a boundary condition, but by choosing the appropriate ω_i and U values, one can, in the optical limit, obtain again the same loss function as the Drude-Lindhard model with $C_1 < 1$. For details see ref. [27]. An example of a MLL loss loss function and the corresponding stopping is given in fig. 2.7.

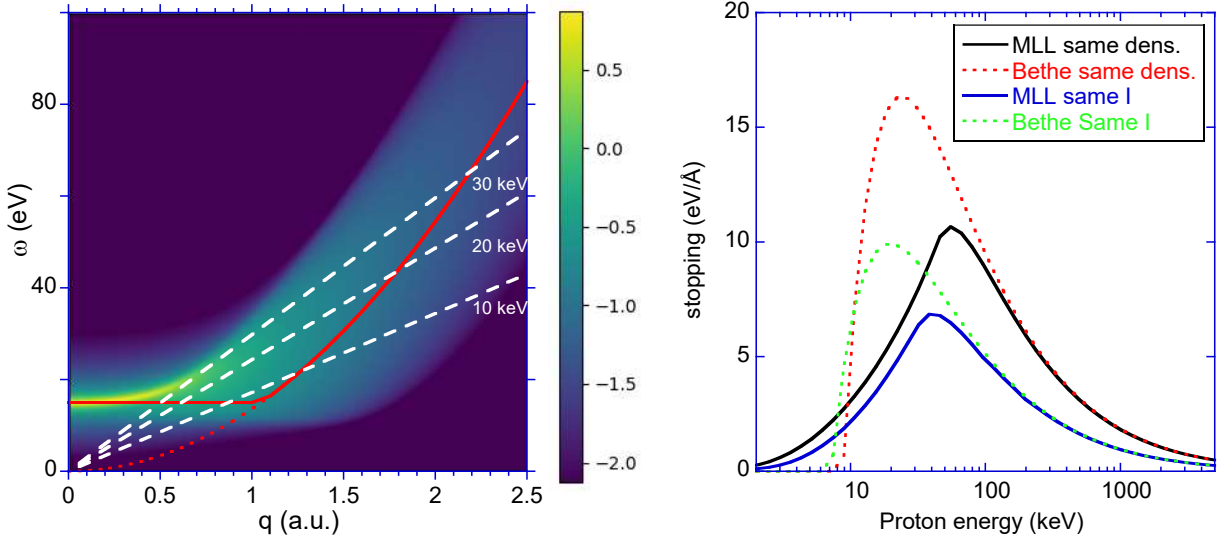


Figure 2.7: Same as fig. 2.6 but now for a MLL dielectric function corresponding to a material with half the electron density (i.e. $\omega_{\text{pl}} = 15/\sqrt{2}$) but with a band gap U of 10.6 eV. In this way the peak in the ELF is again at 15 eV and the I value is not changed. The structure of the loss function shows again a plasmon branch and a branch due to electron-hole excitation, but the intensity of the latter is suppressed in the gap. For large proton energies the stopping is now half that of the Mermin case (due to lower electron density) but at low energies the stopping is reduced by more than a factor of 2. Also shown is the stopping when the density n is left unchanged, but the same gap is introduced. This shifts the maximum of the ELF to $\sqrt{15^2 + 10.6^2}$ and changes thus the I value.

Dielectric function using Gaussian occupation

In the Lindhard (free-electron) approach all states are fully occupied for $|q| < k_f$ with k_f the Fermi wave vector and empty for $|q| > k_f$. Deeper levels have often an occupation that decreases more gradually, and for s levels the momentum occupation resembles roughly a Gaussian shape. This led Kaneko to derive a dielectric function based on a Gaussian occupation proportional to: $\exp(-q^2/Q^2)$ with Q the characteristic momentum for that level. In the most simple case (one electron in the shell) this gives for the plasmon energy: $\omega_p^2 = Q^3/\sqrt{\pi}$. For $Q = 0.64$ we obtain thus again a plasmon energy of 15 eV, just as in our earlier examples. The corresponding loss function and stopping are presented in fig. 2.8.

GOS based dielectric functions

For the description of deeper levels a plane-wave derived description (as is the Lindhard dielectric function and its derivatives) may not be the most appropriate starting point. Hydrogenic wavefunctions would appear more appropriate. Then the dielectric function is closely related to the GOS (Generalized Oscillator Strengths)

Considering the GOS [21]:

$$f_{j0}(q) = 2\omega_{j0} \frac{|F_{j0}(q)|^2}{q^2} \quad (2.23)$$

and continuum states we can rewrite Eq.(2.21) as

$$\epsilon(\omega, q) = 1 + \omega_p^2 \int_0^\infty \frac{d\omega'}{2\omega'} \frac{df}{d\omega'}(\omega', q) \left(\frac{1}{\omega' - \omega - i\Gamma} + \frac{1}{\omega' + \omega + i\Gamma} \right) \quad (2.24)$$

where ω_{j0} and $f_{j0}(q)$ are replaced by ω' and $\frac{df}{d\omega'}(\omega', q)$ respectively. The real and imaginary parts of Eq.(2.24) can be evaluated using the mathematical relation

$$\lim_{\Gamma \rightarrow 0^+} \frac{1}{x - a + i\Gamma} = \mathcal{P} \frac{1}{x - a} - i\pi\delta(x - a) \quad (2.25)$$

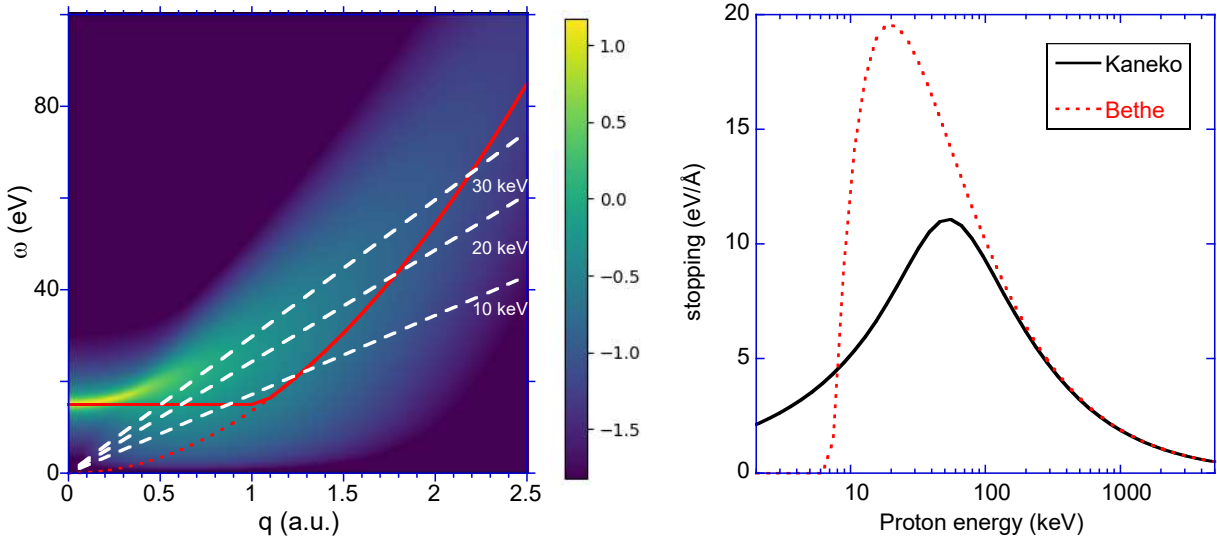


Figure 2.8: Same as fig. 2.2 but now for the Kaneko dielectric function using $Q = 0.64$ a.u. The $\text{Im}[-1/\epsilon(\omega, q)]$ distribution resembles the Mermin one, except that the edges of the electron-hole excitation branch is now not sharp, due to the more gradual decrease of the momentum density. The stopping curve is again similar to the Mermin one except for the absence of the little kink near the maximum.

where, \mathcal{P} indicates the Cauchy principal value of the integral, and read

$$\text{Re}[\epsilon(\omega, q)] = 1 - \omega_p^2 \mathcal{P} \left[\int_0^\infty d\omega' \frac{df}{d\omega'}(\omega', q) \frac{1}{\omega^2 - \omega'^2} \right] \quad (2.26)$$

and

$$\text{Im}[\epsilon(\omega, q)] = \frac{\omega_p^2 \pi}{2\omega} \frac{df}{d\omega}(\omega, q) \quad (2.27)$$

In the dilute limit ($\omega_p \rightarrow 0$) $\text{Im}[\epsilon(\omega, q)]$ is small and $\text{Re}[\epsilon(\omega, q)] \approx 1$. Then $\text{Im}[-1/\epsilon(\omega, q)] \approx \text{Im}[\epsilon(\omega, q)]$ and ω -times the loss function is proportional to the GOS. The loss function and the corresponding stopping is shown in fig. 2.9.

If one increases the H density then the situation changes as shown in fig. 2.10. With increasing density the loss function shifts to larger ω values and the sharp onset of the loss function disappears: the loss function becomes more symmetrical. At the largest density considered, the peak position is very close to the plasmon energy of that density. The change of the shape of the loss function associated with a GOS due to density is often referred to as the density correction.

Dielectric function based on Harmonic oscillator

An RPA-level dielectric function was derived by Belkacem and Sigmund assuming the electrons are bound in a harmonic potential with resonance frequency ω_0 [17]. Here the final state always remains bound. In the dilute limit the ELF has contributions at energy losses $n\omega_0$ with n an integer. In Chapidif the dielectric function is obtained directly from eq. 8 or ref [17]. (If significant broadening Γ is applied then a Mermin-type corrections may have to be considered [18] but this is not done in Chapidif. If the width is of the order of the harmonic oscillator frequency then deviations of the sum rules can be expected.)

For $q = 0$ all intensity is in the $n = 1$ branch (dipole limit). The peak positions change at significant densities. Then there is a q -dependence of the energy loss, especially at small n values. This q -dependence increases the position of the $n = 1$ peak from ω_0 to $\sqrt{\omega_0^2 + \omega_p^2}$ with ω_p again the plasmon energy corresponding to the density of the system.

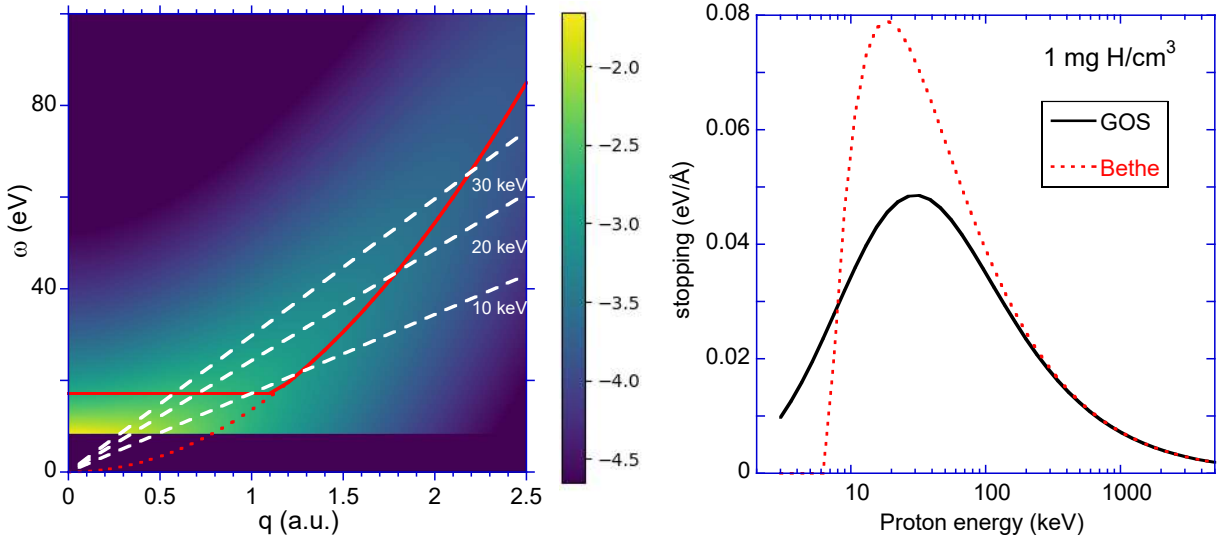


Figure 2.9: Same as fig. 2.7 but now for the GOS of H 1s atoms. The energy of the edge was taken at 8.4 eV, rather than the H 1s binding energy (13.6 eV) or minimum excitation energy (10.4 eV), to approximately take into account excitations to bound states. With this value the sum rule gives 1 and the mean excitation energy of $I = 14.9$ eV is obtained in close agreement with literature value of $I = 15.1$ eV. The right panel shows the stopping for atomic H with a density of $1 \text{ mg}/\text{cm}^3$ (solid line) together with the Bethe stopping for this I value (dashed line).

The loss function and stopping for parameters such that at $q = 0$ the ELF of this model is the same as that used for MLL is shown in fig. 2.11. The discrete nature of the final state is clearly visible in the ELF distribution. The stopping is slightly less than the MLL case with the same density and $U = \omega_0$.

2.4 Compton profiles

In the preceding we presented many dielectric functions that have, in the optical limit, a maximum at 15 eV loss. To stress their differences it is also worthwhile to show their energy distribution in the high momentum transfer case. This is done in fig. 2.12. There is a clear difference between the Compton profiles derived from classical and quantum-physics based dielectric functions. The classical dielectric function have loss functions at large q with the same width as the loss function at $q = 0$. The quantum-based ones have a much increased width. Interpreting the loss function at high- q in terms of binary collisions of the projectile with a target electron with momentum \mathbf{p} one gets for the energy loss:

$$\omega = q^2/2 + \mathbf{q} \cdot \mathbf{p} \quad (2.28)$$

The Mermin Compton distribution stops at $p = k_f$ as it is the projection of the density of states within the Fermi sphere on the \mathbf{q} direction. Kaneko's Compton profile is a Gaussian with width Q , reflecting the assumed momentum occupation for the initial state. Our MLL dielectric function corresponds to half the electron density of the Mermin one. Hence the diameter of its Fermi sphere is reduced by a factor $2^{1/3}$ and thus the Compton profile cuts off at smaller $|p|$ values. The Belkacem Compton profile consist of a set of sharp peaks, separated by the oscillator energy (10.6 eV). Here the final state is always one of the eigenfunctions of the harmonic oscillator and the excited electron always remains bound in the potential. The envelope of this set of peaks (plotted as a function of p) has the same shape as the density of the (momentum-space) ground state of this oscillator.

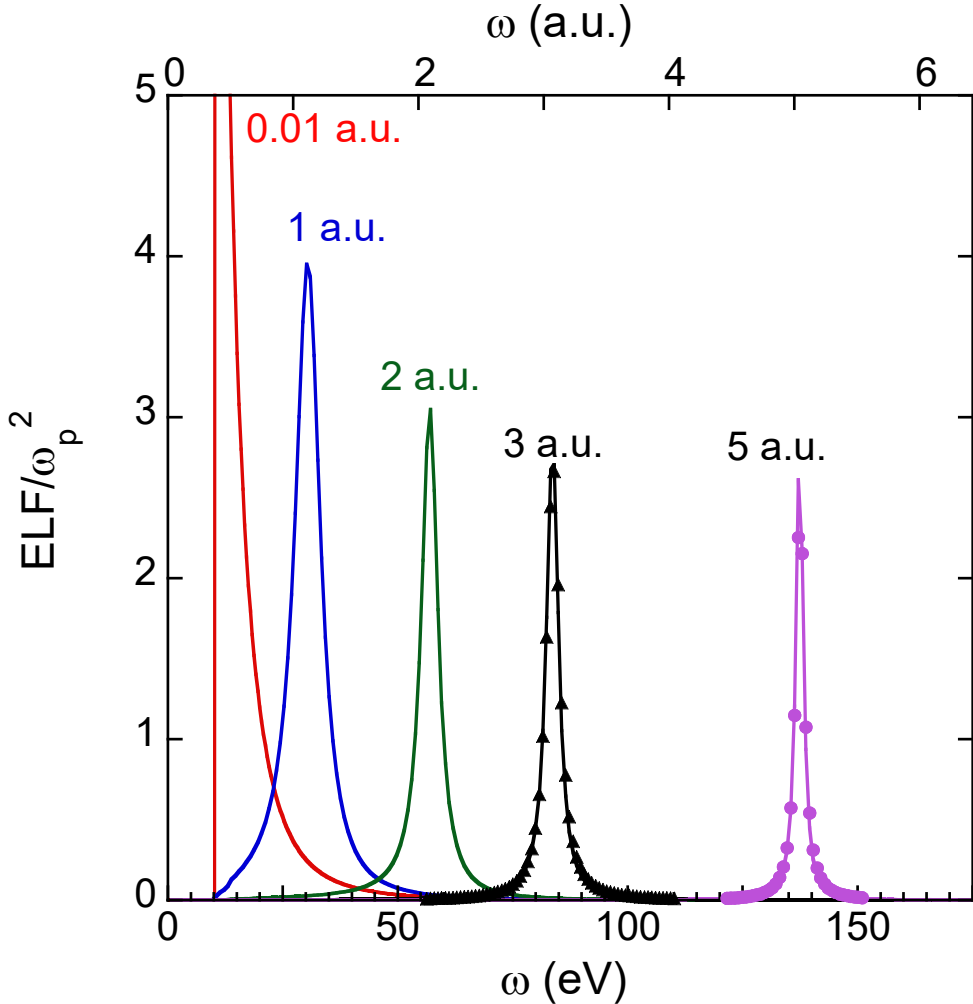


Figure 2.10: The influence of the density on the loss function of H atoms. The loss function is divided by $\omega_p^2 = 4\pi n$ i.e is proportional to the loss per atom. The peak in the loss function shifts to larger values, and is ω_p at the larger densities. Then it resembles the Mermin loss function shown here by triangles and circles for the $\omega_p = 3$ and $\omega_p = 5$ cases. ($\omega_p = 5$ a.u. corresponds to a H density of 21 g/cm^3).

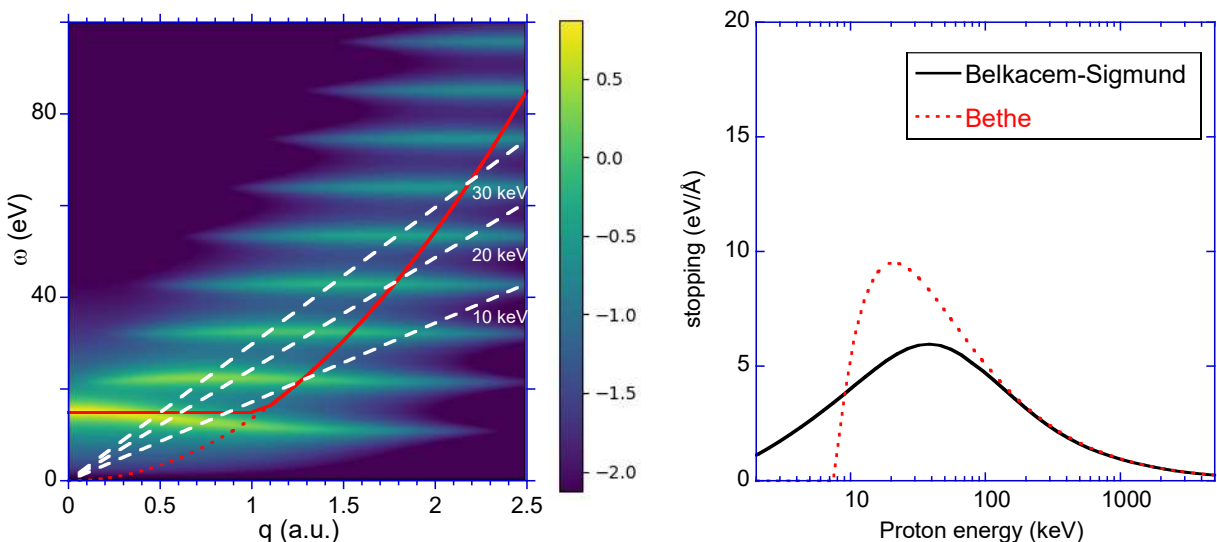


Figure 2.11: Same as fig. 2.7 but now for the Belkacem-Sigmund loss dielectric function. The density is the same as the reduced density of the MLL case, and the oscillator energy (gap) is again 10.4 eV.

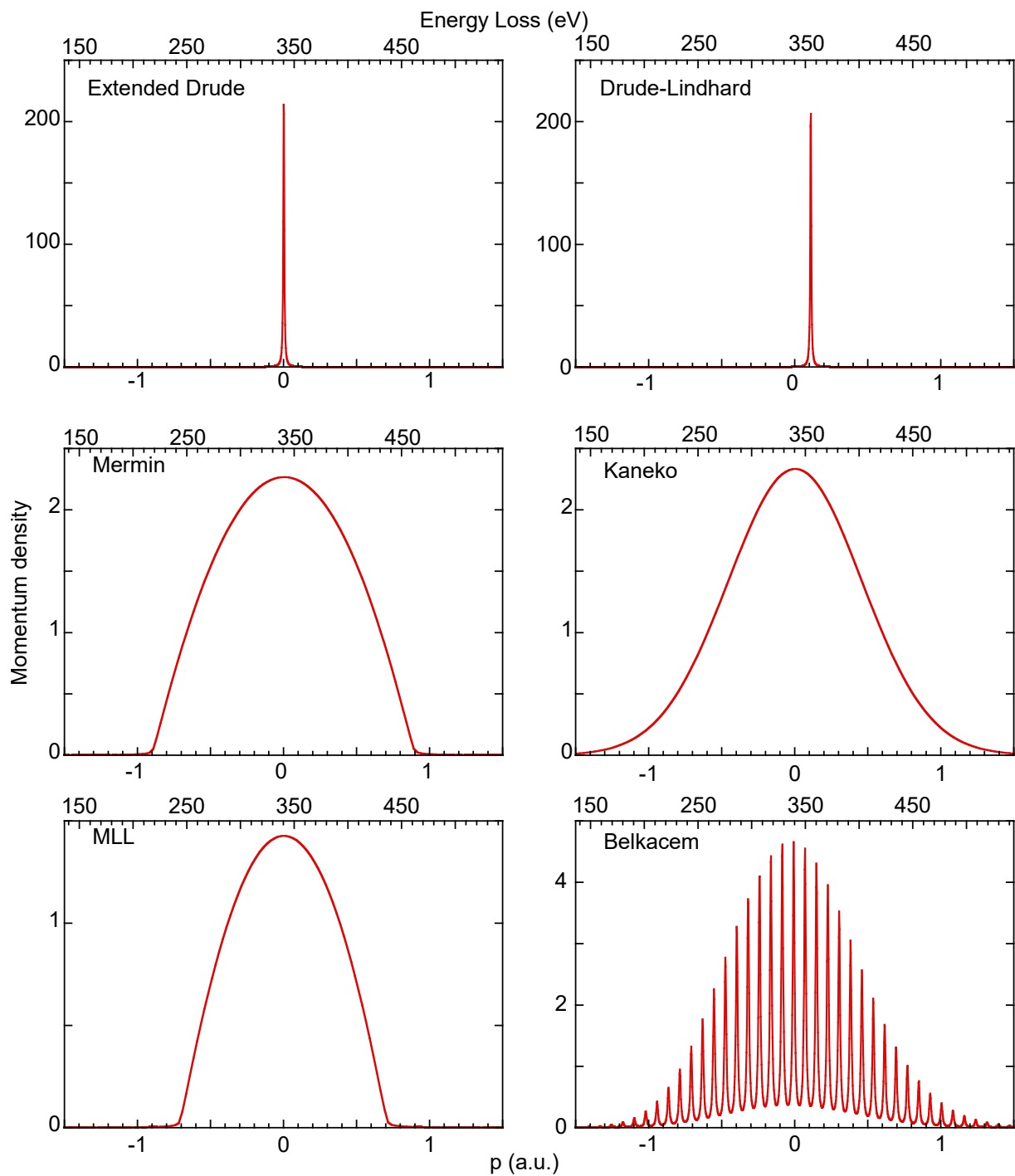


Figure 2.12: the loss function at $q = 5$ a.u. for the various dielectric functions as indicated. The scale at the top axis refers to the energy loss ω . At $q = 5$ a.u. we can interpret these loss function as Compton profiles. The corresponding target electron momentum is given in the lower axis.

2.5 Multiple oscillators

It is generally not possible to model the observed optical ELF with a single oscillator. Then the dielectric function is often described by a sum of oscillators each with different values for the A_i or C_i , ω_i and Γ_i parameter. The question than raises how to add their contributions to $\epsilon(\omega, q) = 1 + \chi(\omega, q)$. Here there are two options:

-add their χ values. This is most appropriate if one considers the contribution due to more than one type of electron inside the same volume. The polarisation of one wavefunction affects the electric field seen by the other electron. The induced dipole moment will add up, i.e. their χ contributions will add up. In this mode it appears that the contributions to the ELF of the different components will ‘repel’ each other and e.g. for the extended Drude model the peaks positions in the ELF deviate from $\sqrt{A_i + \omega_i(q)^2}$ [26]. This approach is often used when one aims to only describe the valence band part of the loss spectra. For example, it was used by Tung *et al*[36] and Werner *et al* [37] to describe the differential inverse inelastic mean free path DIIMFP of several metals as measured in reflection electron energy loss spectroscopy (REELS). In the case of metals one of the parameters ω_i in the extended Drude model is taken to be 0. In the description of REELS experiments some of the α_i parameters are sometimes taken less than one, when one expects that dispersion for low q values is limited. This works for REELS, as the DIIMFP is dominated by contributions at low ω and low q . However, then the dielectric function does not center at $q^2/2$ at high- q values an essential property for getting the right stopping and straggling values.

-add their loss functions. This comes natural if one assumes the different components occupy different parts of the unit cell. For example, it is often assumed that the volume of the unit cell with density n_x behaves as a free electron gas with that density. In that case it is natural to assume that each fraction of the unit cell has its own loss function and one adds the ELF of all components. Within this framework C_i is the fraction of the unit cell that is filled by component i . Clearly $\sum_i C_i \leq 1$ (one can leave part of the unit cell empty). In the case of the extended Drude model the fraction of the unit cell occupied by an oscillator is determined by ω_i . If one takes $\omega_i = 0$ then that component will occupy the whole unit cell.

This approach, adding the ELFs from Drude-Lindhard dielectric function is used e.g. in the QUASUS program, popular for the analysis of REELS spectra [38] for the determination if the electron inelastic mean free path. Abril *et al* used a sum of Mermin loss functions to fit a optical data [19] or REELS data (e.g. [39]) to describe the proton stopping. Denton *et al* used the Mermin dielectric function to calculate the electron inelastic mean free path [40]. Da *et al* used a large number of positive and negative Mermin oscillator to fit the ELF of Cu and calculate its inelastic mean free path [41].

In either way (add χ or add ELF) one obtains a sum dielectric function that adheres to the sum rules and Kramers Kronig relations but they can be very different! An example of this is given in fig. 2.13. Note that adding the ELF in this case results in a metal ($\text{Re}[1/\epsilon] = 0$) whereas adding the χ values results in an insulator ($\text{Re}[1/\epsilon] > 0$). For larger energy losses (beyond the valence band) where ($\text{Re}[\epsilon(\omega, q)] \approx 1$) these considerations are not important and either method gives very similar results.

Modeling the ELF of an actual solid by choosing the most appropriate model and obtaining the best parameters to fit the available experimental data (optical absorption, refractive index, Compton profiles etc.) is a complex problem, and the procedure one chooses depends, in part on the the physics question one wants to answer. We will not attempt it here, but focus instead on the shell corrections in one of the simplest cases: an electron gas that resembles Aluminum.

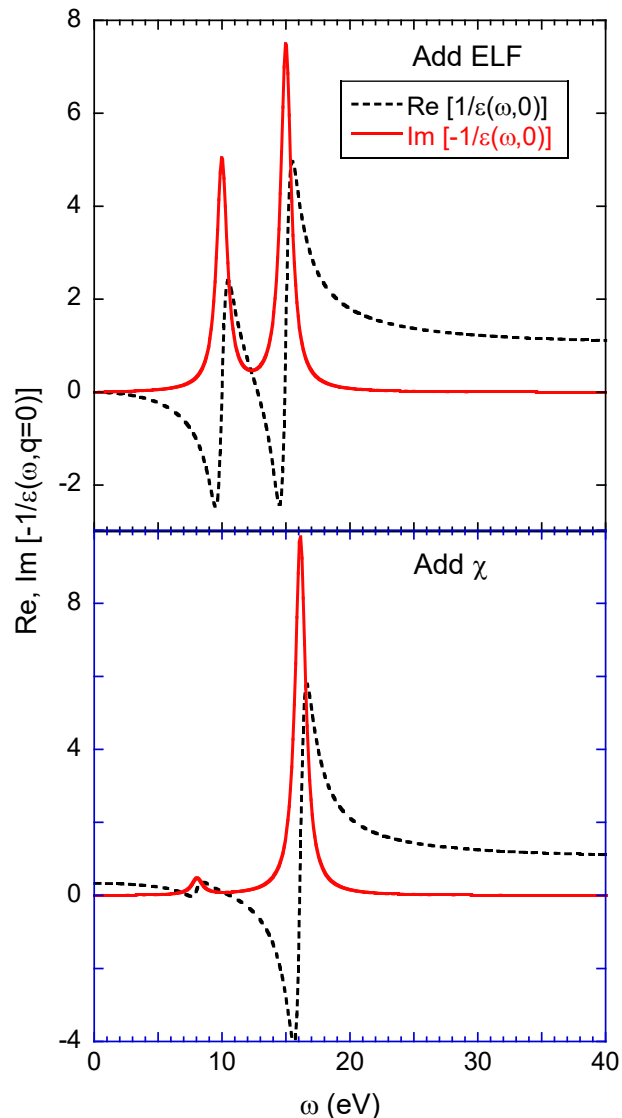


Figure 2.13: A Drude Lindhard dielectric function comprised out of 2 oscillators ($A_1=0.5$, $\omega_1 = 10\text{ eV}$, $\Gamma_1 = 1\text{ eV}$, $A_2=0.5$, $\omega_2 = 15\text{ eV}$, $\Gamma_2 = 1\text{ eV}$) obtained by either adding the ELF (top) or their $\chi(q, \omega)$ values.

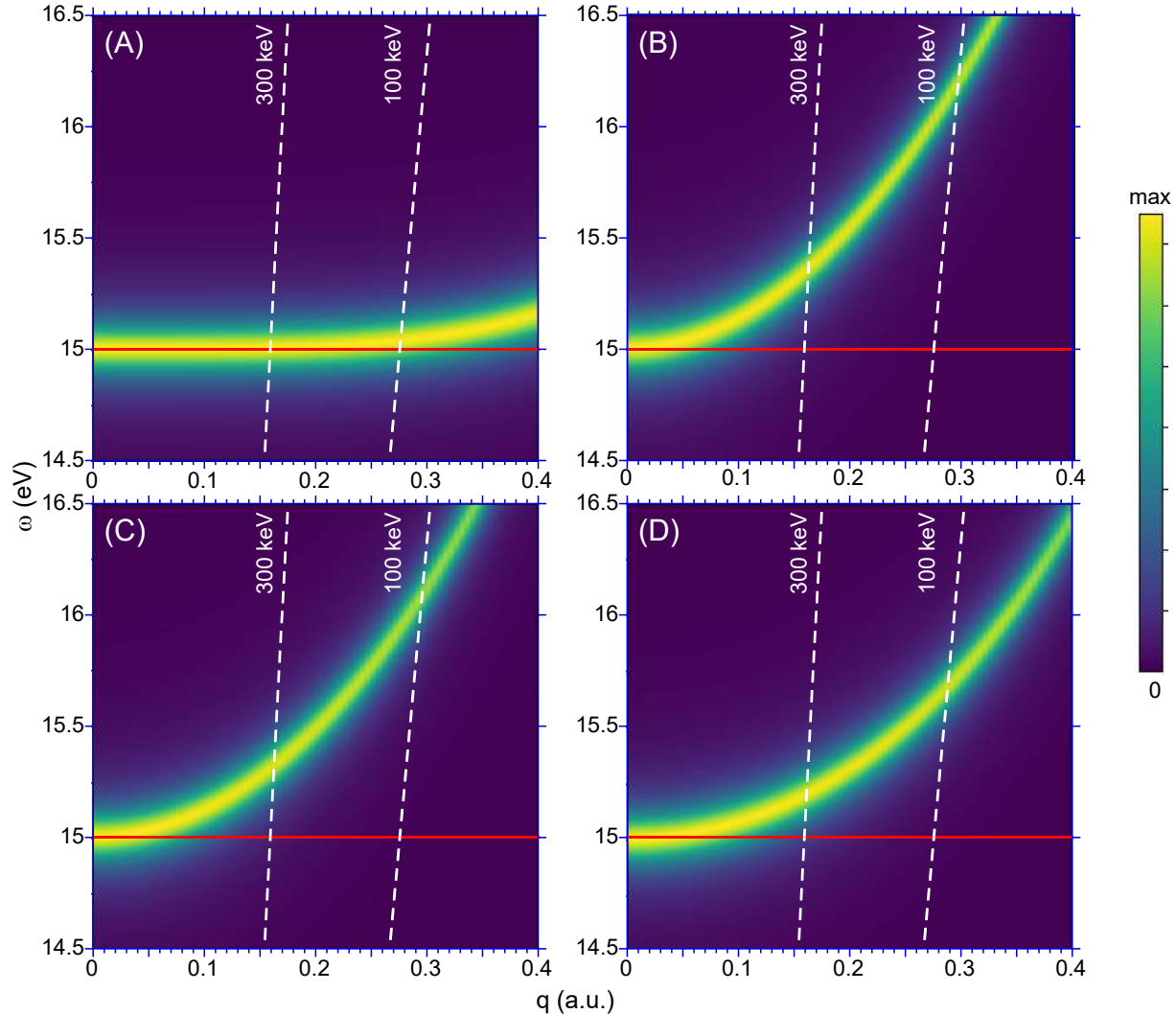


Figure 2.14: The ELF distribution of the extended Drude (A) Drude-Lindhard (B), Mermin (C) and Mermin-Levine-Louie (D) dielectric function for small momentum values and energies close to the plasmon energy. The red line is again the dispersion of our ‘ad-hoc’ dielectric function. The dashed lines are the qv lines at 100 keV and 300 keV.

2.6 Shell corrections in stopping

Shell effects have been ascribed as the difference of stopping as calculated from Eq.(2.3) from the Bethe value [5, 42] and are attributed to velocity distribution of electrons in the medium. The stopping is then usually written as a product of two factors: ($-\frac{dE}{dx} = \frac{4\pi n Z^2}{v^2} L$). L can thus be defined in terms of the dielectric function:

$$L = \frac{1}{2\pi^2} \int_0^\infty \frac{dq}{q} \int_0^{qv} \omega d\omega \text{Im} \left[\frac{-1}{\epsilon(\omega, q)} \right] \quad (2.29)$$

and, by convention, the shell effect is then given by:

$$\Delta L = L_{\text{Bethe}} - L, \quad (2.30)$$

with $L_{\text{Bethe}} = \ln(2v^2/I)$. Full expressions for the shell effect in terms of the velocity-distribution momenta is given in [5] and values for some atoms and nucleobases in refs[42, 43, 44]. These are usually studied at high projectile velocities. Then the qv line is much steeper, and also for the quantum-based dielectric function the cut-off at low- q is due to the intersection of the qv line with the plasmon branch. It turns out that details in the plasmon dispersion near $q = 0$ are also important. Hence we show an enlargement of the loss distribution for 4 dielectric functions in fig. 2.14. For clarity the width Γ was now taken to be only 0.2 eV but further the models are the same as in the previous section. Clearly the dispersion is different for the models. The dispersion is largest for Mermin and Drude-Lindhard (peak position given by $\omega_p + q^2/2$), intermediate for MLL (peak dispersion given by $\sqrt{U^2 + (\omega_p^{\text{MLL}} + q^2/2)^2}$) and smallest for extended Drude (peak dispersion given by $\sqrt{(\omega_p^{\text{MLL}})^2 + q^4/4}$). Note however, that the similarity of the Mermin and Drude-Lindhard dispersion is *not* a general property of that dielectric function but a coincidence for the electron density of the valence band of Al. The Mermin dispersion increases with increasing electron density.

The dispersion affects the q -value for which the qv line intersects the plasmon branch. For these low q values almost all intensity is in the plasmon branch, and then the Bethe sum rule determines the contribution of that q interval to the stopping.

Besides these differences at low- q there is also a contribution at the high- q crossing of the qv line and the dispersing ELF feature. For the Mermin case this is illustrated in fig. 2.15. The loss function near $q = 10$ a.u. is wide (Compton profile) hence the contribution of the ELF to the stopping decreases gradually when the qv -line crosses the Compton profile. The crossing of the ELF of the ‘ad-hoc dielectric function’ is however abrupt, at $q = 10$ a.u. As, when calculating L the ELF contribution is weighted by $1/q$ there remains a net effect when integration is done over all q . It is predicted by the ‘equipartition principle’ [45] the contribution at low and high- q to the shell corrections are equal, and this turns out to be indeed the case.

Shell corrections for Mermin and Drude-Lindhard are very similar. However the latter has no ‘Compton broadening’. The Drude-Lindhard ELF is shifted by 15 eV relative to the Mermin ELF, at large q values, see fig. 2.12. In 2.A it is shown that this shift is responsible for the shell correction in the Drude-Lindhard case. For Drude-Lindhard the equipartition principle is adhered to well.

In fig. 2.16 we show the obtained the effects. There is good agreement between the analytical calculation of the shell effect using the formulae derived in 2.A for extended Drude and Drude-Lindhard and the values obtained by numerically integrating the stopping integral for the corresponding dielectric functions. As expected the extended Drude model, with a dispersion that is closest to our ad-hoc dielectric function has the smallest shell effect, virtually absent for $v > 3$ a.u.. The shell effect for the Drude-Lindhard decreases almost 10 times slower with increasing v . The shell effect for Mermin is negative at very low v values, as it has significant stopping even at very low v values, but for $v > 2$ a.u. it appears to be about 10% less than

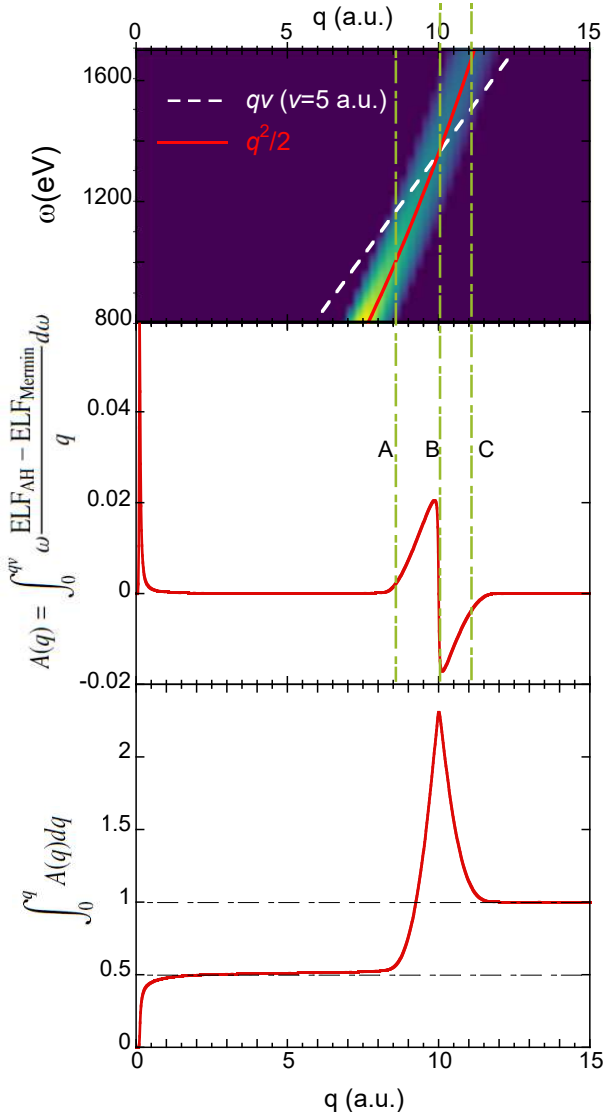


Figure 2.15: Analysis of the shell corrections for the Mermin case for protons with $v = 5$ a.u. The top panel shows the ELF for the region of the high- q crossing of the qv line and the ELF. The ad-hoc dielectric function is the red line, the dashed line is the qv line for $v = 5$ a.u. (625 keV). The central panel shows the shell correction contribution as a function of q . For q -values between A and C the contribution of the Mermin loss function to the stopping integral decreases. The Bethe contribution (at $q^2/2$) drops abruptly to zero at B. Lower panel - fractional shell correction : Integrating over all q the residual shell correction is equally due to low- q and high- q contribution.

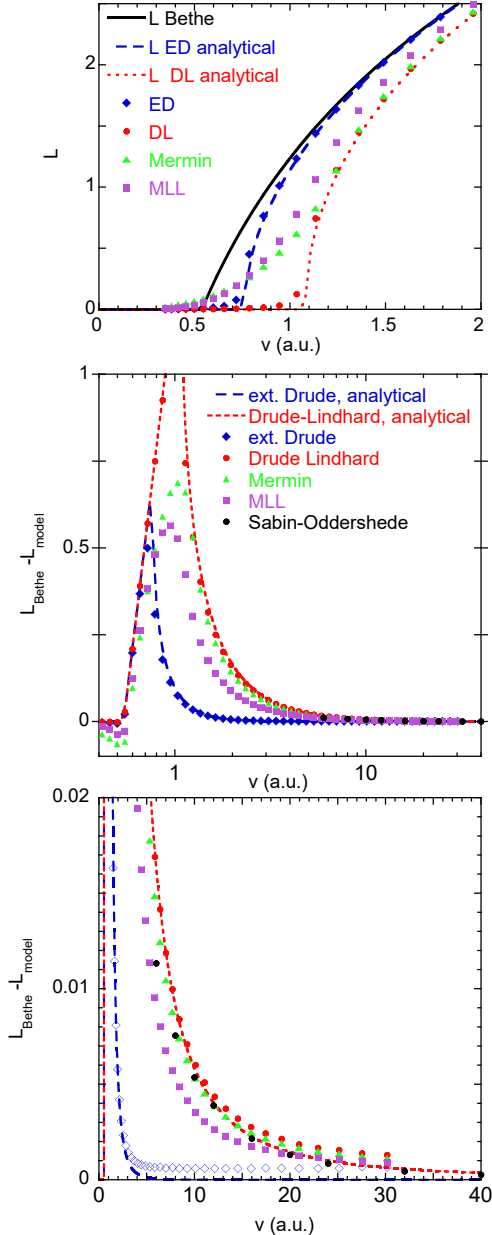


Figure 2.16: Top panel shows the $L-$ values for proton as a function of its velocity v for the models as indicated. The lines are L values corresponding to the analytical expressions 2A.4, 2A.6, 2A.8, the symbols are obtained by evaluating the stopping integral for the model dielectric functions . The central panel shows the shell effect: $L_{\text{Bethe}} - L_{\text{model}}$, the lower panel has an expanded vertical scale. The black dots were taken from the calculation by Sabin et al for the 3s and 3p electrons of atomic Al [42].

the shell effect for Drude-Lindhard. The shell effect for the MLL model is in between extended Drude and Drude-Lindhard, in agreement with the reduced dispersion of its plasmon branch.

Similar considerations apply to straggling, as is sketched in 2.B.

2.7 Conclusion

In this paper we showed the loss function of a large number of model dielectric functions, both classical models and based on quantum physics. All models adhere to sum rules and Kramers-Kronig relations at any q . Their stopping was compared to the Bethe stopping. All models converge to the Bethe stopping, but the rate at which they do differs greatly. In other words, the models predict different shell corrections. It was demonstrated for selected cases that shell corrections have a contribution at low q and at high q , i.e at the q values the qv line crosses the maxima of the ELF.

The models used were chosen so the ELF at $q = 0$ has a peak at the same energy loss as aluminum. Most materials have a much more complicated loss function at $q = 0$ and require more than one oscillator to be described properly. Considerations how to combine different oscillators were discussed. The modeling of more complex solids over the whole $q - \omega$ plane remains a challenging topic. The description given here of the different model dielectric functions may aid the reader in devising schemes that accomplish such a description. That will make shell corrections available for a larger group of materials, extending the work initiated by Sabin and Oddershede over four decades ago.

Bibliography

- [1] N. Bohr, On the theory of the decrease of velocity of moving electrified particles on passing through matter, *Philos. Mag.* 25 (1913) 10. doi:/10.1080/14786440108634305.
- [2] H. Bethe, Zur Theorie des Durchgangs schneller Korpuskularstrahlen durch Materie, *Ann. Phys.* 397 (3) (1930) 325–400. doi:10.1002/andp.19303970303.
URL <http://dx.doi.org/10.1002/andp.19303970303>
- [3] J. Lindhard, On the properties of a gas of charged particles, *K. Dan. Vidensk. Selsk. Mat.-Fys. Medd.* 28 (8) (1954) 1–57.
- [4] S. Knapen, J. Kozaczuk, T. Lin, Python package for dark matter scattering in dielectric targets, *Phys. Rev. D* 105 (1) (2022) 015014. doi:10.1103/physrevd.105.015014.
- [5] P. Sigmund, Particle Penetration and Radiation Effects, Vol. 151 of Springer Series in Solid-State Sciences, Springer, Berlin, 2006.
- [6] M. Nastasi, J. Mayer, J. K. Hirvonen, Ion–solid Interactions, Cambridge University Press, 1996. doi:10.1017/cbo9780511565007.
- [7] H. Nikjoo, S. Uehara, D. Emfietzoglou, Interaction of radiation with matter, CRC press, 2012.
- [8] R. Garcia-Molina, I. Abril, S. Heredia-Avalos, I. Kyriakou, D. Emfietzoglou, A combined molecular dynamics and Monte Carlo simulation of the spatial distribution of energy deposition by proton beams in liquid water, *Phys. Med. Biol.* 56 (2011) 6475. doi:10.1088/0031-9155/56/19/019.
- [9] R. Garcia-Molina, I. Abril, I. Kyriakou, D. Emfietzoglou, Energy loss of swift protons in liquid water: Role of optical data input and extension algorithms, in: G. G. Gomez-Tejedor, M. C. Fuss (Eds.), Radiation Damage in Biomolecular Systems, Springer, 2012, pp. 239 – 261.
- [10] H. Nikjoo, D. Emfietzoglou, T. Liamsuwan, R. Taleei, D. Liljequist, S. Uehara, Radiation track, DNA damage and response—a review, *Rep. Prog. Phys.* 79 (2016) 116601. doi:10.1088/0034-4885/79/11/116601.
- [11] D. Emfietzoglou, R. Garcia-Molina, I. Kyriakou, I. Abril, H. Nikjoo, A dielectric response study of the electronic stopping power of liquid water for energetic protons and a new I-value for water, *Phys. Med. Biol.* 54 (2009) 3451. doi:10.1088/0031-9155/54/11/012.
- [12] D. Emfietzoglou, I. Kyriakou, R. Garcia-Molina, I. Abril, Inelastic mean free path of low-energy electrons in condensed media: beyond the standard models, *Surf. Interface Anal.* 49 (2017) 4. doi:10.1002/sia.5878.
- [13] J. D. Bourke, C. T. Chantler, Momentum-dependent lifetime broadening of electron energy loss spectra: A self-consistent coupled-plasmon model, *J. Phys. Chem. Lett.* 6 (2015) 314. doi:10.1021/jz5023812.

- [14] C. T. Chantler, J. D. Bourke, New constraints for low-momentum electronic excitations in condensed matter: fundamental consequences from classical and quantum dielectric theory, *J. Phys.: Condens. Matter* 27 (45) (2015) 455901. doi:10.1088/0953-8984/27/45/455901.
- [15] N. Mermin, Lindhard dielectric function in the relaxation-time approximation, *Phys. Rev. B* 1 (1970) 2362–2363. doi:10.1103/physrevb.1.2362.
- [16] T. Kaneko, Wave-packet theory of stopping of bound electrons, *Phys. Rev. A* 40 (1989) 2188. doi:10.1103/physreva.40.2188.
- [17] A. Belkacem, P. Sigmund, Stopping power and energy loss spectrum of a dense medium of bound electrons, *Nucl. Instrum. Methods Phys. Res., Sect. B* 48 (1-4) (1990) 29–33. doi:10.1016/0168-583x(90)90066-4.
- [18] N. J. Al-Bahnam, The description of quantum dielectric function for insulators over bethe surface, *Pramana* 92 (2). doi:10.1007/s12043-018-1675-1.
- [19] I. Abril, R. Garcia-Molina, C. Denton, F. Pérez-Pérez, N. Arista, Dielectric description of wakes and stopping powers in solids, *Phys. Rev. A* 58 (1998) 357. doi:10.1103/physreva.58.357.
- [20] E. Palik, *Handbook of Optical Constants of Solids II*, Academic Press: New York, 1991.
- [21] R. F. Egerton, *Electron energy-loss spectroscopy in the electron microscope*, Plenum Press, New York, 1996.
- [22] P. E. Batson, J. Silcox, Experimental energy-loss function, $Im[-\frac{1}{\epsilon}(\omega, q)]$, for aluminum, *Phys. Rev. B* 27 (1983) 5224–5239. doi:10.1103/PhysRevB.27.5224.
- [23] H. Hayashi, N. Hiraoka, Accurate measurements of dielectric and optical functions of liquid water and liquid benzene in the VUV region (1–100 eV) using small-angle inelastic x-ray scattering, *J. Phys. Chem. B* 119 (2015) 5609. doi:10.1021/acs.jpcb.5b01567.
URL <http://dx.doi.org/10.1021/acs.jpcb.5b01567>
- [24] M. J. Cooper, P. E. Mijnarends, N. Shiotani, N. Sakai, A. Bansil, *X-Ray Compton Scattering*, Oxford University Press, 2004.
- [25] F. Wooten, *Optical Properties of Solids*, Academic Press, 1972.
- [26] H. Raether, *Excitation of plasmons and interband transitions by electrons*, Springer tracts in modern physics ; v.88, Springer Verlag, Berlin, 1979.
- [27] M. Vos, P. Grande, Simple model dielectric functions for insulators, *J. Phys. Chem. Solids* 104 (2017) 192. doi:10.1016/j.jpcs.2016.12.015.
- [28] M. Vos, P. Grande, Extracting dielectric function from high-energy REELS measurements, *Surf. Interface Anal.* in press. doi:10.1002/sia.6227.
- [29] R. Ferrell, Characteristic energy loss of electrons passing through metal foils. II. dispersion relation and short wavelength cutoff for plasma oscillations, *Phys. Rev.* 107 (1957) 450. doi:10.1103/physrev.107.450.
- [30] R. H. Ritchie, A. Howie, Electron excitation and the optical potential in electron microscopy, *Philos. Mag.* 36 (1977) 463. doi:10.1080/14786437708244948.
- [31] D. Emfietzoglou, I. Kyriakou, R. Garcia-Molina, I. Abril, H. Nikjoo, Inelastic cross sections for low-energy electrons in liquid water: Exchange and correlation effects, *Radiat. Res.* 180 (2013) 499. doi:10.1667/rr13362.1.

- [32] D. Emfietzoglou, I. Kyriakou, R. Garcia-Molina, I. Abril, The effect of static many-body local-field corrections to inelastic electron scattering in condensed media, *J. Appl. Phys.* 114 (2013) 144907. doi:10.1063/1.4824541.
- [33] K. L. Kliewer, R. Fuchs, Lindhard dielectric functions with a finite electron lifetime, *Phys. Rev.* 181 (2) (1969) 552–558. doi:10.1103/physrev.181.552.
- [34] Z. Levine, S. Louie, New model dielectric function and exchange-correlation potential for semiconductors and insulators, *Phys. Rev. B* 25 (1982) 6310. doi:10.1103/physrevb.25.6310.
- [35] C. Archubi, N. Arista, A comparative study of threshold effects in the energy loss moments of protons, electrons and positrons using dielectric models for band-gap materials, *Europ. Phys. J.B* 90. doi:10.1140/epjb/e2016-70637-9.
- [36] C. Tung, Y. Chen, C. Kwei, T. Chou, Differential cross sections for plasmon excitations and reflected electron-energy-loss spectra, *Phys. Rev. B* 49 (1994) 16684–16693. doi:10.1103/PhysRevB.49.16684.
- [37] W. Werner, K. Glantschnig, C. Ambrosch-Draxl, Optical constants and inelastic electron-scattering data for 17 elemental metals, *J. Phys. Chem. Ref. Data* 38 (2009) 1013–1092. doi:10.1063/1.3243762.
- [38] F. Yubero, S. Tougaard, Model for quantitative analysis of reflection-electron-energy-loss spectra, *Phys. Rev. B* 46 (1992) 2486–2497. doi:10.1103/PhysRevB.46.2486.
- [39] S. Limandri, R. Fadanelli, M. Behar, L. Nagamine, J. Fernandez-Varea, I. Abril, R. Garcia-Molina, C. Montanari, J. Aguiar, D. Mitnik, J. E. Miraglia, N. Arista, Stopping cross sections of TiO₂ for H and He ions, *Eur. Phys. J. D* 68 (2014) 194. doi:10.1140/epjd/e2014-40782-6.
- [40] C. Denton, I. Abril, R. Garcia-Molina, J. Moreno-Marín, S. Heredia-Avalos, Influence of the description of the target energy-loss function on the energy loss of swift projectiles, *Surf. Interface Anal.* 40 (2008) 1481. doi:10.1002/sia.2936.
- [41] B. Da, H. Shinotsuka, H. Yoshikawa, Z. J. Ding, S. Tanuma, Extended Mermin method for calculating the electron inelastic mean free path, *Phys. Rev. Lett.* 113 (2014) 063201. doi:10.1103/physrevlett.113.063201.
- [42] J. Sabin, J. Oddershede, Shell corrections to electronic stopping powers from orbital mean excitation energies, *Phys. Rev. A* 26 (6) (1982) 3209–3219. doi:10.1103/physreva.26.3209.
- [43] J. Sabin, . Oddershede, An analytical representation of shell corrections for stopping power, *Int. J. Quantum Chem.* 109 (13) (2009) 2933–2936. doi:10.1002/qua.22126.
- [44] S. Sauer, J. Oddershede, J. Sabin, Theory and calculation of stopping cross sections of nucleobases for swift ions, Springer, United States, 2012, Ch. 12, pp. 191–200.
- [45] J. Lindhard, A. Winther, Stopping power of electron gas and equipartition rule, *Mat Fys Medd Dan Vid Selsk* 34 (4) (1964) 1.
URL <http://gymarkiv.sdu.dk/MFM/kdvs/mfm%2030-39/mfm-34-4.pdf>
- [46] B. I. Lundqvist, Single-particle spectrum of the degenerate electron gas, *Physik der Kondensierten Materie* 6 (3) (1967) 206. doi:10.1007/bf02422717.
- [47] R. H. Ritchie, W. Brandt, P. M. Echenique, Wake potential of swift ions in solids, *Phys. Rev. B* 14 (11) (1976) 4808–4812. doi:10.1103/physrevb.14.4808.

2.A Appendix: Stopping formulae and shell corrections for simple dispersion relations

For completeness we show here explicitly that the dispersion relation assumed in eq. 2.11 indeed leads to the Bethe-like stopping (eq. 2.12). The stopping power is given in terms of the ELF as

$$-\frac{dE}{dx} = \frac{2Z^2}{\pi v^2} \int_0^\infty \frac{dq}{q} \int_0^{qv} \omega d\omega \text{Im} \left[\frac{-1}{\epsilon(q, \omega)} \right], \quad (2A.1)$$

where Z is the projectile charge. Assuming the ELF given by the Drude model with a narrow peak ($\Gamma \rightarrow 0$) at $\omega_p(q)$ the inner integral of the above equation will be given by the Bethe sum rule (Eq.2.7) for $\omega_p(q) < qv$ and zero otherwise. Therefore,

$$-\frac{dE}{dx} = \frac{4\pi n Z^2}{v^2} \int_0^\infty \frac{dq}{q} \Theta(qv - \omega(q)), \quad (2A.2)$$

where $\Theta(x)$ is the Heaviside function. The condition $\omega_p(q) < qv$ is realized by $q_{\min} < q < q_{\max}$ see Fig. 2.2. For this case the stopping power reads

$$-\frac{dE}{dx} = \frac{4\pi n Z^2}{v^2} \ln \left(\frac{q_{\max}}{q_{\min}} \right). \quad (2A.3)$$

For the dispersion relation from Eq. 2.11 we have $q_{\min}^{\text{Bethe}} = \omega_p/v$ and $q_{\max}^{\text{Bethe}} = 2v$ and therefore we get the Bethe-like formula:

$$-\frac{dE}{dx} = \frac{4\pi n Z^2}{v^2} \ln \left(\frac{2v^2}{\omega_p} \right). \quad (2A.4)$$

The parabola and the straight line in the ‘Bethe dispersion’ meet at $q_c = \sqrt{2\omega_p}$. The integral can be divided into two parts $q_{\min} < q < q_c$ and $q_c < q < q_{\max}$.

$$-\frac{dE}{dx} = \frac{4\pi n Z^2}{v^2} \left(\ln \left(\frac{q_{\max}}{q_c} \right) + \ln \left(\frac{q_c}{q_{\min}} \right) \right). \quad (2A.5)$$

Inspection shows that $q_{\max}/q_c = 2v/\sqrt{2\omega_p}$ and $q_c/q_{\min} = \sqrt{2\omega_p}/(\omega_p/v)$ are identical. This is an example of the ‘equipartition principle’[45] which state that the plasmon and electron-hole excitations contribute equally to the stopping.

One can use exactly the same approach to derive an analytical expression for the stopping in the case of simple quadratic dispersion (in the limit of $\Gamma \rightarrow 0$). Then one has to replace simply q_{\max} and q_{\min} by the solutions of $qv = q^2/2 + \omega_p$. ($q_{\min, \max}^{\text{DL}} = v \mp \sqrt{v^2 - 2\omega_p}$) One obtains:

$$-\frac{dE}{dx} = \frac{4\pi n Z^2}{v^2} \ln \left(\frac{v + \sqrt{v^2 - 2\omega_p}}{v - \sqrt{v^2 - 2\omega_p}} \right), \quad (2A.6)$$

which should not overestimate the stopping at the stopping maximum as much as the Bethe-like equation does.

$q_{\max}^{\text{Bethe}} > q_{\max}^{\text{DL}}$ and similarly $q_{\min}^{\text{Bethe}} < q_{\min}^{\text{DL}}$. The contribution to the stopping integral between q_{\min}^{DL} and q_{\max}^{DL} is the same for the Bethe and DL dielectric function. The shell effect $L_{\text{Bethe}} - L_{\text{DL}}$ is thus equal to

$$L_{\text{Bethe}} - L_{\text{DL}} = \ln \left(\frac{q_{\min}^{\text{DL}}}{q_{\min}^{\text{Bethe}}} \right) + \ln \left(\frac{q_{\max}^{\text{Bethe}}}{q_{\max}^{\text{DL}}} \right) \quad (2A.7)$$

The contribution to the shell corrections of each part of eq.2A.7, namely $\frac{\omega_p}{2v^2}$, are identical at high projectile velocities and reflects the equipartition principle, which is also fulfilled for DL : $q_{\max}^{\text{DL}}/q_c = q_c/q_{\min}^{\text{DL}}$ as can be easily verified.

In the extended Drude case for a free electron gas the limits of integration are obtained from $(qv)^2 = A_1^2 + q^4/4$ ($(q_{\min,\max}^{\text{ED}} = \sqrt{v^2 \mp \sqrt{v^4 - \omega_p^2}}$). Then the stopping becomes:

$$-\frac{dE}{dx} = \frac{4\pi n Z^2}{v^2} \ln \left(\frac{q_{\max}^{\text{ED}}}{q_{\min}^{\text{ED}}} \right) \quad (2A.8)$$

The extended Drude dielectric function corresponds to the static electron gas, as described by Sigmund and this formula was also derived there (ref. [5], eq. 5.77). Of course its shell corrections are given by:

$$L_{\text{Bethe}} - L_{\text{ED}} = \ln \left(\frac{q_{\min}^{\text{ED}}}{q_{\min}^{\text{Bethe}}} \right) + \ln \left(\frac{q_{\max}^{\text{Bethe}}}{q_{\max}^{\text{ED}}} \right) \quad (2A.9)$$

Now both contributions are similar, but not exactly the same, as the q value separating hard and soft collisions is different for ED compared to Bethe.

Similarly, when using full dispersion ($\omega_p(q)^2 = \omega(0)^2 + \beta^2 q^2 + q^4/2$) the stopping becomes:

$$-\frac{dE}{dx} = \frac{4\pi n Z^2}{v^2} \ln \left(\frac{\sqrt{-\beta^2 + v^2 + \sqrt{(\beta^2 - v^2)^2 - \omega_p^2}}}{\sqrt{-\beta^2 + v^2 - \sqrt{(\beta^2 - v^2)^2 - \omega_p^2}}} \right), \quad (2A.10)$$

with $\beta^2 = 2/3 E_f$ [46] or $\beta^2 = 6/5 E_f$ [47].

2.B Appendix: Straggling formula for Ad-hoc and Drude-Lindhard DF

renewcommand2A.02B.0

The Ad-hoc loss function eq. 2.11 also leads to the Bohr-like straggling for high projectile velocities according to

$$\begin{aligned} \frac{d\Omega^2}{dx} &= \frac{2Z^2}{\pi v^2} \int_0^\infty \frac{dq}{q} \int_0^{qv} \omega^2 d\omega \text{Im} \left[\frac{-1}{\epsilon(q, \omega)} \right] \\ &= \frac{2Z^2}{\pi v^2} \int_0^\infty \frac{dq}{q} \int_0^{qv} \omega_p(q) d\omega A_{AH} \delta(\omega - \omega_p(q)), \end{aligned} \quad (2B.1)$$

with $\omega_p(q) = \max(\omega_p, q^2/2)$. As in 2.A, assuming $q_{\min} < q < q_{\max}$ and $q_c = \sqrt{2\omega_p}$, with $q_{\min} < q_c < q_{\max}$ we have

$$\begin{aligned} \frac{d\Omega^2}{dx} &= \frac{4\pi n Z^2}{v^2} \left(\omega_p \ln \left(\frac{q_c}{q_{\min}} \right) + \frac{1}{4} (q_{\max}^2 - q_c^2) \right) \\ &= \frac{4\pi n Z^2}{v^2} \left(\frac{\omega_p}{2} \ln \left(\frac{2v^2}{\omega_p} \right) + \left(v^2 - \frac{\omega_p}{2} \right) \right), \end{aligned} \quad (2B.2)$$

which gives the Bohr straggling $\frac{d\Omega_B^2}{dx} = 4\pi n Z^2$ at high projectile velocities and is valid for $2v^2 > \omega_p$. It is similar to one derived for atomic systems [5] presenting a Bethe-Livingston-like shoulder.

Using the same arguments we get for the Drude-Lindhard dielectric function:

$$\left(\frac{d\Omega^2}{dx} \right)_{\text{DL}} = \frac{4\pi n Z^2}{v^2} \left(\omega_p \ln \left(\frac{q_{\max}}{q_{\min}} \right) + \frac{1}{4} (q_{\max}^2 - q_{\min}^2) \right) \quad (2B.3)$$

with now $q_{\min,\max} = v \mp \sqrt{v^2 - 2\omega_p}$. Results are compared in fig. 2A.1.

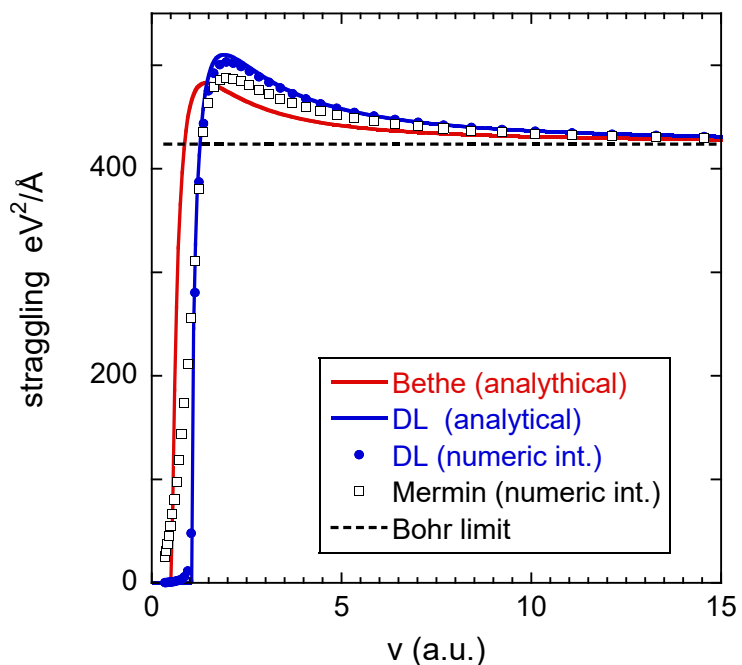


Figure 2A.1: The straggling for protons in a plasma with $\omega_p = 15$ eV as calculated analytically for our "ad-hoc" (Bethe) dielectric function (eq. 2B.2, Drude-Lindhard dielectric function (eq. 2B.3) as well as the numerical integration of the same Drude-Lindhard dielectric function and the Mermin dielectric function.

Chapter 3

RPA Dielectric Functions: Streamlined Approach to Relaxation Effects, Binding and High Momentum Dispersion¹

3.1 abstract

The implementation of dielectric functions based on the Random Phase Approximation (RPA), including those by Lindhard, Kaneko, and Levine-Louie, is presented systematically, incorporating the effects of electron relaxation (finite width) and lattice interactions. A straightforward approach is proposed to introduce electron relaxation time and binding effects without needing Mermin corrections or Kramers-Kronig (KK) relations. This method yields the same dielectric function as the Mermin-corrected Lindhard and Kaneko models in several limiting cases (optical, high momentum transfer, and static limits). Moreover, this method adheres to the Bethe and F sum rule and the real and imaginary part are Kramers-Kronig pairs. Still, it shows some variation at intermediate energy and momentum transfer. Additionally, the description of dispersion at high momentum transfer is refined to account for relativistic effects. A small library containing the implement

3.2 Introduction

The description of the interaction of matter with both static electric fields and those varying in space and/or time has a long history, starting with the Drude dielectric function. Introduction of the random phase approximation (RPA) [1] made a quantum-based approach possible, and this was applied first to the simplest case of a free electron gas. Lindhard introduced an imaginary part to the energy ($\omega + i\Gamma$), mainly as a tool to facilitate the mathematical derivation, and used that dielectric function always in the limit of $\Gamma \rightarrow 0$ [2]. This gives loss functions that consist of a dispersing line ('delta function' in energy) for the plasmon contribution and a distributed intensity due to single-electron excitations. Description of experimental results in terms of the dielectric function, e.g. the measured (transmission) electron energy loss spectra, is more easily done in terms of distributions with finite width. However, the use of non-zero Γ values causes inconsistencies [3]. The Lindhard dielectric function with finite Γ does not describe a metal, and the corresponding loss function is too wide. This problem was overcome by Mermin who designed a 'correction' method that recovers the metallic behaviour also for $\Gamma > 0$ and reduces the width [4].

¹preprint of J Phys Chem of Solids 198 112470 2024

Of course, in many cases a free electron approach has severe limitations, and variations of the dielectric function were introduced that overcome these shortcomings to a certain extent. In particular, Levine and Louie [5] introduced a parameter U that models the influence of a band gap, facilitating the description of semiconductors. Kaneko used the RPA in combination with a Gaussian dependency of the occupancy (rather than a step function at the Fermi wave vector) making the description of the contribution of core levels to the dielectric function more realistic [6]. Archubi and Arista added again a U parameter to the Kaneko approach [7]. These dielectric functions are mainly used in the limit of $\Gamma \rightarrow 0$.

These dielectric functions, describing the reaction of matter to an electric field that varies in space and time, are all in Fourier space and thus a function of ω (energy) and q (momentum). In the low- q limit the electric field varies slowly in space and one probes properties of matter on a macroscopic scale, where classical physics should apply. In this limit all these RPA-derived dielectric functions approach the classical Drude-Lindhard model (extended here also with an additional U parameter).

In this paper we first discuss the role of Γ in the classical Drude-Lindhard dielectric function. Then the results of various RPA models are summarised. It is discussed what is gained if one corrects the DF with the Mermin procedure when $\Gamma > 0$, for free electrons and also for the case with $U > 0$ and/or for a Gaussian occupancy. Finally we introduce a new approach for the choice of complex energy, that reproduces the required behaviour of ϵ_1 at $q = 0$ (as well as the correct width of the loss function), without requiring a ‘Mermin’ normalisation, based on the earlier discussion of the Drude-Lindhard dielectric function. In addition, a small modification is introduced that leads to dispersion of the loss function, consistent with relativity for these RPA theories.

We will use atomic units, unless otherwise noted (electron mass $m_e = 1$, $\hbar = 1$, elementary charge $e = -1$).

3.3 Classical Drude dielectric function

First consider the classical dielectric function, as introduced by Drude. This case is somewhat trivial, but the formulation used here will be used later for quantum-physics-based dielectric functions. The Drude dielectric function ϵ_D is in the optical limit ($q = 0$):

$$\epsilon_D(\omega) = 1 - \frac{\omega_p^2}{\omega(\omega + i\Gamma) - U^2} \quad (3.1)$$

with $\omega_p = \sqrt{4\pi n}$ and n the electron density. U is the binding energy of the electron, and $U = 0$ models the valence electrons in metals. Γ corresponds to the width due to the ‘damping’ of the oscillator.

For the calculation of many physical properties, one has to extend this dielectric function to non-zero momentum transfer. For the purpose of this paper, it is best done in terms of $1/\epsilon$ as suggested by Ritchie and Howie [8], and then the dielectric function (DF) is often referred to as the Drude-Lindhard (DL) dielectric function. The DL DF is usually defined as having a real part:

$$\text{Re} \left[\frac{1}{\epsilon^{\text{DL}}(\omega, q)} \right] = 1 + \frac{(\omega^2 - \omega_p(q)^2 - U^2)\omega_p(0)^2}{(\omega^2 - \omega_p(q)^2 - U^2)^2 + \omega^2\Gamma^2} \quad (3.2)$$

and the imaginary part is usually given in terms of the loss function (i.e. $\text{Im}[-1/\epsilon]$) :

$$\text{Im} \left[\frac{-1}{\epsilon^{\text{DL}}(\omega, q)} \right] = \frac{\omega\Gamma_i\omega_p(0)^2}{(\omega^2 - \omega_p(q)^2 - U^2)^2 + \omega^2\Gamma^2}, \quad (3.3)$$

and $\omega_p(q)$ the plasmon frequency, which now depends on q . For the momentum dependence of ω_p one uses usually either quadratic dispersion ($\omega_p(q) = \omega(0) + q^2/2$) or ‘full dispersion’

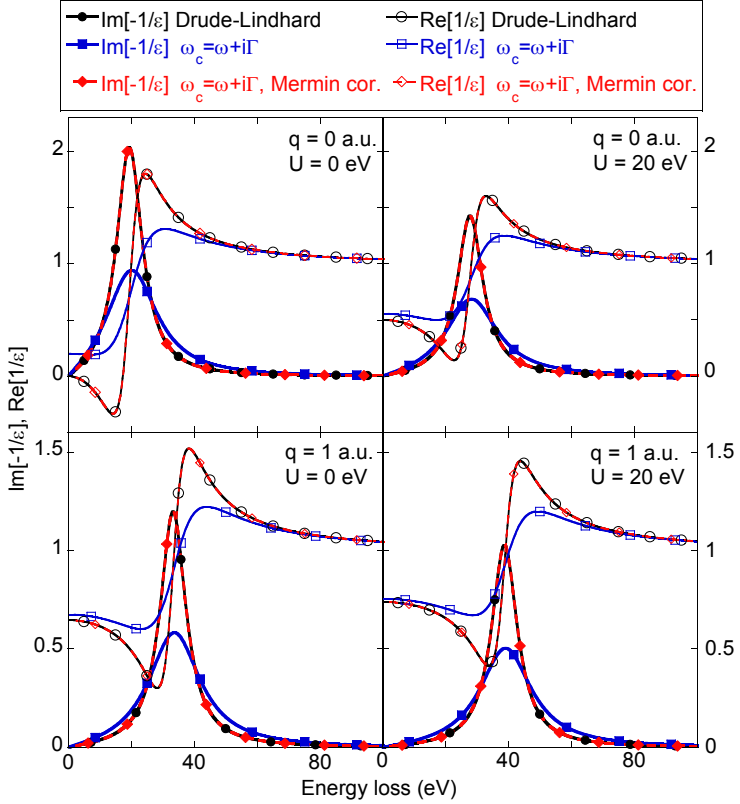


Figure 3.1: The Drude Lindhard dielectric function for $\omega_p = 20$ eV and $\Gamma = 10$ eV at $q = 0$ (top) and $q = 1$ (bottom), using a U value of 0 eV (left panels) and 20 eV (right panels). The dielectric function is calculated in 3 ways: using eq: 3.5 (the definition of the Drude-Lindhard dielectric function), using eq. 3.6 with $\omega_c = \omega + i\Gamma$ (which gives different results), and with the result of the second calculation, corrected using the Mermin formula, (eq: 3.17). After the Mermin correction the initial DF is recovered in all 4 cases.

$(\omega_p(q) = \sqrt{\omega(0)^2 + v_f^2 q^2/3 + q^4/4}$ with v_f the Fermi velocity [9]). The U term is usually omitted. However, $U > 0$ can be used to model an insulator. With $U = 0$ one has $\text{Re} \left[\frac{1}{\epsilon(0,0)} \right] = 0$, as required for a metal. In general one has:

$$\text{Re} \left[\frac{1}{\epsilon(0,0)} \right] = 1 - \frac{\omega_p(0)^2}{\omega_p(0)^2 + U^2}, \quad (3.4)$$

and thus $\epsilon(0,0)$ does not depend on Γ .

In this paper we want to emphasise the simplifications that occur if one uses complex parameters to describe the dielectric function. As a first, trivial, step one can combine the real (ϵ_1) and imaginary (ϵ_2) parts (eq. 3.2 and eq. 3.3) and then the DL DF reduces to:

$$\frac{1}{\epsilon^{\text{DL}}(\omega, q)} = 1 + \frac{\omega_p(0)^2}{(\omega^2 - \omega_p(q)^2 - U^2) + i\omega\Gamma} \quad (3.5)$$

This equation suggests that one could get further simplifications when one combines ω and $i\omega\Gamma$, just like $1/\epsilon^{\text{DL}}$, into a single, complex, quantity. We will refer to this quantity as ω_c . The question arises then: what is the best way to define ω_c ?

Without relaxation ($\Gamma = 0$) eq. 3.5 function reduces to:

$$\frac{1}{\epsilon^{\text{DL}}(\omega, q)} = 1 + \frac{\omega_p(0)^2}{\omega^2 - \omega_p(q)^2 - U^2} \quad (3.6)$$

Now if one introduces relaxation by simply substituting ω by $\omega_c = \omega + i\Gamma$ in eq. 3.6 then one obtains:

$$\begin{aligned} \frac{1}{\epsilon(\omega_c, q)} &= 1 + \frac{\omega_p(0)^2}{(\omega_c^2 - \omega_p(q)^2 - U^2)} \\ &= 1 + \frac{\omega_p(0)^2}{(\omega^2 - \Gamma^2 - \omega_p(q)^2 - U^2) + 2i\omega\Gamma} \end{aligned} \quad (3.7)$$

which, as illustrated in fig 3.1, differs from $1/\epsilon^{\text{DL}}(\omega, q)$ in two ways:

- the complex part of the denominator is $2\omega\Gamma$, rather than $\omega\Gamma$, i.e. the width in the peak of the loss function has doubled.
- there is a contribution Γ^2 to the real part of the denominator, i.e. the dielectric function corresponds to an insulator, even if $U = 0$.

One can, of course, describe $1/\epsilon^{\text{DL}}(\omega_c, q)$ as:

$$\frac{1}{\epsilon^{\text{DL}}(\omega_c, q)} = 1 + \frac{\omega_p(0)^2}{\omega_c^2 - \omega_p(q)^2} \quad (3.8)$$

with ω_c defined as:

$$\omega_c = \sqrt{\omega^2 - U^2 + i\omega\Gamma}. \quad (3.9)$$

This obviously corresponds to the DL dielectric function (eq. 3.5). Also the Drude DF (eq. 3.1) is then just $\epsilon_D = 1 - \omega_p^2/\omega_c^2$. One of the aims of this paper is to explore if the definition of ω_c , as defined in eq. 3.9, also leads to internally consistent results for quantum dielectric functions based on the RPA. In the process, we show that, when using complex variables, one can formulate various forms of the RPA DF in a more compact form.

3.4 RPA based dielectric functions

In the RPA the general expression for the dielectric function for a free electron gas (FEG) with electron density n reads:

$$\varepsilon(\omega, q) = 1 + \frac{4\pi n}{q^2} \int d^3k \frac{F(\vec{q} + \vec{k}) - F(\vec{k})}{\hbar\omega + i\Gamma - (E_{\vec{q} + \vec{k}} - E_{\vec{k}})} \quad (3.10)$$

with q the momentum transferred to the electron gas, k the momentum of an electron in the electron gas before excitation, and Γ a (usually infinitely-small) width. $F(q)$ is the probability density of q normalized as:

$$\int d^3q F(q) = 1. \quad (3.11)$$

For a FEG (at 0 K) one takes for $F(q)$

$$F_{\text{FEG}}(q) = \left(\frac{4\pi}{3} q_f^3 \right)^{-1} \Theta(q_f - q) \quad (3.12)$$

with Θ the Heaviside step function and q_f the Fermi wave vector ($(3\pi^2n)^{1/3}$). Then, this equation leads to the Lindhard dielectric function.

The dielectric function does not depend on the spatial coordinate. Core electrons are localised near the nucleus. The description of the contribution of the core electrons to the dielectric function is thus necessarily dependent on some local approximation. Lindhard assumed that the local contribution of a core level is equal to that of a free electron gas with the same density.

An alternative was formulated by Kaneko that emphasizes the momentum density distribution over the coordinate-space electron density for the calculation of the core-level contribution to the dielectric function. $F(q)$ is assumed to be equal to $|\phi(q)|^2$, i.e. the modulus square of the momentum-space wave function of the core level. Then, after approximating $|\phi(q)|^2$ by a Gaussian, Kaneko succeeded in deriving an analytical expression for the dielectric function. Such a Gaussian function:

$$F(q) = |\phi(q)|^2 \approx \frac{1}{\bar{q}^3 \pi^{3/2}} \exp(-q^2/\bar{q}^2), \quad (3.13)$$

where \bar{q} is the characteristic momentum of the orbitals is quite appropriate for an s -level.

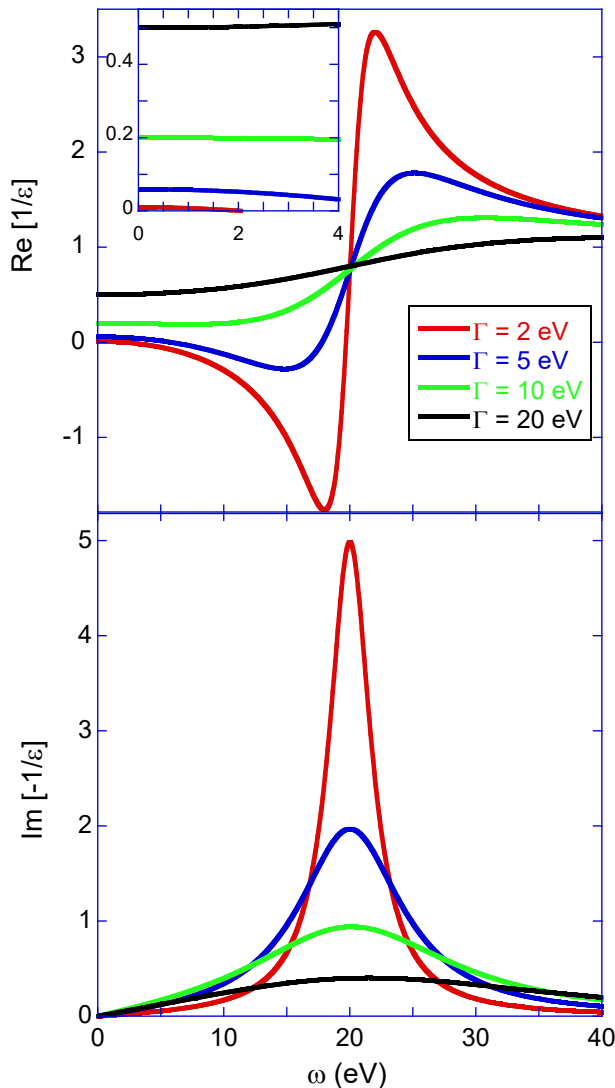


Figure 3.2: The Lindhard dielectric function for $\omega_p = 20 \text{ eV}$ near $q = 0$ as obtained by replacing ω with $\omega + i\Gamma$ with Γ values as indicated. The insert in the top panel shows $1/\epsilon_1$ on an expanded scale. Note that the width of the loss function is 2Γ and the value of $1/\epsilon_1$ at $\omega = 0$ follows $1 - 1/(1 + (\Gamma/\omega_p)^2)$, i.e. the dielectric function does not correspond to a metal (which has $1/\epsilon_1 = 0$ for $\omega = 0$, $q = 0$)

3.4.1 RPA dielectric function for a free electron gas

The Lindhard dielectric function for an electron gas with density n is usually derived in terms of the Fermi velocity v_f (or the Fermi energy $E_f = \frac{1}{2}v_f^2$) and the dimensionless variables $u' = (\omega + i\Gamma)/qv_f = \omega_c/qv_f$ and $z = q/2k_f$. When one uses atomic units $v_f = k_f$. Using this notation the dielectric function is given by: [2, 10]

$$\epsilon^L(\omega_c, q) = 1 + \frac{3\omega_p^2}{q^2 v_f^2} f(u', z) \quad (3.14)$$

where

$$f(u', z) = \frac{1}{2} + \frac{g(z + u') + g(z - u')}{8z}$$

with

$$g(a) = (1 - a^2) \ln \left(\frac{1 + a}{1 - a} \right)$$

When programming the Lindhard DF with finite width, these are the equations to use, and are convenient as most computer languages nowadays support intrinsically complex numbers. Usually the derivation of the Lindhard dielectric function continues by taking the limit of $\Gamma \rightarrow 0$. Then all parameters become real. However, the argument of one of the two log functions involved can still be negative and one still has to use the properties of the complex log function as $\ln(x) = \ln(|x|) + i\pi$ for $x < 0$.

3.4.2 Relativistic dispersion

The definition of the dielectric function of eq. 3.14 is independent of the speed of light c (≈ 137 a.u.), and hence the result is non-relativistic. At large q values the loss function is centered around the Bethe ridge i.e. at $\omega = q^2/2$. This becomes an issue if one wants to calculate ion stopping and, in particular, ion straggling based on this dielectric function for very energetic projectiles. Then energy transfer to a target electron can then be significant relative to the electron rest mass (511 keV), and proper relativistic kinematics is required.

For the diagonal in the $u - z$ plane ($u = \omega/(qv_f)$) one has $u = z$, i.e. $\omega = q^2/2$ and the diagonal corresponds to the (non-relativistic) Bethe ridge. In order to get dispersion consistent with relativity, one has to adjust the definition of u and z slightly. Relativistically, the recoil energy Q is given by $Q = \sqrt{c^2 q^2 + c^4} - c^2$. For small q values $Q \approx q^2/2$. If one defines $u = \omega/(\sqrt{2Q}v_f)$ and $z = \sqrt{2Q}/(2v_f)$ then the diagonal in the $u - v$ plane corresponds always to $\omega = Q$. The F and Bethe sum rules are not affected by this ‘new’ definition of u and z , (see supplementary material). In the preceding we gave the formulae for u and v in the familiar non-relativistic form, but for large q values, ($q \gtrsim 10$ a.u.), one should replace q with $\sqrt{2Q}$, in the definition of u (u') and z , as is done in the remainder of the paper. However, we restrict ourselves to low plasma densities, i.e. the Fermi velocity $v_f \ll c$.

3.4.3 RPA for Gaussian occupancy

This model was introduced by Kaneko [6] and it still assumes plane waves as eigenstates, but describes the occupancy as decreasing as:

$$F_{\text{Gaussian}}(q) = e^{-q^2/\bar{q}^2}, \quad (3.15)$$

rather than as a step function at the Fermi momentum, as appropriate for a free-electron gas. The electron density defined by \bar{q} corresponds to a plasmon energy $\omega_p^2 = \bar{q}^3/\sqrt{\pi}$. Following Kaneko, we define now the dimensionless variables u'_k , z_k that are defined in terms of its characteristic

momentum \bar{q} of the orbital under consideration: $u'_k = (\omega + i\Gamma)/(\sqrt{2Q}\bar{q})$, $z_k = \sqrt{2Q}/(2\bar{q})$. One obtains then the dielectric function $\epsilon^K(\omega, q)$:

$$\epsilon^K(\omega_c, q) = 1 + i \frac{\bar{q}^2}{q^3} (w(u'_k - z_k) - w(u'_k + z_k)) \quad (3.16)$$

with $w(z)$ the Faddeeva function, which is the extension of the Dawson function in the complex plane:

$$w(z) = e^{-z^2} \left(1 + \frac{2i}{4\pi} \int_0^z e^{t^2} dt \right)$$

The Faddeeva function is well-behaved in the first two quadrants of the complex plane and available e.g. in the SciPy python package or the C++ open-source Faddeeva library.

In the limit of $\Gamma \rightarrow 0$, u'_K becomes real and the expressions for ϵ_1 and ϵ_2 in terms of the Dawson and exponential functions from ref [6, 7] are recovered.

3.4.4 Mermin Correction

Over half a century ago, it was already pointed out by Mermin[4] that for finite Γ -values, the Lindhard dielectric function does not have the desired properties. In the context of this paper the most obvious shortcoming is that, for the case that $U = 0$, $\text{Re}[1/\epsilon_1(\omega, q)]$ does not approach 0 for $\omega \rightarrow 0$, $q \rightarrow 0$, as appropriate for a metal, see Fig. 3.2.

Also the width of the loss function near $q = 0$ corresponds to 2Γ , rather than Γ . The same applies to the Kaneko dielectric function with finite Γ values. This behavior is the same as was seen for the classical Drude-Lindhard dielectric function if one tries to introduce Γ as the complex part of ω , see eq. 3.7 and Fig. 3.1.

In response to this, Mermin devised a correction method using arguments based on relaxation to the correct density matrix:

$$\epsilon^M(\omega, q) = 1 + \frac{(1 + i\Gamma/\omega)(\epsilon^L(\omega + i\Gamma, q) - 1)}{1 + \left(\frac{i\Gamma}{\omega}\right) \left(\frac{\epsilon^L(\omega + i\Gamma, q) - 1}{\epsilon^L(0, q) - 1}\right)} \quad (3.17)$$

This procedure restores the metallic character (i.e. $\text{Re } \epsilon(\omega, q) \rightarrow \infty$ when $\omega \rightarrow 0$ and $q \rightarrow 0$ for any value of Γ). It also reduces the width of the plasmon peak by a factor of 2. The same procedure can be applied to ϵ^K , instead of ϵ^L , which again results in a dielectric function with a metallic character. More generally, after Mermin correction the RPA-derived dielectric function coincides with the Drude-Lindhard dielectric function in the limit of $q \rightarrow 0$.

Surprisingly, the Mermin correction also works for the classical Drude-Lindhard dielectric function if one starts with the one obtained after substituting $\omega_c = \omega + i\Gamma$ in eq. 3.6. The obtained dielectric function differs from the proper DL DF (see Fig. 3.1), but the Mermin correction applied to this result recovers the correct Drude-Lindhard result. This works for any q or U or Γ value, as is illustrated in Fig. 3.1.

3.4.5 Inclusion of ‘binding energy’ or ‘band gap’ effects

Levine and Louie suggested that the effect of band gap on the dielectric function can be modelled as a shift in the energy scale [5]:

$$\omega \Rightarrow \sqrt{\omega^2 - U^2}, \quad (3.18)$$

and then the definition of u' changes to

$$u'_{LL} = \frac{\sqrt{\omega^2 - U^2} + i\Gamma}{\sqrt{2Q}v_f}, \quad (3.19)$$

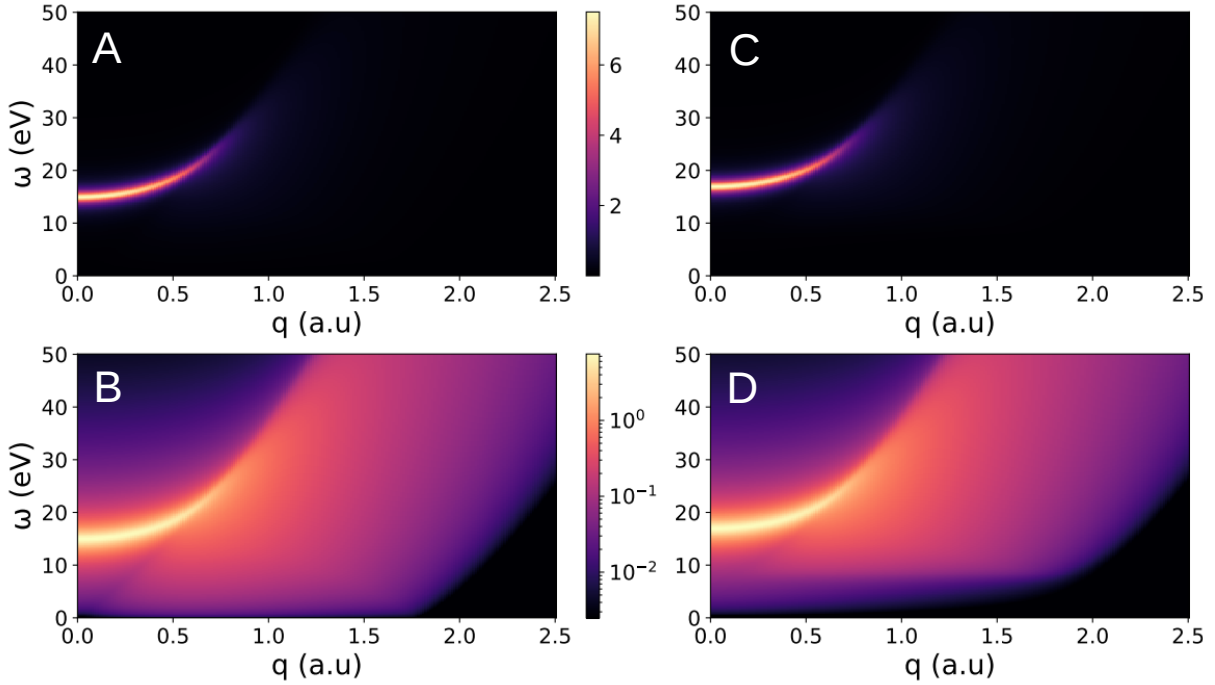


Figure 3.3: The loss function for $\omega_p = 15$ eV, $\Gamma = 2$ eV as a false color plot. (A) shows the case of $U = 0$, on a linear scale, (B) shows the same calculation using a log color scale. There is a sharp intense plasmon feature starting at 15 eV and a wide, much less intense contribution due to single-electron excitations extending (for $\omega \approx 0$ eV) up to $2k_f$ ($k_f = 0.89$ a.u. for $\omega_p = 15$ eV)). (C) and (D) are identical to (A) and (B) respectively except that $U = 8$ eV. Now the plasmon peak is shifted to slightly larger losses, but the main difference is suppression of the single-electron excitations in the band gap. The Gamma-value affects how quickly the intensity approaches 0 inside the gap. The direct method (see section 3.5) was used for both calculations but an almost identical plot is obtained when using eq. 3.20 in combination with eq. 3.17.

resulting in:

$$\epsilon^{LL}(\omega_c, q, U) = 1 + \frac{3\omega_p^2}{q^2 v_f^2} f(u'_{LL}, z). \quad (3.20)$$

In the original paper of Levine and Louie, the energy was taken as a real variable. That means that the shift in energy according to eq. 3.18 is only possible for $\omega > U$. For $\omega < U$ a Kramers-Kronig transform was required to obtain ϵ_1 . For a complex representation of the energy such a restriction does not occur, and the value of the dielectric function for any (ω, q) combination is directly obtained from eq. 3.20. It turns out that Eq. 3.20 indeed does not correspond to a metal anymore, and in the limit of $\Gamma \rightarrow 0$ one has:

$$\text{Re} \left[\frac{1}{\epsilon(0, 0)} \right] = 1 - \frac{\omega_p^2}{\omega_p^2 + U^2}. \quad (3.21)$$

Levine and Louie only considered the case with $\Gamma \rightarrow 0$. For non-zero Γ , the value of $\text{Re} \left[\frac{1}{\epsilon(0, 0)} \right]$ increases. This Γ -dependence is again removed if one applies the Mermin correction (eq. 3.17) to this dielectric function using with $\epsilon^L(0, q)$ replaced by $\epsilon^{LL}(0, q, U)$. Indeed, in the limit of $q \rightarrow 0$, ϵ^{LL} goes over in the Drude-Lindhard DF with the same parameters (including U). An example of the effect of U on the loss function is given in Fig. 3.3. Introducing a band gap in this way, rather than just simply truncating the loss function inside the band gap, ensures that all mathematical properties of the dielectric function (e.g. sum rules at any q , real and imaginary part are Kramers-Kronig-pairs at any q . see supplementary material) rigorously apply.

Archubi and Arista implemented a similar energy shift for the Kaneko dielectric function [7]. Then u'_k in eq. 3.16 has to be replaced by:

$$u'_k^{AA} = \frac{\sqrt{\omega^2 - U^2} + i\Gamma}{\sqrt{2Qq}}. \quad (3.22)$$

Also in this case, the dielectric function is obtained for all (ω, q) values and no Kramers-Kronig transforms are required even for $\omega < U$. The Γ -dependence of $\text{Re}\left[\frac{1}{\epsilon(0,0)}\right]$ is again removed if one corrects the dielectric function using the Mermin procedure (eq. 3.17) with $\epsilon^L(0, q)$ replaced by $\epsilon^K(0, q, U)$ and this procedure ensures that ϵ^K coincides with Drude-Lindhard for $q \rightarrow 0$.

3.5 Alternative definition of ω_c

We have seen that, if one starts with a classical dielectric function without Γ (eq. 3.6), one does not obtain the correct DL dielectric function if one just replaces ω by $\omega_c = \omega + i\Gamma$. The correct dielectric function is obtained, however, using this definition of ω_c and Mermin correction. The Mermin correction is not required if one takes $\omega_c = \sqrt{\omega^2 - U^2 + i\omega\Gamma}$ in eq. 3.6.

This raises the question: Is the Mermin correction required if one uses this definition for ω_c in the RPA formulae, i.e. take $u' = \sqrt{\omega^2 - U^2 + i\omega\Gamma}/(\sqrt{2Qv_f})$. We will refer to this way as the ‘direct’ method (i.e. without Mermin correction). In Fig. 3.4 the results of this ‘direct method’ are compared with those of DL, Lindhard (with Γ) and Mermin-corrected Lindhard. In the limit of $q \rightarrow 0$ the loss function for the classical DL DF, the Mermin DF and the DF obtained by the direct method are all identical, only the Lindhard DF loss function differs, as it is wider and $\text{Re}[1/\epsilon]$ has a non-metallic character, see Fig. 3.4. The classical DL DF has a width that does not depend on q . At very high momentum transfer (here 40 a.u.) all RPA-based loss functions are identical and represent a Compton profile of the electron momentum distribution. Here, there is a noticeable shift if one uses the proper relativistic kinematics. At intermediate q values, e.g. 0.5 a.u., the direct method gives a peak slightly sharper than the one obtained after Mermin correction. The Lindhard DF is still too wide. At 2 a.u. the loss functions of all 3 RPA-based DFs are already very similar.

All 4 DFs adhere to the Bethe and F sum rules and the real and imaginary parts are related by the Kramers-Kronig relations (see supplementary material). We have no interpretation for the small difference between the Mermin and the ‘direct DF’ at intermediate q values.

An example of a Kaneko dielectric function with non-zero U is given in Fig. 3.5. For the direct method one takes $u'_k = \sqrt{\omega^2 - U^2 + i\omega\Gamma}/(\sqrt{2Qq})$. Except for the Kaneko DF (without Mermin correction), all DF have $\text{Re}[1/\epsilon(0,0)] = 0.5$. At $q = 40$ a.u. $\text{Re Im}[-1/\epsilon(0,0)]$ has, for the RPA-based DFs, a Gaussian shape reflecting the assumed momentum distribution. For intermediate cases ($q = 0.5$ a.u., $q = 2$ a.u.) the dielectric functions obtained by the direct calculation and the Mermin-corrected one are very similar, but not the same.

Another interesting test case is the q -dependence of $\text{Re}[\epsilon]$ in the $\omega \rightarrow 0$ limit. Then it is expected that for a metal ($U = 0$), one obtains for low q values the Thomas-Fermi dielectric function:

$$\epsilon_1^{\text{TF}} = 1 + \frac{3\omega_p^2}{q^2 v_f^2} \quad (3.23)$$

This is indeed the case, as shown in Fig. 3.6 for both the Mermin and ‘direct’ dielectric function, but not for the Lindhard one. Another well-known property of ϵ_1 describing a free electron gas, near $\omega = 0$ is a sudden change in slope at $2k_f$. Both the ‘direct’ and the Mermin calculations display this behavior; see the insert of Fig. 3.6. This kink is absent for the Kaneko DF.

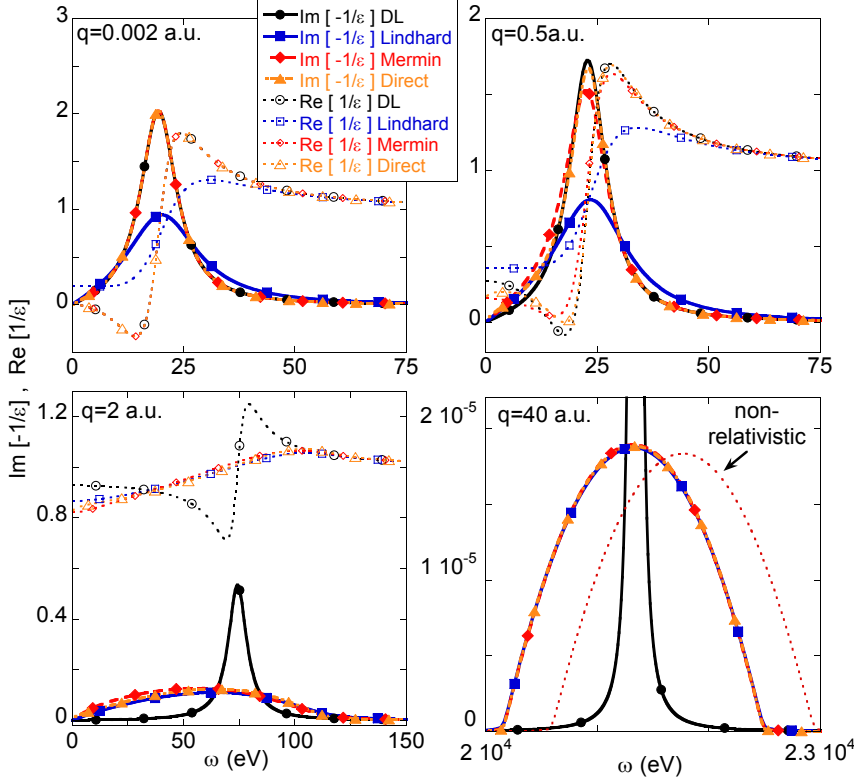


Figure 3.4: The loss function and the real part of $1/\epsilon$ as obtained using the DL, Lindhard, Mermin and ‘Direct’ method at the q values as indicated. For the highest q value only the loss function is plotted. In that case also the loss function is plotted for the Mermin case if non-relativistic kinematics is assumed. This calculation used $\omega_p = 20$ eV, $\Gamma = 10$ eV, and $U = 0$ eV. For the intermediate q values all 4 methods result in different results, but at $q = 0$ only the Lindhard method deviates, whereas at $q = 40$ the only deviation is for the DL case.

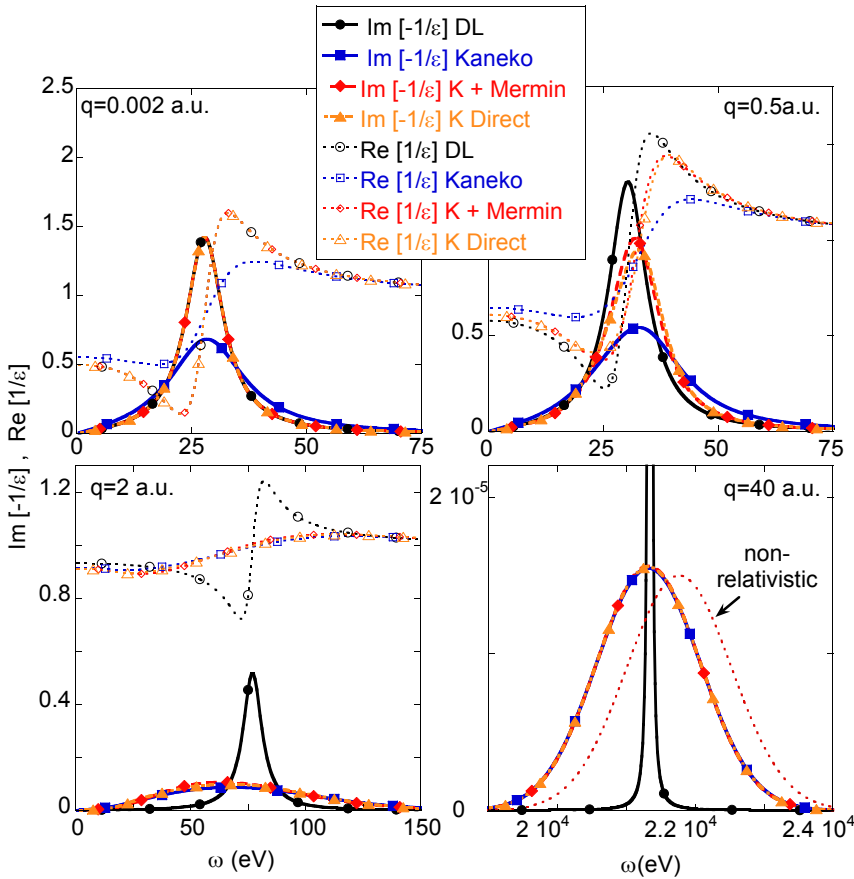


Figure 3.5: Same as Fig. 3.4, but now for a Kaneko dielectric function with $\bar{q} = 0.98$ a.u., $\Gamma = 10$ eV and $U = 20$ eV. The electron density of this dielectric function is the same as that of Fig. 3.4

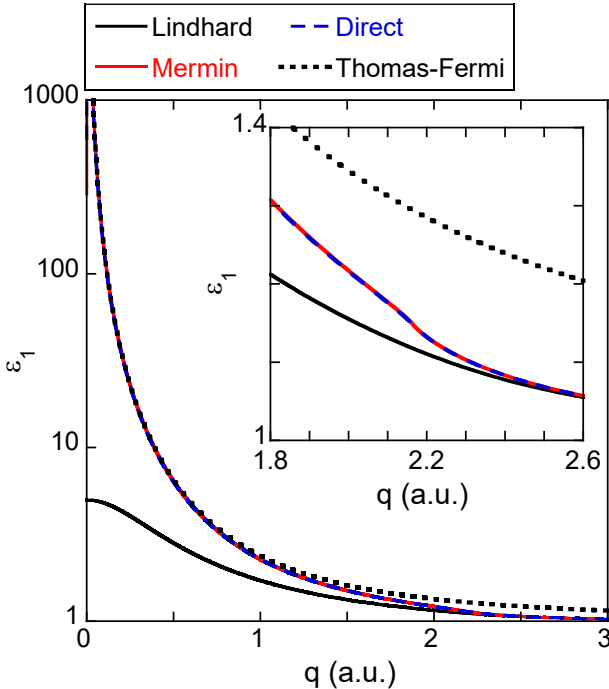


Figure 3.6: ϵ_1 as a function of q for $\omega = 1$ meV for a dielectric function with $\omega_p = 20$ eV, $\Gamma = 10$ eV and $U = 0$ eV. Calculations were done using the Lindhard, Mermin and Direct approach. Also shown is the Thomas Fermi estimate of ϵ_1 . The direct and Mermin approaches converge with the Thomas-Fermi value in the limit $\omega \rightarrow 0$. The insert shows ϵ_1 plotted on a linear scale near $2k_f$ ($k_f = 1.08$ a.u. for $\omega_p = 20$ eV)

3.6 Proton stopping

One of the application of dielectric function is the calculation of ion stopping. The simplest case here, avoiding complications due to the ion's charge state is the calculation of proton stopping. Most relevant for this paper is the MELF-GOS method that describes the valence band in terms of Mermin dielectric functions with finite width. For a recent review, see de Vera et al[11]. Such a theory is expected to apply for incoming energies above the stopping power maximum, as at lower energies the first Born approximation used is not sufficient. At these higher energies the direct and Mermin approach give very similar results, and considerably higher than the Lindhard result with the same Γ -value. At lower energies, the slightly different shape of the loss function at intermediate q values is reflected in somewhat different stopping values for the Mermin and direct approach.

At very high proton energies stopping calculations is affected by relativistic effects. For these energies, it is a good approximation to assume that the target electron is at rest, and then the stopping theory was worked out by Fano [12]. Incorporating the relativistic stopping in the Mermin dielectric function makes it possible to calculate the proton stopping at relativistic energies, without resorting to the approximation that the target electron is at rest. The relativistic effect enhances the proton stopping for energies over 1 GeV as is shown in the insert of Fig. 3.7. The influence of incorporating relativistic kinematics in the Mermin DF on straggling is much more dramatic and causes strong deviations of the Bohr limit at these high energies [13].

3.7 Conclusion

We summarised the properties of various RPA-derived dielectric functions and how they relate in the limit of $q \rightarrow 0$ to the classical Drude-Lindhard DF. In particular, it was investigated how Γ affects the results. This led to a new definition of the complex energy ω_c that makes it possible to directly calculate any of these RPA-based dielectric functions (Lindhard, Levine-Louie, and Kaneko) without requiring the Mermin re-normalisation. These new dielectric functions are identical in the limit $q \rightarrow 0$, $q \rightarrow \infty$, and $\omega \rightarrow 0$, with their Mermin-corrected counterparts but differ slightly for the intermediate cases. The ‘derivation’ of the direct method is relatively simple and makes a clear link with the classical DFs. We do not claim that the DFs obtained by

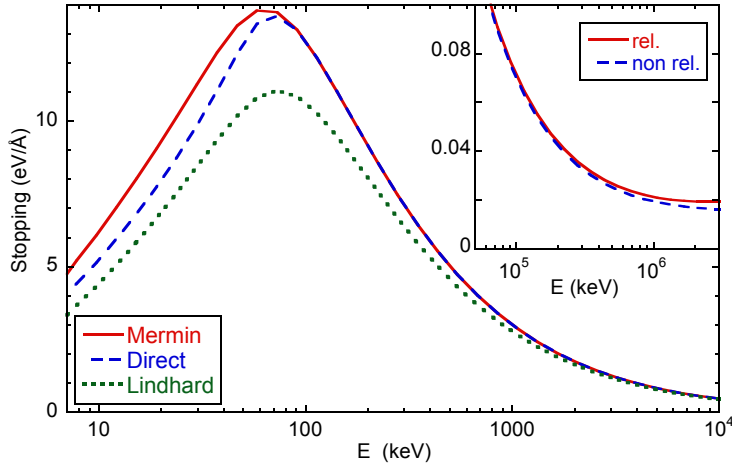


Figure 3.7: A comparison of the proton stopping as calculated using the Lindhard, Mermin and ‘direct’ dielectric function for $\omega_p = 20$ eV and $\Gamma = 10$ eV. For energies above the stopping maximum there is good agreement between the direct and Mermin approach. As an insert the effect of incorporating relativistic kinematics is shown for the Mermin case. Relativistic kinematics results in a slight increase of the stopping power at very high energies.

the direct approach are an improvement over the Mermin-corrected DFs. Future interpretation of the differences between both sets of DFs at intermediate q and ω values may further enhance our understanding of the field.

Bibliography

- [1] D. Pines, Collective Energy Losses in Solids, *Rev. Mod. Phys.* 28 (1956) 184–198.
- [2] J. Lindhard, On the properties of a gas of charged particles, *K. Dan. Vidensk. Selsk. Mat.-Fys. Medd.* 28 (8) (1954) 1–57.
- [3] K. L. Kliewer, R. Fuchs, Lindhard dielectric functions with a finite electron lifetime, *Phys. Rev.* 181 (2) (1969) 552–558. doi:[10.1103/physrev.181.552](https://doi.org/10.1103/physrev.181.552).
- [4] N. Mermin, Lindhard dielectric function in the relaxation-time approximation, *Phys. Rev. B* 1 (1970) 2362 –2363. doi:[10.1103/physrevb.1.2362](https://doi.org/10.1103/physrevb.1.2362).
- [5] Z. Levine, S. Louie, New model dielectric function and exchange-correlation potential for semiconductors and insulators, *Phys. Rev. B* 25 (1982) 6310. doi:[10.1103/physrevb.25.6310](https://doi.org/10.1103/physrevb.25.6310).
- [6] T. Kaneko, Wave-packet theory of stopping of bound electrons, *Phys. Rev. A* 40 (1989) 2188. doi:[10.1103/physreva.40.2188](https://doi.org/10.1103/physreva.40.2188).
- [7] C. D. Archubi, N. R. Arista, Extended wave-packet model to calculate energy-loss moments of protons in matter, *Phys. Rev. A* 96 (6) (2017) 062701. doi:[10.1103/physreva.96.062701](https://doi.org/10.1103/physreva.96.062701).
- [8] R. H. Ritchie, A. Howie, Electron excitation and the optical potential in electron microscopy, *Philos. Mag.* 36 (1977) 463. doi:[10.1080/14786437708244948](https://doi.org/10.1080/14786437708244948).
- [9] B. I. Lundqvist, Single-particle spectrum of the degenerate electron gas, *Physik der Kondensierten Materie* 6 (3) (1967) 206. doi:[10.1007/bf02422717](https://doi.org/10.1007/bf02422717).
- [10] P. Sigmund, Particle Penetration and Radiation Effects, Vol. 151 of Springer Series in Solid-State Sciences, Springer, Berlin, 2006.
- [11] P. de Vera, I. Abril, R. Garcia-Molina, Electronic cross section, stopping power and energy-loss straggling of metals for swift protons, alpha particles and electrons, *Front. Mater.* 10. doi:[10.3389/fmats.2023.1249517](https://doi.org/10.3389/fmats.2023.1249517).
- [12] U. Fano, Penetration of protons, alpha particles, and mesons, *Annu. Rev. Nucl. Sci.* 13 (1) (1963) 1. doi:[10.1146/annurev.ns.13.120163.000245](https://doi.org/10.1146/annurev.ns.13.120163.000245).
- [13] F. Salvat, L. Barjuan, P. Andreo, Inelastic collisions of fast charged particles with atoms: Bethe asymptotic formulas and shell corrections, *Phys. Rev. A* 105 (4). doi:[10.1103/physreva.105.042813](https://doi.org/10.1103/physreva.105.042813).
- [14] M. Altarelli, D. Y. Smith, Superconvergence and sum rules for the optical constants: Physical meaning, comparison with experiment, and generalization, *Phys. Rev. B* 9 (1974) 1290–1298. doi:[10.1103/physrevb.9.1290](https://doi.org/10.1103/physrevb.9.1290).

3.A Appendix: Python Library DF_complex_lib

```

1  from scipy import special # scipy version 0.12 and above
2  import math
3  import cmath
4  # helper functions=====
5  def RecoilEnergy(q):
6      if q < 1:
7          return q*q/2.0
8      else:
9          c = 137.036
10         Q=math.sqrt(c**2*q**2+c**4)-c*c # relativistic recoil energy of electron
11         return Q
12
13 def sqrt_2Q(q):
14     if q < 1:
15         return q
16     else:
17         c = 137.036
18         Q=math.sqrt(c**2*q**2+c**4)-c*c # relativistic recoil energy of electron
19         return (math.sqrt(2*Q))
20
21 def g_c (A): # used by Lindhard DF
22     log_result = cmath.log((A+1.0)/(A-1.0));
23     out = (1.0 -A*A)*log_result; #following notation Sigmund's appendix
24     return out
25
26 # classical Drude Lindhard related functions=====
27 def DrudeLindhard(q,omega,gamma,w_p,U):
28     w_c_U_square=omega*omega-U*U+complex(0,omega*gamma)
29     w_p_at_q=w_p+RecoilEnergy(q) # simple quadratic but relativistic
30     # for full dispersion comment use:
31     # v_f=pow(w_p*w_p*3.0/4.0*math.pi,1.0/3.0)
32     # w_p_at_q=math.sqrt(w_p*w_p + 0.5 *v_f*v_f* q*q+q*q*q*q/4);
33     oneovereps=1.0+ w_p*w_p/(w_c_U_square-w_p_at_q**2)
34     eps=1.0/oneovereps
35     return eps
36
37 def DrudeLindhard_wrong(q,omega, gamma,w_p,U): # this DrudeLindhard gives at q=0 the Lindhard result
38     w_c=complex(omega, gamma) # we do not divide gamma by two here, so turns out twice as wide (and not a metal)
39     w_c_U_square=w_c**2 - U*U
40     w_p_at_q=w_p+RecoilEnergy(q) # simple quadratic
41     oneovereps=1.0+ w_p*w_p/(w_c_U_square-w_p_at_q**2)
42     eps=1.0/oneovereps
43     return eps
44
45 def DrudeLindhard_wrong_Mermin(q,omega,gamma,w_p,U):
46     w_c=complex(omega, gamma)
47     Im_g_over_w = complex(0.0, gamma / omega) # hence omega can not be zero
48     eps = DrudeLindhard_wrong(q, omega, gamma, w_p,U)
49     z1 = 1.0 + Im_g_over_w
50     chi_L = eps-1.0
51     eps_0=DrudeLindhard_wrong(q, 0.0,0.0,w_p,U)
52     chi_0 = eps_0-1.0
53     top = z1*chi_L
54     z2 = chi_L/chi_0
55     bottom = 1.0+Im_g_over_w*z2
56     chi_M = top/bottom
57     return (1.0+chi_M)
58
59 # FEG RPA related routines=====
60 def Lindhard_LL(q,omega,gamma,w_p,U):
61     w_c=complex(omega, gamma)
62     w_c_U= cmath.sqrt(w_c**2-U**2)
63     eps=Lindhard_complex(q,w_c_U,w_p)
64     return eps
65
66 def Lindhard_Mermin_LL(q,omega,gamma,w_p,U):
67     Im_g_over_w = complex(0.0, gamma / omega)

```

```

68     eps = Lindhard_LL(q, omega, gamma, w_p,U)
69     z1 = 1.0 + Im_g_over_w
70     chi_L = eps-1.0
71
72     eps_0=Lindhard_LL(q, 0.0000,1e-10,w_p,U) # gamma towards 0 rateher than =0 in the Linhard case
73     chi_0 = eps_0-1.0
74     top = z1*chi_L
75     z2 = chi_L/chi_0
76     bottom = 1.0+Im_g_over_w*z2
77     chi_M = top/bottom
78     eps_final=1.0+chi_M
79     return (1.0+chi_M)
80
81 def Lindhard_direct(q,omega,gamma,w_p,U):
82 # not the same as Mermin different DF, but presents a metal and converge
83 # to same Compton profile, and same in optical limit and same omega=0 limit
84
85     w_c_U=cmath.sqrt(omega**2+complex(0.0,omega*gamma)-U**2 )
86     eps=Lindhard_complex(q,w_c_U,w_p)
87     return eps
88
89 def Lindhard_complex(q,w_c_U,w_p):
90     v_f=pow(w_p*w_p*3.0/4.0*math.pi,1.0/3.0)
91     Q=RecoilEnergy(q)
92     sqrt_2Q=math.sqrt(2*Q)
93     u= w_c_U / (sqrt_2Q*v_f)
94     z = sqrt_2Q/ (2 * v_f)
95     d1 = g_c(z + u)
96     d2 = g_c(z - u)
97     f=0.5+ (d1 + d2)/(8*z) #following notation Sigmund's appendix and Lindhard 3.6
98     prefactor=3*w_p*w_p/(2*Q*v_f*v_f)
99     eps=1.0+prefactor*f
100    return eps
101
102 # Gaussian occupancy RPA related routines =====
103
104 def Kaneko_LL(q,omega,gamma,q_mean,U):
105     w_c = complex(omega, gamma)
106     w_c_U = cmath.sqrt(w_c**2-U*U)
107     eps=Kaneko_complex(q,w_c_U,q_mean)
108     return eps
109
110 def Kaneko_Mermin_LL(q,omega, gamma,q_mean,U):
111     Im_g_over_w = complex(0.0, gamma / omega)
112     eps = Kaneko_LL(q, omega, gamma, q_mean,U)
113     z1 = 1.0 + Im_g_over_w
114     chi_L = eps-1.0
115     eps_0=Kaneko_LL(q, 0.0,0.0,q_mean,U)
116     chi_0 = eps_0-1.0
117     top = z1*chi_L
118     z2 = chi_L/chi_0
119     bottom = 1.0+Im_g_over_w*z2
120     chi_M = top/bottom
121     return (1.0+chi_M)
122
123 def Kaneko_direct(q,omega,gamma,w_p,U):#
124     w_c_U=cmath.sqrt(omega**2+complex(0.0,omega*gamma)-U**2 )
125     eps=Kaneko_complex(q,w_c_U,w_p)
126     return eps
127
128 def Kaneko_complex(q,w_c_U,q_mean):
129     chi2 = 1/(math.pi*q_mean)
130     u= w_c_U/(sqrt_2Q(q)*q_mean)
131     z = sqrt_2Q(q)/(2*q_mean)
132     sqrt_pi=math.sqrt(math.pi)
133     c=complex(0,-1)*sqrt_pi/2.0
134     dd= sqrt_pi*chi2/z**3 /4.0 *c*(special.wofz(u+z) - special.wofz(u-z))
135     eps=1.0+dd
136     return eps

```

3.B Appendix: Sum Rules, Kramers-Kronig Relations

Free electron gas

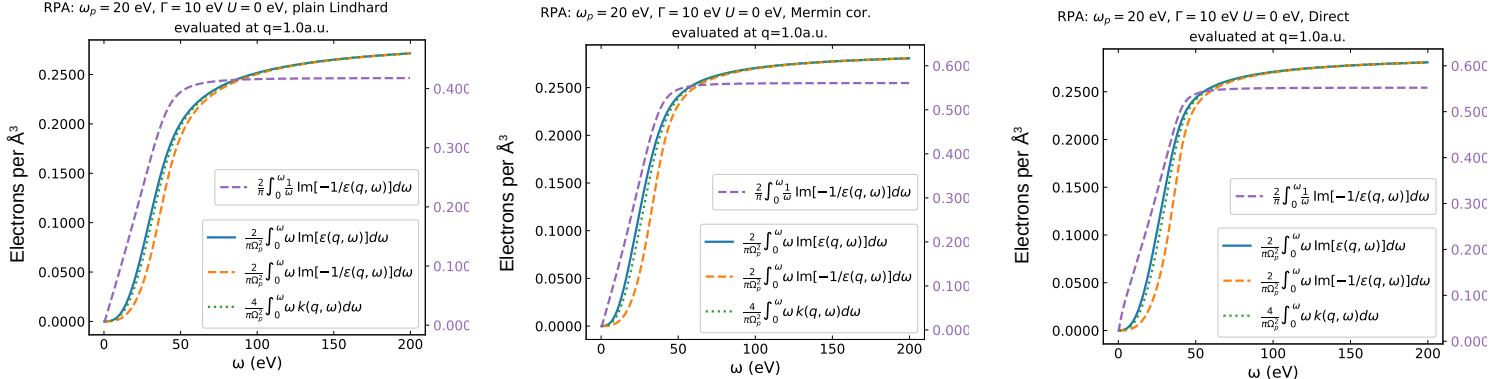


Figure 3B.1: Sum rules evaluated at $q = 1$ a.u. where all three dielectric functions differ. Plasmon energy of 20 eV corresponds to an electron density of $0.29 e^-/\text{\AA}^3$. The lower 3 integrals (F sum rule, Bethe sum rule, and k sum rule) should converge to this value. The top integral is an example of the Koster-Kronig relations and should converge to $\text{Re}[1/\epsilon(\omega = 0, q = 1)] + 1$ (right vertical axis). $\text{Re}[1/\epsilon(\omega = 0, q = 1)] + 1 = 0.58$ for the Lindhard DF, but 0.44 for the Mermin-corrected and direct method.

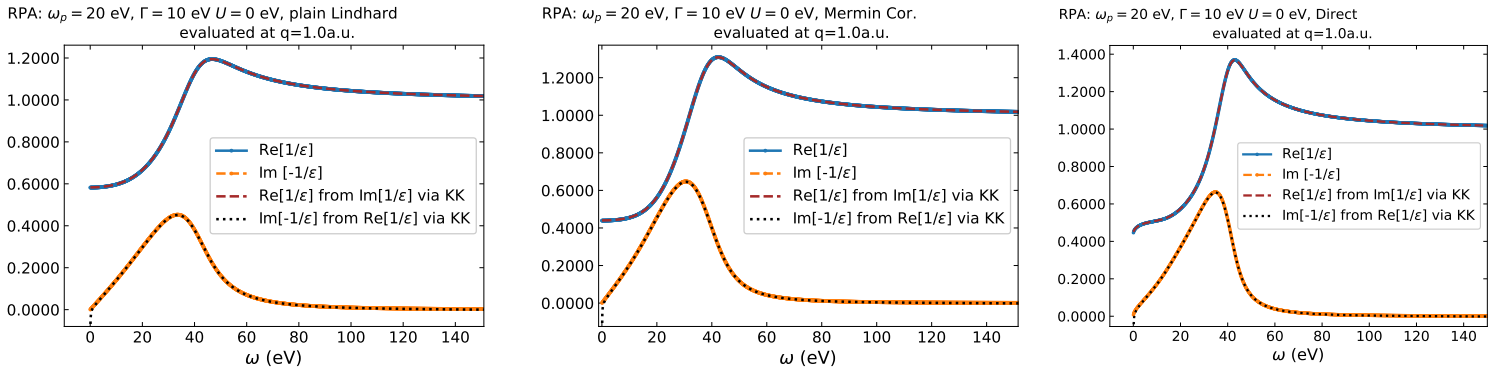


Figure 3B.2: Same Free electron gas dielectric function as used in fig. 3B.1. Real and imaginary part of $1/\epsilon(\omega, q = 1)$ as calculated directly from the formula (blue and yellow lines) and the real part as obtained by Kramers-Kronig transform of the imaginary part (red dashed line) and the imaginary part obtained by Kramers-Kronig transform of the real part (dotted line). Near $\omega = 0$ the Kramers-Kronig derived imaginary part is somewhat different, due to the discrete nature of the transform used. The energy range over which this difference extends can be made smaller by repeating the calculation with smaller energy step size.

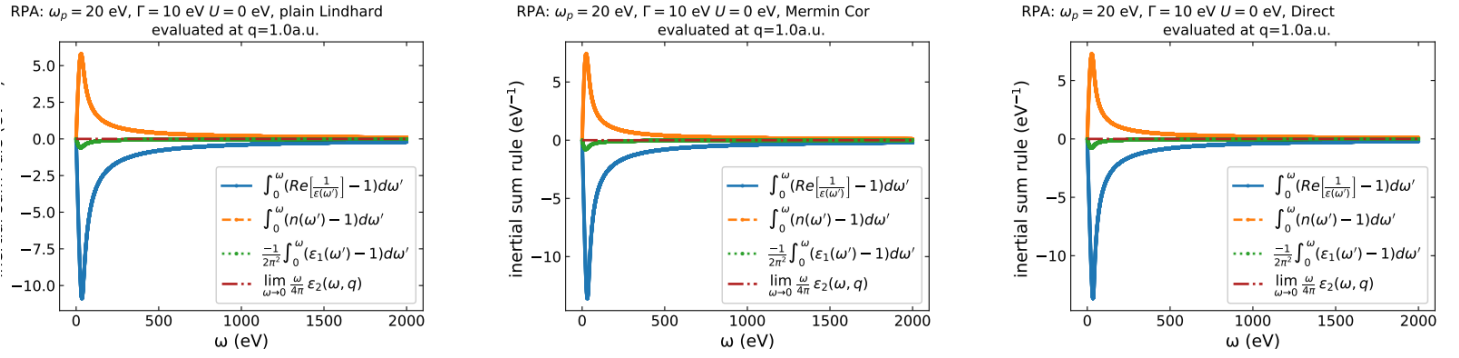


Figure 3B.3: Same Free electron gas dielectric function as used in fig. 3B.1. Demonstration of the inertia sum rules at $q = 1$ a.u. This requires integration to much larger energy losses before convergence is reached. For explanation of these sum rules see [14]

Levine-Louie (LL) model (with finite width)

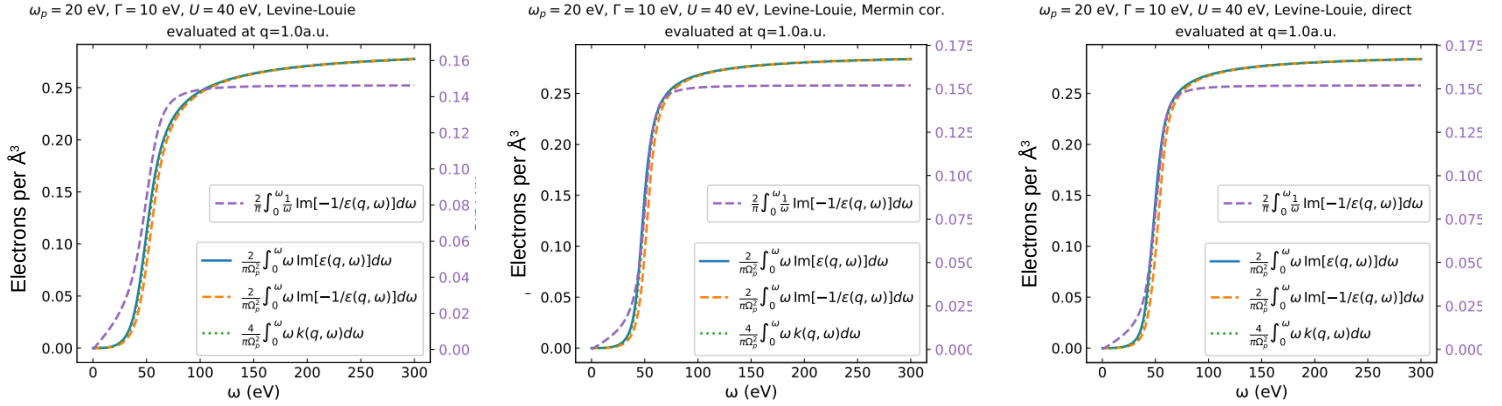


Figure 3B.4: Levine-Louie dielectric function. Same parameters as used in fig. 3B.1 except for $U = 20$ eV. Plasmon energy of 20 eV still corresponds to an electron density of $0.29/\text{\AA}^3$. The lower 3 integrals should converge to this value, but contributions to this Integral are shifted to larger ω values compared to the $U = 0$ case. The top integral is related to Kramers-Kronig integral and should converge to $\text{Re}[1/\epsilon(\omega = 0, q = 1)] + 1$ (right vertical axis). $\text{Re}[1/\epsilon(\omega = 0, q = 1)] + 1 = 0.854$ for the LL DF, but 0.848 for both the Mermin-corrected and direct method.

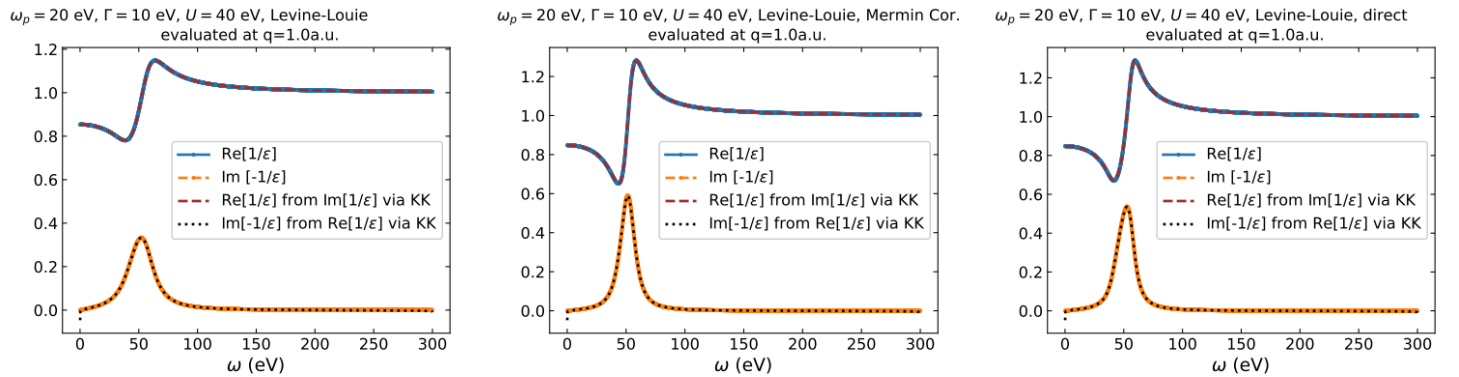
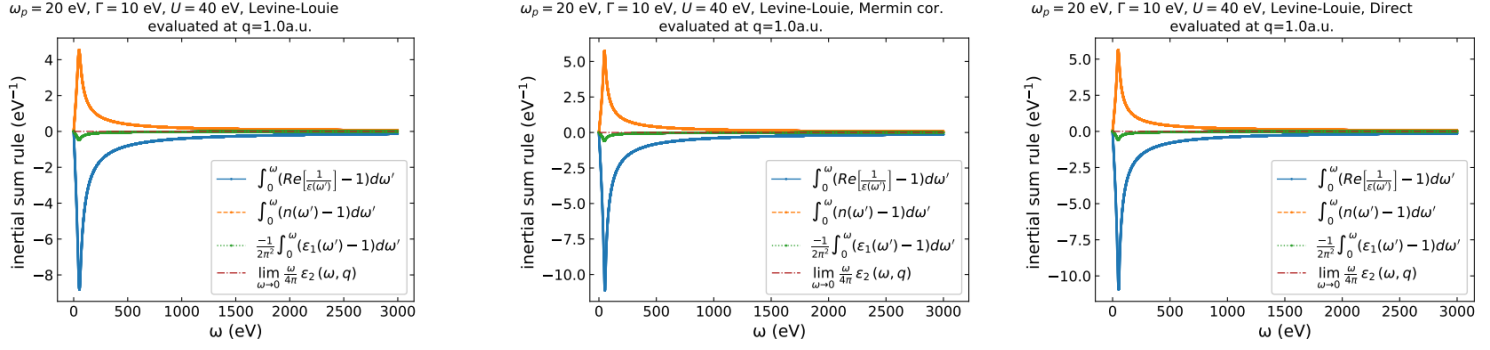


Figure 3B.5: Test of Kramers-Kronig relations. Same as fig. 3B.2 but now with $U = 20$ eV

Figure 3B.6: Test of inertia sum rules. Same as fig. 3B.3 but now with $U = 20 \text{ eV}$

Kaneko + U (with finite width)

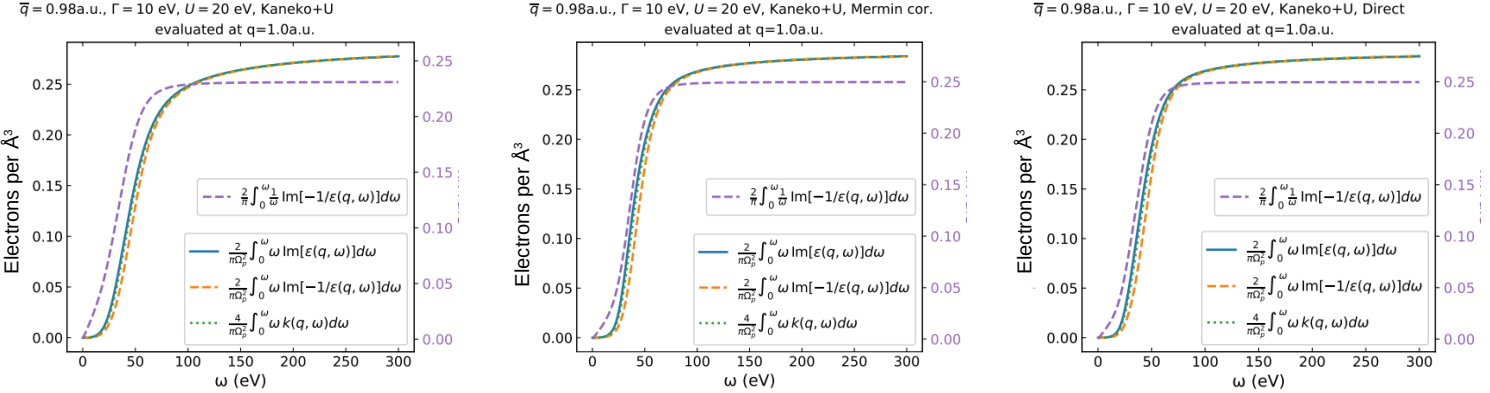
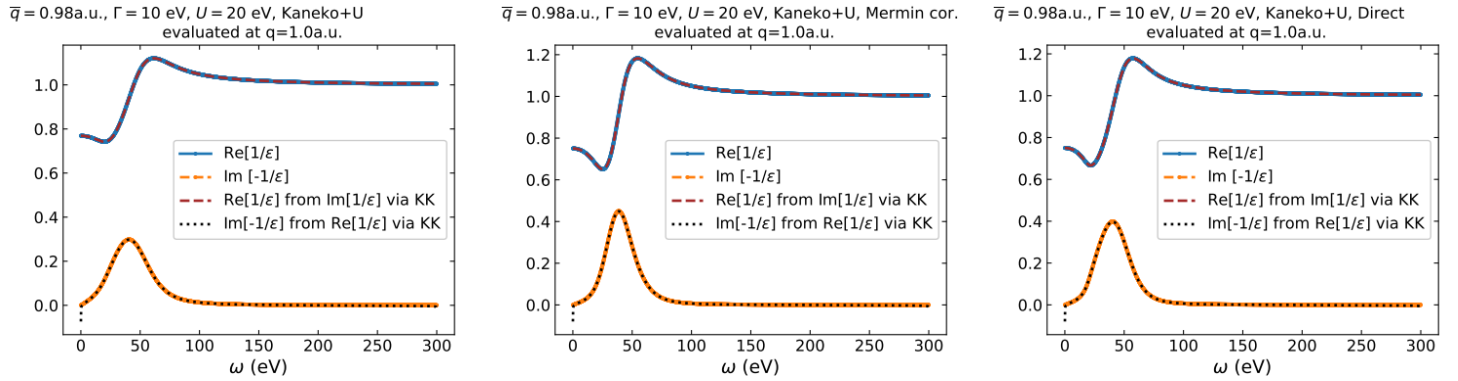
Figure 3B.7: Kaneko + U dielectric function. A value of $\bar{q} = 0.98 \text{ a.u.}$ correspond to a plasmon energy of 20 eV and thus the electron density is still $0.29/\text{\AA}^3$. The lower 3 integrals should converge to this value. The top integral is related to Kramers-Kronig integral and should converge to $\text{Re}[1/\epsilon(\omega = 0, q = 1)] + 1$ (right vertical axis). $\text{Re}[1/\epsilon(\omega = 0, q = 1)] + 1 = 0.77$ for the Kaneko DF, but 0.75 for the Mermin-corrected and direct method.

Figure 3B.8: Test of Kramers-Kronig relations. Same DF as fig. 3B.7. Further the same as fig. 3B.2.

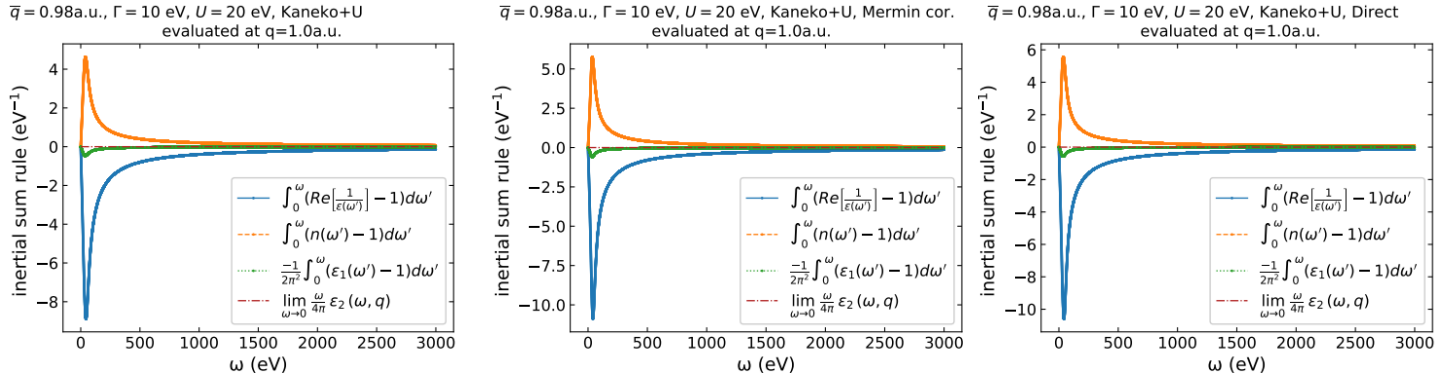


Figure 3B.9: Test of inertia sum rules. Same as fig. 3B.3 but now for the Kaneko DF as in fig. 3B.7

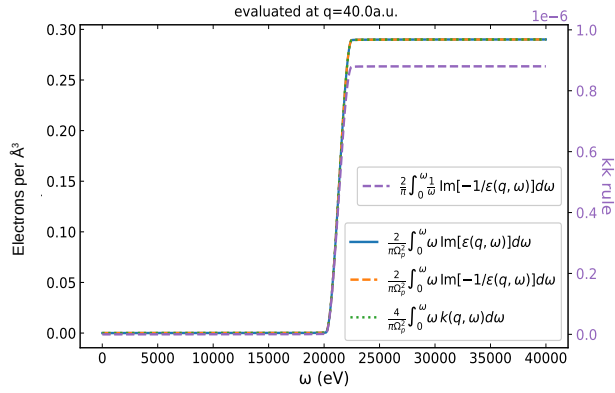


Figure 3B.10: Sum rules evaluated at $q = 40\text{a.u.}$ They remain valid at momentum transfer where relativistic effects become noticeable

Chapter 4

Dielectric functions, their properties and their relation to observables: investigations using the Chapidif program for the case of aluminum

4.1 abstract

We introduce the Chapidif program by describing a study of the properties of aluminum based on simple model dielectric functions. Dielectric functions are generally not available from the first principle, and one is forced to describe the dielectric function of a material in terms of (a sum of) model dielectric functions. The Chapidif program is used to visualize the dielectric function, check sum rules and the mathematical relations between the real and imaginary part of the dielectric function. In addition, several properties related to the interaction of charged particles (here either protons or electrons) with matter are derived and compared with experiment. By having a single program that can calculate a range of properties, it becomes easy to ensure that the dielectric function used is not just able to describe a single observable, but it is transferable, i.e. describes reasonably well a larger range of materials properties. A reflection electron energy loss measurement is used as an example of how a comparison of calculated results with experiment can be used to improve the model dielectric function and thus enhance the quality of the properties derived from the dielectric function.

PROGRAM SUMMARY

Program Title: Chapidif

CPC Library link to program files: (to be added by Technical Editor)

Licensing provisions CC BY NC 3.0

Programming language: Python, C++

Nature of problem: Frequency- and momentum-dependent dielectric functions can describe a wide variety of material properties. The dielectric function has many intricate mathematical properties and is subject to constraints due to sum rules. The Chapidif program (CHArged Particle Interactions from Dielectric Functions) can be used to visualize a dielectric function, check its sum rules, and calculate a wide range of quantities, in particular relating to the interaction of protons and electrons with matter. Details of how the classical and quantum-based dielectric functions are implemented are given elsewhere [1]. The program makes it easy to investigate if the assumed dielectric function has the required mathematical properties and how the choice of the model dielectric function and the corresponding parameters influences the calculated observables such as ion stopping and electron inelastic mean free path.

Solution method: The program consist of a Python/Tkinter user interface and C++ backend that does the actual calculations. Results are displayed using Matplotlib library and, if desired, text-based output files containing the input parameters used and the calculated quantities can be generated.

4.2 Introduction

It is well established that the interaction of charged particles with matter can be adequately described, at sufficiently high energies, in terms of the dielectric function (DF): $\epsilon(\omega, q)$, with $\hbar\omega$ the energy transfer and $\hbar q$ the momentum transfer. Then the question arises: What is the appropriate DF? In the optical limit, $q = 0$, the DF can be obtained from experiments employing photons. Away from $q = 0$, the DF differs (dispersion) and is more difficult to access experimentally, and one often resorts to the use of approximate and simple dispersion relations.

In many studies, one focuses on calculating a single property. For example, one wants to calculate either the electron inelastic mean free path, ion stopping, differential inelastic electron scattering cross sections, Compton profile, or an electron energy loss spectrum. All these quantities (when the first Born approximation applies, i.e., not too low energies) can be calculated from $\epsilon(\omega, q)$. Chapidif facilitates the calculation of different physical observables based on the same DF.

Chapidif is a program that aims to make it easy to visualize the DF, check its properties, and derive a number of observables. The program can be based on several different model dielectric functions. Classical-physics-based dielectric functions can be used (extended Drude, Drude-Lindhard) as well as quantum-physics-based ones (Generalized Oscillator Strength (GOS) based on hydrogenic wave functions [1], Lindhard/Mermin model for free electron materials [2, 3], Mermin-Levine-Louie model for insulators [4], Kaneko model based on momentum space representation [5, 6, 7] and Belkacem-Sigmund model based on harmonic oscillators [8]).

‘Real’ materials are usually modeled by combining several contributions with different parameters. Then, one must consider how to add the different contributions. Either the energy loss function of the different components can be added (see, e.g. Ritchi and Howie [9]) or the electric susceptibility χ ($\chi(\omega, q) = \epsilon(\omega, q) - 1$) (see, e.g. the work by Tung *et al.*[10]). The consequences of these choices can be investigated with the program, and the underlying physics has been summarized in a previous paper [11].

Here we demonstrate how to use the program for the case of aluminum, which is relatively well understood, and emphasize the desirability that the DF used is transferable, i.e. can be used to describe different physical phenomena. For aluminum, there are many experimental and theoretical results available in the literature, making it a good case for establishing the level of agreement one can expect for the approaches used in the Chapidif program.

Unless stated otherwise, atomic units are used throughout this article. 1 a.u. of energy corresponds to 27.211 eV. The mass of an electron is 1 a.u., and the mass of a proton is 1836.15 a.u.

Almost all figures in this paper are composed from plots taken straight from the Chapidif program, sometimes after manual editing of the labels. The exceptions are Fig. 4.14 (lower left panel) and Fig. 4.15, where a comparison is made between two different Chapidif calculations and literature data. 4.A gives some details about how to install and run the program.

4.3 Model Dielectric Function

Chapidif implements several model dielectric functions. This paper will consider models based on DL or Mermin dielectric functions for the valence band and GOS-based contributions for the core electrons.

4.3.1 Drude-Lindhard model

First, consider the Drude-Lindhard (DL) DF, which can be derived from classical physics. For more than one component, the total DL DF is most conveniently defined as having a real part:

$$\text{Re} \left[\frac{1}{\epsilon^{\text{DL}}(\omega, q)} \right] = 1 + \sum_i C_i \frac{(\omega^2 - \omega_i(q)^2 - U_i^2) \omega_i(0)^2}{(\omega^2 - \omega_i(q)^2 - U_i^2)^2 + \omega^2 \Gamma_i^2} \quad (4.1)$$

and the imaginary part is usually defined in terms of the loss function (i.e. $\text{Im}[-1/\epsilon]$) :

$$\text{Im} \left[\frac{-1}{\epsilon^{\text{DL}}(\omega, q)} \right] = \sum_i C_i \frac{\omega \Gamma_i \omega_i(0)^2}{(\omega^2 - \omega_i(q)^2 - U_i^2)^2 + \omega^2 \Gamma_i^2} \quad (4.2)$$

Here C_i is the amplitude of the oscillator (it is often helpful to interpret C_i as the fraction of space that is occupied by electrons described by this oscillator), Γ_i the width ('damping'), and $\omega_i(q)$ the dispersion and the U_i term is usually omitted. However, $U_i > 0$ can be used to model the interaction of electrons with the lattice (which causes the band gap). In the program one can select for the DL model either quadratic dispersion ($\omega(q) = \omega(0) + \alpha q^2/2$), or 'full dispersion' ($\omega(q) = \sqrt{\omega(0)^2 + v_f^2 q^2/3 + q^4/4}$ with v_f the Fermi velocity [12]).

For large momentum transfer q , one has hard collisions, i.e., billiard-ball-like collisions with one electron at a time. This means that the DF at large q should always be centered near $\omega = q^2/2$, which is referred to as the Bethe ridge, and this requires $\alpha = 1$. The α term is traditionally used in the REELS (reflection electron energy loss spectroscopy) literature with values $\alpha < 1$ to mimic slower dispersion at small q values [13, 14]. This makes the obtained DF useless for e.g. ion stopping calculations, where convergence to the Bethe ridge at large q is essential, and this approach is thus best avoided. Slower dispersion at small q -values can be obtained by using non-zero values for the U parameter, while maintaining convergence to the Bethe Ridge at large q . For very large q values, relativistic effects alter the dispersion, see 4.B.

Note that the real and imaginary part of both $\epsilon(\omega, q)$ and $1/\epsilon(\omega, q)$ are Kramers-Kronig (KK) pairs, e.g. for $1/\epsilon(\omega, q)$:

$$\text{Re} \left[\frac{1}{\epsilon(\omega, q)} \right] - 1 = \frac{2}{\pi} \mathcal{P} \int_0^\infty \frac{\omega' \text{Im} \left[\frac{1}{\epsilon(\omega', q)} \right]}{(\omega')^2 - \omega^2} d\omega' \quad (4.3)$$

and:

$$\text{Im} \left[\frac{1}{\epsilon(\omega, q)} \right] = -\frac{2\omega}{\pi} \mathcal{P} \int_0^\infty \frac{\text{Re} \left[\frac{1}{\epsilon(\omega', q)} \right] - 1}{(\omega')^2 - \omega^2} d\omega' \quad (4.4)$$

with \mathcal{P} the Cauchy principal value. These Kramers-Kronig relation apply for any value of ω and q . As is described e.g. in ref. [15], the KK relations are a consequence of causality in the frequency domain and should apply to any DF, not just the DL model.

Consider $U = 0$ here. Inspection of eq. 4.1 shows that for a single component and $C_1 = 1$ (or multiple components with $\sum_i C_i = 1$) we have $\text{Re}[1/\epsilon(\omega, q)] = 0$, for $\omega = 0, q = 0$, which corresponds to perfect screening as is the case for a metal (Thus $\sum_i C_i = 1$ is a requirement for a metal). For $\sum_i C_i < 1$, $\text{Re}[1/\epsilon(\omega, q)]$ has a finite, positive value, and for the static refractive index, n one has: $1/n^2 = 1/\epsilon(0, 0) = 1 - \sum_i C_i$ [16]. When $\sum_i C_i > 1$, the results for $\text{Re}[1/\epsilon(\omega, q)]$ become negative near $\omega = 0, q = 0$, clearly a non-physical situation, and such a 'DF' should not be used.

From eq. 4.3 one obtains the Kramers-Kronig (KK) sum rule by taking $\omega = 0$ and $q = 0$, and written in terms of the loss function (rather than $\text{Im}[1/\epsilon(\omega', 0)]$):

$$\frac{2}{\pi} \int_0^\infty \frac{1}{\omega'} \text{Im} \left[\frac{-1}{\epsilon(\omega', 0)} \right] d\omega' = 1 - \text{Re} \left[\frac{1}{\epsilon(0, 0)} \right]. \quad (4.5)$$

4.3.2 Quantum physics-based models

Within quantum physics, the DF is usually defined by the random phase approximation (RPA). In the non-relativistic RPA, $\epsilon(\omega, q)$ is given by [17, 18] :

$$\begin{aligned} \epsilon(\omega, q) = & 1 + \Omega_p^2/q^2 \sum_j |F_{j0}(q)|^2 \times \\ & \left(\frac{1}{\omega_{j0} - \omega - i\Gamma} + \frac{1}{\omega_{j0} + \omega + i\Gamma} \right), \end{aligned} \quad (4.6)$$

where $\Omega_p^2 = 4\pi N_a$ with N_a the atomic density, i.e. the plasmon energy for one electron per unit cell. ω_{j0} is the transition energy from the ground-state ($j = 0$) to an excited state j . $F_{j0}(q)$ is the form factor which should be evaluated using an appropriate basis set, and is normalized to the number of electrons per unit cell it represents.

Lindhard evaluated the RPA based on plane waves, representing a free-electron gas with density n . The resulting Lindhard DF contains both a collective (plasmon) response and electron-hole pair excitations. At zero momentum, all intensity is in the plasmon branch, and then it coincides with a DL oscillator with $\omega_i = \sqrt{4\pi n}$ and a negligible small Γ value. At larger momentum transfer, the loss function broadens due to the range of possible energy losses for electron-hole pair excitations, which dominate the loss function at larger momentum transfer. For very large q -values relativistic effects come again into play, see 4.B.

Mermin added relaxation to the Lindhard DF (allowing for non-negligible Γ values) [3]. Chapidif can calculate the Lindhard DF with finite Γ values, both with and without the Mermin re-normalization factor. This lets the user explore under what conditions the Mermin correction is significant. For non-negligible Γ values, the Mermin DF is always preferred.

The Mermin model is the quantum-physics-based equivalent of the DL DF with $U = 0$. Indeed, the plasmon pole approximation of the Mermin DF is just the DL DF with ‘full dispersion.’ The quantum-physics-based equivalent for the case $U > 0$ was derived by Levine and Louie [4]. For finite Γ values, one must apply a Mermin-type re-normalization to the Levine-Louie DF again [19].

For deeper levels, the free-electron approximation seems less appropriate. Hydrogenic wave functions are still a poor approximation for core electrons but should capture much more of the physics of bound electrons than plane waves. For most core levels (K, L, M shells), there are simple expressions for the matrix elements $|F_{j0}(q)|$ based on hydrogenic wave functions, and $\text{Im}[\epsilon(\omega, q)]$ is readily obtained. $\text{Re}[\epsilon(\omega, q)]$ is then calculated via the Kramers-Kronig relations. For tightly bound core levels $\text{Re}[\epsilon(\omega, q)] \approx 1$ for ω values of the order of the core level binding energy and then $\text{Im}[-1/\epsilon(\omega, q)] \approx \text{Im}[\epsilon(\omega, q)]$, i.e. ‘density effects’ can be neglected (see section 4.4.2 for an explanation of this terminology). Calculation without density effect can reduce the run time of Chapidif dramatically, but this approximation often causes discrepancies in the sum rules, which will be discussed next. The program allows you to choose the maximum energy loss for which the density effect is considered.

4.3.3 Sum rules

In addition to the Kramers-Kronig relation (eq. 4.3 and eq. 4.4), there are several other sum rules. For example, there is the Bethe sum rule:

$$Z = \frac{2}{\pi\Omega_p^2} \int_0^\omega \omega \text{Im}[-1/\epsilon(\omega, q)] d\omega, \quad (4.7)$$

the F sum rule:

$$Z = \frac{2}{\pi\Omega_p^2} \int_0^\omega \omega \text{Im}[\epsilon(\omega, q)] d\omega, \quad (4.8)$$

level	1	n_e	(n_e)	U
1s	0	2	(1.623)	1564
2s	0	2	(2.147)	121.5
2p	1	6	(6.259)	76.75

Model I				
C_i	ω_i	Γ	n_e	
0.946	16 eV	1 eV	3	
Model II				
C_i	ω_i	Γ	n_e	
0.925	15.15 eV	0.5 eV	2.56	
0.018	26 eV	15 eV	0.15	
0.007	57 eV	45 eV	0.27	

Table 4.1: the DF used, model 1 is the simplest combination of GOS (top) and a Mermin oscillator (Bottom) that gives the ‘right’ number of electrons in each shell. The value for n_e in between brackets is the occupation of the core level according to the ICRU publication [21]. Model 2 is a refinement, as explained in section 4.4.11

with Z the number of electrons per unit cell (i.e. the atomic number if the unit cell contains a single atom).

Closely related to $\text{Re}[\epsilon] = \epsilon_1$ and $\text{Im}[\epsilon] = \epsilon_2$ are the refractive index $n(\omega, q)$ and the extinction coefficient $k(\omega, q)$:

$$n(\omega, q) + ik(\omega, q) = \sqrt{\epsilon_1(\omega, q) + i\epsilon_2(\omega, q)}. \quad (4.9)$$

A similar sum rule can then be expressed in terms of k :

$$Z = \frac{4}{\pi\Omega_p^2} \int_0^\infty \omega k(\omega, q) d\omega. \quad (4.10)$$

In addition, there are inertial sum rules [20], a consequence of causality in the time domain. The program can be used to check whether the defined DF adheres to these sum rules. The inertial sum rule in terms of $n(\omega, q)$, $\text{Re}\left[\frac{1}{\epsilon(\omega, q)}\right]$, and $\text{Re}[\epsilon(\omega, q)]$ are given by:

$$\begin{aligned} \int_0^\infty (n(\omega, q) - 1) d\omega &= 0 \\ \int_0^\infty \left(\text{Re}\left[\frac{1}{\epsilon(\omega, q)}\right] - 1 \right) d\omega &= 0 \\ \int_0^\infty (\text{Re}[\epsilon(\omega, q)] - 1) d\omega &= -2\pi^2\sigma(0, q) \end{aligned} \quad (4.11)$$

with $\sigma(0, q)$ the conductivity:

$$\sigma(0, q) = \lim_{\omega \rightarrow 0} \frac{\omega}{4\pi} \epsilon_2(\omega, q).$$

The inertial sum rules seem to work for any q , but in the literature $q = 0$ seems to be assumed implicitly [20]. The inertial sum rules often require small step sizes in ω integration for sufficient numerical precision.

In general, sum rules can be used to check that the constructed ‘DF’ has indeed the mathematical properties of a DF and that the DF corresponds to the correct electron density.

4.3.4 Model used for Aluminum

As an instructive example, we now construct a very simple model DF for aluminum that is consistent with the most basic properties of its electronic structure. In this model, the valence

band is described by a Mermin oscillator (which coincides at $q = 0$ with the DL oscillator), and the core levels of the 1s, 2s, and 2p electrons by hydrogenic GOS-type contributions [22, 23, 11]. It was assured that the GOS contributed the same amount to the sum rules at any q values by the method described in ref. [24]. It will be clear from the previous that adding a GOS to a DF affects the Kramers-Kronig relations. Indeed, applying the Kramers-Kronig relation for $\omega = 0$ to the GOS part of our model DF, gives a contribution of ≈ 0.054 . This can be interpreted as the fraction of the volume occupied by the core electrons.

Thus, for a model of a DL or Mermin oscillator (representing the valence band) *plus* GOS (representing the core electrons), one has, for the case of Al, the condition that the sum of the amplitudes of the oscillators should be $\sum_i C_i = 0.946$. The simplest possible valence band DF would then be a single component with $C_1 = 0.946$, with a density such that there are 3 electrons per unit cell. This corresponds to $\omega_p \approx 16.0$ eV. The width of the oscillator is taken (rather arbitrarily) to be 1 eV. This is the model I showed in table 4.1. Later the model will be refined somewhat, resulting in model II. The primary aim of this paper is *not* to establish the best DF for Al, but to show what are the consequences of adopting a model and how the Chapidif program can be used to compare the model with a variety of experimental data and, based on the comparison with experiment, how one can improve the model. For some examples of alternative model DF of Al, mainly in the context of ion stopping, see the recent paper by de Vera *et al* [25] and Shukri and Al Shorman [26].

4.4 Results from Chapidif Calculations

4.4.1 Visualizing the DF and checking sum rules

In order to get an intuitive understanding of the model, one has to be able to visualize it. In Fig. 4.1 we show a plot of the model loss function ($\text{Im}[-1/\epsilon(\omega, q)]$), as well as the real part ($\text{Re}[1/\epsilon(\omega, q)]$) at $q = 0$ and $q = 1$ a.u. Here it was subsequently checked that the real and imaginary parts are related by the Kramers-Kronig relations (eq. 4.3, 4.4). The dotted lines are the result of the Kramers-Kronig transformations. Indeed there is good agreement between the result obtained straight from the definition and that obtained for the real (imaginary) part by applying the Kramers-Kronig transform to the imaginary (real) part.

At $q = 1$ a.u. the shape of the loss function is completely different, as now electron-hole excitations are dominant, rather than plasmon excitations. The width now reflects k_f the diameter of the Fermi sphere and is not strongly affected by the value used for Γ . Again, it was demonstrated that the real and imaginary parts are Kramers-Kronig pairs, also away from $q = 0$.

It is always useful to check if the model DF is consistent with the various sum rules. This is done in the right part of the figure. For our model (as it should be for any metal) $\text{Re}[1/\epsilon(0, 0)] = 0$, as can be seen in the top left panel of Fig. 4.1. Thus the KK sum rule (eq. 4.5) should give 1. The Bethe, F and absorption-related sum rule should correspond to Z (according to eqs (4.7-4.10)). As is obvious from the top right panel of Fig. 4.1, our model DF is in agreement with all four sum rules.

Small changes in the DF can have a large consequence on the sum rule behavior. If one changes the coefficient of the Mermin oscillator from 0.95 to 1 (and keeps the GOS contribution to the DF unchanged), then the sum rules do not work anymore, as is seen in the lower right panel of Fig. 4.1. The KK sum rule exceeds 1 slightly, a non-physical situation. As a consequence, there are large differences between, in particular, the F and Bethe sum rules. These deviations are thus an indication of non-physical input parameters. Sum rules can be checked at $q = 0$ and at other q values and e.g. the F and Bethe sum rules should give the same Z value at any q . Integration has to be done up to larger ω values with increasing q , in order to reach saturation of the integrals.

In Fig. 4.2, top panel, we show the ‘inertial sum rules’ [20]. The inertial sum rule at $q = 0$ a.u for $\text{Re}[\epsilon]$ should converge to $-2\pi^2$ times the conductivity at $\omega = 0$. For $q = 0$, the inertial

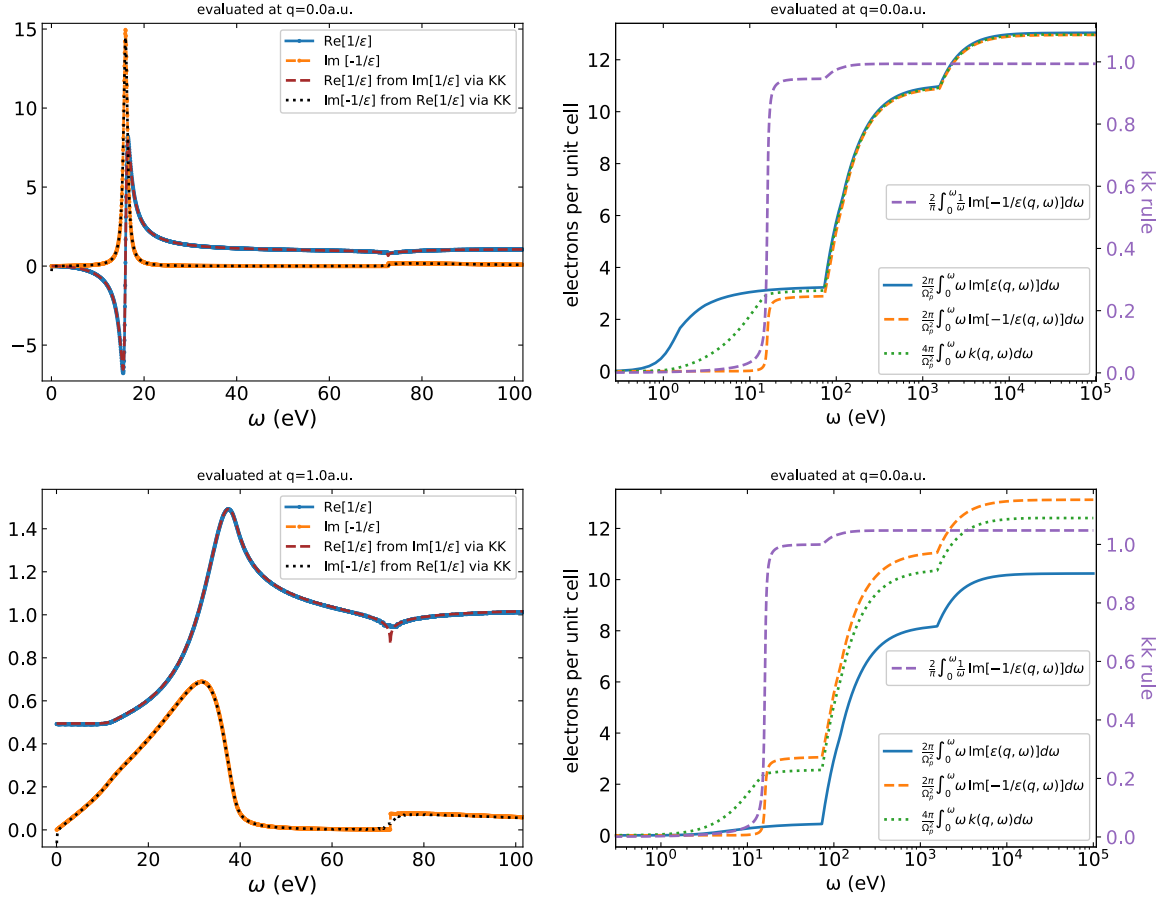


Figure 4.1: The real and imaginary part of $1/\epsilon(\omega, q)$ at $q = 0$ (top left) and $q = 1$ a.u. (bottom left) for our simple model DF of Al. They were obtained directly from the formulae but it is also demonstrated that the real and imaginary part are related by Kramers-Kronig transform, both at $q = 0$ and $q = 1$ a.u. Results for the sum rules (right panels) depend critically on the values assumed for C_i . The top right show that, for our DF, with the amplitude $C_1 = 0.946$ good results for the sum rules are obtained and the Kramers-Kronig integral goes to 1, as required. The bottom right panel shows that the combination of a GOS description of the core levels and a valence band oscillator with amplitude $C_1 = 1$ has a Kramers-Kronig integral that exceeds 1, and then the model does not adhere to sum rules, i.e., it does not have the mathematical properties of a DF.

sum rules are extremely sensitive to details of the DF near $\omega = 0$, which, in practice, precludes the use of the sum rule here for DFs that are a combination of GOS contributions and oscillators.

Closely related to the loss function is the dynamical structure factor [27, 28, 29]:

$$S(\omega, q) = \frac{q^2}{4\pi^2 n} \text{Im}(-1/\epsilon(\omega, q)) \quad (4.12)$$

with n the electron density of the target. Here one has the q^2 sum rule (closely related to the Bethe sum rule eq. 4.7):

$$\int_0^\infty S(\omega, q) \omega d\omega = q^2 \quad (4.13)$$

for the dynamical structure factor, as is shown in the lower right panel of Fig. 4.2.

Many observables, such as ion stopping and the electron inelastic mean free path, depend on the DF over a range of $\omega - q$ values. It is thus desirable to be able to visualize the loss function and the kinematic boundaries of the region of the loss function that contributes to these quantities. In Fig. 4.3, we show as a false color plot the intensity of the loss function. In order to visualize the intensities that differ by several orders of magnitude, the color is based on the

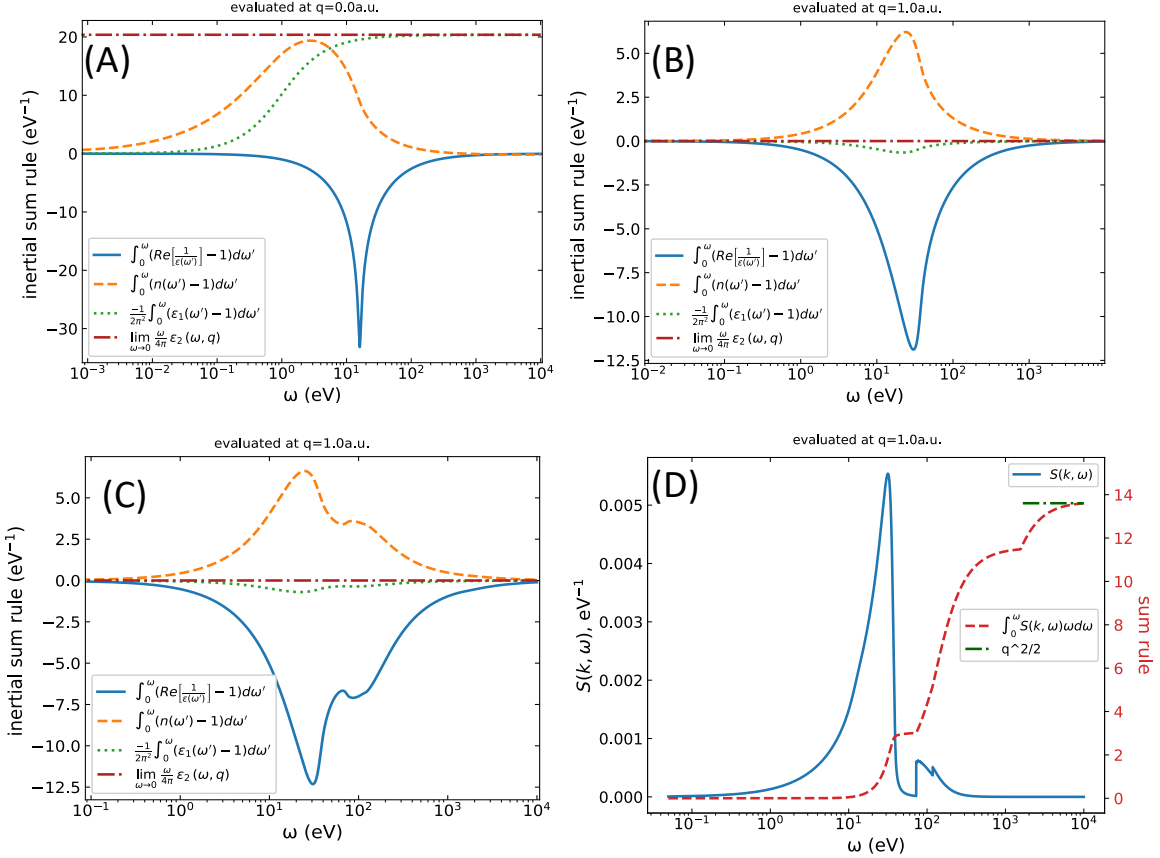


Figure 4.2: Top left panel shows the inertial sum rules [20] at $q = 0$ a.u. for a single Mermin oscillator with $\omega_p = 16$ eV, Top right panel shows the inertial sum rules for the same oscillator at $q = 1$ a.u. The bottom-left panel uses the Al DF (model 1) also at $q = 1$ a.u. Finally the bottom right panel shows for our Al DF the dynamical structure factor at 1 a.u., central in the description of inelastic X-ray scattering. It corresponds to a scaled loss function weighted by q^2 , and the corresponding sum rule converges to $q^2/2$ (i.e. 13.6 eV)

log of the loss function rather than the loss function itself. In the left panels, we interpreted the valence band oscillator as a (classical) DL oscillator. The valence band then contributes a single sharp structure to the loss function (with width Γ) located at $\omega = \omega_p + q^2/2$. The 2p and 2s edges are visible as horizontal lines around $\omega = 75$ eV and 120 eV extending up to $q \approx 3$ a.u.

Not all $\omega - q$ combinations of the loss function can be excited by an energetic charged particle, there are limits due to energy and momentum conservation. The momentum of a particle (mass M) with kinetic energy $E_{0,1}$ (E_0 before the collision, E_1 after the collision) is given at non-relativistic energies simply by $|p_{0,1}| = \sqrt{2M E_{0,1}}$ and at relativistic energies one obtains $|p_{1,2}|$ from $|p_{0,1}| = \sqrt{E_{0,1}(E_{0,1} + 2Mc^2)/c}$. As $E_0 > E_1$ one has $|p_0| > |p_1|$. The minimum momentum transfer $|q_-|$ is when \mathbf{p}_1 is directed along \mathbf{p}_0 and is given by $q_- = |p_0| - |p_1|$. The maximum momentum transfer q_+ is obtained for collisions with \mathbf{p}_1 anti-parallel to \mathbf{p}_0 and then $|q_+| = |p_0| + |p_1|$.

The limit of the accessible $\omega - q$ -space for electrons with $E_0 = 200$ eV is indicated by the red line in the upper panels of Fig. 4.3. Obviously, the maximum energy loss (neglecting the effects of exchange for now) is 200 eV at $q = |p_0| = 3.8$ a.u., and then $|p_1| = 0$, so for this limiting case $|q_-| = |q_+| = |p_0|$. For $\omega \rightarrow 0$ one has $|q_-| \rightarrow 0$ and $|q_+| \rightarrow 2|p_0|$.

In the right panels, the valence band oscillator was interpreted as a Mermin oscillator. Now, in addition to the sharp plasmon peak starting at $\omega = \omega_p$ we see a broad distribution with sharp edges due to electron-hole pair excitation. Its intensity is much smaller but clearly visible when plotting the false-color plot based on the log of the loss function. For very low energy electrons

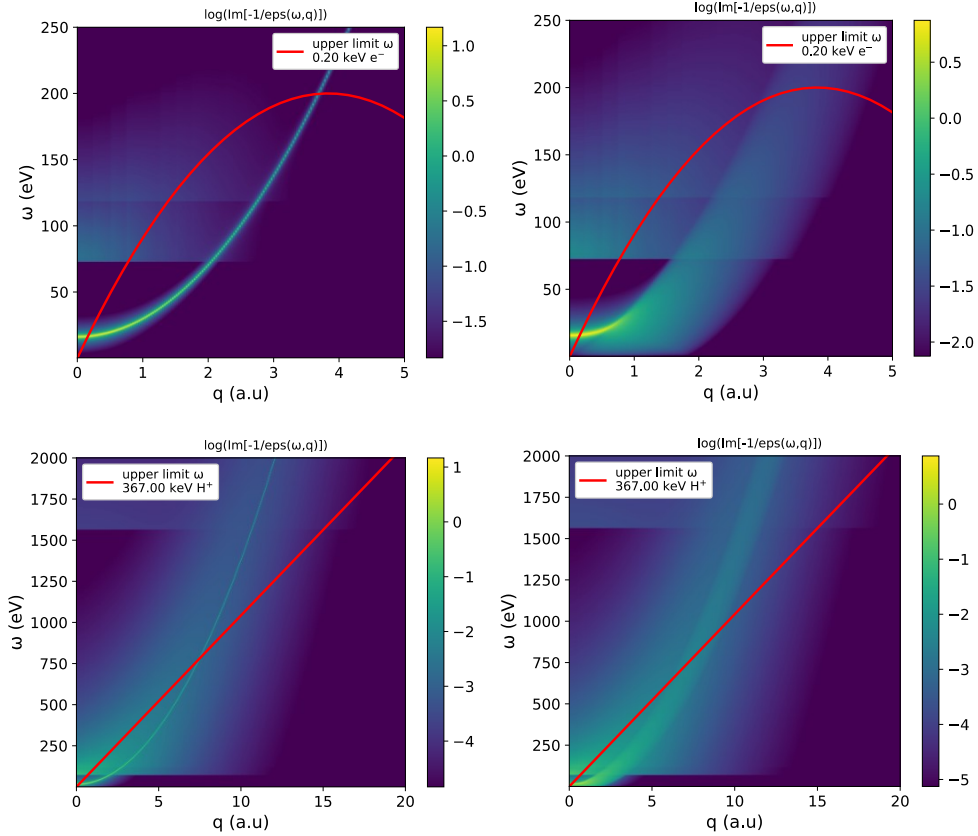


Figure 4.3: The distribution of the loss function in the $\omega - q$ plane. Our simple model function for Al is plotted with the valence band oscillator interpreted as a DL oscillator (left) and a Mermin oscillator (right). The former oscillator has a single dispersing feature, the latter has a plasmon branch merging with a broader distribution for electron-hole pair excitation. The 2p and 2s GOS distributions are visible for energy losses larger than their threshold, which gradually decrease in intensity with increasing q . The red line is the upper limit of excitations that are possible by 200 eV electrons (neglecting exchange). The lower panel shows the same loss function over an extended range of the $\omega - q$ plane, but now the red line is the accessible part for protons with an energy of 367 keV, i.e., with the same velocity v as 200 eV electrons. The red line for both protons and electrons initially follows $\omega = qv$, and this remains in good approximation linear for protons, but for electrons, the curve has a maximum at $\omega = 200$ eV.

($E_0 \approx 30$ eV and below), the kinematic boundary line does not intersect the plasmon branch, and the only allowed excitations are due to electron-hole pairs. At these energies, the electron mean free path as calculated using the Mermin model, is much smaller than obtained using the DL model

In the lower panels, similar plots are shown for 367 keV protons. Protons of this energy have the same velocity as 200 eV electrons, and as a consequence, the boundary of accessible $\omega = q$ space has the same slope for low q values. For these protons, the boundary is again an inverted parabola with a maximum at $\omega = 367$ keV, and then $q = |p_0| = 7038$ a.u. For the limited ω range plotted here, the boundary is thus an almost straight line (with slope v and referred to as the ‘ qv -line’), and hence much larger ω values are possible for a proton compared to an electron with the same velocity.

4.4.2 Density effect for valence band

The valence band was previously treated as a free electron gas, and GOS was used for the core electrons. It is instructive to see what happens if one also treats the valence electrons as a GOS. This is done in Fig. 4.4. Here, the GOS is assumed to be from two Al 3s electrons (binding energy was chosen somewhat arbitrarily as 2 eV) and one Al 3p electron (binding energy 1 eV).

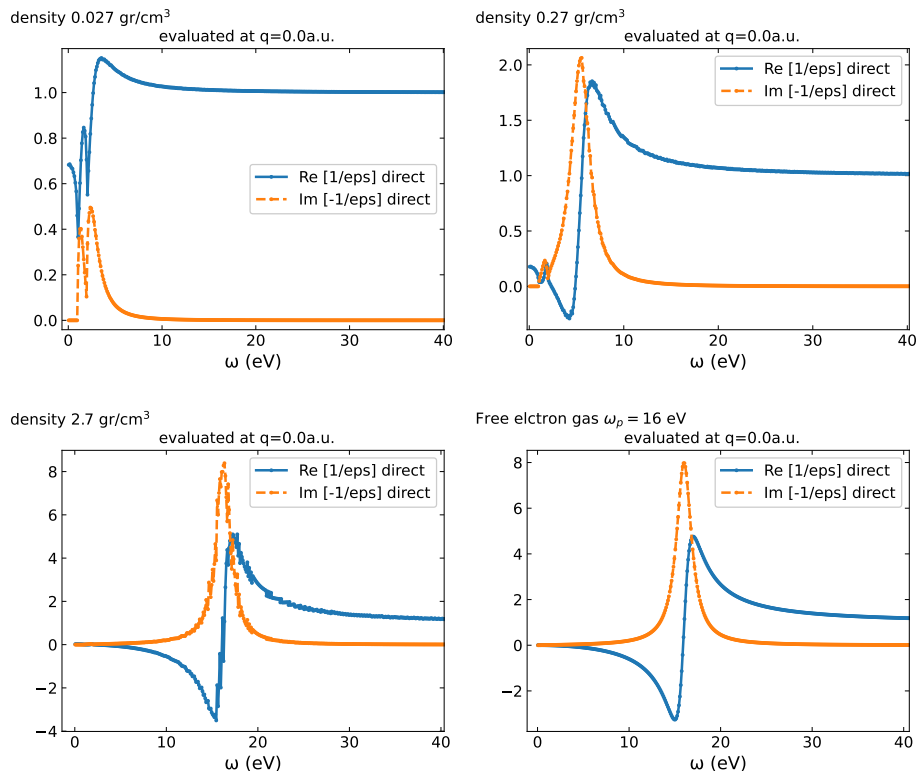


Figure 4.4: The calculated dielectric function for the valence band region for a target of Al atoms with varying densities. The Al 3s and 3p GOS describe the valence electrons. At low density (top left) the GOS contributions of both levels are evident. Increasing the target density (and hence increasing the plasmon energy corresponding to the higher electron density) shifts the loss spectrum to higher values, but the edge remains visible (top right). Increasing the target density to the value of that of Al metal, then the loss function, as derived from the atomic GOS contribution, shows a relatively sharp peak at 16 eV (bottom left) and resembles that of a free electron gas with the electron density of the Al valence band (bottom right) as now the binding energies of the Al 3p and 3s electrons are small compare to the plasmon energy.

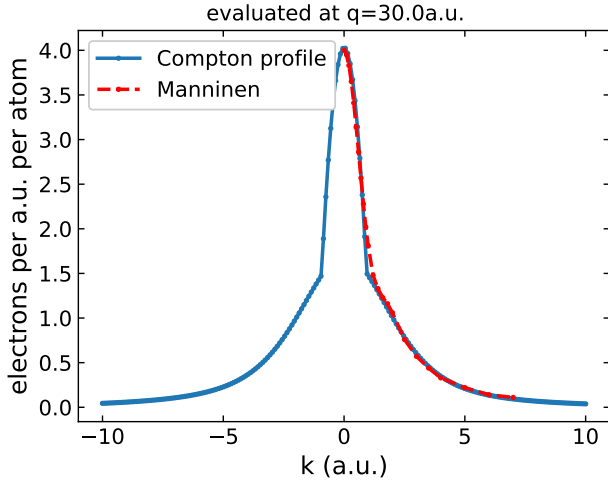


Figure 4.5: Calculated Compton profile compared (for positive k values) with the measured one as published by Manninen obtained from X-ray scattering measurements[30].

If one takes the atomic density of the target very low (here 0.027 gr/cm^3) the small value of Ω_p (the plasmon energy corresponding to one electron per atom) in eq. 4.6 assures that the real part of ϵ is close to 1, and the imaginary part $\ll 1$. Then $\text{Im}[-1/\epsilon(\omega, q)] \approx \text{Im}[\epsilon(\omega, q)]$ and the loss function shows the characteristic shape of the GOS of the 3p and 3s level.

Increasing the target density in the calculation to 0.27 gr/cm^3 increases Ω_p in eq. 4.6 and this causes the shape of the loss function to differ from the shape of $\text{Im}[\epsilon(\omega, q)]$, but the edges corresponding to the threshold of the 3s and 3p electrons are still visible. The ω value corresponding to the maximum intensity of the loss function shifts to larger ω values.

If one further increases the density to 2.7 gr/cm^3 (corresponding to the density of Al metal), then the loss function evolves into a fairly narrow peak centered at 16 eV, and the dielectric function resembles that of a free electron gas with plasmon energy of $\omega_p = 16 \text{ eV}$. Thus, if one considers the density effect, the GOS picture evolves naturally into a free-electron model when the density of the target is increased. (In this calculation, the dielectric function due to both the 3p and 3s electrons was obtained from the sum of their susceptibilities, as explained in ref. [11].)

4.4.3 Compton profiles

For large E_0 values, a large momentum transfer is possible, and for those collisions, the interaction with the target simplifies. One then has hard, ‘billiard-ball-like’ collisions with a single electron, and binding energy effects can be neglected. Momentum and energy conservation again dictate which energy transfers are possible at a certain q , e.g., for scattering from a stationary electron $\omega \approx q^2/2$. It turns out that the motion of the target electron causes Doppler broadening, and the spectra at large q are Compton profiles, i.e., the intensity is an almost symmetrical distribution centered at $q^2/2$. The energy loss is given by:

$$\omega = q^2/2 + \mathbf{q} \cdot \mathbf{k}, \quad (4.14)$$

with \mathbf{k} the momentum of the target electron *before* the collision. From a precise energy loss measurement, one can recover the initial momentum component of the target electron along \mathbf{q} .

An example is shown in Fig. 4.5 for our Al DF compared to a gamma-ray Compton measurement from Manninen [30]. Our simple model follows the measured Compton profile nicely. However, more detailed calculations result in even more precise descriptions of the Compton profile, and e.g. the effect of the orientation of single crystals and the influence of electron-electron correlation can be resolved [31].

4.4.4 Measurement of the loss function at specific momentum transfers

Within the framework of dielectric functions, one can calculate the probability that, per unit length traveled, a projectile with energy E_0 loses ω energy and changes its momentum by q . This

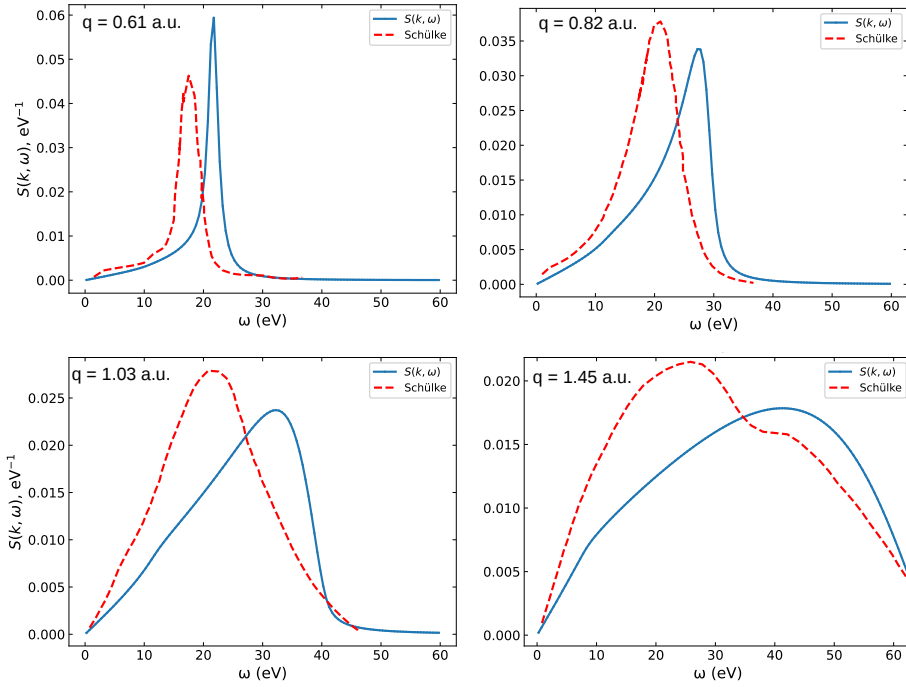


Figure 4.6: The IXSS results of Schülke [32] for q values as indicated for measurements of Al single crystals with q along $[1, 0, 0]$, compared to $S(k, \omega)$ calculated from our model, which takes the DF to be isotropic.

is the double differential inverse inelastic mean free path (DDIIMFP) $\frac{d\Lambda}{d\omega dq}$. Here $\Lambda = N_a \sigma$ with σ the inelastic cross section. The DDIIMFP is given by [33]:

$$\frac{d\Lambda}{d\omega dq} = \frac{2Z_1^2}{\pi v^2} \frac{1}{q} \operatorname{Im} \left[\frac{-1}{\epsilon(\omega, q)} \right], \quad (4.15)$$

where Z_1 refers to the charge of the projectile. v^2 is related to the kinetic energy E_0 by [22, 34]:

$$v^2 = 2E_0 \frac{1 + E_0/(2Mc^2)}{M(1 + E_0 Mc^2)^2}.$$

with M its mass of the projectile. For low energy electrons it is important take the kinetic energy relative to the bottom of the valence band, rather than the vacuum level or the Fermi level.

As Chapidif only considers protons or electrons as charged particles, $Z_1^2 = 1$ and this term will be omitted from now on. The DDIIMFP can be measured by either transmission electron energy loss spectroscopy, in combination with a detector that can resolve the scattering angle [35] or by inelastic X-ray scattering spectroscopy (IXSS)[27, 28]. Of these techniques, IXSS is the easiest to compare with theory, as it is not significantly affected by multiple scattering. Results of measurements by Schülke *et al* [36] from Al crystals are shown in Fig. 4.6. Broad structures are observed, as predicted by the Mermin approach, but contrasting to the sharp peaks expected based on the DL loss function. The calculations using the Mermin model (based on the valence electrons only, the inclusion of the core electrons causes a change in the vertical scale, which explains the difference with Fig. 4.2(D)) show the same general trend as the experiment, but details of the dispersion are different. If this is due to shortcomings of the RPA calculation or the measurement, will not be discussed here. Changing the plasmon energy to, e.g., $\omega_p = 15 \text{ eV}$ does not significantly alter the level of agreement between the experiment and calculation.

4.4.5 Differential cross sections and scattering angles

If, in a scattering experiment, one measures the energy and direction of propagation of the projectile after a collision, one obtains the double differential cross section $\frac{d^2\sigma}{d\Omega d\omega}$. Its momentum

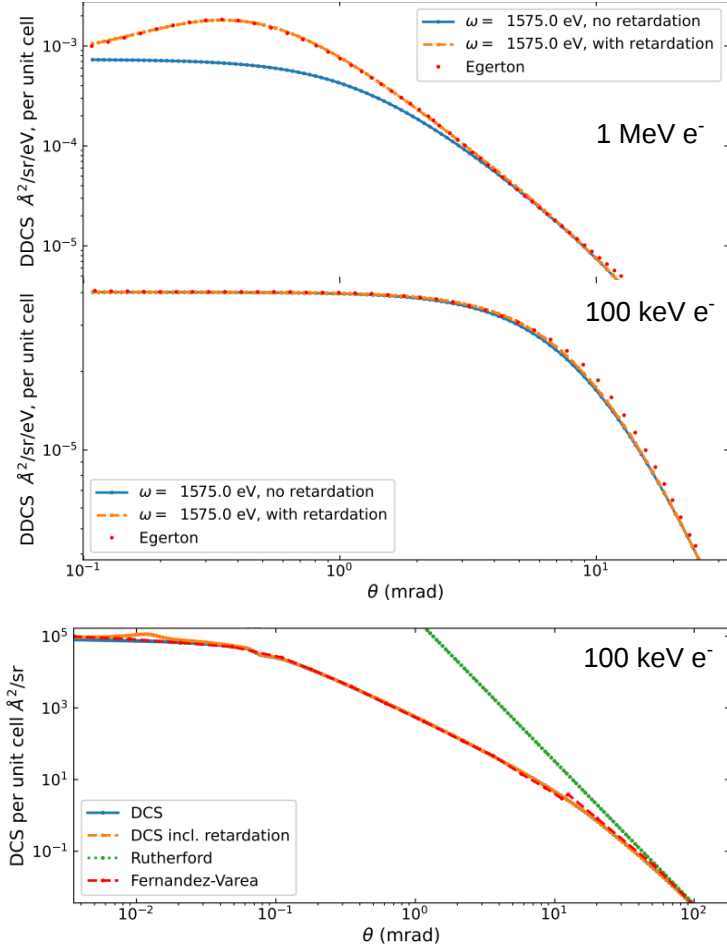


Figure 4.7: The top panel shows the double differential cross section at 1575 eV (i.e., for energy losses slightly larger than the Al K edge position) for 1 MeV and 100 keV e^- scattered from Aluminum, compared to a similar calculation by Egerton [22]. Calculations are done without and with retardation effects, the latter becomes significant at 1 MeV. To make a detailed comparison possible, the ICRU recommended value for the occupation of 1.623 was used (see table 4.1), rather than the occupation of 2 used in our simple model. The lower panel shows this cross section integrated over energy loss and compared with a similar calculation of ref.[37]. Also shown is the Rutherford cross section, and for large θ values, both cross sections converge, indicating that for large-angle scattering, the collisions resemble those between free particles.

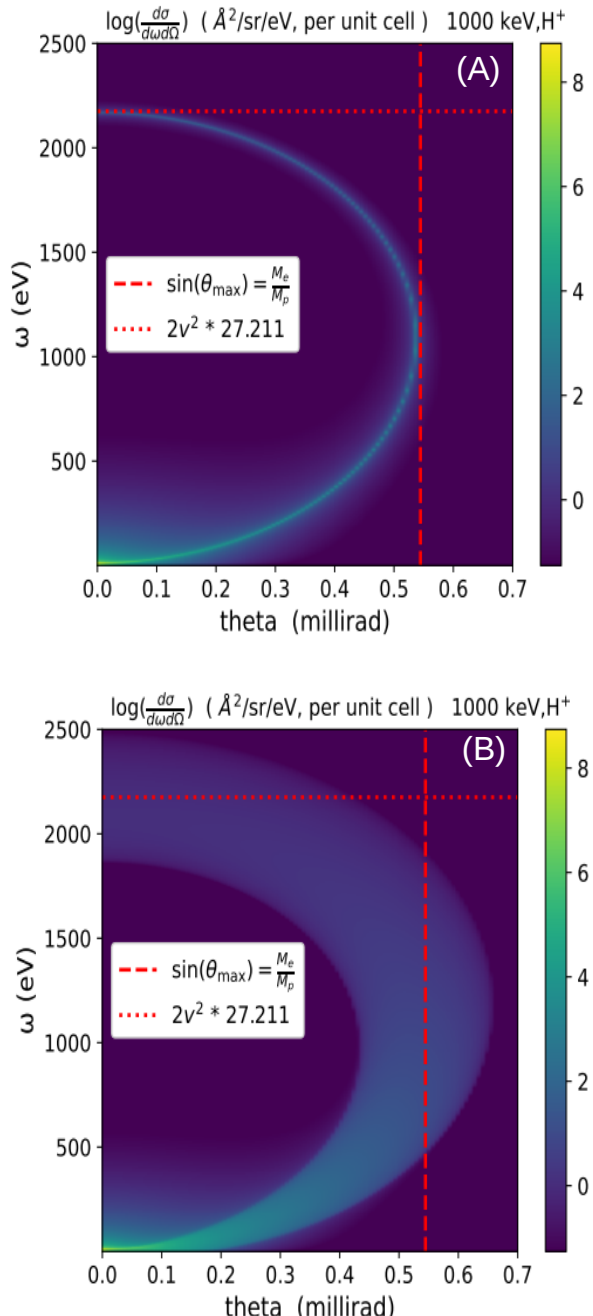


Figure 4.8: The differential cross section for 1 MeV protons scattering from valence electrons. In contrast to electron-scattering, there is a maximum deflection that is possible, which corresponds, for scattering from stationary electrons, to M_e/M_p rad. Without deflection ($\theta = 0$) there are two contributions. The proton can either excite a plasmon (distant collision) or experience a hard collision with impact parameter 0. In the latter case the energy transfer is (in atomic units) $2v^2$. The top panel shows this for the DL oscillator of the Al valence band. The Mermin model was used for the lower panel. In this model, the electrons have a momentum distribution up to the Fermi wave vector k_f , which causes broadening relative to the distribution observed in the DL case.

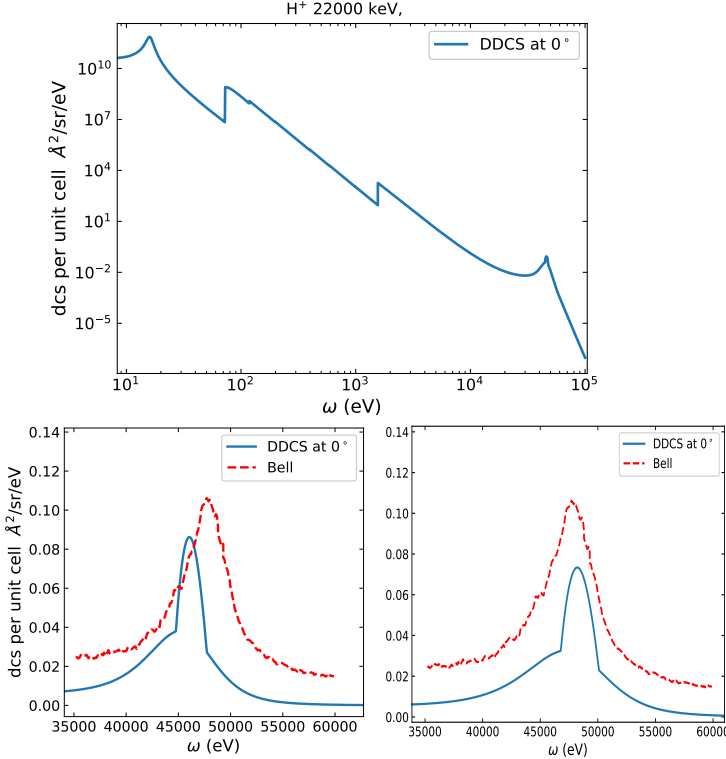


Figure 4.9: The calculated differential cross section for scattering of 22 MeV protons from Al at $\theta = 0$ (top). The plasmon peak, L, and K edges are followed near 45 keV by the ‘binary encounter’ peak. The measured (Bell et al) [38] and calculated binary encounter peak are shown in the lower panels. The left panel uses non-relativistic dispersion for the DF (both the GOS and Mermin components), and a clear error is observed for the peak position. In the right panel, relativistic dispersion is used for both components. This results in a much-improved peak position.

changes from \mathbf{p}_0 before the interaction to \mathbf{p}_1 after the collision, and $\mathbf{q} = \mathbf{p}_0 - \mathbf{p}_1$. Two factors affect the momentum transfer.

- Contribution due to the energy loss: $|p_1| < |p_0|$. If the direction of propagation does not change, this is the only contribution, and one has simply: $|q| = |p_0| - |p_1|$. These events correspond to (ω, q) combinations on the red boundary lines Fig. 4.3. The momentum transfer of this component is directed along \mathbf{p}_0 , and is magnitude (at non-relativistic energies) is usually expressed as [22]: $|p_0|\theta_E$ with $\theta_E = (|p_0| - |p_1|)/|p_0| \approx \frac{M\omega}{2E_0}$.

- The contribution due to the change in direction. For small energy losses, it can be approximated by $2|p_0|\sin(\theta/2) \approx |p_0|\theta$, with θ the scattering angle. It is directed approximately perpendicular to \mathbf{p}_0 .

For small scattering angles, one has thus: $q \approx p_0\sqrt{\theta_e^2 + \theta^2}$.

The relation between the double differential cross section (DDCS) (per atom) and the DF is then given by [22]:

$$\frac{d^2\sigma}{d\Omega d\omega} = \frac{\text{Im}[-1/\epsilon(\omega, q)]}{\pi^2 M v^2 N_a} \frac{1}{\theta^2 + \theta_e^2}, \quad (4.16)$$

Knowledge of the DDCS is important if one wants to simulate, by Monte Carlo methods, how deflections due to inelastic collisions influence the trajectories of energetic particles in matter. Integrating this quantity over ω gives the differential scattering cross section (DCS).

Electron scattering

For not too large a momentum transfer, the energy loss can be used to separate the contribution of the different electronic shells. Just beyond its excitation threshold a specific core electron will dominate the loss function. It is thus possible to check the angular dependency of the DDCS of a core electron by measuring the intensity at different angles for an energy losses just exceeding the core level binding energy. In Fig. 4.7 we show the double differential cross section for 100 keV e^- scattering from the Al 1s level, as obtained for the Al 1s GOS component of our DF, at energy losses just about the K edge. At small scattering angles (up to $\theta \approx 2$ mrad for $E_0 = 100$ keV) θ_e dominates over θ , and thus the cross-section is fairly constant. This angular region is

often referred to as the dipole region. This result is compared to a similar calculation by Egerton [22], and consistent results are obtained. Unfortunately, we do not know of any experimental values to compare to.

At E_0 -values above 100 keV, retardation effects become important. They are calculated in Chapidif by replacing eq. 4.16 by the one derived by Festenberg and Kröger[39, 40, 22]. The cross-section with retardation is given as well in Chapidif, and good agreement at 1 MeV was found compared to the calculation by Egerton.

At very large momentum transfer, the intensity due to the core level moves away from the threshold and becomes centered at the Bethe ridge. Then, the interaction can again be described as the collision between a projectile and a free electron. In this semi-classical picture, there is then no upper limit of the energy transfer possible, and the scattering angle can be up to 90°. When taking exchange into account and identifying the fastest electrons after the scattering event as the scattered one, the largest scattering angle is 45°, and the largest possible energy loss is then $0.5E_0$

In the lower panel we show the DCS for electron scattering as obtained from our DF. The largest contribution comes from the valence electrons. As their excitation energy (of the order of the plasmon energy) and corresponding θ_E is much smaller, the angular range for which the DCS is fairly constant extends only up to ≈ 0.1 mrad. Above about 10 mrad the DCS approaches the Rutherford DCS as for these larger angles these collisions resemble the collisions with free electrons. The results from Chapidif program for the DCS are comparable to those published by Fernandez-Varea [37].

Proton scattering

Similar calculations can be done for proton scattering. However, due to their much larger mass (M_p) compared to the mass of the electron (M_e), there is now a maximum angle over which a proton can be deflected. The maximum deflection angle (in radians) is $\approx M_e/M_p = 0.00055$, and for that angle, the energy loss $\omega \approx v^2$. See Sigmund [18] section 3.2 for details. This is illustrated in the top panel of Fig. 4.8 for a single DL oscillator with $\omega_0 = 16$ eV and 1 MeV H⁺. Measurements close to 0.6 mrad show indeed an enhancement of the intensity in the energy loss, indicative of such proton-electron collisions [41].

Related to this, there are two contributions to the scattered electron intensity near $\theta \approx 0$: one due to the excitation of plasmons by large impact-parameter (i.e. ‘soft’) collisions and one due to ‘hard’ proton-electron collisions with near-zero impact parameter. The soft collisions correspond to the first crossing of the red line with the dispersing structure in the lower panels of Fig. 4.3, and the hard collisions with the second crossing. For scattering from a free (stationary) electron, the latter energy transfer is $2v^2$.

If one calculates the DDCS for protons for a Mermin oscillator, then the distribution gets Doppler broadened, as wave functions up to the Fermi wave vector k_f are occupied. This is illustrated in the lower panel of Fig. 4.8. Note that intensities of the features of these plots vary by a large factor, as scattering at large energy losses has a small cross-section (intensity ratio of the two features at $\theta = 0$ for 1 MeV protons is $\approx 10^6$).

In light of this, it is somewhat surprising that, indeed, the second peak, due to hard collisions and its Doppler broadening, can be measured experimentally [38, 42]. In Fig. 4.9 we show the DDCS at $\theta = 0$ for our DF of Al and 22 MeV protons on a log scale ($\theta = 0$ corresponds to $\omega - q$ combinations along the red line in Fig. 4.3. However, Fig. 4.3, lower panels, is for a much lower projectile energy. At $E_0 = 22$ MeV, as applies here, this line would be considerably steeper). For 22 MeV H⁺ the binary encounter peak is visible near $\omega = 50$ keV. The measurement detects the energy of the ejected electrons near $\theta = 0$, rather than the energy loss of the proton. By treating the collision as if it happens between a proton and a free electron (often referred to as the ‘plane-wave impulse approximation’, which is quite good at these energies), it is obvious that the energy lost by the projectile is the same as the energy gained by the electron.

The measurements by Bell *et al* [38] are compared in the lower panel using a linear scale. The general shape of the measurement seems to agree with the calculation, although it is somewhat broadened due to finite resolution. However, there is a clear shift of a few keV in position. This is mainly because the standard implementation of the Mermin DF and the GOS model neglects relativistic effects, which become important when ω (50 keV here) is not small compared to the electron rest mass (511 keV). Incorporating relativistic dispersion resolves this issue, as explained in 4.B.

4.4.6 Differential inelastic inverse mean-free-path

The next step in the application to the DF for the analysis of charged-particle matter interaction is the integration of eq. 4.15 over all accessible q values:

$$W_b(\omega) = \int \frac{d\Lambda}{d\omega dq} dq = \frac{2}{\pi v^2} \int_{q_-}^{q_+} \frac{dq}{q} \operatorname{Im} \left[\frac{-1}{\epsilon(\omega, q)} \right]. \quad (4.17)$$

The obtained quantity W_b is usually called the ‘Differential inelastic inverse mean-free path’ or DIIMFP for short. It is the probability that the projectile loses energy ω per unit length traveled. It can be measured directly in a transmission electron microscopy experiment using a large opening aperture (so a wide range of q values are measured by the detector) and very thin films (so no multiple scattering occurs). At the high energies of an electron microscope, W_b is dominated by contributions very close to $q = 0$. For lower projectile energies, the shape of the DIIMFP will change with E_0 , and then the shape is sensitive to the dispersion. Reflection electron energy loss spectroscopy (REELS) can be used to obtain estimates of W_b for smaller E_0 values. Interpretation of these measurements is more difficult, as they are always affected by multiple scattering, and we will come back to this later (section 4.4.11). If $W_b(\omega)$ is normalised to unit area, it is usually referred to as w_b and it is then the probability distribution that in an inelastic event (collision) an amount ω energy is transferred. It is central to Monte Carlo simulations of the trajectories of a projectile.

An example of the electron DIIMFP for our DF is shown in Fig. 4.10 for $E_0 = 0.2$ keV. The intensity of the plasmon peak at 16 eV is almost 2 orders of magnitude larger than the contribution at the Al 2p edge near 75 eV. It is instructive to split up the contributions to the DIIMFP over the different momentum ranges (‘partial DIIMFP’) as in the lower panel of Fig. 4.10. For $|q| < 0.1$ a.u. only electron-hole pair creation is possible, as the plasmon peak is above the ‘red line’ (Fig. 4.3) for these q -values. Plasmon creation becomes possible for $0.1 < |q| < 0.2$ a.u., and the ‘partial DIIMFP’ intensity increases dramatically. The Al 2p edge only starts contributing for $q > 0.7$ a.u..

4.4.7 IMFP, stopping and straggling

If one integrates W_b over ω , then the obtained quantity is the probability that any collision occurs per unit length. If one takes the reciprocal value of the integral, one obtains the inelastic mean free path λ :

$$\frac{1}{\lambda} = \int_0^{E_0} W_b(\omega) d\omega. \quad (4.18)$$

The total cross section for inelastic scattering per atom is then $\sigma_{\text{in}} = \frac{1}{N_a \lambda}$.

In order to obtain the stopping (mean energy loss per unit length $\frac{dE}{dx}$) one weights the integral over the loss function by ω :

$$\frac{dE}{dx} = \int_0^{E_0} \omega W_b(\omega) d\omega. \quad (4.19)$$

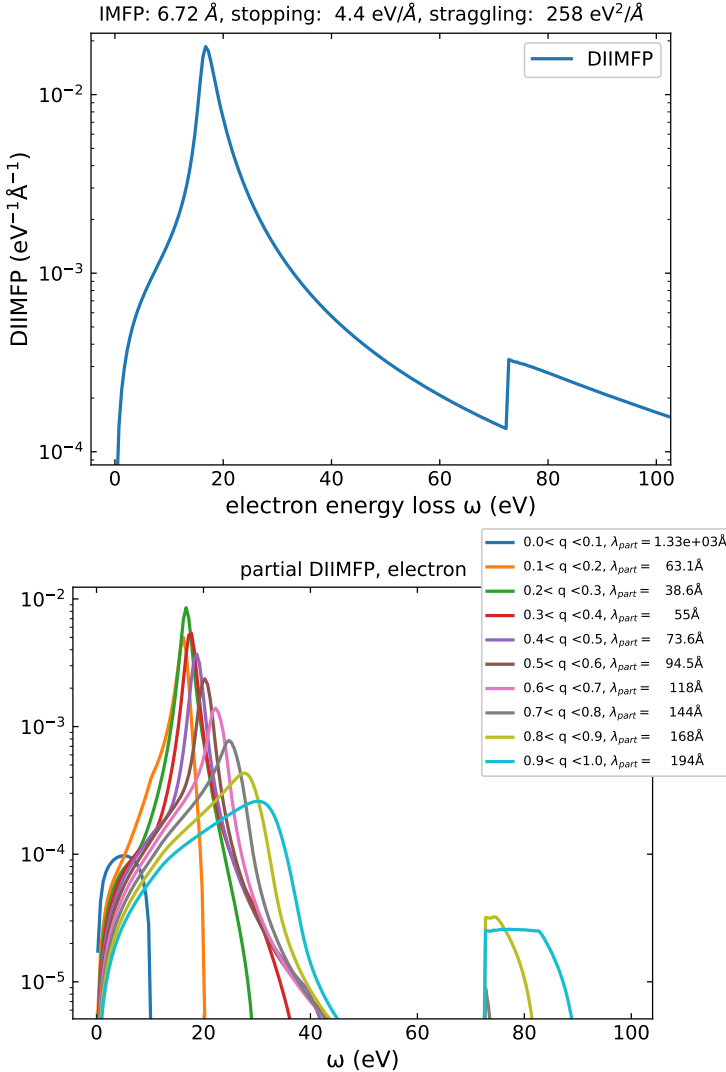


Figure 4.10: The differential inverse inelastic mean free path plotted for 200 eV electrons in Al. IMFP, stopping and straggling values obtained by integrating over the energy range of this plot are printed above the plot. In the lower panel we show how different ranges of q values contribute to the DIIMFP integral. The intensity of the distribution never extends beyond the red line in Fig. 4.3, top panels.

For straggling $\frac{d\Omega^2}{dx}$ ('spread' in energy loss) the weighting factor in the DIIMFP is ω^2 :

$$\frac{d\Omega^2}{dx} = \int_0^{E_0} \omega^2 W_b(\omega) d\omega. \quad (4.20)$$

Infrequently occurring collisions with high ω values will affect the IMFP very little, but these events will have larger impact on the stopping and especially the straggling due to the ω and ω^2 weighting factors.

In Chapidif, if one requests the calculation of the DIIMFP, the IMFP, stopping, and straggling values are given in the plot. These correspond to all collisions with ω smaller than the upper bound of the plot (see Fig. 4.10), and the user should check that these values do not change anymore if the upper bound of the plot changes.

Usually, one is interested in how these quantities change with E_0 . Chapidif can calculate the energy dependence of these quantities, and this calculation always extends over all allowed ω values, and hence should give the proper IMFP, stopping and straggling for a given DF. For our DF, the electron IMFP and the proton stopping are shown in Fig. 4.11. They are compared with calculations by Shinotsuka *et al* [43] for the IMFP and almost perfect agreement is found. Also, in Fig. 4.11, the calculated proton stopping is compared with those of the SRIM database [44]. The calculation of ref.[43] is, just like Chapidif, a first-Born type calculation, but based on the measured DF in the optical limit ($q = 0$) and always assumes dispersion obtained from a free electron gas. These calculations include relativistic kinematics in the same way as Chapidif.

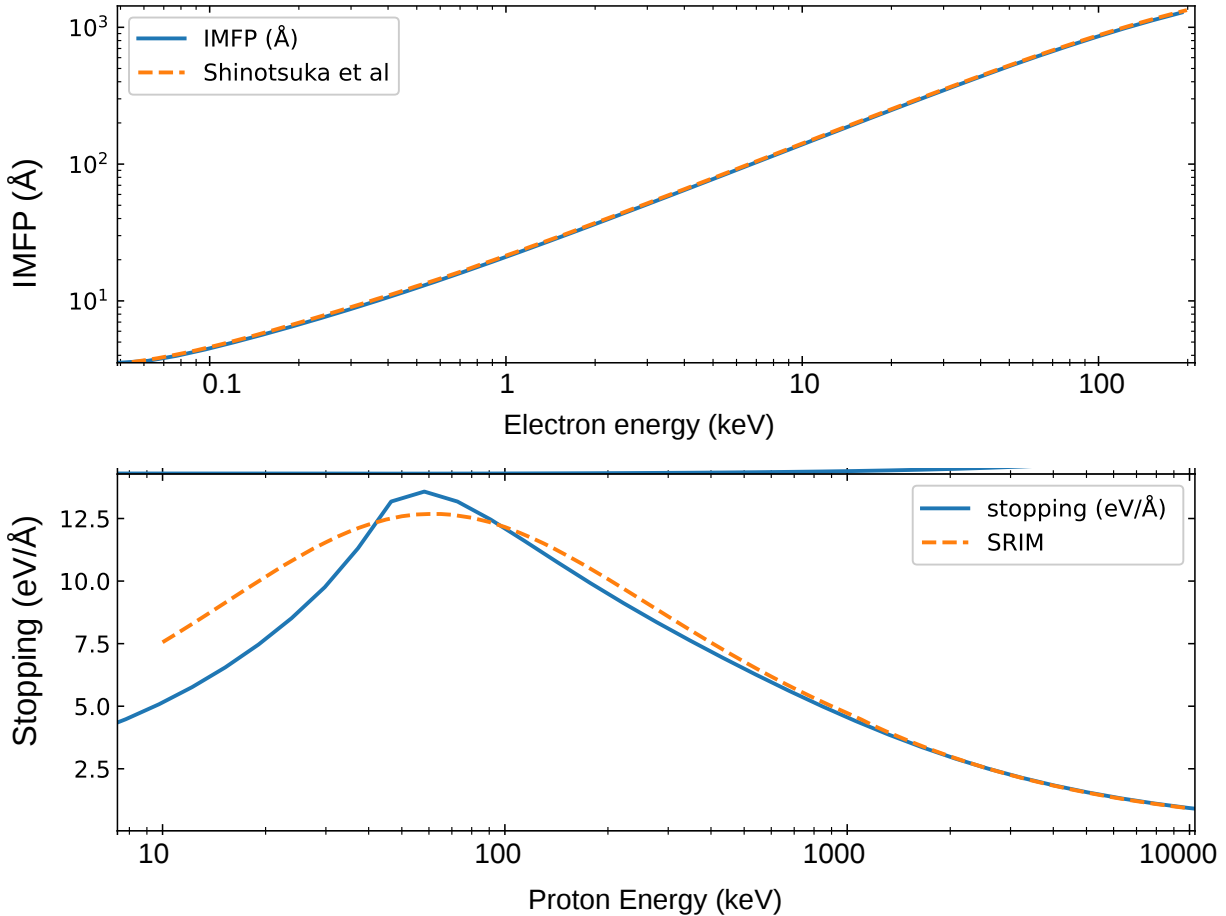


Figure 4.11: The electron inelastic mean free path (top) and proton stopping (bottom) as calculated for our simple model compared to the calculated IMFP values from Shinotsuka et al ([43] and the semi-empirical proton stopping values as given by SRIM-2013

The SRIM calculation is semi-empirical in nature and not a simple first-Born approximation. Deviations at lower energies in the proton-stopping case reflect shortcomings of the first Born approximation, i.e., the importance of non-linear effects at low energies[45, 46].

The stopping is often written as a product of two factors: $-\frac{dE}{dx} = \frac{4\pi n}{v^2} L$. L can thus be defined in terms of the DF:

$$L = \frac{1}{2\pi^2} \int_0^\infty \frac{dq}{q} \int_0^{qv} \omega d\omega \text{Im} \left[\frac{-1}{\epsilon(\omega, q)} \right] \quad (4.21)$$

The first quantum-physics-based stopping description by Bethe divides the projectile's interaction with the target into two components: 'soft collisions,' which correspond to plasmon creation, and 'hard collisions,' for which it is assumed that the interaction can be described as if it were a collision of the projectile with a free, stationary electron. [1, 50]. This simple approximation is surprisingly good, and it is then possible to solve the stopping problem up to very high energies, including a number of relativistic effects [51, 52, 47].

$$L_{\text{Bethe}} = \ln \frac{2v^2}{I} + \ln \gamma^2 - \beta^2 + 0.5f(\gamma), \quad (4.22)$$

with $\beta = v/c$ and $\gamma = \sqrt{1/(1 - \beta^2)}$ and $f(\gamma)$ a correction factor, very small for protons, but substantial for electrons as defined in ref. [47]. The only material-dependent variable in this equation is the mean excitation energy I , which is obtained from the ELF (Energy Loss Function

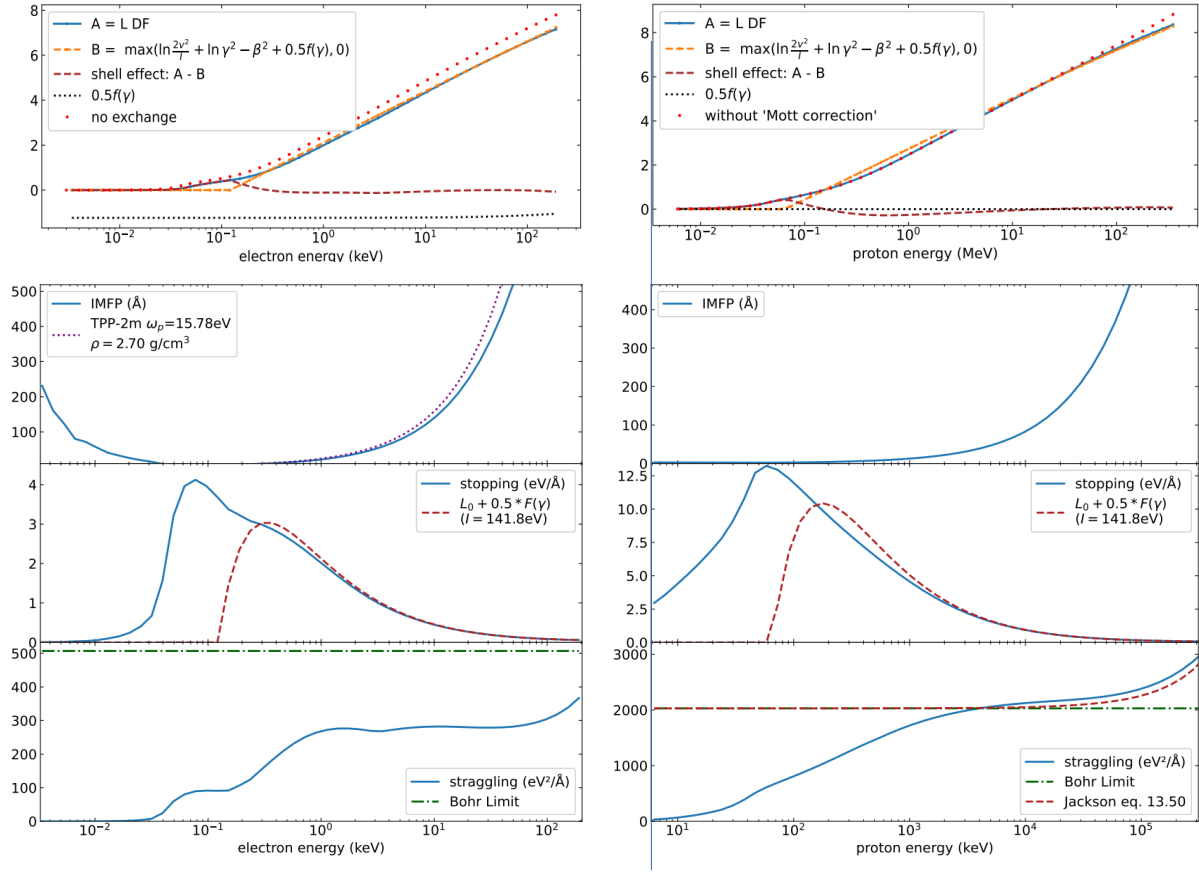


Figure 4.12: Top panel: The stopping number L (eq. 4.21) as obtained for electrons (left) and protons (right) compared to the values obtained from the relativistic Bethe theory as described in ref. [47]. The values of the relativistic Bethe theory are expected to be correct in the high energy limit. For electrons, the obtained L values agree with the relativistic Bethe theory at high energies, if exchange is included. For protons, it is only if one takes the deviations of the Mott cross section from the Rutherford cross section into account. The lower panels show the corresponding IMFP, stopping and straggling, compared to the TPP formula for the electron IMFP ([48] and the stopping values obtained from the relativistic Bethe theory (protons and electrons). For protons, the straggling is compared with a formula given by Jackson [49]

at $q = 0$):

$$I = \exp \left[\frac{\int_0^\infty \omega' \ln \omega' \operatorname{Im} \left[\frac{-1}{\epsilon(\omega', 0)} \right] d\omega'}{\int_0^\infty \omega' \operatorname{Im} \left[\frac{-1}{\epsilon(\omega', 0)} \right] d\omega'} \right]. \quad (4.23)$$

For projectiles with lower energy, the stopping will differ from the Bethe value, as the electrons of an atom are not in a single level with binding energy I but distributed over different shells and thus different binding energies. By convention (neglecting some smaller corrections such as the density effect and the Lindhard-Sørensen and Barkas corrections for simplicity, which are small in this energy range) the difference between the actual stopping and the Bethe value (ΔL) is referred to as the shell effect :

$$\Delta L = L_{\text{Bethe}} - L. \quad (4.24)$$

In figure 4.12 we compare the L values obtained from the model Al DF with those of the relativistic Bethe theory. The dispersion of the loss function at high energy loss was calculated using relativistic kinematics, as explained in the 4.B. At large projectile energies, we obtain good agreement for electrons with the relativistic Bethe theory, provided exchange effects are included. Exchange effects are discussed in some more detail in section 4.4.9.

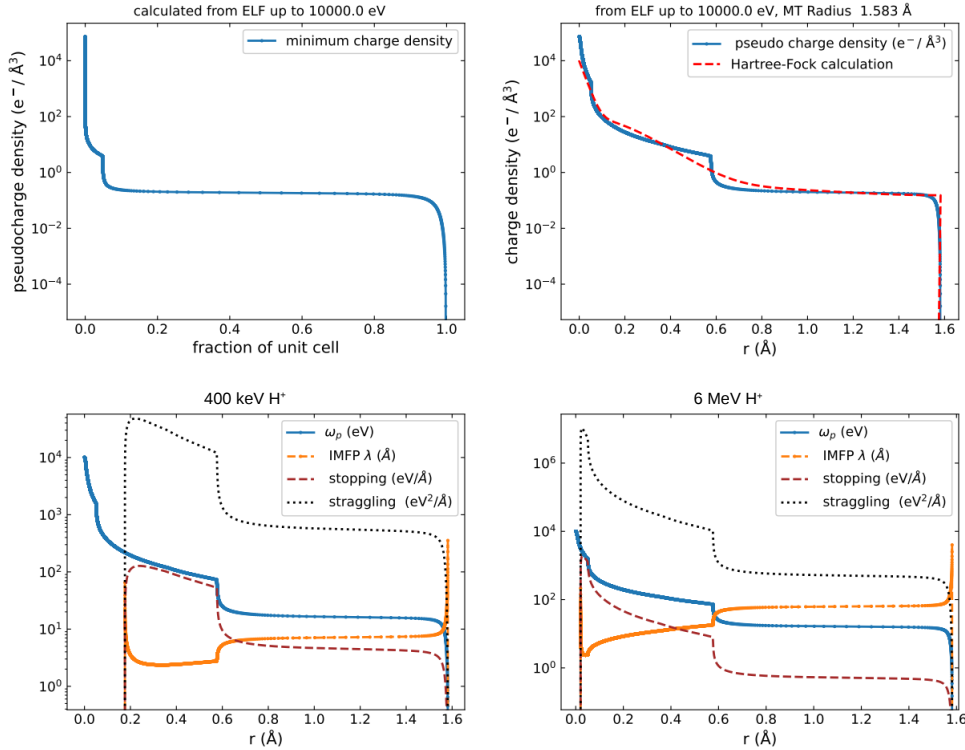


Figure 4.13: The fraction of the unit cell with a charge density equal to at least the indicated value (top left), as obtained from our DF interpreted in the local density approximation. If one assumes a radial distribution, then one can translate this into a radial charge density for a Muffin-Tin sphere with equal volume as the unit cell. This is compared with the radial charge density obtained from Hartree-Fock calculations. For this we used charge density within the muffin-tin sphere as is provided by the ELSEPA package [54]. The lower panels show the IMFP, stopping, and straggling values for an electron gas with the radial density value at both 0.4 and 6 MeV H^+ . Note that at 0.4 MeV the IMFP in the Al 2p region is of the order of 2 \AA , of the same order as the diameter of the Al 2p charge distribution ($\approx 1 \text{\AA}$). There is thus a significant chance that a H^+ ion penetrating the 2p shell at this energy creates two 2p excitations. This can be seen as a contribution to the ‘bunching effect’ in straggling, as observed for protons.

For protons, the calculated stopping starts deviating from eq. 4.22 result above 100 MeV, using a Rutherford scattering cross-section. For large energies, the Mott cross-section should be used instead. It was suggested [52] that in semi-classical calculations one can approximate the Mott cross section in stopping calculations by using the first term of the McKinley-Feshbach expansion of the Mott cross section [53], i.e. scaling the Rutherford cross section by a factor $1 - \omega/\omega_{\max}$, with $\omega_{\max} = 2\beta^2\gamma^2C^2$.

In this way, we obtain within 1% results consistent with eq. 4.22 at the highest energy of our calculation (up to $\beta = 0.8$). For electrons the same level of agreement is obtained provided one takes exchange into account, as will be discussed in section 4.4.9.

4.4.8 Pseudo Charge-Density

For a free-electron gas, one can calculate the interaction with a charged particle using the Lindhard (or, when including relaxation, Mermin) DF. In that case the free-electron gas is characterised by its electron density. For a real material, dielectric functions are not easily obtained from the first principle, and the electron density varies. In order to proceed in this case, one has to make a simplifying assumption. Usually, the statistical approximation is made: the volume fraction of the material with electron density $n(r)$ interacts with the projectile as a free electron gas with the same density [55, 56]. The density $n(r)$ can be obtained from e.g. Hartree-Fock

calculations.

Later optical measurements of the ELF, $\text{Im}[-1/\epsilon(\omega, 0)]$) became more generally available over an extended ω range [57], and this ELF is often used as the starting point of the stopping calculation. The observed intensity at an energy loss ω is attributed to part of the material that acts as a free electron gas with electron density n such that $\omega = \sqrt{4\pi n}$. The fraction of the unit cell $C(\omega)$ with an electron density such that ω is in between ω and $\omega + \delta\omega$ is then related to the measured ELF by: $C(\omega) = \frac{2}{\pi\omega} \text{Im}[-1/\epsilon(\omega, 0)] d\omega$ [58]. Using this definition of $C(\omega)$, integration of the charge density over the unit cell should give the total charge Z per unit cell:

$$Z = \int_0^\infty \frac{C(\omega)n(\omega)d\omega}{N_a} \quad (4.25)$$

$$= \int_0^\infty \frac{2}{\pi\omega} \text{Im}[-1/\epsilon(\omega, 0)] \frac{\omega^2}{4\pi N_a} d\omega \quad (4.26)$$

$$= \frac{2}{\pi\Omega_p^2} \int_0^\infty \omega \text{Im}[-1/\epsilon(\omega, 0)] d\omega, \quad (4.27)$$

that is, this assignment of $C(\omega)$ gives an integral over the unit cell that corresponds to the Bethe sum rule (eq. 4.7).

The measured ELF has been normalized (eq. 4.7) such that it corresponds to the correct number of electrons per unit cell. However, the charge-density distribution obtained in this way from the measured ELF will generally differ from the results of, e.g., Hartree-Fock calculations. In this context, Penn introduced the term 'pseudo-charge density', the charge density derived within the statistical approximation from the measured ELF [58].

Thus, it is of interest to see how the charge density obtained, in the statistical approximation, from the ELF of our simple model DF compares to the one obtained from a Hartree-Fock calculation. The fraction of the unit cell with a pseudo-charge density larger than n is given by:

$$\int_{\sqrt{4\pi n}}^\infty \frac{2}{\pi\omega} \text{Im}[-1/\epsilon(\omega, 0)] d\omega \quad (4.28)$$

In Fig. 4.13, top left panel shows the result of this integral. A very small volume (corresponding to the volume of the 1s shell) is filled with an electron gas with density larger than $30 \text{ e}^-/\text{\AA}^3$. About 5% of the volume is occupied by the n=2 shell and has charge densities of the order of $3 \text{ e}^-/\text{\AA}^3$. and in our model, most of the unit cell is filled with an electron gas with density of $\approx 0.2 \text{ e}^-/\text{\AA}^3$, corresponding to $\omega_p = 16 \text{ eV}$.

For a compound with more than one element, this is as far as one can go. For the elements, one can assume that the electron density is maximum right at the nucleus and decreases monotonically with r , the distance from the nucleus. If one also approximates the unit cell by a muffin-tin sphere with the same volume as the unit cell, then one can calculate the charge density as a function of r , as is done in the top-right panel. Again, one sees the extent of the K and L shell in this plot and the rather constant density of the free-electron gas formed by the valence electrons. The density obtained from our model is compared with a Hartree-Fock calculation within the muffin-tin sphere. Such a density is conveniently obtained from e.g. the ELSEPA, a program for elastic electron scattering cross sections, which gives this density within the muffin-tin sphere in one of the auxiliary output files [59]. There are clear differences and similarities between the actual and pseudo-charge densities. In particular, the pronounced K and L edges visible in the ELF cause abrupt increases in the pseudo-charge density, which is absent in the one obtained by Hartree-Fock calculations, where the density increases more smoothly when r decreases.

Within the statistical approximation, one can assign a mean free path, stopping power, and straggling value for a charged particle with energy E_0 as a function of r . This is done in the lower panels of Fig. 4.13 for 400 keV and 6 MeV protons. To speed up this calculation, the

Mermin DF is evaluated in the plasmon-pole approximation using an analytical formula for the IMFP, stopping and straggling, similar to the one derived in ref. [60].

At 400 keV protons (lower left panel), the stopping and straggling vanishes (and the IMFP is infinite) in the 1s region, as the associated plasmon energy is too high to be excited by 400 eV H^+ ions. The proton IMFP corresponding to the density of the L shell is small ($\approx 2 - 3 \text{ \AA}$), and the stopping and straggling are large. The small r (r again the distance from a nucleus) region is probed by ions that are significantly deflected by atoms. Indeed, in experiments using thin foils, excess inelastic energy loss is measured for deflected ions compared to those transmitted without significant deflection [61, 62]. Note that at 400 keV the diameter of the L shell ($\approx 1 \text{ \AA}$) is only a factor 3-4 smaller than the inelastic mean free path at the L electron density. Within the statistical model, there is thus a non-negligible probability that the projectile causes 2 excitations in a single L shell. This correlation in electron density (bunching) can contribute to the enhanced straggling seen for energies of 1 MeV or less [63, 64].

At 6 MeV (lower right panel) excitation of densities corresponding to the K shell are possible. The IMFP in the L region is now an order of magnitude larger than the L shell diameter, suggesting less influence of multiple collisions within the same shell on the obtained straggling value.

4.4.9 Consequences of the assumptions for dispersion and exchange

Often, the loss function has been measured in the optical limit and is used as the starting point for IMFP or stopping calculations. To obtain the IMFP and stopping, one has to integrate the loss function over the accessible part of $\omega - q$ space, and the outcome will thus depend on the q -dependence of the loss function. We will discuss this in detail now, considering the Al 2p contribution only. Chapidif let you fit any calculated ELF with a series (up to 250) of Mermin (or equivalently DL) oscillators. The fit of the ELF extends over the current energy range of the plot window. The energy of each oscillator is slightly larger than that of the previous oscillator, in such a way that the energy of the lowest and highest oscillator corresponds to the edges of the plot window. The Γ value is 1.2 times the oscillator separation. The amplitude is chosen such that the oscillator's number of electrons corresponds to the original ELF's contribution to the Bethe sum over its energy interval. The Al 2p as calculated from the GOS is shown in Fig. 4.14 (A). The ELF obtained after fitting the GOS with many oscillators is shown in Fig. 4.14 (B). The fitted spectrum has a somewhat smoothed edge, and a small ripple is present. In the limit of infinitely-many oscillators with vanishing small increments and Γ values, this procedure should give the same result as the analytical approach by Penn [58], but the difference in terms of the calculated IMFP between the Penn approach and the one described here with a finite number of oscillators is negligibly small.

One can calculate $\text{Im}[-1/\epsilon(\omega, q)]$ directly from the GOS or using the set of oscillators approximating the GOS. This is done in the lower panels of Fig. 4.14. The $\text{Im}[-1/\epsilon(\omega, q)]$ distributions are quite different (except near $q = 0$), see the color panels of Fig. 4.14 (C-E).

Rather than the IMFP, the cross-section for L shell excitation per Al atom was calculated, for electrons as a projectile. The cross-section per atom σ and IMFP λ are related by $\sigma = 1/(N_a \lambda)$. These cross sections are quite different at lower E_0 values. The calculations are compared to those obtained by Boteet *al.* [65] using a distorted-wave-Born calculation and a more realistic basis set. Our calculations based directly on the GOS from hydrogenic wave functions resemble the shape of the Boteet calculations best, but are 15% larger. Interpreting the oscillators as DL oscillators, one gets an onset of the spectrum at about twice the value of the distorted wave calculation. This is due to the upward dispersion (see right panels of Fig. 4.14). Interpreting the oscillators as Mermin oscillators then there is no sharp onset. This is because Mermin is a free-electron-type model, and then electron-hole pair creation is possible below the edge. Above $\approx 1.0 \text{ keV}$ the GOS, DL and Mermin-based calculation resemble each other closely.

Electrons are fermions, and hence, events when a secondary electron is created with energy

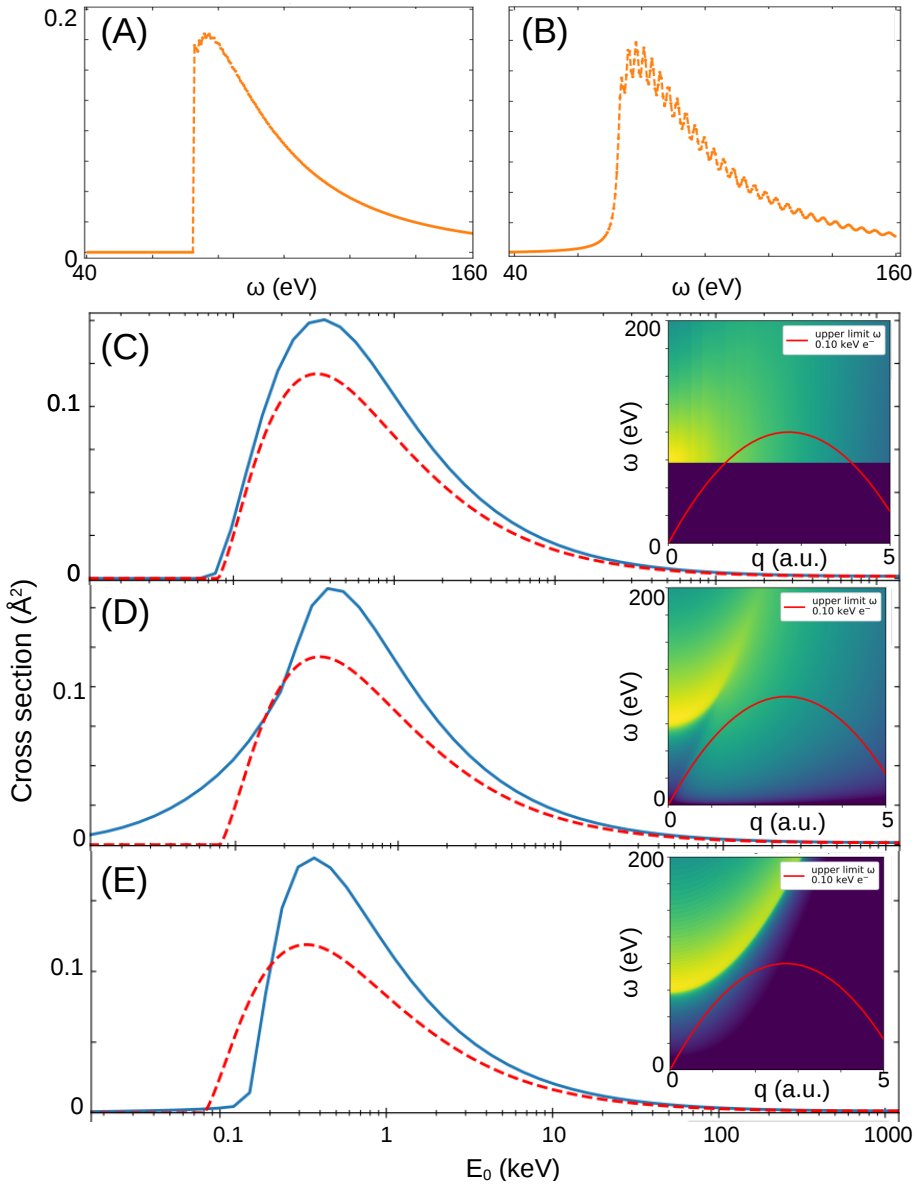


Figure 4.14: The influence of the assumed dispersion on the excitation cross section for the Al 2p level. (A) shows the ELF calculated from the Al 2p GOS. (B) is the description of this ELF based on many Mermin (or equivalently DL) oscillators. (C) shows the excitation cross-section for electrons as calculated from the GOS as a function of the electron beam energy E_0 . (D) is this cross-section based on the fit with DL oscillators. Finally, (E) the cross-section of these oscillators is interpreted as Mermin oscillators. The calculations were done without considering exchange (solid line) and by taking exchange into account (long dashed line) in an approximation outlined in the main text. In all 3 cases, the cross-section is compared with the one calculated by Bote et al [65]. The right panels show the corresponding $\log(\text{Im}[-1/\epsilon(\omega, q)])$ distributions with the red line the boundary of the accessible phase space for 100 eV electrons. These distributions are rather different, except near $q = 0$.

E_1 are indistinguishable from events where, after the collision, the incoming electron has energy $E' = E_0 - \omega = E_1$. Taking, by convention, the fast electron after the collision as the primary electron, then the maximum energy loss is $\omega_{\max} = 0.5(E_0 + U)$ with U the binding energy of the struck electron ($E_1 = \omega - U$). In Chapidif, one can consider these exchange effects using the approximate procedure introduced by Ashley [66]. The DIIMFP (including exchange) at energy loss ω is then given by:

$$W_b^{\text{exch}}(\omega) = W_b(\omega) + W_b(E_0 - \omega + U) - \sqrt{W_b(\omega)W_b(E_0 - \omega + U)} \quad (4.29)$$

where the 3rd term is a quantum effect. Taking exchange into account (using $U = 73$ eV, i.e., the Al2p binding energy), the agreement with the Bote calculation [65] improves. For the Mermin model, the cross-section with exchange correction has a peculiar shape. This can be understood as it is essentially a free-electron model, implying $U = 0$ rather than the value used. Within this model, part of the loss is due to plasmon creation (collective mode), which does not correspond to a secondary electron, and the theory has to be modified to incorporate this.

For the Al 1s level, there are experimental results, as the electron-beam induced 1s excitation cross section can be tracked based on the measured X-ray yield [67, 68]. Results are shown in Fig. 4.15, again with and without considering exchange effects. The shape obtained for the GOS-based calculation reproduces the experiment quite well, and incorporating the exchange effect improves the agreement. Describing the optical ELF, as calculated from the GOS by a set of DL or Mermin oscillators, deteriorates the agreement noticeably. The DL calculation was done with simple quadratic dispersion. Using full dispersion (quite different for an electron gas with densities such that ω_p is in the keV range) would shift the maximum to larger E_0 values, in line with the maximum position in the Mermin case.

Using protons as a projectile, very similar results are obtained by Chapidif for the Al 1s level when using the GOS-based DF as is obtained by using the ESCPSSR theory [69] as implemented in the ERCS08 code [70], not surprising as both are calculated from GOS-based hydrogenic wave functions, see Fig. 4.16.

4.4.10 Using tabulated oscillator strength as input

Optical oscillator strengths are often available from either experiment or calculations. One convenient source is the SBethe program from Salvat and co-workers [47] that for each run produces a text file with a .mat extension that contains the OOS of the target. This file (or any file that has the same structure as the .mat file from SBethe) can be read by Chapidif and is used to derive a set of Drude-Lindhard (or Mermin) oscillators that has approximately the same OOS. As is clear from Fig. 4.17 top panel, the description of the externally-defined OOS by the set of oscillators is very good, except for some smoothing near the core-level edges. Subsequently, this set of oscillators can be used for any Chapidif calculation. In the lower panel of Fig. 4.17 we calculate the ELF obtained from this set of oscillators and compare it to the ELF of our model 1, (table 4.1, with the core level occupation taken here from the ICRU publication). The plasmon peak of the model 1 ELF is sharper than the peak at low ω values of the OOS-derived ELF, as the latter was derived from atomic calculations.

4.4.11 Electron energy loss spectra

Finally, we want to discuss how electron energy loss spectra can be derived from a DF. Electron energy loss spectroscopy is, besides optical measurements, one of the main tools to obtain experimental information about the DF. Two types of excitations play a role: surface and bulk excitations. The other ingredient required for constructing a spectrum is the path-length distribution [71].

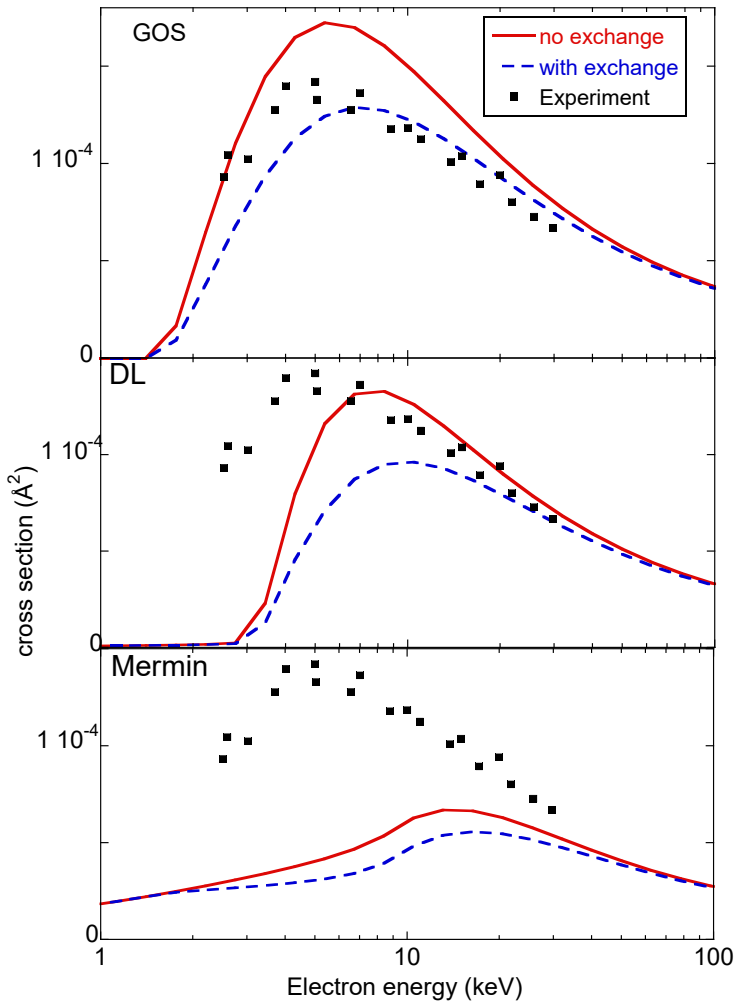


Figure 4.15: Cross sections obtained similarly as in Fig. 4.14, but now for the Al 1s level. The calculated results are compared to experimental values obtained in ref. [67, 68] (dots)

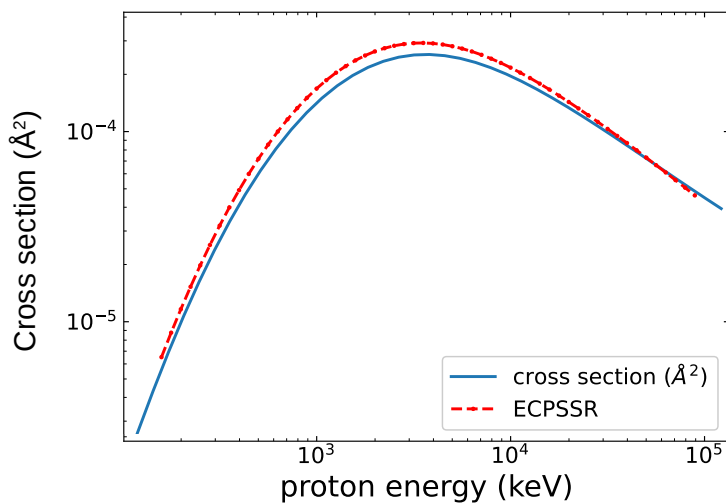


Figure 4.16: Cross section for proton-induced Al 1s excitation calculated using the 1s GOS component of the DF. It is compared to calculations based on the ECPSSR theory [69] as implemented in the ERCS08 code [70]. To make a detailed comparison possible, the ICRU recommended value for the occupation of 1.623 was used (see table 4.1, rather than the occupation of 2 used in our simple model).

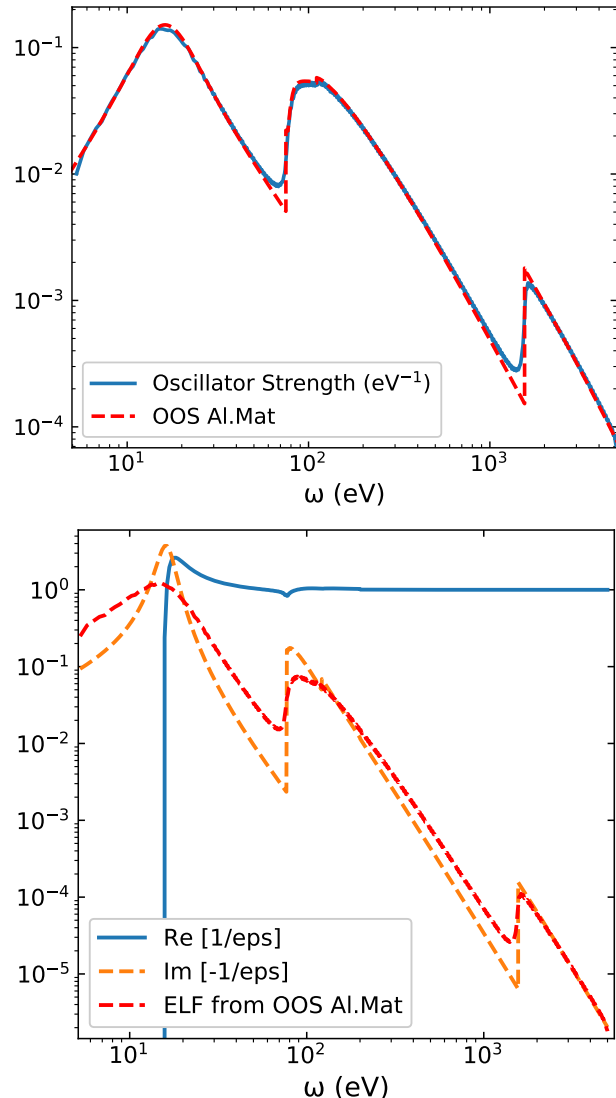


Figure 4.17: The top panel shows the OOS from aluminum as obtained from an output file of the SBethe program (dashed red line) compared to the one calculated from a set of oscillators designed to fit this OOS. The lower panel shows the ELF obtained from this set, compared to the ELF of our simple model dielectric function

Surface excitations can be calculated by Chapidif at the level of the approximate theory of Tung *et al* [10, 72]. Here, the surface plasmon intensity is calculated, assuming that all projectile electrons cross the surface layer completely. Some electrons may be backscattered before this is the case. The surface plasmon excitation probability calculated is thus an upper limit [72]. For more advanced approaches, see, e.g., ref. [73]. The surface energy loss (SELF) function given by $(\epsilon - 1)^2 / (\epsilon(\epsilon + 1))$, where the ω and q dependence was omitted for brevity.

The SELF is shown in Fig. 4.18. The top panel is for $q_{\parallel} = 0$ (the component of q directed along the surface plane), and the false color plot shows how it changes with q_{\parallel} . The SELF has a peak due to the surface plasmon excitation and is negative near the bulk plasmon energy. The latter indicates that the bulk plasmon excitation rate is reduced near the surface. Integrating over q_{\parallel} in the accessible $\omega - q_{\parallel}$ space following [10], one obtains the DSEP, i.e., the Differential Surface Excitation Probability. Integrating this over ω , using the approach by Tung *et al* the probability that any surface excitation occurs ($P_s(E_0, \theta)$) ≈ 0.05 for $E_0 = 5$ keV and $\theta = 0$ for our model DF of Al). The DSEP normalised to the unit area is indicated by w_s

Chapidif has a simple model implemented for the calculation of transmission EELS spectra. For a transmission experiment, it is assumed that elastic deflections have no dramatic influence on the path length traveled by the electrons. For perpendicular incidence the path length of all transmitted electrons is thus simple the film thickness t . A Poisson distribution then gives the probability that N bulk excitations occur:

$$P_N(t) = \left(\frac{t}{\lambda} \right)^N \frac{e^{-t/\lambda}}{N!} \quad (4.30)$$

The shape of the contribution to the spectrum of the trajectories with N collisions is then $w_b^{\otimes N}$: the $N - 1$ self-convolution of w_b , the normalised differential inelastic mean free path (a large opening angle of the detector is assumed here, i.e., deflections due to inelastic excitations do not deflect the electrons outside the detector). The transmission EELS spectrum, without considering surface excitations, is then proportional to:

$$I_b = \sum_N P_N w_b^{\otimes N}. \quad (4.31)$$

Here, both w_b and λ are calculated from the same DF.

Including surface excitation, one obtains the final spectrum I_f :

$$I_f = (1 - 2P_s)I_b + 2P_s I_b \otimes w_s \quad (4.32)$$

where \otimes indicates a convolution. The factor of 2 is because surface excitations can occur at the entrance and exit surface, and the probability that 2 surface plasmons are created is neglected. In Fig. 4.19 the calculated transmission EELS spectrum is compared with the pioneering measurement of an Al film by Ruthemann [74] assuming a thickness of 350 Å. There is a qualitative agreement. Changing the film thickness in the calculation changes its shape but does not lead to improved agreement with the experiment. One possible explanation here is the presence of inhomogeneities in the film thickness.

In reflection electron energy loss spectroscopy (REELS), using thick samples, trajectories of any length can occur. First, consider the case where any trajectory length is equally likely. For trajectory length x the contribution of partial intensity N is $P_N(x)$ and given by eq. 4.30 with $t = x$. The total contribution A_N of partial intensity N to the spectrum is then $A_N = \int_0^\infty P_N(x)dx = \lambda$ for any N . Thus, when any trajectory length is equally likely, all partial intensities contribute equally. With increasing N , $P_N(x)$ will peak at larger x values (and $w_b^{\otimes N}$ at larger ω values). The total REELS spectrum I_b (neglecting surface effects) is then proportional to:

$$I_b = \sum_N w_b^{\otimes N}. \quad (4.33)$$

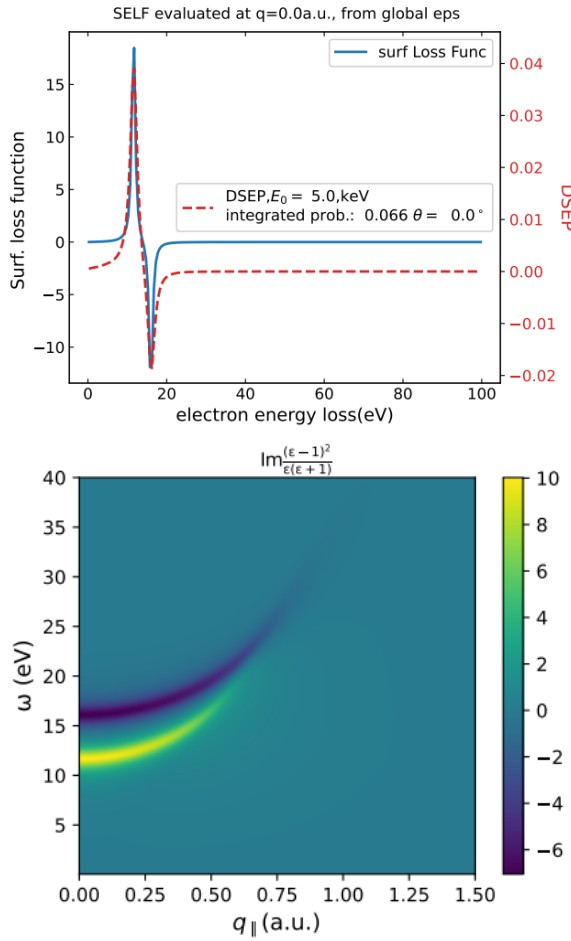


Figure 4.18: Surface loss function for our model DF at $q = 0$ (upper panel), and as a false color plot for the $\omega - q_{\perp}$ plane (lower panel). Integrating over the allowed q_{\parallel} values gives the differential surface excitation probability (DSEP), shown in the top panel for $E_0 = 5$ keV and normal incidence. Integrating this DSEP over all energies, one obtains a value of 0.067 for the surface excitation probability.

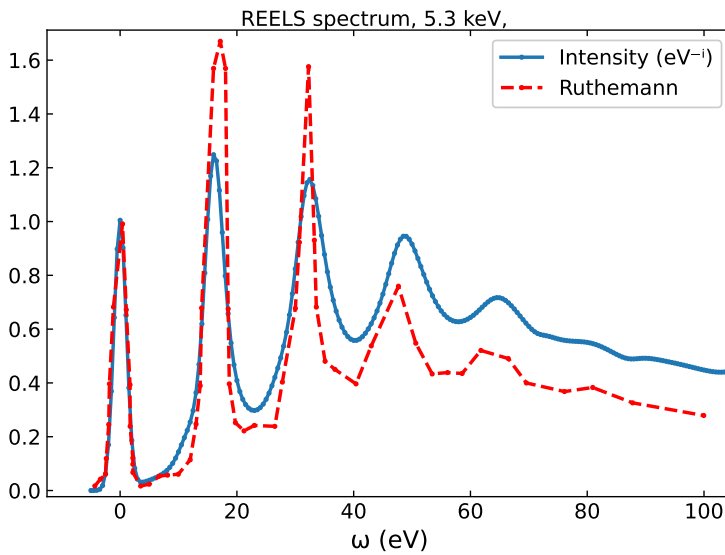


Figure 4.19: The original transmission EELS spectrum of Ruthemann [74] simulated using a thickness of 330 Å

Making the simplifying assumption that the incoming and outgoing surface crossings are two independent events one obtains for the probability of a surface plasmon creation: $P_s^{\text{tot}} = P_s(\theta_{\text{in}}, E_0) + P_s(\theta_{\text{out}}, E_0)$

$$I_b = (1 - P_s^{\text{tot}}) \sum_N w_b^{\otimes N} + P_s^{\text{tot}} I_b \otimes w_s \quad (4.34)$$

In addition, the experimental result will be affected by broadening due to e.g. finite energy resolution. Often, Monte Carlo simulations show that the approximation that all path lengths are equally probable is poor, and then the partial intensities PI_i will differ. Then in Chapidif one can model the contribution of PI_i as a simple polynomial of i , but in this case $PI_i = 1$ for all i worked quite well.

In Fig. 4.20, top left panel, we show the result of the REELS calculation (broadened by the energy resolution matching the width of the elastic peak). The surface plasmon is quite clearly visible near $\omega = 10$. The surface plasmon excitation probability is overestimated by the theory [72], and was reduced, rather arbitrarily here, by a factor of 2 to get reasonable agreement for this feature with the experiment. However, our simple model fails to predict the right energy loss for the position of the plasmon peaks. Clearly (and not surprisingly) $\omega_p = 16$ eV for the plasmon peak is too large.

Now, if one just changes ω_p to e.g. 15 eV, then the number of valence electrons this oscillator represents is too small. Correcting this by changing its amplitude C_1 is not possible without resulting in deviations of the sum rules. The only way around this is by describing the valence band of Al by more than one oscillator.

For aluminum, high-quality results are available for the refraction (n) and extinction (k) coefficients based on optical measurements, as published by Rakić [75]. The n and k values obtained from our simple model are compared to the k values of Rakić in the top right panel of Fig. 4.20. The main features in k are (from left to right) due to the K edge, the L edge, and the plasmon, respectively. The main disagreement between our simple model and the optical data for k is in between the L edge and the plasmon feature. Hence, two additional oscillators were added to our model (Model II in table 4.1) in such a way that $\sum_i C_i$ remains 0.95 and the total number of valence electrons remains 3 per unit cell. The position and width was chosen in such a way that the extinction results resemble that of Rakić as much as possible (lower right panel of Fig. 4.14).

Indeed, the k values between the L edge and the plasmon for the new model are much closer to those of Rakić. Also, the calculated REELS spectrum based on model II agrees better with the measurement. Note that the L edge is not resolved in either the experiment or the simulation. This does not mean that the 2p electrons have no influence on the REELS spectrum. Without the inclusion of the GOS, the plasmon excitation is visible in the calculated spectrum up to larger ω values as, due to the large width of the GOS contribution, for trajectories that include Al 2p excitation, the plasmon structures are not resolved anymore [76].

4.5 Some Numerical Details

All oscillators are required to have non-zero width. For meaningful plots of ω -dependent quantities, the step size in the energy plots should be significantly smaller than the sharpest feature of the loss function (step size of plot $<< \Gamma$). Sum rules and Kramers-Kronig transformation are evaluated on a grid nine times smaller than the energy step size of the plot. In the Kramers-Kronig transformation, the principal Cauchy value is obtained by performing a symmetric summation around the pole. This approach is effective as long as the loss dielectric function remains relatively constant over the chosen step size. In practice, the error in the Kramers-Kronig transformation can be made arbitrarily small by decreasing the step size.

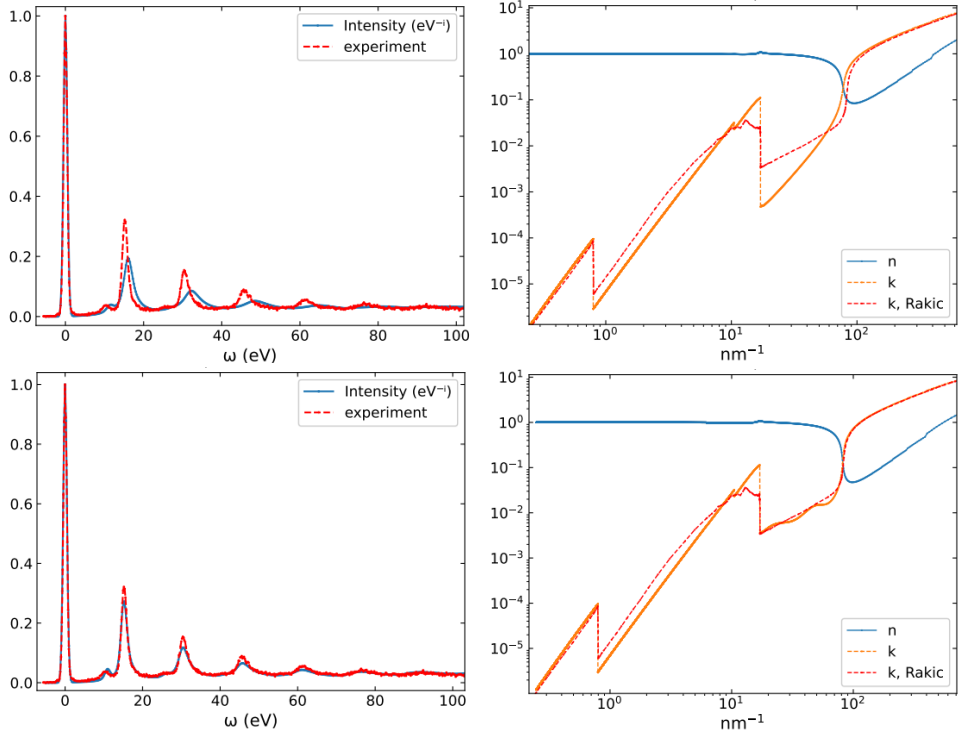


Figure 4.20: 40 keV REELS data of Al simulated with the simple DF (top left) and a DF describing the valence band using 3 components. (bottom left). The position of the 2 new components was chosen such that the agreement of the calculated extinction coefficient k and those published by Rakic [75] improves.(left panels)

Calculation of the DIIMFP at a specific E_0 requires integration over q , and contributions at very small q becomes significant for large E_0 values. Thus, integration is performed from the calculated values for q_- and q_+ in eq. 4.17, but is *not* affected by the momentum stepsize in the momentum plots. For this integration, the QUANC8 algorithm is used [77].

For the calculation of the IMFP, stopping and straggling an additional integration of the DIIMFP over ω is required. The DIIMFP extends up to E_0 . For the smallest energy loss the step size in ω in the integration is taken to be that of the energy plots. As the E_0 can be many orders of magnitude larger than this initial step size, it is for efficiency reasons necessary to increase the step size gradually. This is done by an amount $F\omega$ with F varying from 0.08 for a ‘rough’ calculation to 0.005 for a ‘precise’ calculation (precision of calculation can be selected in the user interface).

At $q = 0$ there are complications for the Lindhard and Mermin DF. It is calculate in terms of reduced variables u and v which are proportional to $1/q$. Hence the algorithm is not stable for $q \rightarrow 0$. However, in the small q limit, the quantum-based Mermin (or Lindhard) DF approaches the classical Drude-Lindhard DF. If $q\omega < 0.0001$, then the Drude-Lindhard DF is used instead.

4.6 Conclusion and Outlook

Frequency- and momentum-dependent dielectric functions can be used to describe a wide range of phenomena. In most research, one focuses on one such phenomenon and aims to obtain a DF that describes that phenomenon well. Chapidif is a program that should make studying the implications of adopting a DF for various phenomena easier. It is demonstrated here for a very simple target (a free electron metal with few shells), and for more complicated systems, our understanding is more limited, and tests of the DF are thus even more desirable. When a larger range of phenomena can be described well with a model DF, then the level of confidence that,

indeed, it approaches the actual DF increases. The program aims to aid such research.

4.7 Acknowledgement

We want to thank Dr. Flávio Matias for testing some aspects of the program. This study was financed in part by the Coordenação de Aperfeiçoamento de Pessoal de Nível Superior - Brazil (CAPES) - Finance Code 001, by FINEP, by Conselho Nacional de Desenvolvimento Científico e Tecnológico (CNPq) process number 403722/2023-3, and by Instituto Nacional de Engenharia de Superfícies (INES) project number 465423/2014-0.

Bibliography

- [1] H. Bethe, Zur Theorie des Durchgangs schneller Korpuskularstrahlen durch Materie, *Ann. Phys.* 397 (3) (1930) 325–400. doi:10.1002/andp.19303970303.
URL <http://dx.doi.org/10.1002/andp.19303970303>
- [2] J. Lindhard, On the properties of a gas of charged particles, *K. Dan. Vidensk. Selsk. Mat.-Fys. Medd.* 28 (8) (1954) 1–57.
- [3] N. Mermin, Lindhard dielectric function in the relaxation-time approximation, *Phys. Rev. B* 1 (1970) 2362 –2363. doi:10.1103/physrevb.1.2362.
- [4] Z. Levine, S. Louie, New model dielectric function and exchange-correlation potential for semiconductors and insulators, *Phys. Rev. B* 25 (1982) 6310. doi:10.1103/physrevb.25.6310.
- [5] T. Kaneko, Wave-packet theory of stopping of bound electrons, *Phys. Rev. A* 40 (1989) 2188. doi:10.1103/physreva.40.2188.
- [6] T. Kaneko, Partial and total electronic stoppings of solids and atoms for energetic ions, *Physica Status Solidi (b)* 156 (1) (1989) 49–63. doi:10.1002/pssb.2221560104.
- [7] T. Kaneko, Partial and total electronic stopping cross sections of atoms and solids for protons, *At. Data Nucl. Data Tables* 53 (2) (1993) 271–340. doi:10.1006/adnd.1993.1007.
- [8] A. Belkacem, P. Sigmund, Stopping power and energy loss spectrum of a dense medium of bound electrons, *Nucl. Instrum. Methods Phys. Res., Sect. B* 48 (1-4) (1990) 29–33. doi:10.1016/0168-583X(90)90066-4.
- [9] R. H. Ritchie, A. Howie, Electron excitation and the optical potential in electron microscopy, *Philos. Mag.* 36 (1977) 463. doi:10.1080/14786437708244948.
- [10] C. Tung, Y. Chen, C. Kwei, T. Chou, Differential cross sections for plasmon excitations and reflected electron-energy-loss spectra, *Phys. Rev. B* 49 (1994) 16684–16693. doi:10.1103/PhysRevB.49.16684.
- [11] M. Vos, P. Grande, Model dielectric functions for ion stopping: The relation between their shell corrections, plasmon dispersion and Compton profiles, in: *Advances in Quantum Chemistry*, Elsevier, 2022, pp. 267 –301. doi:10.1016/bs.aiq.2022.07.001.
- [12] B. I. Lundqvist, Single-particle spectrum of the degenerate electron gas, *Physik der Kondensierten Materie* 6 (3) (1967) 206. doi:10.1007/bf02422717.
- [13] W. Werner, K. Glantschnig, C. Ambrosch-Draxl, Optical constants and inelastic electron-scattering data for 17 elemental metals, *J. Phys. Chem. Ref. Data* 38 (2009) 1013–1092. doi:10.1063/1.3243762.

- [14] S. Hajati, O. Romanyuk, J. Zemek, S. Tougaard, Validity of Yubero-Tougaard theory to quantitatively determine the dielectric properties of surface nanofilms, *Phys. Rev. B* 77 (2008) 155403. doi:10.1103/physrevb.77.155403.
- [15] F. Wooten, *Optical Properties of Solids*, Academic Press, 1972.
- [16] M. Vos, P. Grande, Simple model dielectric functions for insulators, *J. Phys. Chem. Solids* 104 (2017) 192. doi:10.1016/j.jpcs.2016.12.015.
- [17] D. Pines, *Elementary excitations in solids*, Benjamin, New York, 1963.
- [18] P. Sigmund, *Particle Penetration and Radiation Effects*, Vol. 151 of Springer Series in Solid-State Sciences, Springer, Berlin, 2006.
- [19] M. Vos, P. Grande, Random phase approximation dielectric functions: Streamlined approach to relaxation effects, binding and high momentum dispersion, *J. Phys. Chem. Solids* 198 (2024) 112470.
- [20] M. Altarelli, D. Y. Smith, Superconvergence and sum rules for the optical constants: Physical meaning, comparison with experiment, and generalization, *Phys. Rev. B* 9 (1974) 1290–1298. doi:10.1103/physrevb.9.1290.
- [21] P. Sigmund, P. Deluca, A. Wambersie, Stopping of ions heavier than helium, *Journal of the International Commission on Radiation Units and Measurements* 5 (1) (2005) 0–0. doi:10.1093/jicru/ndi001.
- [22] R. F. Egerton, *Electron energy-loss spectroscopy in the electron microscope*, third edition Edition, Plenum Press, New York, 2011. doi:10.1007/978-1-4419-9583-4.
- [23] S. Heredia-Avalos, R. Garcia-Molina, J. M. Fernández-Varea, I. Abril, Calculated energy loss of swift He, Li, B, and N ions in SiO₂, Al₂O₃, and ZrO₂, *Phys. Rev. A* 72 (2005) 052902. doi:10.1103/physreva.72.052902.
- [24] M. Vos, P. L. Grande, Modeling the contribution of semi-core electrons to the dielectric function, *J. Phys. Chem. Solids* 124 (2019) 242. doi:10.1016/j.jpcs.2018.09.020.
- [25] P. de Vera, I. Abril, R. Garcia-Molina, Electronic cross section, stopping power and energy-loss straggling of metals for swift protons, alpha particles and electrons, *Front. Mater.* 10. doi:10.3389/fmats.2023.1249517.
- [26] A. A. Shukri, M. Al Shorman, Highly accurate ab initio electronic stopping power results for protons in al material: a lindhard stopping theory investigation, *Phys. Scr.* 99 (2024) 075966. doi:10.1088/1402-4896/ad55bf.
- [27] W. Schülke, H. Nagasawa, S. Mourikis, Dynamic structure factor of electrons in Li by inelastic synchrotron x-ray scattering, *Phys. Rev. Lett.* 52 (1984) 2065. doi:10.1103/physrevlett.52.2065.
- [28] W. Schülke, H. Schulte-Schrepping, J. R. Schmitz, Dynamic structure of electrons in Al metal studied by inelastic x-ray scattering, *Phys. Rev. B* 47 (19) (1993) 1242. doi:10.1103/physrevb.47.12426.
- [29] K. Sturm, W. Schülke, J. R. Schmitz, Plasmon-Fano resonance inside the particle-hole excitation spectrum of simple metals and semiconductors, *Phys. Rev. Lett.* 68 (1992) 228–231.
- [30] S. Manninen, T. Paakkari, V. Halonen, Experimental Compton profile of water, *Chem. Phys. Lett.* 46 (1977) 62. doi:10.1016/0009-2614(77)85163-4.

- [31] M. J. Cooper, P. E. Mijnarends, N. Shiotani, N. Sakai, A. Bansil, X-Ray Compton Scattering, Oxford University Press, 2004.
- [32] W. Schülke, Electronic excitations investigated by inelastic x-ray scattering spectroscopy, *J. Phys.: Condens. Matter* 13 (2001) 7557. doi:[10.1088/0953-8984/13/34/307](https://doi.org/10.1088/0953-8984/13/34/307).
- [33] H. Nikjoo, S. Uehara, D. Emfietzoglou, Interaction of radiation with matter, CRC press, 2012.
- [34] H. Shinotsuka, S. Tanuma, C. J. Powell, D. R. Penn, Calculations of electron inelastic mean free paths. X. Data for 41 elemental solids over the 50 eV to 200 keV range with the relativistic full Penn algorithm, *Surf. Interface Anal.* 47 (2015) 871. doi:[10.1002/sia.5789](https://doi.org/10.1002/sia.5789).
- [35] P. E. Batson, J. Silcox, Experimental energy-loss function, $Im[-\frac{1}{\epsilon}(\omega, q)]$, for aluminum, *Phys. Rev. B* 27 (1983) 5224–5239. doi:[10.1103/PhysRevB.27.5224](https://doi.org/10.1103/PhysRevB.27.5224).
- [36] W. H. Schulte, B. W. Busch, E. Garfunkel, T. Gustafsson, G. Schiwietz, P. L. Grande, Limitations to depth resolution in ion scattering experiments, *Nucl. Instr. and Meth. B* 183 (2001) 16–24.
- [37] J. M. Fernández-Varea, F. Salvat, M. Dingfelder, D. Liljequist, A relativistic optical-data model for inelastic scattering of electrons and positrons in condensed matter, *Nucl. Instrum. Methods Phys. Res., Sect. B* 229 (2005) 187. doi:[10.1016/j.nimb.2004.12.002](https://doi.org/10.1016/j.nimb.2004.12.002).
- [38] F. Bell, H. Bockl, M. Z. Wu, H. D. Betz, On the measurement of solid-state Compton profiles from secondary electrons induced in fast-ion-atom collisions, *J. Phys. B: At. Mol. Phys.* 16 (1983) 187. doi:[10.1088/0022-3700/16/2/008](https://doi.org/10.1088/0022-3700/16/2/008).
- [39] E. Kröger, Berechnung der Energieverluste schneller Elektronen in dünnen Schichten mit Retardierung, *Zeitschrift für Physik* 216 (1968) 115–135. doi:[10.1007/bf01390952](https://doi.org/10.1007/bf01390952).
- [40] C. Von Festenberg, E. Kröger, Retardation effects for the electron energy loss probability in GaP and Si, *Phys. Lett. A* 26 (1968) 339–340. doi:[10.1016/0375-9601\(68\)90360-5](https://doi.org/10.1016/0375-9601(68)90360-5).
- [41] G. Schiwietz, P. L. Grande, C. Auth, H. Winter, A. Salin, Angular dependence of energy loss in proton-helium collisions, *Phys. Rev. Lett.* 72 (1994) 2159–2162. doi:[10.1103/physrevlett.72.2159](https://doi.org/10.1103/physrevlett.72.2159).
- [42] H. Böckl, F. Bell, Compton profiles by inelastic ion-electron scattering, *Phys. Rev. A* 28 (1983) 3207. doi:[10.1103/physreva.28.3207](https://doi.org/10.1103/physreva.28.3207).
- [43] H. Shinotsuka, B. Da, S. Tanuma, H. Yoshikawa, C. J. Powell, D. R. Penn, Calculations of electron inelastic mean free paths. XI. data for liquid water for energies from 50 eV to 30 keV, *Surf. Interface Anal.* 49 (2016) 238. doi:[10.1002/sia.6123](https://doi.org/10.1002/sia.6123).
- [44] J. Ziegler, M. Ziegler, J. Biersack, SRIM – the stopping and range of ions in matter (2010), *Nucl. Instrum. Methods Phys. Res., Sect. B* 268 (11-12) (2010) 1818–1823. doi:[10.1016/j.nimb.2010.02.091](https://doi.org/10.1016/j.nimb.2010.02.091).
- [45] P. L. Grande, G. Schiwietz, Nonperturbative stopping-power calculation for bare and neutral hydrogen incident on He, *Phys. Rev. A* 47 (1993) 1119–1122. doi:[10.1103/PhysRevA.47.1119](https://doi.org/10.1103/PhysRevA.47.1119).
- [46] N. R. Arista, Energy loss of ions in solids: Non-linear calculations for slow and swift ions, *Nucl. Instr. and Meth.B* 195 (2002) 91–105. doi:[10.1016/S0168-583X\(02\)00687-0](https://doi.org/10.1016/S0168-583X(02)00687-0).

- [47] F. Salvat, P. Andreo, Sbethe: Stopping powers of materials for swift charged particles from the corrected Bethe formula, *Comput. Phys. Commun.* 287. doi:10.1016/j.cpc.2023.108697.
- [48] S. Tanuma, C. J. Powel, D. R. Penn, Calculation of electron inelastic mean free paths, *Surf. Interface Anal.* 20 (1993) 77–89. doi:10.1002/sia.740200112.
- [49] J. Jackson, *Classical Electrodynamics*, John Wiley & Sons, 1975.
- [50] P. Sigmund, *Stopping of Heavy Ions - A Theoretical Approach*, 1st Edition, Springer, Springer Berlin Heidelberg New York, 2004.
- [51] U. Fano, Penetration of protons, alpha particles, and mesons, *Annu. Rev. Nucl. Sci.* 13 (1) (1963) 1. doi:10.1146/annurev.ns.13.120163.000245.
- [52] F. Salvat, Bethe stopping-power formula and its corrections, *Phys. Rev. A* 106. doi:10.1103/physreva.106.032809.
- [53] W. McKinley, H. Feshbach, The Coulomb scattering of relativistic electrons by nuclei, *Phys. Rev.* 74 (1948) 1759–1763. doi:10.1103/physrev.74.1759.
- [54] F. Salvat, A. Jablonski, C. J. Powell, ELSEPA Dirac partial-wave calculation of elastic scattering of electrons and positrons by atoms, positive ions and molecules, *Comput. Phys. Commun.* 165 (2005) 157–190. doi:10.1016/j.cpc.2004.09.006.
- [55] J. Lindhard, M. Scharff, Energy loss in matter by fast particles of low charge, *Mat Fys Medd Dan Vid Selsk* 27 (1953) 15.
- [56] C. Tung, J. Ashley, R. Ritchie, Electron inelastic mean free paths and energy losses in solids ii: Electron gas statistical model, *Surf. Sci.* 81 (2) (1979) 427. doi:10.1016/0039-6028(79)90110-9.
- [57] E. Palik, *Handbook of Optical Constants of Solids II*, Academic Press: New York, 1991.
- [58] D. Penn, Electron mean-free-path calculations using a model dielectric function, *Phys. Rev. B* 35 (1987) 482. doi:10.1103/PhysRevB.35.482.
- [59] F. Salvat, Optical-Model Potential for Electron and Positron Elastic Scattering by Atoms, *Phys. Rev. A* 68 (2003) 012708. doi:10.1103/PhysRevA.68.012708.
- [60] H. T. Nguyen-Truong, Analytical formula for high-energy electron inelastic mean free path, *The Journal of Physical Chemistry C* 119 (41) (2015) 23627–23631. doi:10.1021/acs.jpcc.5b09048.
- [61] M. M. Jakas, G. H. Lantschner, J. C. Eckardt, V. H. Ponce, Study on the angular dependence of the average energy loss for ions in solids, *Phys. Rev. A* 29 (1984) 1838–1843. doi:10.1103/physreva.29.1838.
- [62] G. H. Lantschner, J. C. Eckardt, M. M. Jakas, N. E. Capuj, H. Ascolani, Variation of peak energy for energy loss with angle of observation, *Phys. Rev. A* 36 (1987) 4667–4671. doi:10.1103/physreva.36.4667.
- [63] Q. Yang, D. O'Connor, Z. Wang, Empirical formulae for energy loss straggling of ions in matter, *Nucl. Instrum. Methods Phys. Res., Sect. B* 61 (1991) 149. doi:10.1016/0168-583x(91)95454-1.

- [64] F. Selau, H. Trombini, R. Fadanelli, M. Vos, P. Grande, On the energy-loss straggling of protons in elemental solids: The importance of electron bunching, *Nucl. Instrum. Methods Phys. Res., Sect. B* 497 (2021) 70. doi:10.1016/j.nimb.2021.03.006.
- [65] D. Bote, F. Salvat, A. Jablonski, C. J. Powell, Cross sections for ionization of K, L and M shells of atoms by impact of electrons and positrons with energies up to 1 GeV: Analytical formulas, *At. Data Nucl. Data Tables* 95 (2009) 871. doi:10.1016/j.adt.2009.08.001.
- [66] J. Ashley, Interaction of low-energy electrons with condensed matter: stopping powers and inelastic mean free paths from optical data, *J. Electron Spectrosc. Relat. Phenom.* 46 (1988) 199. doi:10.1016/0368-2048(88)80019-7.
- [67] W. Hink, A. Ziegler, Der Wirkungsquerschnitt für die Ionisierung der K-Schale von Aluminium durch Elektronenstoß (3–30 keV), *Zeitschrift für Physik A Hadrons and nuclei* 226 (1969) 222. doi:10.1007/bf01392087.
- [68] S. P. Limandri, M. A. Z. Vasconcellos, R. Hinrichs, J. C. Trincavelli, Experimental determination of cross sections for K-shell ionization by electron impact for C, O, Al, Si, and Ti, *Phys. Rev. A* 86. doi:10.1103/physreva.86.042701.
- [69] W. Brandt, G. Lapicki, Energy-loss effect in inner-shell Coulomb ionization by heavy charged particles, *Phys. Rev. A* 23 (1981) 1717. doi:10.1103/physreva.23.1717.
- [70] V. Horvat, Ercs08: A fortran program equipped with a windows graphics user interface that calculates ecpssr cross sections for the removal of atomic electrons, *Comput. Phys. Commun.* 180 (2009) 995. doi:10.1016/j.cpc.2008.12.034.
- [71] W. S. M. Werner, Electron transport in solids for quantitative surface analysis, *Surf. Interface Anal.* 31 (2001) 141. doi:10.1002/sia.973.
- [72] N. Pauly, M. Novák, A. Dubus, S. Tougaard, Comparison between surface excitation parameter obtained from QUEELS and SESINIPAC, *Surf. Interface Anal.* 44 (2012) 1147–1150. doi:10.1002/sia.4829.
- [73] F. Yubero, S. Tougaard, Model for quantitative analysis of reflection-electron-energy-loss spectra, *Phys. Rev. B* 46 (1992) 2486–2497. doi:10.1103/PhysRevB.46.2486.
- [74] G. Ruthemann, Diskrete Energieverluste schneller Elektronen in Festkörpern, *Die Naturwissenschaften* 29 (1941) 648. doi:10.1007/bf01485870.
- [75] A. D. Rakić, Algorithm for the determination of intrinsic optical constants of metal films: application to aluminum, *Appl. Opt.* 34 (1995) 4755. doi:10.1364/ao.34.004755.
- [76] M. Vos, P. Grande, G. Marmitt, The influence of shallow core levels on the shape of REELS spectra, *J. Electron Spectrosc. Relat. Phenom.* 229 (2018) 42 – 46. doi:10.1016/j.elspec.2018.09.006.
URL <https://doi.org/10.1016/j.elspec.2018.09.006>
- [77] G. E. Forsythe, Computer methods for mathematical computations, Prentice-Hall, 1977.

4.A Appendix: Installation

Installation of the program requires Python3, several widely-used extensions (matplotlib,tkinter, numpy) and a c compiler. After unpacking the zip file there will be a subdirectory ‘clib-source’ containing the c++ files. Several batchfiles are provided facilitating compilation of the code for Windows, Mac or Linux. After compilation invoke ‘Chapidif.py’ as one executes any python file.

The user interface consists of 3 panels. The first panel is used to define the dielectric function. The second panel let the user choose which property to calculate, over which range etc. The third panel allows for the change of certain defaults. The download also contains a file ‘chapidif_manual_plus_background.pdf’, which, in addition to this paper, also contains a button-by-button description of the interface.

4.B Appendix: Relativistic Kinematics

At large q the DF should resemble the collision with a free electron. This means that the loss function at large q should be centered around $Q_{\text{recoil}} = q^2/2$ (the ‘Bethe ridge’). This is a non-relativistic approach. If q is not small compared to the speed of light ($C \approx 137.036$ in a.u.), relativistic effects can not be neglected. For the DL DF the dispersion is usually given by: $\omega(q) = \omega(0) + q^2/2 = \omega(0) + Q_{\text{recoil}}$. Proper behaviour at large q is accomplished by using $Q_{\text{recoil}} = \sqrt{C^2 q^2 + C^4 - C^2}$.

For the GOS the theory is developed in terms of Q_{recoil} [23], and a relativistic consistent behaviour is thus again accomplished by replacing $Q_{\text{recoil}} = q^2/2$ by $Q_{\text{recoil}} = \sqrt{C^2 q^2 + C^4 - C^2}$.

For the Lindhard (and thus also Mermin) DF the theory is developed in terms of reduced variables: $u = \frac{\omega}{qv_f}$ and $z = \frac{q}{2k_f}$. For the valence band the electron densities are non-relativistic and hence (in a.u.) $k_f \approx v_f$. Then one has:

$$\frac{u}{z} = \frac{\omega}{q^2/2} \quad (4B.1)$$

where the denominator is the non-relativistic recoil energy. For the diagonal in the $u - z$ plane, one has $u/z = 1$, and this corresponds thus to the (non-relativistic) Bethe ridge ($\omega = q^2/2$). In order for the diagonal to coincide with the Bethe ridge also at relativistic energies, some change in the definition of u and/or z is required. If one replaces u by u' such that :

$$\frac{u'}{z} = \frac{\omega}{Q_{\text{recoil}}} = \frac{\omega}{\sqrt{C^2 q^2 + C^4 - C^2}} \quad (4B.2)$$

then $u'/z = 1$ corresponds to the Bethe ridge. Hence, one replaces u in the Mermin DF with the new reduced variable u' :

$$u' = \frac{\omega}{\sqrt{C^2 q^2 + C^4 - C^2}} \frac{q}{2k_f}. \quad (4B.3)$$

alternatively one could leave the definition of u the same and introduce z' :

$$z' = \frac{\sqrt{C^2 q^2 + C^4 - C^2}}{qv_f} \quad (4B.4)$$

Unfortunately, although both approaches result in the ‘correct’ dispersion, these substitutions affect the sum rules (eq. 4.7,4.8,4.10). Using eq. 4B.2 the sum rules are too small, using eq. 4B.4 the sum rules are too large. So, neither solution is acceptable and one has to change both u and z .

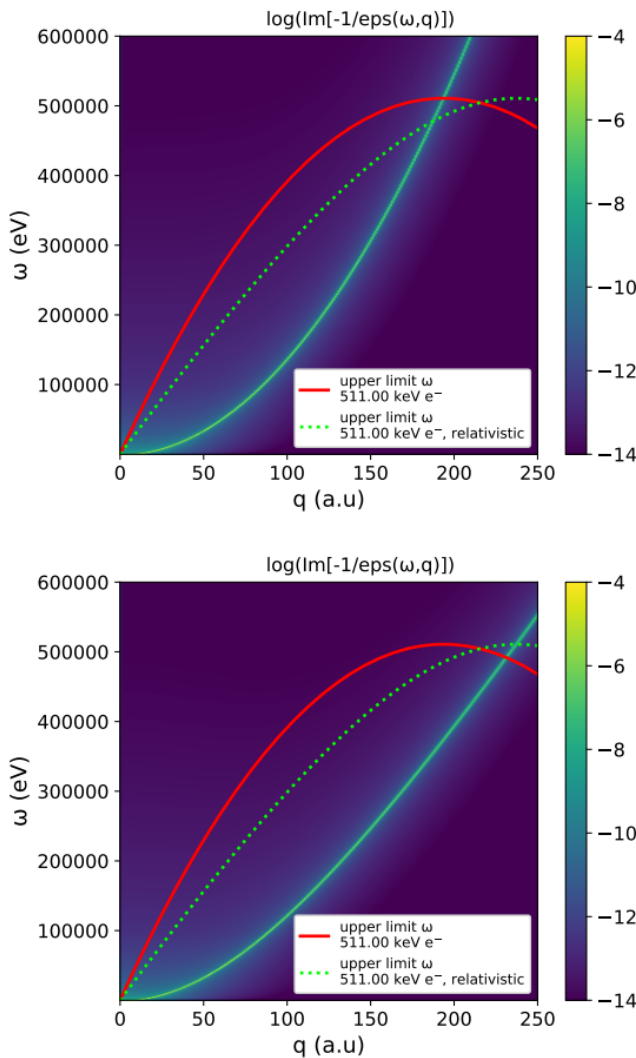


Figure 4B.1: Intensity distribution of the (log of the) loss function of a single Mermin DF with $\omega_p = 16$ eV. The top panel shows the distribution assuming a non-relativistic approach, whereas the lower panel uses the relativistic approach sketched here. Also shown are the limit of integration of the DIIMFP for 511 keV electrons ($q_- = |p_0| - |p_1|$, $q_+ = |p_0| + |p_1|$), assuming $|p_0|$ and $|p_1|$ are obtained using non-relativistic kinematics (full line), or using relativistic kinematics (dashed line).

One can try something more symmetric:

$$\frac{u'}{z'} = \frac{\omega}{Q_{\text{recoil}}} = \frac{\omega}{\sqrt{Q_{\text{recoil}}}\sqrt{Q_{\text{recoil}}}} \quad (4B.5)$$

and then one replaces q in the definition of u and z by $\sqrt{2Q_{\text{recoil}}}$. This obviously leaves the definitions of u and z unchanged for non-relativistic energies. Thus:

$$u' = \frac{\omega}{\sqrt{2Q_{\text{recoil}}}v_f} = \frac{\omega}{\sqrt{2}\sqrt{Q_{\text{recoil}}}v_f} \quad (4B.6)$$

and simultaneously:

$$z' = \frac{\sqrt{2Q_{\text{recoil}}}}{2k_f} = \frac{\sqrt{Q_{\text{recoil}}}}{\sqrt{2}k_f} \quad (4B.7)$$

It is easy to check that $u'/z' = 1$ indeed corresponds to $\omega = Q_{\text{recoil}}$. This indeed gives thus the correct dispersion *and also* the correct sum rules.

Note that this is *not* a solution of the relativistic RPA, but just an ad hoc change to ensure the proper dispersion for a Mermin DF describing an electron gas with a non-relativistic density. Numerically, one just takes $u' = u$ and $z' = z$ for small q (in Chapidif for $q < 3$ a.u.) as the relativistic expression for the recoil energy is not numerically stable when $q \rightarrow 0$. The effects of replacing u by u' and z by z' in the formula for Mermin DF are evident in Fig. 4B.1 and mirrors the changes observed for the DL DF if one replaces the non-relativistic Q values with the relativistic ones.

Chapter 5

Extensions of Kaneko's wave-packet model for non-zero angular momentum orbitals

5.1 abstract

A wavefunction-derived theory of stopping of bound electrons was proposed by Kaneko [1, 2, 3] and extended by Arista and Archubi [4, 5]. In what follows, we show how the main expressions of this theory can be formulated for orbitals with angular momentum $\ell \neq 0$, compare the assumed momentum densities with the experiment, and introduce a local-density-based approach that makes it possible to approach the measured dielectric function both in the optical limit and at high momentum transfer.

5.2 Introduction

The interaction of charged particles with matter has been an important topic since the early days of quantum physics. At large enough projectile velocities, the interaction between projectile and target is weak, and a first-Born approximation should be suitable. Then, ion stopping and electron inelastic mean free path can be calculated based on the momentum and energy transfer (k, ω) dependent dielectric function $\varepsilon(k, \omega)$.

The dielectric function and the associated energy loss function (ELF) has generally been determined for $k = 0$ (optical limit). For an actual calculation, e.g. the calculation of ion stopping, one needs to know the dielectric function away from $k = 0$.

Within the free-electron gas model, Lindhard derived an expression for $\varepsilon(k, \omega)$ [6]. In this model all states are fully occupied up to the Fermi level and empty for larger energies. Such a sharp drop-off with momentum is not present for inner-shell electrons making the Lindhard dielectric function questionable for the calculation of the contribution to stopping from the inner-shell electrons.

The general expression of the dielectric function for a free electron gas (FEG) with electron density n reads:

$$\varepsilon(k, \omega) = 1 + \frac{4\pi n}{k^2} \int d^3 q \frac{F(\vec{k} + \vec{q}) - F(\vec{q})}{\hbar\omega + i\Gamma - (E_{\vec{k}+\vec{q}} - E_{\vec{q}})} \quad (5.1)$$

with k the momentum transferred to the electron gas, q the momentum of an electron in the electron gas before excitation, and Γ an infinitely-small width. (We use atomic units $\hbar = e = m = 1$ unless otherwise specified.) $F(q)$ is the probability density of q normalised as

$$\int d^3 q F(q) = 1. \quad (5.2)$$

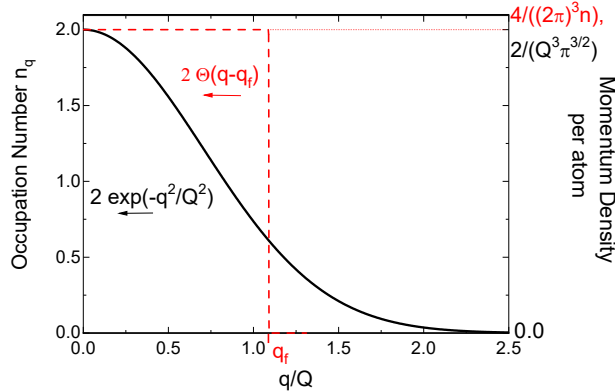


Figure 5.1: Illustration of the original idea of Kaneko. The Fermi distribution is replaced by a Gaussian distribution with the same width as the momentum distribution of the atomic orbital. For Kaneko's choice of the normalising formula V the momentum density of the electron gas ($2V/(2\pi)^3$) is the same as the maximum momentum density of the filled s shell ($(2/(Q^3\pi^{3/2}))$.

For a FEG (at 0 K) one takes for $F(q)$

$$F_{\text{FEG}}(q) = \left(\frac{4\pi}{3}q_f^3\right)^{-1} \Theta(q_f - q) \quad (5.3)$$

with Θ the Heaviside step function and q_f the Fermi wave vector ($(3\pi^2n)^{1/3}$). Then, this equation leads to the Lindhard dielectric function.

The dielectric function does not depend on the spatial coordinate. Core electrons are localised near the nucleus. The description of the contribution of the core electrons to the dielectric function is thus necessarily dependent on some local approximation. Lindhard assumed that the local contribution of a core level is equal to that of a free electron gas with the same density.

An alternative was formulated by Kaneko that emphasizes the momentum density distribution over the coordinate-space electron density for the calculation of the core-level contribution to the dielectric function. $F(q)$ is assumed to be equal to $|\phi(q)|^2$, i.e. the modulus square of the momentum-space wave function of the core level. Then, after taking a Gaussian approximation for $|\phi(q)|^2$, Kaneko succeeded in deriving an analytical expression for the dielectric function. Such a Gaussian function:

$$F(q) = |\phi(q)|^2 \approx \frac{1}{Q^3\pi^{3/2}} \exp(-q^2/Q^2), \quad (5.4)$$

where Q is the characteristic momentum of the orbitalis quite appropriate for an s -level. The appropriate choice of the density n in eq. 5.1 (here often called the reference density n_{ref}) for the description of the core level is based on an argument of matching the momentum densities, and a somewhat different version of this argument is given in the next section. This dielectric function applies to volume V_{shell} such that $n_{\text{ref}}V_{\text{shell}}$ corresponds to the number of electrons in the shell. In this picture the electron density and hence the dielectric function within V_{shell} is homogeneous.

The momentum density of core levels (the modulus-square of its wave function in momentum space) can be obtained from, for example, Hartree-Fock calculations or it can be measured by electron momentum spectroscopy (EMS) [7] or Compton scattering. A comparison of the momentum density distribution, as used by Kaneko based on Hartree-Fock calculations, and measured by EMS is given in fig. 5.2. For s levels the agreement is generally quite good, but for p levels the distribution is totally different. The experiment displays a minimum at $q = 0$, whereas Kaneko's density has a maximum at this momentum. We want to show, quite similar as was done by Mathar & Posselt [8], how this problem can be overcome. Moreover, we demonstrate how a Gaussian basis set, rather than a single Gaussian can be used to obtain the stopping with $|F(q)|^2$ values that closer approximate the actual momentum density.

For both the Lindhard and Kaneko dielectric functions $\text{Im}[-1/\varepsilon(k, \omega)]$ (the ‘loss function’) consist of 2 branches: a broad distribution describing electron-hole excitations and a sharp line corresponding to collective (‘plasmon’) excitations. At $k = 0$ the only contribution to the loss

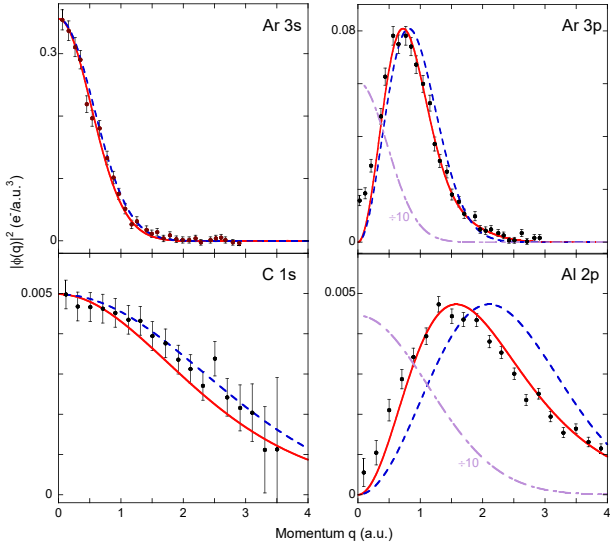


Figure 5.2: Measured momentum densities, as obtained by electron momentum spectroscopy for Ar 3s, Ar 3p [9], C 1s [10] and Al 2p orbitals [11] (error bars) compared to those calculated from the wave function as given by Koga et al [12] (full line) and fitting these calculations to the modified Kaneko's wave packet model described here (dashed line). The dash-dotted line, shown for the p levels, is the momentum density used in the original Kaneko's theory [2].

function is from the plasmon at an energy loss of $\omega_p = \sqrt{4\pi n}$, in both the Lindhard and Kaneko approach. In reality the contribution of the core level to the dielectric function in the optical limit is spread out over a large range of energy losses. We will show how the introduction of a ‘local approximation’ results in more realistic loss functions, while retaining a dielectric function behaviour at high k that is determined only by the Q parameter.

In summary, in this paper we improve the Kaneko approach in several ways:

- Improve the way that spin degeneracy is incorporated for $\ell = 0$ states, that avoid re-scaling of Q as present in the original Kaneko approach.
- use a description of the momentum density distribution for $\ell \neq 0$ that has the right symmetry and approaches the measured momentum density to derive the dielectric function.
- show how a description of the wave function (rather than the electron density) based on the sum of several Gaussian-type wave functions, as is widely used in quantum chemistry, can be used within the Kaneko framework and thus we can obtain an estimate of the stopping based on a more accurate description of the wave function.
- introduce a local approximation to construct a dielectric function reproducing for some cases the actual loss function in the optical limit, as well as the approximate description at high k values, based on the calculated wave function of the core level in both real and coordinate space.

Finally the results of the various variations of the theory are compared with other calculations and or experiments.

5.3 Modifications and extensions of Kaneko's model

5.3.1 $\ell = 0$ states

Consider the electron wave function of a core electron in momentum space $\phi(q)$. It is normalised such that $|\phi(q)|^2$ is the probability density that the electron has a momentum q . For each orbital there is a q value for which this distribution has a maximum. Consider s levels which have maximum density at $q = 0$. If both spin levels are occupied the shell density is $2|\phi(q)|^2$. For a rough approximation of the momentum space s level wave function a single Gaussian can be used (eq. 5.4) Inner core levels are characterised by large Q values and their wave function is diffuse in momentum space, but very localized in coordinate space. The maximum value of momentum density depends obviously on Q .

Now consider a reference free electron gas occupying a volume V_{total} with an electron density n_{ref} . The momentum density of this FEG is, when both spin states are occupied, two times the density of allowed q vectors, i.e. $2V_{\text{total}}/(2\pi)^3$. There are $N_e = V_{\text{total}}n_{\text{ref}}$ electrons in this system. It could be compared to a system consisting of $N_a = N_e/2 = V_{\text{total}}n_{\text{ref}}/2$ atoms (two electrons per atom for $\ell = 0$). The momentum density per atom of this free electron gas is thus $2(V_{\text{total}}/(2\pi)^3)/N_a = 4/((2\pi)^3 n_{\text{ref}})$

Further, as suggested by Kaneko, if one requires that the momentum density per atom of the electron gas is the same as the maximum density of the s shell (two times the maximum of $|\phi(q)|^2$ in eq. 5.4) one obtains:

$$\frac{2}{Q^3 \pi^{3/2}} = \frac{4}{(2\pi)^3 n_{\text{ref}}}, \quad (5.5)$$

i.e. $n_{\text{ref}} = Q^3/4\pi^{3/2}$ or, in terms of the plasmon energy: $\omega_p^2 = 4\pi n$, simply:

$$\omega_p^2 = Q^3/\sqrt{\pi}. \quad (5.6)$$

Under this condition the momentum density per atom of a free electron gas and the atomic wave function compare as in fig. 5.1.

5.3.2 extension for $l \neq 0$

The momentum distribution given by Eq.(5.4) has a maximum at $q = 0$ and therefore cannot describe a p-shell, which has zero density at $q = 0$. This is illustrated in Fig. 5.2, where we compare the momentum densities, as measured by EMS with the Gaussian model of Eq.(5.4). Hence, we assume, following Mathar & Posselt [8], that the wave function (in momentum space) can be described by a single Gaussian-type orbital of the form:

$$\phi_{\ell,m}(\mathbf{q}) = R_\ell(q) Y_\ell^m(\theta, \varphi) = \sqrt{A_\ell} q^\ell \exp\left(-\frac{q^2}{2Q^2}\right) Y_\ell^m(\theta, \varphi) \quad (5.7)$$

and the momentum distribution by the modulus square of this wave function. A_ℓ is determined by the required normalisation of the wave function (i.e. $\int d^3q |R_\ell(q)|^2 = 1$), and Q is again a characteristic momentum that should be matched to the orbital under consideration. The momentum density of a completely filled sub-shell $\rho_\ell(\mathbf{q})$ is therefore:

$$\rho_\ell(\mathbf{q}) = 2(2\ell + 1) |R_\ell(q)|^2 \quad (5.8)$$

As shown in appendix 5.A this density has a maximum at $q_{\max} = \sqrt{\ell}Q$ and an expression for $|R_\ell(q_{\max})|^2$ is given in the appendix as well.

A reference FEG with N_e electrons occupies a volume $V_{\text{total}} = N_e/n_{\text{ref}}$ and correspond now to $N_a = N_e/(2(2\ell + 1))$ atoms and the momentum density of the filled shell per atom is thus:

$$\frac{2 \frac{V_{\text{total}}}{(2\pi)^3}}{N_a} = \frac{2 \frac{N_e/n_{\text{ref}}}{(2\pi)^3}}{N_e/(2(2\ell + 1))} = \frac{4(2\ell + 1)}{(2\pi)^3 n_{\text{ref}}}. \quad (5.9)$$

n_{ref} is now chosen such that its momentum density per atom correspond to the maximum momentum density of the shell:

$$\rho_\ell(\mathbf{q}_{\max}) = 2(2\ell + 1) |R_\ell(q_{\max})|^2 = \frac{4(2\ell + 1)}{(2\pi)^3 n_{\text{ref}}}. \quad (5.10)$$

The dielectric function for this ℓ level is then obtained by evaluating eq. 5.1 for this value of n_{ref} and using:

$$F(q) = |R_\ell(q)|^2, \quad (5.11)$$

and the corresponding plasmon frequency is:

$$\omega_p^2 = 4\pi n_{\text{ref}} = \frac{4(2\ell + 1)}{2\pi^2 \rho_\ell(q_{\max})} = \frac{1}{\pi^2 |R_\ell(q_{\max})|^2} \quad (5.12)$$

By considering the momentum density of the whole sub-shell we derive a description of the dielectric function in appendix 5.A. The advantage of a sub-shell based approach is that it avoids the introduction of a new variable $\bar{q} = N^{1/3}Q$, with N the degeneracy of the subshell, as is required by the approach of Kaneko [1] and Mathar & Posselt [8] to account for the actual number of electrons present.

5.3.3 using Gaussian basis sets

Within quantum chemistry the the description of a wave function in terms of a single Gaussian primitive as given by eq. 5.7 is considered a very poor approximation. Often the wave function is considered as a weighted sum of several such Gaussians. If the wave function is expressed as the sum of, for example, 3 Gaussians, then the momentum density consists of a weighted sum of 6 Gaussians. As the dielectric theory is linear it can be described in terms of the sum of the dielectric functions of these 6 components. The current theory can be straight-forwardly extended for this case as worked out in appendix 5.B.

5.3.4 introducing a minimum excitation energy

In both Lindhard and Kaneko cases the electron-hole pair region extends to $\omega = 0$ eV. When these dielectric functions are meant to represent core levels this seems non-physical and the low-loss intensity can be removed by introducing a gap (U) parameter as suggested by Levine, Louie for the Lindhard (or Mermin) case [13] and by Archubi and Arista for the Kaneko case. It shifts the intensity in the loss function from ω to $\sqrt{\omega^2 + U^2}$ in such a way that the Bethe sum rule does not change. In our case the obvious choice of the ‘band gap’ U is the core level binding energy.

5.3.5 changing the reference density

The equation of the maximum momentum density of the sub-shell with the momentum density of the electron gas (and hence the value of n_{ref}) is somewhat arbitrary. One could change this density in eq. 5.1, while keeping $F(q)$ the same. This was done by Archubi and Arista [5] in terms of a γ parameter: $n_{\text{used}} = \gamma n_{\text{ref}}$. The volume (per atom) to which the dielectric function applies has then to be adjusted such that $V_{\text{shell}} n_{\text{used}}$ remains equal to the number of electrons in the shell. ω_p^2 is then proportional to γ and e.g. for an s level given in terms of Q as $\omega_p^2 = \gamma Q^3 / \sqrt{\pi}$. In general:

$$\omega_p^2 = \frac{\gamma}{\pi^2 |R_\ell(q_{\max})|^2} \quad (5.13)$$

One could use γ as a tuning parameter to ensure that the plasmon energy is at the mean excitation energy, ensuring the right stopping contribution of the level in the high-energy limit. However, the loss function at $q = 0$ remains a single peak, in contrast to the measured loss function.

5.3.6 local approximation

One could abandon the idea that the core electron is represented by an uniform dielectric function filling a volume around the nucleus. For example, one could consider the coordinate-space representation of the core electron wave function of the shell. Between r and $r + \delta$ the coordinate-space wave function would contribute a charge density n_r . This is similar to what one does when describing the contribution of the core level within a free electron model and the shell-wise local plasmon approximation (SLPA) [14]. However, now we take as the dielectric function of this

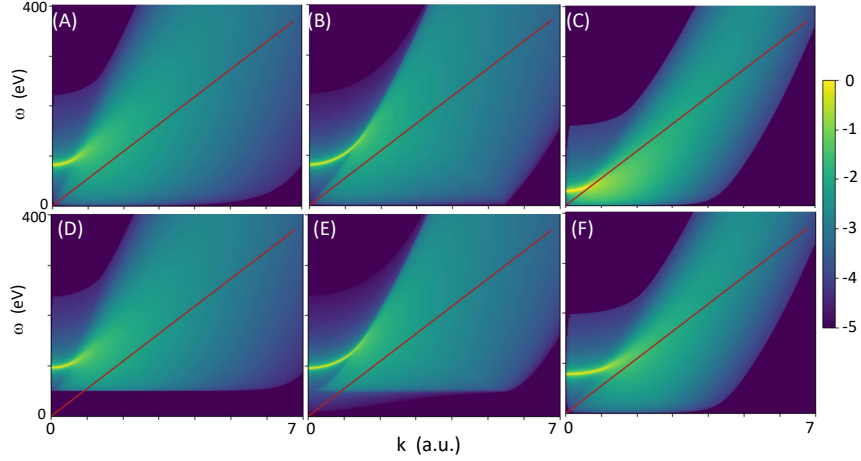


Figure 5.3: $\text{Log}(\text{Im}[-1/\varepsilon(k, \omega)])$ for (A) a Kaneko dielectric function with $Q = 2$ a.u., $\gamma = 1$, $\ell = 0$, $U = 0$ eV, (B) a Mermin dielectric function with $\omega_{p\ell} = 81$ eV, $U = 0$ eV, (C) a Kaneko dielectric function with $Q = 1$ a.u. $\gamma = 1$, $\ell = 0$, $U = 0$ eV, (D) a Kaneko dielectric function with $Q = 1$, $\gamma = 1$, $\ell = 0$, $U = 50$ eV, (E) a Mermin dielectric function with $\omega_{p\ell} = 81$ eV, $U = 50$ eV, and (F) a Kaneko dielectric function with $Q = 1$, $\gamma = 8$, $\ell = 0$, $U = 0$ eV. The width of the plasmon branch near $q = 0$ was always taken to be 2 eV. The red line correspond to the kv line for 100 keV protons (v here refers to the protons's velocity). Only the dielectric function under the kv -line contributes to the stopping at that energy.

density the Kaneko dielectric function with γ_r such that $\gamma_r n_{\text{ref}} = n_r$. In this way we obtain the same ELF at $q = 0$ as the SLPA, but the high- q behaviour of the dielectric function is controlled by the Q parameter.

5.4 Comparing model dielectric functions

In order to get some insight in the behavior of the Kaneko dielectric function we plot in fig. 5.3(A) the Kaneko loss function for $Q = 2$ a.u. (typical for a shallow core level) and $\ell = 0$. We can distinguish a line of intensity starting, for $k = 0$ at $\omega \approx 81$ eV and a broad distribution at larger k values. This is not dissimilar from a Mermin dielectric function shown in fig 5.3(B) with $\omega_p = 81$ eV. The line of intensity is attributed to collective oscillations (plasmons) whereas the broad distribution is associated with electron-hole pair creation. The Mermin dielectric function has a sharp cut-off of the electron hole-pair region (due to the well defined Fermi cut-off of a free electron gas), whereas the Kaneko case the decrease in intensity is more gradual.

In both cases the electron-hole pair region extends down to $\omega = 0$ eV. Using the U parameter this intensity near $\omega = 0$ can be removed, see fig 5.3 (D) and (E) for ω values less than U , taken to be 50 eV, in this case. The ‘plasmon peak’ at $q = 0$ shifts then to larger energy losses according to $\omega' = \sqrt{\omega^2 + U^2}$ (close to 100 eV, in this example).

The effect of reducing Q from 2 a.u. to 1 a.u. is shown in fig. 5.3 (C). Halving Q causes a decrease in the width of the electron-hole excitation region, but also reduces ω_p by a factor $\sqrt{8}$, see eq. 5.6. The original ω_p value can be recovered by increasing the γ parameter from 1 to 8, see fig. 5.3 (F), but the electron-hole pair energy distribution is not affected much by the increased γ value.

In the high- k limit the loss function $\text{Im}[-1/\varepsilon(k, \omega)]$ describes binary collisions. The loss function is then centered at the Bethe ridge (corresponding to the energy loss when interacting with a stationary electron i.e. $k^2/2$) but the energy loss distribution is Doppler broadened, depending on the momentum \mathbf{q} of the electron one interacts with:

$$\omega = k^2/2 + \mathbf{k} \cdot \mathbf{q} . \quad (5.14)$$

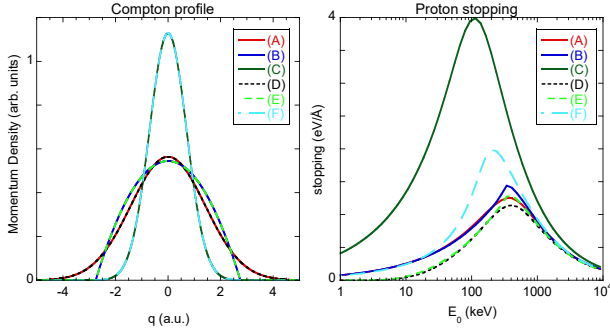


Figure 5.4: The Compton profile (left) and proton stopping (right) for the dielectric functions of fig. 5.3. The Compton profile does not depend on U (curve A is virtual identical to D as is curve B and curve E), or γ (curve C is indistinguishable from F). The largest stopping is for C, where ω_p is smallest. Non-zero U values reduce the stopping at low proton energies. Stopping for case (A) and (F) differ significantly, whereas their ω_p value is the same, showing the influence of the Q parameter on stopping, and the stopping is thus not solely determined by the ELF in the optical limit.

Plotting the loss function as a function of q , rather than ω one gets the so-called Compton profile, and the intensity at a certain q value corresponds with a projection of the momentum density on k . See ref. [15] for a more extensive discussion on the relation between Compton profiles and the dielectric function.

The Compton profiles of these dielectric function are shown in the left panel of fig. 5.4. As expected the Kaneko-derived Compton profiles decreases gradually to 0 with increasing q magnitude, whereas the Mermin derived ones show an abrupt decrease to 0 at $q = k_f$. Neither the U or the γ parameter affects the Compton profile, which, for the Kaneko case, only depends on the Q (and ℓ) value.

Stopping of a (non-relativistic) particle with energy E_0 is evaluated by the following integral:

$$\frac{dE}{dx} = \int_0^{E_0} \frac{\omega d\omega}{\pi E_0} \int_{k_-}^{k_+} \frac{dk}{k} \text{Im} \left[\frac{-1}{\varepsilon(k, \omega)} \right] \quad (5.15)$$

with q_{\pm} defined by

$$k_{\pm} = \sqrt{2ME_0} \pm \sqrt{2M(E_0 - \omega)}, \quad (5.16)$$

with M the mass of the projectile (here proton). If $\omega \ll E_0$ then $k_- \approx kv$ with v the projectile velocity.

The stopping curves for the model dielectric functions of fig. 5.3 are given in the right panel of fig. 5.4 and are all different. The Mermin stopping curve is somewhat larger near the maximum than the Kaneko one. Introducing non-zero U values reduces the stopping for low proton energies, as there is only contribution to the stopping for k values for which $kv > U$, with v the proton velocity (see fig. 5.3). The stopping curve for case A ($Q = 2$ eV, $\gamma = 1$) differs significantly from case F ($Q = 1$ eV, $\gamma = 8$) near the maximum but their loss functions at $q = 0$ are identical.

So far only $\ell = 0$ cases were compared. To investigate the influence of ℓ on the dielectric function we considered 4 cases with 1 electron per nucleus, $Q=1$ a.u. and with an electron density such that the plasmon is at 25 eV (by varying the γ value), and with ℓ values of 0, 1, 2 and 3 as well as the corresponding Mermin dielectric function. The width of the plasmon peak was 1 eV, and the loss functions at $k = 0$ are thus identical. At $k = 1$ a.u. all loss functions are clearly different, and the effect of dispersion is most severe for the higher angular momentum states. At $k = 5$ a.u. we are close to the Compton limit and all loss functions become symmetrical around $k^2/2$ (the energy transfer for a collision with $k = 5$ to a stationary electron). This higher angular momentum profile has a flat top, as is indeed expected for Compton profiles at higher angular momentum [16]. The value of $Q = 1$ was chosen as then for $\ell = 0$ Kaneko Compton profile have similar width as a Mermin free electron gas with $\omega_p = 25$ eV.

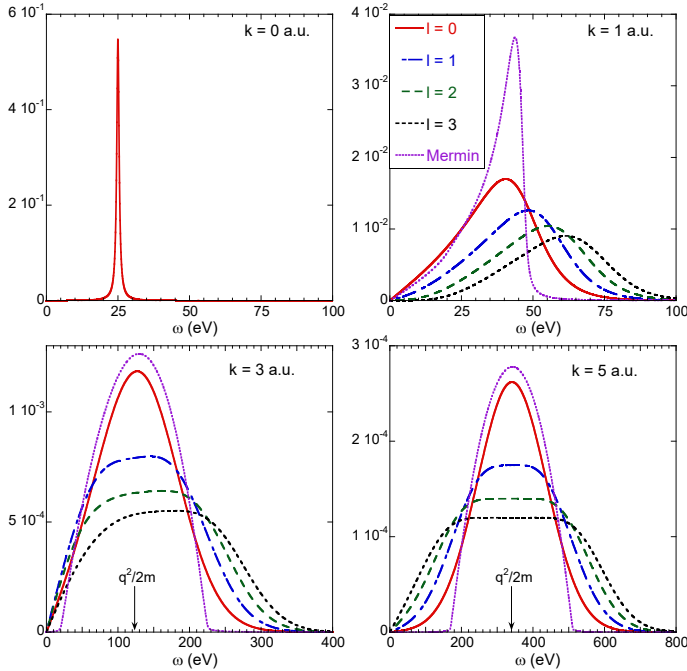


Figure 5.5: The evolution of $\text{Im}[-1/\varepsilon(k, \omega)]$ with k for 3 dielectric functions all with at $k = 0$ a loss function with a plasmon at 25 eV, but different ℓ values. The dispersion affects the Kaneko dielectric function with larger ℓ values the most. At $k = 5$ a.u. we get profiles are symmetric, indicating that the Compton limit has been reached. The arrows for the $k = 3$ and $k = 5$ a.u. case indicate the energy transfer to a stationary electron for a collision. The result for a Mermin loss function with the same ELF at $k = 0$ is given as well.

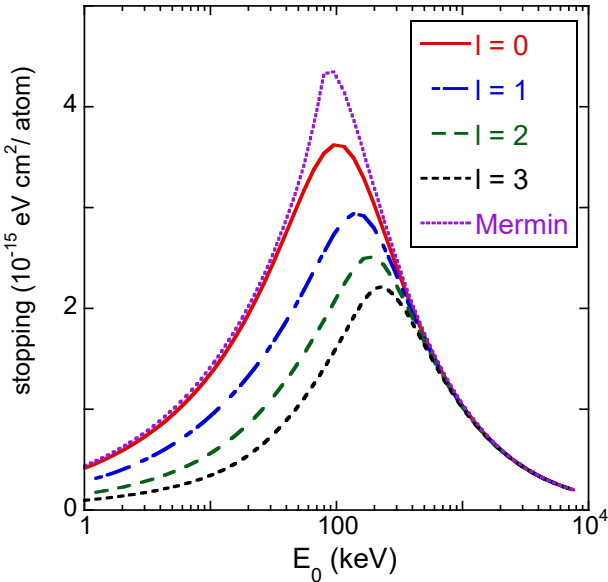


Figure 5.6: The stopping (assuming 1 electron per atom) for the dielectric function given in fig. 5.5.

The stopping per atom obtained from these 5 dielectric functions are all different at low energies. Above 1 MeV their stopping merges, as in the Bethe limit their loss function should be the same (same mean excitation energy, as the ELF at $q = 0$ are identical.) but the stopping at the maximum decreases with ℓ (and the energy E_0 for which the maximum occurs increases with ℓ). Compared to the Mermin case the stopping for $\ell = 3$ at the maximum is reduced by a factor of 2.

5.5 Comparing with experiment

In the previous section we described a number of approximate dielectric functions, based on the momentum-space representation of the wave function of a core level. All dielectric functions are consistent, in the sense that at any q they give the the right Bethe sum, i.e. correspond to the number of electrons in the core level. Does (a combination of) any of the above approximations provide a good description of ion stopping, and what Q value should be used. This will be

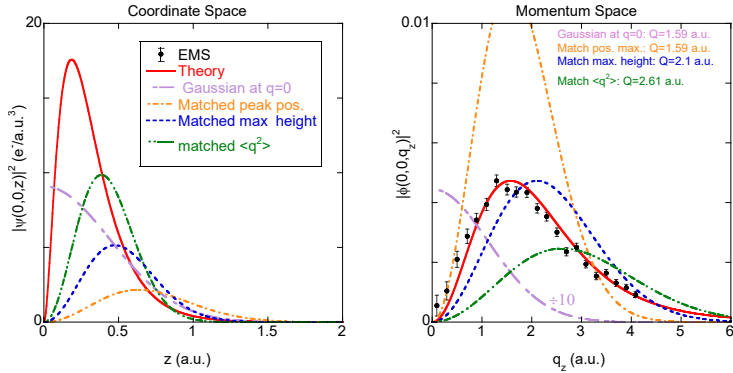


Figure 5.7: Various ways of describing the calculated real and momentum-space density (solid line) by a density derived from a single Gaussian for the case of Ar 3p. Kaneko used a Gaussian centered at $q = 0$ (long dash dotted line) [1]. Mathar and Posselt used a momentum density (dashed-dotted) of the form $q^2 \exp(-q^2/Q^2)$ with a maximum at the same momentum as the theory [8]. Here we mainly use momentum density based on the same formula as Mathar and Posselt but adjust Q such that the model density has the same the same maximum height (dashed). Alternatively one could also use a density with the same expectation value for the kinetic energy None of these options describe the theory well. The error bars are the measured momentum densities scaled to the calculated momentum density.

discussed here.

In order to calculate the contribution of the sub-shell to the stopping we have to obtain an estimate of Q and the density n . In fig. 5.7 we compare the result for different criteria for the choice of Q for the Ar 3p orbital with the result of a Hartree-Fock calculation: equal position of the maximum (as was used by Mathar & Posselt [8]), equal maximum height, or equal expectation value of $\langle q^2/2 \rangle$ (equal ‘kinetic energy’ of the electron). None of the approximations is very good, as the calculated momentum densities deviates significantly from that assumed from eq. 5.7. However, any of these approaches should be better than the Gaussian centered at $q = 0$ as used in the original Kaneko papers. We will obtain Q from matching the height in the following.

5.6 Real materials

5.6.1 homogeneous Kaneko approach

The collective mode, seen in the Kaneko-type model is not reflected in an obvious way in the loss function as observed in the experiment (e.g. electron energy loss spectroscopy). This is intuitively obvious as the interaction with the nucleus plays an important part in the interpretation of the loss function at larger losses. This interaction is not considered in a basic Kaneko-type model. In particular in the optical limit a Kaneko-type dielectric function has a single sharp peak.

It has been established for a long time that the Bethe theory (with I as the single parameter) describes correctly the stopping in the high-energy limit. I is defined as

$$I = \exp \left[\frac{\int_0^\infty \omega' \log \omega' \text{Im}[-1/\varepsilon(0, \omega')] d\omega'}{\int_0^\infty \omega' \text{Im}[-1/\varepsilon(0, \omega')] d\omega'} \right]. \quad (5.17)$$

For the Kaneko dielectric function the logarithmic mean energy loss I is then the same as the plasmon energy. For a good description of the contribution of a core level to the ion stopping at high energies it is thus required that the plasmon energy is close to the expected value of the mean ionisation energy, which is typically close to 2 times the corresponding binding energy [17].

Using a γ -value of 1 we obtain for Au, even for the s levels plasmon energies that bear no simple relation to the binding energy, see fig. 5.8. For the s levels with $\gamma = 1$ the theory described here is quite similar to the original one used by Kaneko [1]. The γ -parameter can be used to

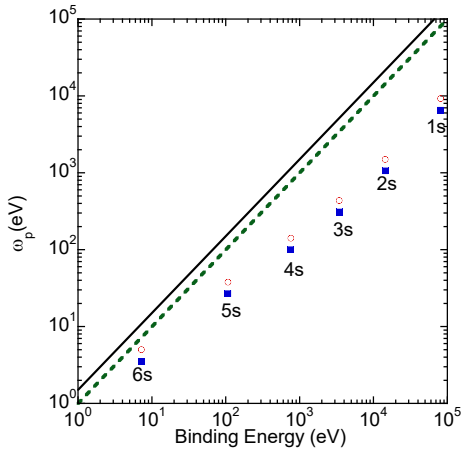


Figure 5.8: A comparison of the binding energy of the Au s levels (taken from [18] with the calculated plasmon energies. The Q values were taken from the compilation by Kaneko[3]. The plasmon energies were obtained from either $\omega_p^2 = Q^3/\sqrt{\pi}$ as derived here (squares), or from $\omega_p^2 = \bar{q}^3/\sqrt{\pi}$ with $\bar{q} = 2^{1/3}Q$ as was used by Kaneko (circles). In either way the calculated plasmon energy is less than the binding energy (dashed line) and much less than the expected mean excitation energy (full line), as explained in the main text.

tune the position of the peak at $k = 0$, while keeping the dielectric function at large k largely unaffected. In order to get the right stopping in the high projectile energy limit it is required that this single peak would correspond to the mean excitation energy of this level. This can be accomplished by adjusting γ in such a way that the mean excitation potential is reasonable (typically 1.5-2 times the binding energy). For the case of s levels of Au this would imply γ values of around 40-70 for the 5s levels and γ values near 300-500 for the 1s and 2s level. On the other hand, the introduction of the U parameter with a value of the core level binding energy would help as well. It would bring the mean excitation energy very close to the s level binding energy.

The poor agreement is not specific for Au or for the s levels. In fig. 5.9 we plot for the $n = 4$ shell the plasmon energy versus Z (using $\gamma = 1$ and $U = 0$) and compare these values with the binding energy, using the theory as described in the appendix. For the s level the plasmon energies are much less than the binding energy, and for the f level much larger. This is understandable. The binding energy decreases with angular momentum, but the electron density increases (larger degeneracy with increasing ℓ whereas the spatial extend does not change dramatically within the same shell.) Thus the plasmon energy derived from the Q values are not expected to give a reasonable description of the mean excitation energy.

Again we can introduce the U parameter. It makes the plasmon energy (and thus mean excitation energy) very close to the binding energy for the s level, but this parameter has hardly any effect for the d and f levels, is in that case the plasmon energy exceeds the binding energy.

Besides the optical limit, it is interesting to compare results for the dielectric function in the high- q limit where it can be interpreted as a Compton profile. The situation is simpler here as the U and γ parameter have very little influence on the Compton profile. For the $n = 4$ case, again for the case of Au we compare Compton profiles, as obtained by the original Kaneko procedure, the Kaneko procedure as described in subsection 5.3.2 and the relativistic Dirac-Hartree-Fock calculation from Biggs [16]. The original Kaneko procedure retains a Gaussian shape, whereas the modified procedure develops a flat top, just as the calculations of Biggs. However, neither the original or the modified procedure reproduces all the structure seen in the Biggs calculation.

In conclusion describing the core electron contribution to stopping as a homogeneous Kaneko-type electron gas does not give a reasonable description of the mean excitation energy, and thus the high-energy stopping. One can use the γ parameter as an ad-hoc tuning parameter to match the mean excitation energy I derived in other ways. This gives then the right high-energy behaviour, but the values at lower energy can not be trusted as the loss function in the optical limit (single peak) is an extremely poor approximation of the actual one (broad distribution above an onset near the binding energy).

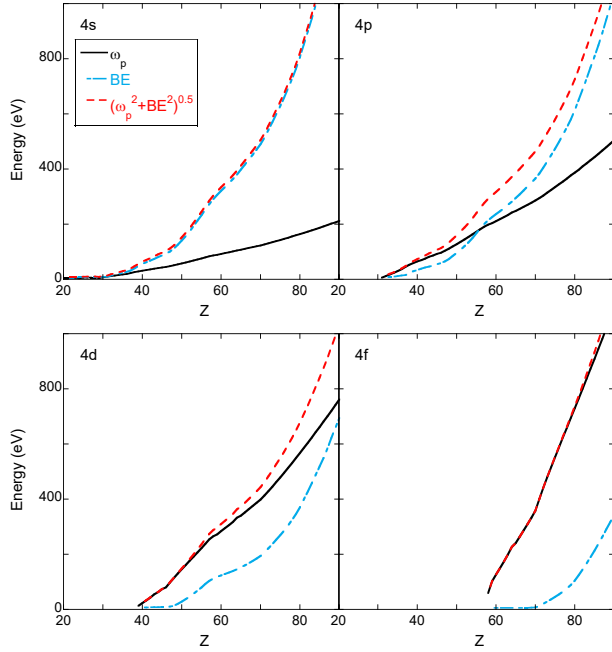


Figure 5.9: The plasmon energies for the different ℓ levels of the $n = 4$ shell as a function of atomic number Z . Q was obtained from matching the height of the Gaussian to the the wave function, and $\gamma = 1$. For the s level the plasmon energy (solid line) is much less than the binding energy (dash-dotted line), for the f level it is much more. Using the binding energy as the U parameter shifts the peak in the ELF to the binding energy for the s level (dashed line), but has hardly any effect for the d and f levels.

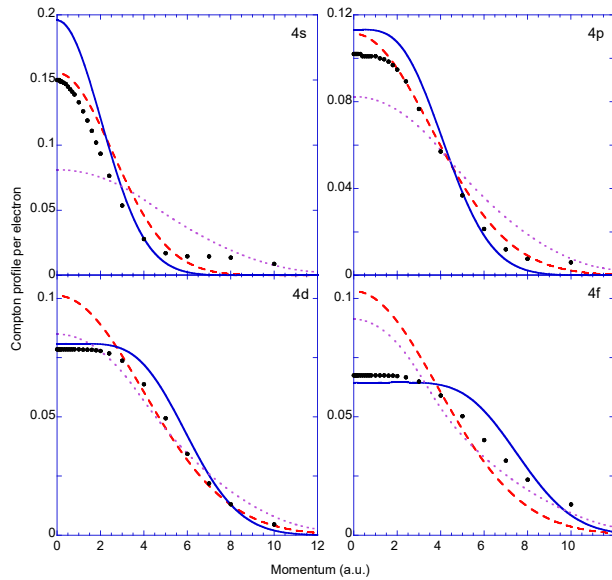


Figure 5.10: The Compton profile for the $n = 4$, s,p,d,f sub-shell of Au. The dashed line is obtained from the original Kaneko papers, the full line is the modified approach as described here. The dotted line is based on a local free electron approximation, as described in section 5.6.2. The points are form the calculation of the Dirac-Hartree-Fock calculations from Biggs [16].

5.6.2 Local Kaneko approach

There are clearly severe limitations to the applicability of eq. 5.1 in combination with occupation level distribution as given by eq. 5.11. The obtained dielectric function, however, adheres to sum rules and gives a reasonable description of the dielectric function in the high- k limit. Moreover, one can treat γ as a free tuning variable that will not affect the dielectric function in the high- k limit i.e. the agreement of the Compton profile.

At $k = 0$ the Kaneko loss function is characterized, just as the Lindhard (Mermin) loss function, by a single peak at the plasmon energy determined by the electron density n . Indeed one can show that for $k \rightarrow 0$ the loss function is independent of the exact functional form of the occupation distribution $F(k)$ assumed in eq. 5.1. In both cases one can incorporate the effect of the binding energy using the Levine-Louie dielectric function [13]. However, for core levels there is no unique choice for n as the electron density varies in space, it is *not* constant. This is one of the causes of the ambiguities described in the previous section.

Using the Lindhard approach the varying density was taken into account in the ‘shell-wise local plasma approximation’ (SLPA [19]). It assumes that the contribution of electrons at a distance r from a nucleus act as a free electron gas with the density $\rho(r)$ of the sub-shell or the total electron density at that r and a U parameter taken from the binding energy. Within the Lindhard-derived SLPA the density $\rho(r)$ is linked to a free-electron gas with the same density. At $k = 0$ the Kaneko dielectric function with the same density has a plasmon peak at the same energy loss. In a similar Kaneko-derived local approximation one links $\rho(r)$ via the γ parameter (now $\gamma(r)$ variable), as this affects the electron density at r , and one keeps Q constant to the value obtained from matching to the wave function in momentum space.

In the actual implementation we use the coordinate-space representation of the wave function to determine $\gamma(r)$ and the momentum-space representation to match Q in order to get the most appropriate single-Gaussian description. Now there are two questions:

- Does this approach give a reasonable description of the ELF at $k = 0$ and is the plasmon energy better described by the subshell density or total density?
- Does the stopping differ if one uses the Lindhard-type approach (SPLA) or the Kaneko-derived local approach?

The first question we try to address in figure 5.11, where the calculation at q is compared with an experimentally measured one [20]. The comparison is made in terms of the optical oscillator strength (OOS or $df/d\omega$), as measurements of the gas phase are usually published using this quantity. It is straightforwardly related to the ELF by [21]:

$$df/d\omega(\omega) = \frac{2\omega}{\pi E_a^2} \text{Im} \frac{-1}{\varepsilon(k=0, \omega)} \quad (5.18)$$

The experimentally measured one was put on absolute scale based on sum rule. In particular the experimental spectrum contains sharp discrete states for excitation of the atom below the ionization threshold, whereas in the model does not contain these discrete states. Note that stopping is obtained by integrating over the energy loss function and will not be very sensitive to small re-distributions in ω of these distributions.

For Ne there is a reasonable correlation between the measured and calculated ELF. For Ar the agreement is less good, and the difference in the 40-70 eV energy range is an order of magnitude. As both theory and experiment are in agreement with the f-sum rule, excess intensity in one range is necessarily accompanied by lower intensity in other ranges, and the experimental result of Chan exceeds the calculated one below 30 eV and in the 80 to 200 eV range. The reason for this is well understood. The ELF is closely related to the photoionization cross section, which displays for the Ar 3p level a Cooper minimum[22]. This is a consequence of a node present in the Ar 3p wave function, and the contribution of the positive and negative part of the wave function to the photoionization cross section cancel to a large extend in this energy range. Such

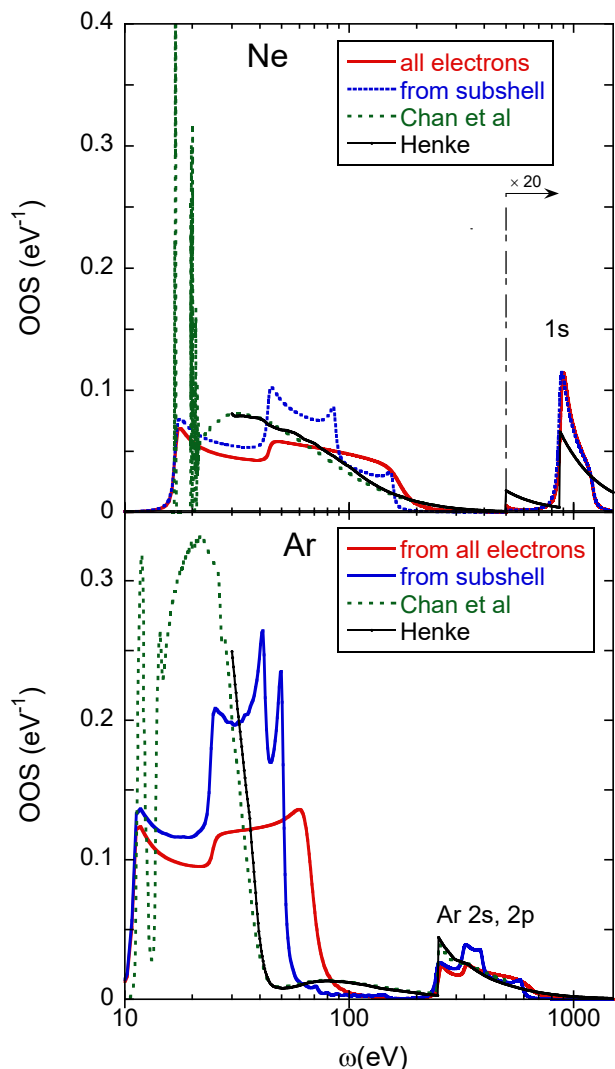


Figure 5.11: The loss function at $k = 0$ for Ne and Ar as obtained from the local density + U model compared to the measured loss function by energy loss spectroscopy [20]. For Ne result of the simple model resembles the experimental observed one somewhat, but for Ar the differences are much larger

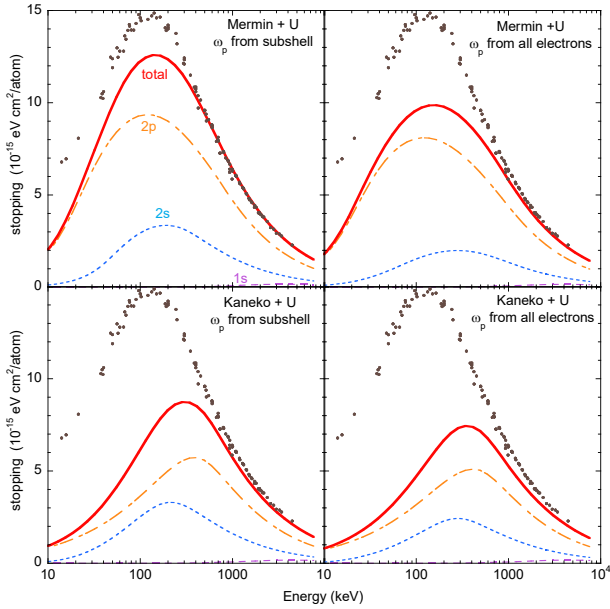


Figure 5.12: The stopping for protons as calculated for Ne in the local approximation, based on Mermin + U (top) and Kaneko + U approximation (bottom, with the plasmon frequency obtained from the sub-shell electron density (left) and total electron density (right). The dots are the compilation of experimental results as listed on the IAEA website. (<https://www-nds.iaea.org/stopping/>)

an effect is necessarily absent in a model that describes the loss function in terms of electron densities. However, both measured and model cross section adhere both to the sum rules.

If one bases the plasmon energy on the total electron density, then the calculated ELF extends to larger energy losses. This affects the s contribution more dramatically than the p contribution. As the electron density remains finite anywhere, the calculated ELF vanishes above $\sqrt{4\pi n_{\max} + U^2}$ with n_{\max} the maximum electron density. Such an upper limit is not evident in the experimentally determined ELF, showing again the approximate nature of this calculation.

The mean excitation energy I for Ne as obtained from these calculations is 120 eV (plasmon energy based on subshell density) and 145 eV (based on total densities). For Ar these values are 169 eV and 206 eV respectively. The literature values for I are 137 eV (Ne) and 188 eV (Ar). In light of the substantial deviations between the measured ELF and the ones calculated here, it is not surprising that the calculations of the I values differ significantly in this calculation.

Let us now take the case of Ne (where the ELF in the optical limit obtained from the local approximation resembles the measured one better than for Ar) and compare the obtained stopping. This is done in fig. 5.12. Clearly the best agreement is obtained for the Mermin-type approach based on the sub-shell electron density. The Kaneko stopping is less, in particular for the 2p sub-shell. This is in agreement with the model calculations from fig. 5.6.

5.7 Discussion and conclusion

The shell-wise derivation of the Kaneko dielectric function avoids the introduction of a variable $\bar{q} = (2(2l+1))^{1/3}Q$ which is present in the original formulation by Kanoko [1] and also in the work of Archubi and Arista [5]. In the original formulation the Compton profile would have a width characterised by \bar{q} , whereas it is well established that the Compton profile is characterised by Q [23]. This re-scaling was necessary in the earlier work in order to account for all the electrons in the shell.

Related to this, there is a difference in the way the γ parameter is defined. eq. 5.6 of this work and eq. (11) from ref. [5] (A&A). Their definition of γ , (referred here to as $\gamma_{A\&A}$), is in terms of \bar{q} : $\omega_p^2 = \gamma_{A\&A} \bar{q}^3 / \sqrt{\pi} = 2\gamma_{A\&A} Q^3 / \sqrt{\pi}$. Thus, in order to get the same plasmon energy one requires $\gamma_{A\&A} = 0.5\gamma$. In this paper we avoid re-scaling Q in order to take into account the degeneracy of a level, as was done by Kaneko [2] and Archubi & Arista [5].

Belkacem and Sigmund (B&S) solved the dielectric function for the one-dimensional harmonic oscillator [24] with resonance frequency ω_0 . The solution of the harmonic oscillator in momentum

space is has also a Gaussian distribution $|\phi(q)|^2 = c \exp(-q^2/\omega_0)$ which suggest that our $\ell = 0$ wave function with characteristic momentum Q is the same as the ground state of a harmonic oscillator with $\omega_0 = Q^2$. In the dilute limit (oscillators do not influence each other) B&S derive that the loss function for $k \approx 0$ has a single peak at energy ω_0 . In order for the model described here and the B&S model to have the same long-wavelength loss function one needs a reference density of $n_{\text{ref}} = \omega_0^2/(4\pi) = Q^4/(4\pi)$ whereas eq. 5.6 describes $\omega_p^2 = Q^3/\sqrt{\pi}$. Thus even though Kaneko and B&S both describe the initial state as a Gaussian distribution their Q dependence of the plasmon energy in the energy loss spectrum is different. Indeed fig. 5.8 seems to suggest that for inner core levels (characterised by larger Q values) the plasmon energy is too low, suggesting a stronger dependence of ω_p on Q than derived in the Kaneko theory.

A dielectric function based on electron gas with a modified occupation reflecting the momentum-space representation of the wave function was derived. It adheres to the f-sum rule and gets a good description of the large- k behaviour of $\text{Im}[-1/\varepsilon(k, \omega)]$. If one considers the core level as a finite volume filled with this modified electron gas with a single density one gets a very poor description of the ELF in the optical limit. Somewhat better results are obtained if one considers the modified electron gas with a density that varies in space, as described by the target electron density and takes into account the binding energy as a Levine-Louie type band gap. A qualitative resemblance is found with the optical ELF as long as the core level wave functions involved do not have nodes.

In the high- k limit the Compton profiles as obtained from these dielectric functions show a broadening of the profile and a flat top developing in the momentum distribution near zero momentum, with increasing ℓ values. This is in accordance with ab-initio calculations of the Compton profile. This is in contrast with the Compton profile derived within the SLPA which remain Gaussian and decrease in width with increasing ℓ

The dispersion of the modified electron gas differs from that obtained with for a Lindhard (Mermin) electron gas. Especially for $\ell \neq 0$ the dispersion is stronger than in the Lindhard case. This results in a reduction of the stopping contribution of these levels at lower projectile energy. The agreement with the experimental stopping is, at lower energies, less good for the modified electron gas, compared to a similar Lindhard-based approach. It is possible that the agreement with experiment could improve if non-linear contributions (beyond first Born) are considered as well or the poor agreement is related to the assumed free-electron nature of the initial and final state in eq. 5.1

One can solve eq. 5.1 for a free electron gas, leading to the Lindhard dielectric function and a momentum distribution given by the Fermi distribution, which differs significantly from the momentum density of a core level. One can solve eq. 5.1 using (an assembly of) harmonic oscillators and then the momentum distribution is given by a Gaussian, more closely resembling the momentum distribution of a (*s*) core level [24]. However now the electron will always remain a bound electron in the excited state.

Kaneko tried to enforce a Gaussian momentum distribution while retaining the free electron nature of the basis set. This paper tried to advance this attempts in a more consistent way. Although we get a dielectric function that adheres to sum rules at all k and gives a good description of the Compton profile at large k , it appears not to result in better estimates of ion stopping. This can be seen as a demonstration of the limited merit of the model based on such an ad-hoc change of the momentum distribution.

Bibliography

- [1] T. Kaneko, Wave-packet theory of stopping of bound electrons, *Phys. Rev. A* 40 (1989) 2188. doi:10.1103/physreva.40.2188.
- [2] T. Kaneko, Partial and total electronic stoppings of solids and atoms for energetic ions, *Physica Status Solidi (b)* 156 (1) (1989) 49–63. doi:10.1002/pssb.2221560104.
- [3] T. Kaneko, Partial and total electronic stopping cross sections of atoms and solids for protons, *At. Data Nucl. Data Tables* 53 (2) (1993) 271–340. doi:10.1006/adnd.1993.1007.
- [4] C. Archubi, N. Arista, A comparative study of threshold effects in the energy loss moments of protons, electrons and positrons using dielectric models for band-gap materials, *Europ. Phys. J.B* 90. doi:10.1140/epjb/e2016-70637-9.
- [5] C. D. Archubi, N. R. Arista, Extended wave-packet model to calculate energy-loss moments of protons in matter, *Phys. Rev. A* 96 (6) (2017) 062701. doi:10.1103/physreva.96.062701.
- [6] J. Lindhard, On the properties of a gas of charged particles, *K. Dan. Vidensk. Selsk. Mat.-Fys. Medd.* 28 (8) (1954) 1–57.
- [7] E. Weigold, I. E. McCarthy, *Electron Momentum Spectroscopy*, Kluwer /Plenum, New York, 1999.
- [8] R. Mathar, M. Posselt, Electronic stopping of heavy ions in the kaneko model, *Phys. Rev. B* 51 (1995) 15798. doi:10.1103/physrevb.51.15798.
- [9] P. Storer, R. S. Caprari, S. A. C. Clark, M. Vos, E. Weigold, Condensed matter electron momentum spectrometer with parallel detection in energy and momentum, *Rev. Sci. Instrum.* 65 (1994) 2214.
URL <https://doi.org/10.1063/1.1144730>
- [10] R. S. Caprari, S. A. C. Clark, I. E. McCarthy, P. J. Storer, M. Vos, E. Weigold, Electron-momentum spectroscopy of the core state of solid carbon, *Phys. Rev. B* 50 (16) (1994) 12078–12083. doi:10.1103/physrevb.50.12078.
- [11] M. Vos, A. S. Kheifets, E. Weigold, Momentum profiles of Aluminum, *J. Electron Spectrosc. Relat. Phenom.* 114-116 (2001) 1031–1036.
URL [https://doi.org/10.1016/S0368-2048\(00\)00284-X](https://doi.org/10.1016/S0368-2048(00)00284-X)
- [12] T. Koga, K. Kanayama, S. Watanabe, A. J. Thakkar, Analytical Hartree-Fock wave functions subject to cusp and asymptotic constraints: He to Xe, Li⁺ to Cs⁺, H⁻ to I⁻, *Int. J. Quantum Chem.* 71 (1999) 491–497. doi:10.1002/(SICI)1097-461X(1999)71:6<491::AID-QUA6>3.0.CO;2-T.
- [13] Z. Levine, S. Louie, New model dielectric function and exchange-correlation potential for semiconductors and insulators, *Phys. Rev. B* 25 (1982) 6310. doi:10.1103/physrevb.25.6310.

- [14] C. Montanari, J. Miraglia, S. Heredia-Avalos, R. Garcia-Molina, I. Abril, Calculation of energy-loss straggling of C, Al, Si, and Cu for fast H, He, and Li ions, *Phys. Rev. A* 75 (2007) 022903. doi:[10.1103/physreva.75.022903](https://doi.org/10.1103/physreva.75.022903).
- [15] M. Vos, A model dielectric function for low and very high momentum transfer, *Nucl. Instrum. Methods Phys. Res., Sect. B* 366 (2015) 6. doi:[10.1016/j.nimb.2015.09.091](https://doi.org/10.1016/j.nimb.2015.09.091).
- [16] F. Biggs, L. Mendelsohn, J. Mann, Hartree-Fock Compton profiles for the elements, *At. Data Nucl. Data Tables* 16 (1975) 201. doi:[10.1016/0092-640X\(75\)90030-3](https://doi.org/10.1016/0092-640X(75)90030-3).
- [17] P. Sigmund, Particle Penetration and Radiation Effects, Vol. 151 of Springer Series in Solid-State Sciences, Springer, Berlin, 2006.
- [18] J. Fuggle, S. Alvarado, Core-level lifetimes as determined by X-ray photoelectron spectroscopy measurements, *Phys. Rev. A* 22 (1980) 1615–1624. doi:[10.1103/PhysRevA.22.1615](https://doi.org/10.1103/PhysRevA.22.1615).
- [19] C. C. Montanari, C. D. Archubi, D. M. Mitnik, J. E. Miraglia, Energy loss of protons in au, pb, and bi using relativistic wave functions, *Phys. Rev. A* 79 (3) (2009) 032903. doi:[10.1103/physreva.79.032903](https://doi.org/10.1103/physreva.79.032903).
- [20] W. F. Chan, G. Cooper, X. Guo, G. R. Burton, C. E. Brion, Absolute optical oscillator strengths for the electronic excitation of atoms at high resolution. III. The photoabsorption of argon, krypton, and xenon, *Phys. Rev. A* 46 (1992) 149–171. doi:[10.1103/PhysRevA.46.149](https://doi.org/10.1103/PhysRevA.46.149).
- [21] R. F. Egerton, Electron energy-loss spectroscopy in the electron microscope, third edition Edition, Plenum Press, New York, 2011. doi:[10.1007/978-1-4419-9583-4](https://doi.org/10.1007/978-1-4419-9583-4).
- [22] J. Cooper, Photoionization from outer atomic subshells. a model study, *Phys. Rev.* 128 (2) (1962) 681–693. doi:[10.1103/physrev.128.681](https://doi.org/10.1103/physrev.128.681).
- [23] M. J. Cooper, Compton scattering and electron momentum determination, *Rep. Prog. Phys.* 48 (1985) 415–481. doi:[10.1088/0034-4885/48/4/001](https://doi.org/10.1088/0034-4885/48/4/001).
- [24] A. Belkacem, P. Sigmund, Stopping power and energy loss spectrum of a dense medium of bound electrons, *Nucl. Instrum. Methods Phys. Res., Sect. B* 48 (1-4) (1990) 29–33. doi:[10.1016/0168-583X\(90\)90066-4](https://doi.org/10.1016/0168-583X(90)90066-4).
- [25] F. Wooten, Optical Properties of Solids, Academic Press, 1972.
- [26] D. Penn, Electron mean-free-path calculations using a model dielectric function, *Phys. Rev. B* 35 (1987) 482. doi:[10.1103/PhysRevB.35.482](https://doi.org/10.1103/PhysRevB.35.482).

5.A Appendix: Kaneko theory based on subshell density

5.A.1 Subshell density

In the following 2 appendices the subscript used for A, n and F refers to the angular momentum ℓ . We assume, following Mathar & Posselt [8], that the wave function (in momentum space) can be described by a single Gaussian-type orbital of the form:

$$\phi_{\ell,m}(\mathbf{q}) = \sqrt{A_\ell} q^\ell \exp\left(-\frac{q^2}{2Q^2}\right) Y_\ell^m(\theta, \varphi) = R_\ell(q) Y_\ell^m(\theta, \varphi) \quad (5A.1)$$

A_ℓ is determined from the normalisation condition:

$$\int d^3q |R_\ell(q)|^2 = \int d^3q A_\ell q^{2\ell} \exp(-q^2/Q^2) = 1 \quad (5A.2)$$

which gives:

$$A_\ell = \frac{2^\ell}{(2\ell+1)!! \pi^{3/2} Q^{2\ell+3}} \quad (5A.3)$$

For $\ell = 0$, $|R_\ell(q)|^2$ has a maximum of $\frac{1}{\pi^{3/2} Q^3}$ and $q_{\max} = 0$,

for $\ell = 1$ a maximum of $\frac{2}{3\pi^{3/2} Q^3} \exp(-1)$ and $q_{\max} = Q$

$\ell = 2$ maximum of $\frac{4}{15\pi^{3/2} Q^3} 4 \exp(-2)$ and $q_{\max} = \sqrt{2}Q$ etc.

(value of $|R_\ell(q)|^2$ at maximum is $A_\ell \ell^\ell Q^{2\ell} \exp(-\ell)$ at $q = \sqrt{\ell}Q$.)

A completely filled shell is again spherical symmetric, with density $\rho_\ell(q)$ as given by eq. 5.8.

Following Kaneko we assume that the dielectric function is still given by Eq. 5.1, but $F(q)$ is given by $|R_\ell(q)|^2$ and the reference electron density for sublevel ℓ : n_ℓ , is such that (see eq. 5.10):

$$\frac{4(2\ell+1)}{(2\pi)^3 n_\ell} = \rho_\ell(q_{\max}) = 2(2\ell+1) A_\ell \ell^\ell Q^{2\ell} \exp(-\ell) \quad (5A.4)$$

The calculated dielectric function applies only to the region V occupied by the core level. The fraction of the total volume occupied by the core level with N_l electrons is $4\pi N_a N_l / \omega_p^2$ with N_a the atomic density. In this way sum rules for the dielectric function will correspond to the number of core electrons.

Combining eq. 5A.3 and eq. 5A.4 we obtain for the reference density n_ℓ :

$$n_\ell = \frac{(2\ell+1)!! Q^3 \exp(\ell)}{\pi^{3/2} 2^{\ell+1} \ell^\ell} \quad (5A.5)$$

and $\omega_p^2 = 4\pi n_\ell$

The calculated dielectric function applies only to the region V occupied by the core level with N_l electrons: $V = N_l / n_\ell$. The fraction of the total volume occupied by the core level is $N_l / n_\ell / V_a$ with V_a the atomic volume.

5.A.2 The relation between dielectric function and sub-shell densities

The function $F_\ell(q)$ (eq. 5.11) can then be written as :

$$F_\ell(q) = A_\ell q^{2\ell} e^{-\alpha q^2} = A_\ell \left(-\frac{d}{d\alpha}\right)^\ell e^{-\alpha q^2}, \quad (5A.6)$$

with $\alpha = 1/Q^2$. The dielectric function, as derived by Kaneko, correspond to $l = 0$ and is given by

$$\begin{aligned}\varepsilon_{\ell=0}(k, \omega) &= 1 + \frac{4\pi n_0}{k^2} \int d^3 k' \frac{F_0(\vec{k} + \vec{k}') - F_0(\vec{k}')}{\hbar\omega + i\Gamma - (E_{\vec{k}+\vec{k}'} - E_{\vec{k}'})} \\ &= 1 + \frac{4\pi n_0 A_0}{k^2} \times \\ &\quad \int d^3 k' \frac{e^{-\alpha(\vec{k}+\vec{k}')^2} - e^{-\alpha(\vec{k}')^2}}{\hbar\omega + i\Gamma - (E_{\vec{k}+\vec{k}'} - E_{\vec{k}'})}\end{aligned}\quad (5A.7)$$

It is pointed out that product $n_0 A_0$ does not depend on α and therefore one can derive the above expression and multiply by A_ℓ to generate F_ℓ as

$$\begin{aligned}A_\ell \left(-\frac{\partial}{\partial \alpha} \right)^\ell (\varepsilon_{\ell=0}(k, \omega) - 1) &= \frac{4\pi n_0 A_0}{q^2} \times \\ &\quad \int d^3 k' \frac{F_\ell(\vec{k} + \vec{k}') - F_\ell(\vec{k}')}{\hbar\omega + i\Gamma - (E_{\vec{k}+\vec{k}'} - E_{\vec{k}'})},\end{aligned}\quad (5A.8)$$

where Eq. (5A.6) was used. Using the definition for the extended Kaneko's DF as

$$\varepsilon_\ell(k, \omega) = 1 + \frac{4\pi n_\ell}{k^2} \int d^3 k' \frac{F_\ell(\vec{k} + \vec{k}') - F_\ell(\vec{k}')}{\hbar\omega + i\Gamma - (E_{\vec{q}+\vec{k}'} - E_{\vec{k}'})} \quad (5A.9)$$

we have

$$A_\ell \left(-\frac{\partial}{\partial \alpha} \right)^\ell (\varepsilon_{\ell=0}(q, \omega) - 1) = \frac{n_0}{n_l} A_0 (\varepsilon_\ell(q, \omega) - 1) \quad (5A.10)$$

or

$$\varepsilon_\ell(q, \omega) = 1 + \frac{n_l}{n_0} \frac{A_\ell}{A_0} \left(-\frac{\partial}{\partial \alpha} \right)^\ell (\varepsilon_{\ell=0}(q, \omega, Q(\alpha)) - 1). \quad (5A.11)$$

(where the Q value used is the Q value obtained from matching the ℓ wave function, not from matching the $\ell = 0$ wavefunction to a Gaussian.)

The above DF (Eq.(5A.11)) also fulfils the following sum rules

$$\int_0^\infty \text{Im}[\varepsilon_\ell(q, \omega)] \omega d\omega = \frac{\pi}{2} \omega_p^2 \quad (5A.12)$$

$$\int_0^\infty \text{Im} \left[\frac{-1}{\varepsilon_\ell(q, \omega)} \right] \omega d\omega = \frac{\pi}{2} \omega_p^2 \quad (5A.13)$$

(at any q) as obtained from analytical properties [25] of ε_ℓ .

5.A.3 Evaluation of dielectric function for $l=0$

We give here for completeness the explicit formula for the Kaneko dielectric function for $\ell = 0$ (eq. 5A.7), similar to that described in ref [1, 2, 3], see also [4]. Results for $\ell \neq 0$ were obtained by numerical differentiation using eq. 5A.11. We consider a Gaussian occupation:

$$F_0(k) = A_0 e^{-\alpha k^2} \quad (5A.14)$$

with $\alpha = 1/Q^2$ and normalised i.e.:

$$A_0 = (\alpha/\pi)^{3/2} \quad (5A.15)$$

Consider the integral:

$$\int d^3k' \frac{F_0(\vec{k} + \vec{k}') - F_0(\vec{k})}{\hbar\omega + i\Gamma - (E_{\vec{k}+\vec{k}'} - E_{\vec{k}})} = \frac{A_0}{\hbar} \Psi(k, \omega), \quad (5A.16)$$

with:

$$\begin{aligned} \Psi(k, \omega) &= \Psi_1(k, \omega) + i\Psi_2(k, \omega) \\ &= \int d^3k' \frac{e^{-\alpha(\vec{k}+\vec{k}')^2} - e^{-\alpha k^2}}{\omega + i\Gamma - (E_{\vec{k}+\vec{k}'} - E_{\vec{k}})/\hbar} \end{aligned} \quad (5A.17)$$

Using the integrals evaluated by Kaneko:

$$\Psi_1(k, \omega) = \frac{\pi}{k} \frac{1}{\alpha} [W(\sqrt{\alpha}s) - W(\sqrt{\alpha}t)] \quad (5A.18)$$

$$\Psi_2(k, \omega) = \frac{\pi^2}{k} \frac{1}{\alpha} [e^{-\alpha t^2} - e^{-\alpha s^2}] \quad (5A.19)$$

with

$$\begin{aligned} s &= s(k, \omega) = \frac{\omega}{k} + \frac{k}{2} \\ t &= t(k, \omega) = \frac{\omega}{k} - \frac{k}{2} \end{aligned}$$

and

$$W(x) = \sqrt{\pi} \int_0^\infty dy \sin(xy) e^{-y^2/4}$$

Hence, for the dielectric function $\varepsilon = \varepsilon_1 + i\varepsilon_2$ we get:

$$\begin{aligned} \varepsilon_1(k, \omega) &= 1 + \frac{4\pi n_0}{k^2} A_0 \Psi_1(k, \omega) = \\ &+ \frac{4\pi n_0}{k^3} \pi A_0 \left[\frac{1}{\alpha} [W(\sqrt{\alpha}s) - W(\sqrt{\alpha}t)] \right] \end{aligned} \quad (5A.20)$$

$$\begin{aligned} \varepsilon_2(k, \omega) &= \frac{4\pi n_0}{k^2} A_0 \Psi_2(k, \omega) \\ &= \frac{4\pi n_0}{k^3} \pi^2 A_0 \left[\frac{1}{\alpha} (e^{-\alpha t^2} - e^{-\alpha s^2}) \right] \end{aligned} \quad (5A.21)$$

5.B Appendix: Use of Gaussian basis sets

In the previous we worked with the momentum densities, i.e. the modulus square of the wave function in momentum space. Within quantum chemistry there is a huge body of work describing the wave function as a combination of Gaussian primitives, their radial part is given by:

$$g_l^i(r) = N_l(\zeta_i) r^l e^{-\zeta_i r^2} \quad (5B.1)$$

with $N_l(\zeta_i)$ chosen such that $|g_l^i(r)|^2$ is normalised to 1. The actual wave function is given by a linear combination of a small number (we will take this to be 3, as is the case in the widely used basis set STO-3G) of these functions:

$$\psi(r) = \sum_i c_i g_l^i(r) \quad (5B.2)$$

The density of the wave function $|\psi(r)|^2 = |c_1g_l^1(r) + c_2g_l^2(r) + c_3g_l^3(r)|^2$ consists of product terms $g_l^i(r)g_l^j(r)$. Note that

$$g_l^i(r)g_l^j(r) = N_l(\zeta_i)N_l(\zeta_j)r^{2l}e^{-(\zeta_i+\zeta_j)r^2} \quad (5B.3)$$

has the familiar form of densities related to ‘Gaussian functions’. The function $g_l^i(r)g_l^j(r)$ is also normalized if $i \neq j$. The cross term has a contribution proportional to $c_i c_j < g_l^i(r)|g_l^j(r) >$. Thus the density $|\psi(r)|^2$ is given by a sum of 6 ‘Gaussian densities’ characterised by exponents proportional to $\zeta_1 + \zeta_1$, $\zeta_2 + \zeta_2$, $\zeta_3 + \zeta_3$, $\zeta_1 + \zeta_2$, $\zeta_1 + \zeta_3$ and $\zeta_2 + \zeta_3$. The parameters c_i and ζ_i have been determined based on various criteria and can be obtained from e.g. <https://www.basissetexchange.org/>

However, we are for our purpose interested in the density in momentum space. We can get the basis in momentum space by Bessel-Fourier transform of $g_l^i(r)$ and obtain (eq. 3.35 from [7])

$$v_l^i(q) = N_l(\zeta_i)(2\zeta)^{-l-3/2}q^l e^{-q^2/(4\zeta_i)} \quad (5B.4)$$

with $N_l(\zeta)(2\zeta)^{-l-3/2}$ a normalisation constant is the momentum space wave function. This implies that $2\zeta_i = Q_i^2$ with Q_i the ‘characteristic momentum of this component’. The momentum space density is thus described in terms of the basis $v_l^i(q)$:

$$|\phi(q)|^2 = |c_1v_l^1(q) + c_2v_l^2(q) + c_3v_l^3(q)|^2 \quad (5B.5)$$

with the coefficients c_i the same as in coordinate space wave function (i.e. the tabulated ones). This will again be the sum of 6 Gaussian densities with exponents equal to $-q^2(1/(4\zeta_i) + 1/(4\zeta_j))$.

With this method is a coefficient c_i can be negative. In that case the cross term proportional to $c_i c_j$ will be negative (provided c_j positive), however observables such as e.g. ion stopping, correspond to the sum of all contributions and is always positive.

In fig. 5B.1 we compare Compton profiles for Al 1s and Al 2p based on a single Gaussian (obtained from matching the height in momentum space, see fig. 5.7) and that calculated using the STO-3G Gaussian basis set. In both cases the single-Gaussian derived momentum densities are too small at large q . For the STO-3G derived profiles this is not the case. However, for the 2p orbital the STO-3G derived Compton profile is too small at $q = 0$, underlining the limitation of this simple basis set.

A significant advantage if this method is that one uses wave functions that have been proven to be useful in a variety of applications, rather than tuning the wave function by an ad-hoc criterion (equal height of equal position (see fig. 5.7)) to obtain the desired outcome.

5.C Appendix: Derive Kaneko-type dielectric function from optical ELF

The aim of this appendix is to obtain a Kaneko-type dielectric function from a energy loss distribution, measured at $q = 0$. It is assumed that the measured intensity can be attributed to a single atomic level for which the appropriate Q and ℓ values have been determined. In order to make the derivation similar to that of Penn ([26], further referred to as ‘Penn’, we assume that γ varies in space ($\gamma(r)$) but other interpretations might work as well. Within the local density approximation $\gamma(r) = n(r)/n_{\text{ref}}$ with $n(r)$ the ‘pseudo’-electron density at r .

We write (compare Penn, eq. 4a, ε_K is our Q and ℓ -dependent Kaneko-like dielectric function)

$$\text{Im}\frac{1}{\varepsilon(k, \omega)} = \int \frac{d^3r}{\Omega} \text{Im}\frac{1}{\varepsilon_K(k, \omega; Q, \ell, \gamma(r))} \quad (5C.1)$$

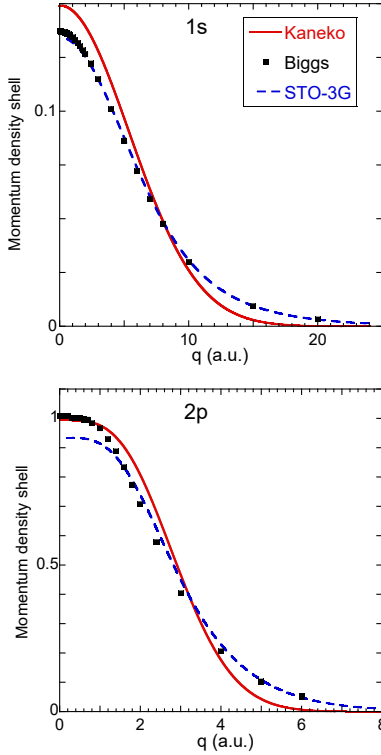


Figure 5B.1: Compton profiles based on a single Gaussian (full line) and the one obtained from the STO-3G basis set (dashed line) compared to the Hartree-Fock calculation of Biggs [16] (dots) for Al 2p and Al 1s

$\gamma(r)$ is a pseudo-occupation density distribution fraction, that takes the place of the pseudo-charge density distribution used by Penn. The integration is over the unit cell with volume Ω . We do not have to solve for $\gamma(r)$ explicitly. $\gamma(r)$ is chosen to ensure that: (compare Penn, eq. 5)

$$\text{Im} \frac{1}{\varepsilon(k=0, \omega)} = \left[\text{Im} \frac{1}{\varepsilon(\omega)} \right]_{\text{obs}} \quad (5C.2)$$

with $\left[\text{Im} \frac{1}{\varepsilon(\omega)} \right]_{\text{obs}}$ the measured ELF of this level in the optical limit. Use of (compare Penn, eq. 6a):

$$\text{Im} \frac{1}{\varepsilon_K(0, \omega; Q, \ell, \gamma(r))} = -\frac{\pi}{2} \omega_p(\gamma(r)) \delta(\omega - \omega_p(\gamma(r))), \quad (5C.3)$$

where $\omega_p^2 = 4\pi n(r) = 4\pi\gamma(r)n_{\text{ref}}$. Again following Penn by changing the integration in eq. 5C.1 from r to $\omega_p(r)$ and integrating over the delta function (eq. 5C.3) gives:

$$\text{Im} \frac{1}{\varepsilon(q, \omega)} = \int_0^\infty d\omega_p G(\omega_p) \text{Im} \frac{1}{\varepsilon_K(q, \omega; Q, \ell, \omega_p)} \quad (5C.4)$$

where

$$G(\omega) = -\frac{2}{\pi\omega} \text{Im} \left[\frac{1}{\varepsilon(\omega)} \right]_{\text{obs}} \quad (5C.5)$$

In this way, we construct a dielectric function that in the high- q limit is determined by the atomic parameters Q and ℓ and, in the optical limit, reproduces the optical ELF.

In reality, the optical ELF is not related to the electron density in a simple way. For example, the ELF can display a Cooper minimum for wave functions with nodes. Then, the contribution to the photo-absorption cross-section of the wave function with different polarity largely cancels, resulting in near zero photo-absorption cross-sections [22]. This effect will be absent in any calculation based on the electron density, which is always larger than 0. In those cases, the ‘pseudo’-density will deviate strongly from the actual density, but the dielectric function defined by eq. 5C.4 can be seen as extending the measured optical ELF to non-zero k values within the Kaneko framework.

Chapter 6

A unified approach to the inelastic mean free path, stopping and straggling of electrons and protons using a simple analytical-solvable model¹

A simple exact-solvable model is presented within the dielectric framework that describes the inelastic mean free path (IMFP), stopping and straggling of positrons, electrons (neglecting exchange) and protons. It is based on one or more Drude-Lindhard oscillators with vanishing width. The parameters used for these oscillators are derived from the valence electron density and the generalised oscillator strength of the core levels. Calculations are done for some low- Z elements ($Z \leq 14$). Results obtained are, at high enough projectile energies, in good agreement with the experiment and/or other calculations. The approximation is valid at rather low projectile energies for the IMFP, medium energies for stopping but only at high energies for straggling. The main aim is to provide a simple, unified framework for these quantities, for light and heavy projectiles, that are usually treated separately.

6.1 Introduction

Understanding the interaction of charged particles with matter is a challenge that has been the subject of research for over a century. Initially, it was an important test-case for the application of quantum physics [1, 2, 3]. In more recent time it is of more practical importance, as surface-analytical techniques require precise estimates of ion stopping and the electron inelastic mean free path [4, 5]. This applies also to medical physics, where charged particles play an important role in cancer therapy [6].

For velocities of the charged particle much larger than the Bohr velocity, the interaction becomes weak, and a first-order Born theory should suffice to describe the interaction well. One framework to obtain numerical values of stopping and mean free path is then the dielectric theory, and, in practice, results are then based on optical measurements of the dielectric function (i.e., the energy loss function (ELF) at zero momentum transfer) in conjunction with extension schemes of the ELF to non-zero momentum transfer. The ion stopping obtained for many different extension schemes was recently reviewed [7].

In many cases, there is no detailed information on the dielectric function in the optical limit, and/or there is a desire to get a rough estimate of the quantities involved based on a less-involved calculation. For example, in surface science, the TPP-2m equation is widely used to obtain estimates of the inelastic mean-free path (IMFP) [5] using a constant chosen to reproduce

¹submitted to: "Radiation Effects and Defects in Solids"

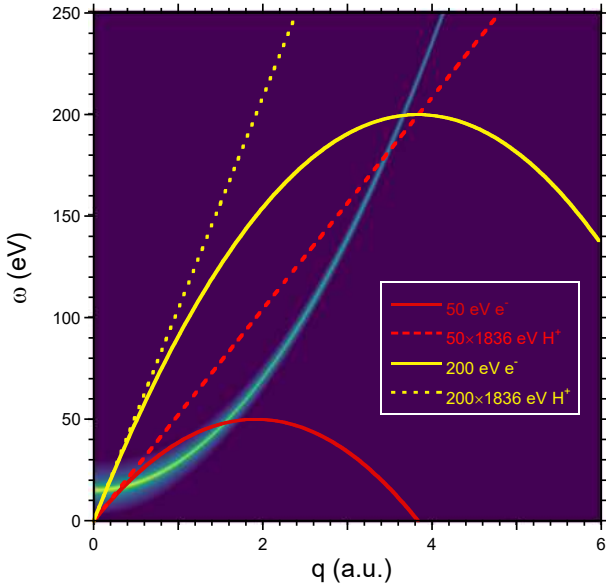


Figure 6.1: The Electron Loss Function (ELF) for a single Drude-Lindhard oscillator with $\omega_p = 15$ eV. Also shown are the kinematic limits (i.e. $\omega_{\max}(q)$) for 50 and 200 eV electrons, corresponding to velocities of 1.9 and 3.8 a.u. respectively, (solid lines) as well as protons with the same velocity (dashed lines).

the IMFP calculated for a selection of materials. For ion stopping a first order estimate is often obtained from the Bethe formula which requires knowledge of the ‘mean ionization energy’. The fact that the same type of physics underpins both quantities remains opaque.

Here we take a different approach. We first introduce a very simple model for the dielectric function (narrow Drude-Lindhard (DL) oscillator), representing valence electrons, and solve this model exactly for (electron and ion) the IMFP, stopping and straggling. The results are described using only 2 parameters with a well-defined meaning: oscillator energy and electron density.

An electron and a proton traveling at the same velocity exposes the material to an electric field that changes in space and time with the same magnitude. The dielectric medium reacts to this field (screening) and, as a consequence, energy and momentum transfer may occur. The range of energy and momentum transfer that is kinematically allowed depends on the projectile mass. Hence, the interaction of the projectile with a medium at a given velocity depends on the projectile mass, but for our simple model dielectric function this difference is readily calculated.

Real materials contain both valence electrons and core levels and both have to be considered to get meaningful results. Here we assume that each core level can also be described by a DL oscillator with a certain energy and amplitude. We demonstrate how the appropriate energy and amplitude of the DL oscillators of a core level can be derived from the optical oscillator strength, which can be estimated based on hydrogenic functions. The optimum parameters for each core level depend on the process (IMFP, stopping and straggling) one aims to describe and are tabulated here for some light elements.

For even higher projectile energies the contribution of the different oscillators are equivalent to a single oscillator with an averaged energy and amplitude. Again the averaging procedure depends on the process one wants to describe. For the IMFP the averaging procedure is dominated by the valence band contribution, but this is less so for stopping and even less for straggling. The optimum parameters, however, are the same for electrons/positrons and protons.

In the following we only consider protons and electrons, and stress how the difference in mass affects the results. The projectile velocity is central to the theory and relativistic effects, for the energies considered here, need only to be considered if one calculates the projectile energy corresponding to a certain velocity. We assume the target to be in the ground state (i.e. $T = 0$) and, for electrons, do not consider exchange effects. Atomic units are used throughout unless indicated otherwise. For heavier elements fluctuations in the charge of the ion become important, hence the restriction to protons.

Many aspects we discuss here have been discussed in the literature before. In particular Nguyen-Truong discussed the electron IMFP in a similar way [8]. The mean excitation energy

for stopping, already introduced by Bethe is ubiquitous. Sigmund derived expressions for stopping for a static electron gas closely related to what is described here, and describes the mean excitation energy for straggling similar to what is obtained here [9]. In a mature field as charged-particle target interaction we expect that many other publications have touched on part what is discussed here. We think, however, that the description of these phenomena for the different moments (IMFP, stopping, straggling) and different particles as is given here, in a consistent way within the framework of dielectric functions is useful as an accessible introduction to the field.

6.2 Dielectric theory

The dielectric theory describes the probability that a certain energy ω and momentum \mathbf{q} is transferred to the target. Within the first Born approximation the interaction is proportional to the square of the projectile charge (and thus the same for positively or negatively charged projectiles). A projectile with velocity v causes a spatial and temporal varying electric field to the target, and the reaction of the target to this field is described by $\epsilon(\omega, \mathbf{q})$. Electrons and protons with the same velocity v present the same perturbation. However, independent from the dielectric function of the target, there are limitations to the combinations of energy (ω) and momentum (\mathbf{q}) transfer allowed in a single collision due to energy and momentum conservation:

$$\omega = E_0 - E_1 = \frac{1}{2M} [\mathbf{p}_0^2 - (\mathbf{p}_0 - \mathbf{q})^2] \quad (6.1)$$

with E_0 and E_1 the energy of the projectile before and after the interaction. For non-relativistic particles $\mathbf{v} = \mathbf{p}_0/M$ with M the mass of the projectile one can write:

$$\omega = \mathbf{q} \cdot \mathbf{v} - \frac{\mathbf{q}^2}{2M} \quad (6.2)$$

The maximum energy loss, for a given $|q|$ -value, is for q directed along v and correspond to $\omega_{\max}(q) = qv - q^2/(2M)$. If one compares in the dielectric theory the interaction of a proton and an electron *with the same velocity* then all difference can be attributed to the recoil term: $q^2/(2M)$. For heavy projectiles, such as protons, one can safely neglect this term, but not for electrons. It is pointed that exchange and temperature and relativistic effects are neglected here. These effects, particularly their influence on the integration limits (minimum and maximum values of ω) have been described recently [10]. The simple model for the dielectric function we will use here is the Drude-Lindhard (DL) model [11]. ϵ^{DL} is defined in terms of $1/\epsilon^{\text{DL}}(\omega, q)$, for minus the imaginary part (also called the loss function):

$$\text{Im} \left[\frac{-1}{\epsilon^{\text{DL}}(\omega, q)} \right] = C \frac{\omega \Gamma \omega_p(0)^2}{(\omega^2 - \omega_p(q)^2)^2 + \omega^2 \Gamma^2} \quad (6.3)$$

and for the real part:

$$\text{Re} \left[\frac{1}{\epsilon^{\text{DL}}(\omega, q)} \right] = 1 + C \frac{(\omega^2 - \omega_p(q)^2) \omega_p(0)^2}{(\omega^2 - \omega_p(q)^2)^2 + \omega^2 \Gamma^2} \quad (6.4)$$

We take here simple quadratic dispersion: $\omega_p(q) = \omega_p + q^2/2$. The atomic density is n_a . We introduce ω_a as the plasmon frequency for the case of one electron per atom ($\omega_a^2 = 4\pi n_a$) and ω_p for the total valence electron density n_p ($\omega_p^2 = 4\pi n_p$). Thus, when there are N valence electrons per atom we have $\omega_p = \sqrt{N}\omega_a$. The constant C can be interpreted as the fraction of the unit cell occupied by this oscillator. For a metal $C = 1$ (and hence $\text{Re} \left[\frac{1}{\epsilon^{\text{DL}}(0,0)} \right] = 0$) but for an insulator $C < 1$ (and hence $\text{Re} \left[\frac{1}{\epsilon^{\text{DL}}(0,0)} \right] > 0$).

It can be easily verified that the Bethe sum rule:

$$\frac{1}{2\pi^2} \int_0^\infty \omega' \text{Im} \left[\frac{-1}{\epsilon(\omega', q)} \right] d\omega' = n, \quad (6.5)$$

for $\epsilon = \epsilon^{\text{DL}}$ is fulfilled for any q , with n the density of target electrons.

An example of a DL loss function (Eq.(6.3)) with $\omega_p = 15$ eV is given in fig. 6.1 together with the $\omega_{\max}(q)$ curve for 50 and 200 eV electrons and protons with 1836× larger energy (i.e. the same velocity).

The mean free path λ for an projectile with charge Q is given by:

$$\frac{1}{\lambda} = \frac{2Q^2}{\pi v^2} \int_0^\infty \frac{dq}{q} \int_0^{\omega_{\max}(q)} d\omega \text{Im} \left[\frac{-1}{\epsilon(\omega, q)} \right]. \quad (6.6)$$

We will only concern ourselves with electrons and protons in which case (in atomic units) $Q^2 = 1$ and we will drop this term for brevity. The integral is over the area of $\omega - q$ space where collisions are kinematically allowed, i.e. within the limitations due to eq. 6.2. For our purpose here it is convenient to first do the integration over ω at a given q . The ω integration extends then from 0 to $\omega_{\max}(q)$.

The inverse inelastic mean free path $1/\lambda$ is the probability that an inelastic event happens per unit length travelled. If one weights the inelastic event by ω one obtains the stopping force, or (average) energy lost per unit length travelled.

$$\frac{dE}{dx} = \frac{2}{\pi v^2} \int_0^\infty \frac{dq}{q} \int_0^{\omega_{\max}(q)} \omega d\omega \text{Im} \left[\frac{-1}{\epsilon(\omega, q)} \right]. \quad (6.7)$$

and similarly for the energy loss straggling:

$$\frac{d\Omega^2}{dx} = \frac{2}{\pi v^2} \int_0^\infty \frac{dq}{q} \int_0^{\omega_{\max}(q)} \omega^2 d\omega \text{Im} \left[\frac{-1}{\epsilon(\omega, q)} \right]. \quad (6.8)$$

For the DL dielectric function one can solve eq. 6.6, 6.7 and 6.8 analytically in the limit of $\Gamma \rightarrow 0$. We will do this first for stopping, resulting in very simple equations. Then we will consider IMFP and straggling resulting in slightly more complicated equations.

A single DL oscillator does not describe an actual solid well. Better approximations can be obtained by considering the sum of oscillators, describing the valence band and core levels. In the high-energy limit it is shown that the contribution can be summed (i.e. represented by a single oscillator), but the sum is different for IMFP, stopping and straggling. Finally the results are generalized to allow for calculations based on a continuous loss function.

6.2.1 Stopping, single oscillator

We consider first the integral over ω at a certain q . For the case $\Gamma \rightarrow 0$ there are now two possibilities, see fig 6.1. All the intensity of the ELF is at an energy loss smaller than $\omega_{\max}(q)$ or at ω values larger than this value. In the first case the value of the integral can be derived directly by integrating eq.6.3 from the Bethe sum rule (eq. 6.5) and is $2\pi^2 n$, in the latter case the integral is 0. It is worth pointing out, that for stopping, even in the case that the ELF at q is not a delta function, the value of the integral remains the same, as it is restricted by the Bethe sum, as long as the intensity does not extend beyond $\omega_{\max}(q)$. This means that in practice the integral is only sensitive to the precise shape of the ELF for q -values near the crossings of the ELF with the curve corresponding to the kinematic limits.

The q -values for which $\omega_{\max}(q)$ crosses the ELF, q_{\min} , q_{\max} , are given for electrons by the solution of:

$$\omega_p + \frac{q^2}{2} = qv - \frac{q^2}{2} \quad (6.9)$$

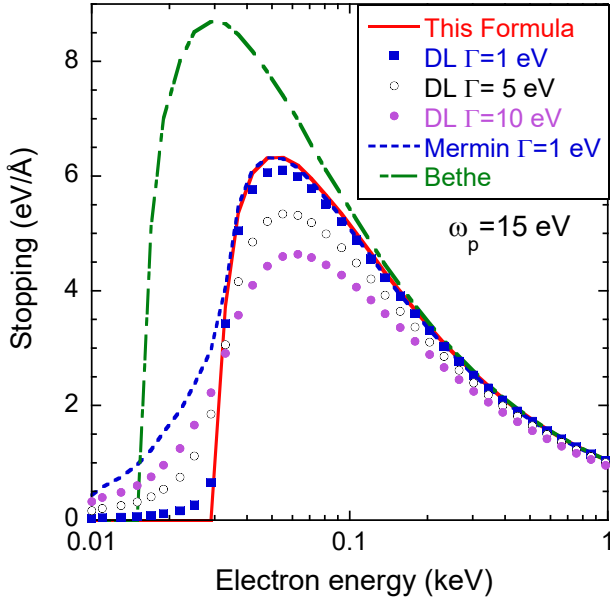


Figure 6.2: The calculated stopping for electrons interacting with an electron gas with $\omega_p = 15\text{ eV}$. The current formula (eq. 6.12) is compared with results of numerical integration of Drude-Lindhard (DL) oscillators with width as indicated. Also shown are results for a Mermin dielectric function, and the Bethe stopping formula. For electron energies $E > 3\omega_p$ the DL description is very similar to the Mermin description with equal width.

and for protons (the recoil term was neglected):

$$\omega_p + \frac{q^2}{2} = qv. \quad (6.10)$$

The momentum values corresponding to the crossing (q_{\min} and q_{\max}) are then given by:

$$q_{\max,\min} = \frac{v \pm \sqrt{v^2 - 4A\omega_p}}{2A} \quad (6.11)$$

with $A = 1$ for electrons and $A = 1/2$ for protons. For small v values ($v^2 < 4A\omega_p$) there are thus no solutions. Then, for this dielectric function all excitations are always forbidden based on the kinematics and the stopping will be 0. Proton stopping becomes non-zero at smaller velocities ($v = \sqrt{2\omega_p}$) compared to electron stopping ($v = 2\sqrt{\omega_p}$).

Hence one can write for the stopping:

$$\frac{dE}{dx} = \frac{2}{\pi v^2} \int_{q_{\min}}^{q_{\max}} \frac{dq}{q} 2\pi^2 n = \frac{4\pi n}{v^2} \ln \left(\frac{q_{\max}}{q_{\min}} \right) = \frac{\omega_p^2}{v^2} \ln \left(\frac{q_{\max}}{q_{\min}} \right). \quad (6.12)$$

In fig. 6.2 we compare the stopping of an electron gas with $\omega_p = 15\text{ eV}$ obtained with eq. 6.12 with the one obtained by numerical integration of the DL dielectric function with non-zero Γ . For small Γ -values the agreement is good, as expected, but the sharp onset disappears, and the maximum value becomes less with increasing Γ . We also compare the result with the stopping obtained from a Mermin dielectric function [12] with small Γ .

The Mermin dielectric function is the (quantum-physics based) solution of the dielectric function within the random phase approximation. It has good agreement for energies above the maximum (indicating that the simple DL model is not too bad at these energies), but the Mermin dielectric function results in non-zero stopping at low energies.

Often, as a first-order approximation, of the stopping the Bethe formula is used. In this high-energy limit ($v^2 \gg 4\omega_p$): $q_{\min} \approx \omega_p/v$ (for both electrons and protons) and $q_{\max} \approx v/A = Bv$ with $B = 1/A$ (i.e. $B = 1$ for electrons and $B = 2$ for protons). Then:

$$-\frac{dE}{dx} = \frac{4\pi n}{v^2} \ln \left(\frac{Bv^2}{\omega_p} \right). \quad (6.13)$$

Thus eq. 6.12 is in the high-energy limit equivalent to the non-relativistic Bethe formula. From fig. 6.2 it is clear however, that the equation derived here is a significantly better approximation near the stopping power maximum of a free-electron gas.

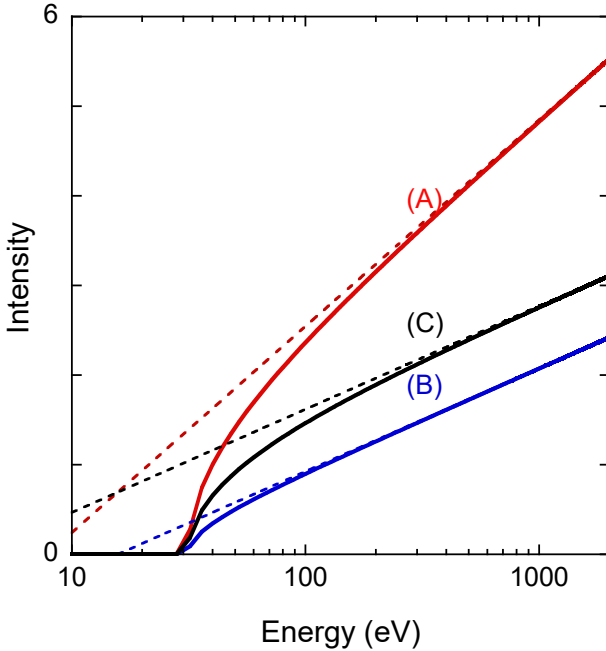


Figure 6.3: The solid lines (A) represent (for electrons) the first term in between the square brackets of eq. 6.15 for the case of electrons for a free electron gas with the density of aluminum valence band. (B) represents the second term and (C) is the difference of (A) and (B). The dashed lines are the high- v limits of the corresponding contributions ($q_{\max} = Bv$, $q_{\min} = \omega_p/v \ll \omega_p$).

6.2.2 IMFP, single oscillator

The inelastic mean free path is obtained from the integration of eq. 6.6 over the kinematically-allowed $q - \omega$ space and is identical to the stopping integral (eq. 6.7), except for the weighting with the energy loss ω . We integrate eq. 6.6 again first over ω up to $\omega_{\max}(q)$ which gives (for a loss function with vanishing width), between q_{\min} and q_{\max} not the Bethe sum (eq. 6.5) but the Bethe sum divided by $\omega(q)$, and zero outside this range.

Integrating over q one obtains for the inverse mean free path for this model:

$$\frac{1}{\lambda} = \frac{2}{\pi v^2} \int_{q_{\min}}^{q_{\max}} \frac{2\pi^2 n dq}{q(\omega_p + \frac{q^2}{2})} \quad (6.14)$$

which gives (using $\omega_p^2 = 4\pi n$):

$$\frac{1}{\lambda} = \frac{\omega_p}{v^2} \left[\ln \left(\frac{q_{\max}}{q_{\min}} \right) - \frac{1}{2} \ln \left(\frac{2\omega_p + q_{\max}^2}{2\omega_p + q_{\min}^2} \right) \right] \quad (6.15)$$

In fig. 6.3 we plot the first and the second term in between the square brackets, as well as their difference. Note that the quantity in between the square brackets, as plotted in fig. 6.3 is proportional to E/λ (E is the electron/proton energy). Plotting E/λ versus $\log E$ is often referred to as a ‘Fano plot’ [13]. Deviations from a straight line in this plot correspond to deviations of the IMFP from simple proportionality to $E/\log E$. In the TPP-2m equation such deviations are obtained by adding explicitly terms proportional to $1/E$ and $1/E^2$. Here such deviations follow directly from the model used.

In the high-energy limit ($v^2 \gg \omega_p$) the contribution of each term simplifies to:

$$\begin{aligned} \frac{1}{\lambda} &= \frac{\omega_p}{v^2} \left[\ln \left(\frac{Bv^2}{\omega_p} \right) - \frac{1}{2} \ln \left(\frac{(Bv)^2}{2\omega_p} \right) \right] \\ &= \frac{\omega_p}{v^2} \left[\frac{1}{2} \ln \left(\frac{v^2}{\omega_p} \right) + \ln B - \frac{1}{2} \ln B^2 + \ln 2 \right] \\ &= \frac{\omega_p}{2v^2} \ln \left(\frac{2v^2}{\omega_p} \right) \end{aligned} \quad (6.16)$$

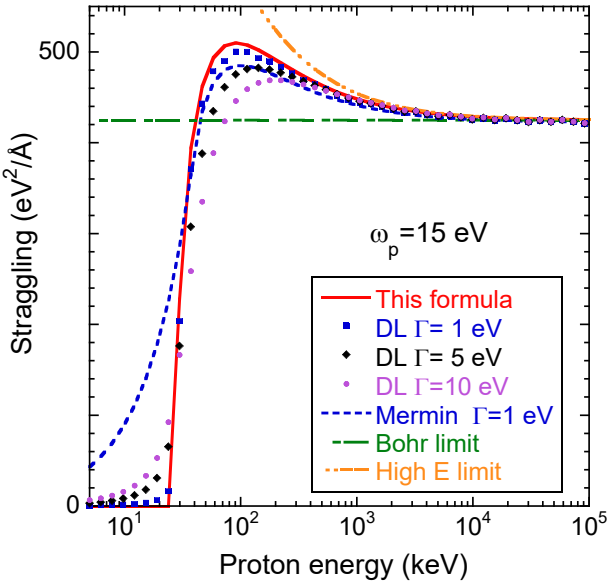


Figure 6.4: Straggling for protons for a single DL oscillator of 15 eV. For small Γ values the straggling obtained from eq. 6.8 (solid line) is very close to that obtained from numerical integration (symbols). Using the Mermin dielectric function (dashed line) instead of the DL dielectric function increases the straggling at low energies. All theories approach at large energy the Bohr limit (dash-dotted line). The high energy limit (double dot-dashed line, eq. 6.18) only describes the analytical integration well at rather high energies.

i.e. in the high energy limit the IMFP for protons and electrons with the same velocity are the same. This can be understood from the fact that in IMFP calculations the contribution of collisions with small q dominates, and q_{\min} is the same for both protons and electrons. This is in contrast to stopping where the difference between proton and electron stopping only converges slowly to zero for large v .

For practical purposes it is often more useful to give the IMFP in terms of the energy. For non-relativistic electrons this is simply: $1/\lambda = \frac{\omega_p}{4E} \ln \left(\frac{4E}{\omega_p} \right)$. This equation is in atomic units. When using eV as units for ω_p and E in this equation one obtains $1/\lambda$ in \AA^{-1} if one divides the right-hand side by the Bohr radius a_0 (0.529 \AA).

6.2.3 Straggling: single oscillator

Using the same argument one can obtain the expression for straggling. Compared to the stopping case one is left with an extra factor $\omega(q)$ after integration over ω :

$$\begin{aligned} \frac{d\Omega^2}{dx} &= \frac{4\pi n}{v^2} \int_{q_{\min}}^{q_{\max}} \frac{\omega_p + \frac{q^2}{2}}{q} dq \\ &= \frac{4\pi n}{v^2} \left(\omega_p \ln \left(\frac{q_{\max}}{q_{\min}} \right) + \frac{1}{4} (q_{\max}^2 - q_{\min}^2) \right) \end{aligned} \quad (6.17)$$

For not too small velocities ($v^2 \gg 2B\omega_p$) this simplifies to:

$$\begin{aligned} \frac{d\Omega^2}{dx} &= \frac{4\pi n}{v^2} \left[\omega_p \ln \left(\frac{Bv^2}{\omega_p} \right) + \frac{(Bv)^2}{4} - \frac{\omega_p^2}{4v^2} \right] \\ &\approx \pi B^2 n + \frac{\omega_p^3}{v^2} \ln \left(\frac{Bv^2}{\omega_p} \right) \end{aligned} \quad (6.18)$$

As is clear from fig. 6.4 In our model (Eq. 6.17) the straggling is zero at small v , then increases and has a maximum [14] before it slowly decreases towards the Bohr limit. This maximum of the calculated straggling relative to the Bohr limit is well known ([14] and can be understood in the following way: If one assumes that all electrons in the medium are stationary and non-interacting (i.e. neglect collective effects, assume $\omega_p = 0$), then the energy loss after a collision with momentum transfer q is just $q^2/2$. If we use this as the dispersion relation ('stationary, non-interacting electron dispersion') then $q_{\min} = 0$ and $q_{\max} = Bv$. Integrating eq. 6.17 for this

dispersion relation gives $\pi B^2 n$ for any v , i.e. always the Bohr limit. Deviations from the Bohr limit can then be interpreted as a consequence of the assumed dispersion.

In fig. 6.5 we compare the ‘stationary non-interacting electron dispersion’ with the DL dispersion for $\omega_p = 15$ eV. At low projectile velocity ($v = 1$ a.u. i.e 13.6 eV electrons or ≈ 25 keV protons, top panel fig. 6.5) no excitations are possible for the DL model, but excitations are possible from $q = 0$ a.u to $q = 2$ a.u. for protons) (up to 1 a.u for electrons) for the ‘stationary electron dispersion’. The straggling for the DL model is thus zero, for the stationary electron model the Bohr limit.

At $v = 2$ a.u. (≈ 54.4 eV for electrons, ≈ 100 keV for protons, central panel fig. 6.5) both the stationary, non-interacting electron dispersion and the DL dispersion cross the lines representing the kinematical limits. For q values where both dispersions allow excitations, the integral over ω for the DL dispersion gives a larger value. (if the integral was weighted by ω (stopping case) they would be the same. But for straggling the integral is weighted by an extra ω factor, so the DL integral will be larger than the stationary electron one.) The fact that the range of allowed q values is slightly smaller for the DL case has a smaller influence, so at these velocities the DL straggling is larger than the Bohr straggling.

At even larger projectile velocities (4 a.u., ≈ 216 eV electrons, ≈ 400 keV protons) the allowed q range becomes larger and thus the energy loss values involved become much larger too. The offset between the two dispersion curve, in relative terms, becomes less significant and the DL straggling values slowly converges to the Bohr limit.

6.2.4 Summary single oscillator results

In fig. 6.6 we summarise the result, comparing electron and proton IMFP, stopping and straggling as a function of projectile velocity v . For the IMFP the proton and electron values converge at relatively low v values, for stopping the convergence is much slower, whereas for straggling the proton values are 4 times larger than the electron values at large v values. This all reflects the different influence of collisions with large q (and hence, in our model, large ω) values on these properties, due to the weighting of the integrals eq. 6.6- 6.8 with different powers of ω .

6.3 Multiple Components

Almost always core levels have also a significant influence on the IMFP, stopping and straggling. Simple analytical expressions can again be obtained if this contribution is assumed to be concentrated at a specific mean energy loss and has a simple quadratic dispersion. We assume that the oscillator representing (sub)shell i is a narrow distribution centered at U_i with amplitude a_i . However, the contribution to the ELF of a core level is usually quite a broad distribution. Later (section 6.4) we will derive what is the best choice of parameter U_i and a_i based on generalized oscillator strength calculations.

In our model the ELF at $q = 0$ representing all electrons is given by:

$$\text{Im} \left[\frac{-1}{\epsilon(\omega, 0)} \right] = C_p \frac{\omega \Gamma \omega_p^2}{(\omega^2 - \omega_p^2)^2 + \omega^2 \Gamma^2} + \sum_i \frac{a_i \omega \Gamma U_i^2}{(\omega^2 - U_i^2)^2 + \omega^2 \Gamma^2} \quad (6.19)$$

For high-projectile energies the combined effect of all levels can be modelled by a single DL oscillator. This DL oscillator will be centered a characteristic energy I_x .

$$\text{Im} \left[\frac{-1}{\epsilon(\omega, 0)} \right]_{HE} = C_x \frac{\omega \Gamma I_x}{(\omega^2 - I_x)^2 + \omega^2 \Gamma^2}, \quad (6.20)$$

with $\Gamma \ll I_x$. However, we will show that the optimum choice of I_x and its amplitude C_x is different for the IMFP, stopping and straggling. We will refer to the optimum parameter for the IMFP as I_0 and C_0 , for stopping as I_1 and C_1 and for straggling as I_2 and C_2 .

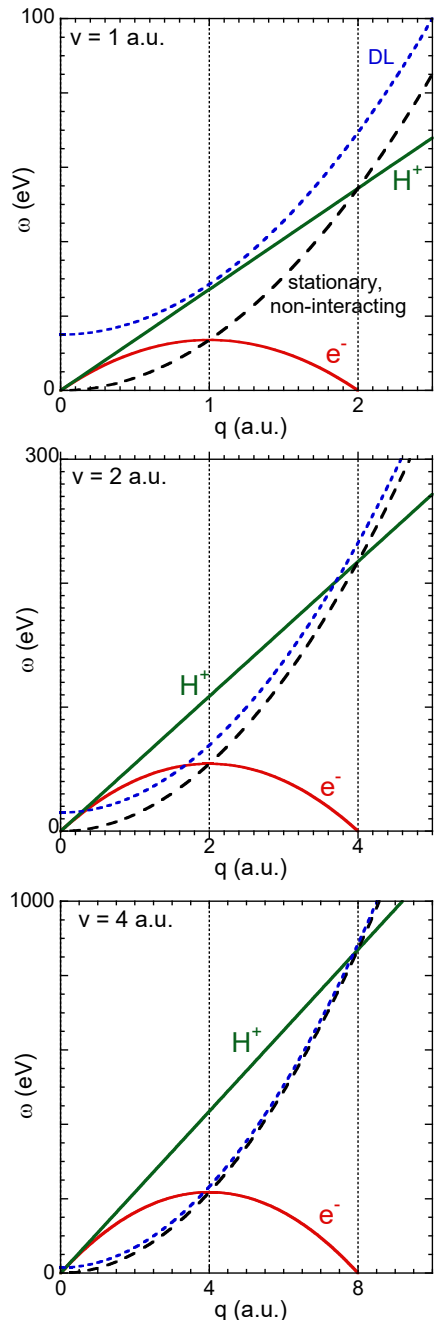


Figure 6.5: Dispersion for the DL model with $\omega_p = 15$ eV (dotted) and for stationary, non-interacting electrons (dashed) as well as the kinematical limit (ω_{\max}) at the projectile velocity v as indicated. As explained in the text, the kinematical limit causes the straggling to be below the Bohr limit at $v = 1$ a.u. (top panel), exceed the Bohr limit at $v = 2$ a.u. (central panel) and approaches the Bohr limit at high $v = 4$ a.u. (lower panel).

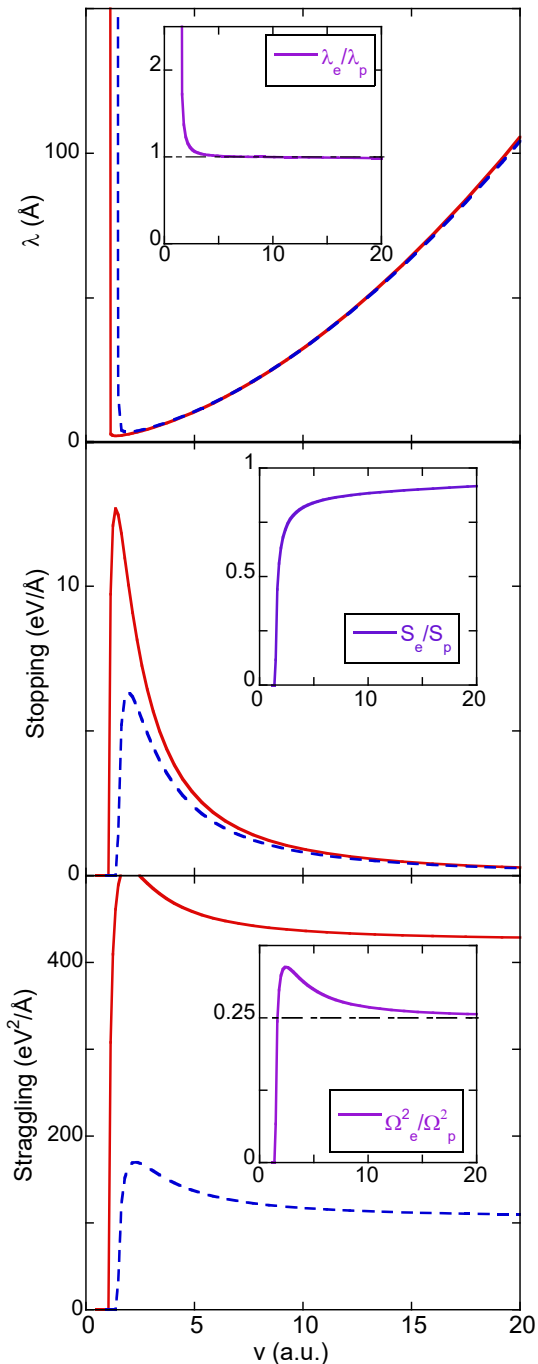


Figure 6.6: IMFP λ (top panel) stopping S (central panel) and straggling $d\Omega^2/dx$ of protons (solid line) and electrons (dashed line) for a single DL oscillator with 15 eV energy as a function of projectile velocity v . The inserts show the ratio of these quantities for both projectiles.

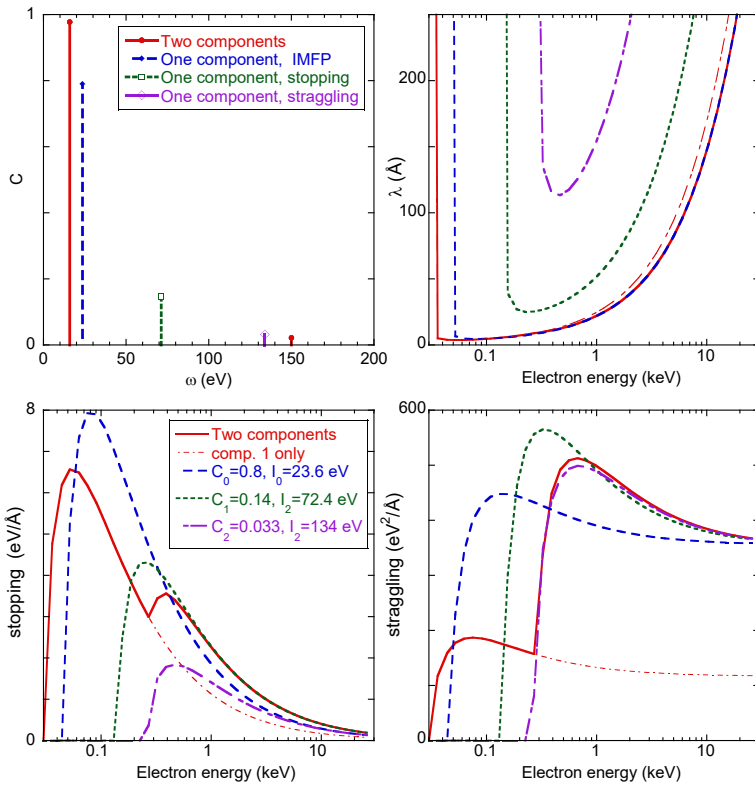


Figure 6.7: Top left panel shows the two-component model, resembling the dielectric function of Al with two components ($C_p = 0.978$, $\omega_p = 15.9$ eV and $C_1 = 0.022$ and $\omega_1 = 150$ eV) representing the valence band and $2p$ electrons respectively. For the IMFP (top right) the influence of the deeper level is minor and in the high-energy limit described by a single component at $I_0 = 23.6$ eV filling a large fraction ($C_0 = 0.80$) of the unit cell. The lower left panel show stopping for the two-component model. The influence of the deeper level is now more distinct. In the high-energy limit the two model gives similar stopping if one component is used based on I_1 (71.3 eV) and C_1 (0.147). and the three one-level models. Only the description based on C_1 and I_1 describes the stopping well at high-energies. The bottom right shows the straggling. At high-energies the influence of the deeper level exceeds that of the outer level. Now the high-energy behaviour is only well described by a one-level oscillator with parameters C_2 and I_2 .

For stopping the quantity I_1 is often referred to as the mean excitation energy and is usually written as simply I [9].

6.3.1 Stopping, multiple components

An oscillator with energy U_i has an electron density $n_i = U_i^2/(4\pi)$ and for an U_i value of the order of a core level binding energy this corresponds to a large electron density. If it would fill the whole unit cell (i.e. the corresponding $a_i = 1$ in eq. 6.19) it would correspond to a much large number of electrons per atom than are present in shell i . Instead one takes a_i much smaller than 1 (i.e. the core level only occupies a small volume fraction) such that its Bethe sum (eq.6.5) gives N_i/V with N_i the number electrons in core level i in a unit cell with volume V . This condition is fulfilled if $a_i = N_i(\omega_a/U_i)^2$.

One can calculate for this electron density again q_{\min}^i and q_{\max}^i (using eq. 6.11) by replacing ω_p by U_i . The total stopping is then obtained from:

$$\begin{aligned} -\frac{dE}{dx} &= \frac{4\pi}{v^2} \left[C_p n \ln \left(\frac{q_{\max}^i}{q_{\min}^i} \right) + \sum_i a_i n_i \ln \left(\frac{q_{\max}^i}{q_{\min}^i} \right) \right] \\ &= \frac{1}{v^2} \left[C_p \omega_p^2 \ln \left(\frac{q_{\max}^i}{q_{\min}^i} \right) + \sum_i a_i U_i^2 \ln \left(\frac{q_{\max}^i}{q_{\min}^i} \right) \right] \end{aligned} \quad (6.21)$$

In the previous we assumed implicitly $C_p = 1$. In fact, if we add different Drude oscillators then the Kramers-Kronig relations (or eq. 6.4) imply that $C_p + \sum_i a_i = 1 - 1/n_r^2$ with n_r the static refractive index [15]. For a metal $C_p + \sum_i a_i = 1$. The electron density of all electrons averaged over the unit cell is then given by $n_{av} = C_p n_p + \sum_i a_i n_i$. To keep the notation concise we will refer now to the plasmon energy ω_p as U_0 and to C_p as a_0 and include it in the sum over i in eq. 6.21.

In the high-energy limit eq.6.21 becomes

$$\begin{aligned}
-\frac{dE}{dx} &= \frac{1}{v^2} \sum_i a_i U_i^2 (\ln(Bv^2) - \ln U_i) \\
&= \frac{1}{v^2} \left[\sum_i a_i U_i^2 \ln(Bv^2) - \sum_i a_i U_i^2 \ln U_i \right] \\
&= \frac{1}{v^2} \left[\sum_i a_i U_i^2 \ln(Bv^2) - \frac{\sum_i a_i U_i^2 \ln U_i}{\sum_i a_i U_i^2} \sum_i a_i U_i^2 \right] \\
&= \frac{C_1 I_1^2}{v^2} \ln \left(\frac{Bv^2}{I_1} \right)
\end{aligned} \tag{6.22}$$

with I_1 the average of the log of the excitation energies defined as :

$$\ln I_1 = \frac{\sum_i a_i U_i^2 \ln U_i}{\sum_i a_i U_i^2} \tag{6.23}$$

and C_1 given by:

$$C_1 = \frac{\sum_i a_i U_i^2}{I_1^2} \tag{6.24}$$

The electron density of a DL oscillator with energy I_1 is $I_1^2/4\pi$ is always larger than n_{av} . The stopping at high energies of this system is thus equivalent to a system with the unit cell fraction $C_1 = 4\pi n_{av}/I_1^2$ filled with a DL oscillator with energy I_1 and the remainder empty. This is illustrated in the right panels of fig. 6.7 for a two-component system resembling the valence band and 2p level of aluminum

6.3.2 IMFP: multiple components

Again, just as in the case of stopping, we add extra oscillators at the characteristic energy of these outer core electrons and then the IMFP becomes:

$$\begin{aligned}
\frac{1}{\lambda} &= \frac{1}{\lambda_{valence}} + \sum_i \frac{1}{\lambda_{core i}} \\
&= \sum_i \frac{a_i U_i}{v^2} \left[\ln \left(\frac{q_{\max}^i}{q_{\min}^i} \right) - \frac{1}{2} \ln \left(\frac{2U_i + q_{\max}^{i^2}}{2U_i + q_{\min}^{i^2}} \right) \right]
\end{aligned} \tag{6.25}$$

As can be seen in fig. 6.7, top right panel, the effect of the deeper level is far less obvious for the IMFP than for the stopping. Thus the collisions involving the inner oscillator (with their large ω values) adds significantly to the stopping, but as these collisions occur relatively infrequent, affect the IMFP only in a minor way.

In the large- v limit it is again possible replace the sum of the contribution by a single oscillator:

$$\begin{aligned}
\frac{1}{\lambda} &= \frac{1}{2v^2} \sum_i a_i U_i (\ln(2v^2) - \ln U_i) \\
&= \frac{1}{2v^2} \sum_i a_i U_i \ln(2v^2) - \frac{\sum_i a_i U_i \ln U_i}{\sum_i a_i U_i} \sum_i a_i U_i \\
&= \frac{C_0 I_0}{2v^2} \ln \left(\frac{2v^2}{I_0} \right)
\end{aligned} \tag{6.26}$$

with:

$$\begin{aligned}
\ln I_0 &= \frac{\sum_i a_i U_i \ln U_i}{\sum_i a_i U_i}, \\
C_0 &= \frac{\sum_i a_i U_i}{I_0}.
\end{aligned}$$

Thus the contributions are now not proportional to $a_i n_i$ i.e. $a_i U_i^2$ (as is the case for stopping) but to $a_i U_i$ i.e. the averaging is now done based on the energy loss of each component and not on their electron density. Thus, as far as the IMFP at high energies is concerned this system is equivalent with a fraction C_0 of the unit cell filled with a DL oscillator with energy I_0 and the remainder empty. Note that $C_1 \leq C_0 \leq 1$. Note also that the electron density corresponding to this oscillator averaged over the unit cell ($C_0 I_0^2 / (4\pi)$) is different from that of the actual system. This single oscillator describes the IMFP well down to quite low energies ($\approx 3I_0$).

An example if the IMFP for a two-component system is given in the top right panel of fig. 6.7. It is clear from this figure that for this model system a good description of the IMFP at high energies is obtained using parameters C_0 and I_0 , but not using C_1 and I_1 . In contrast the stopping (lower left panel) at high v is not well described by C_0 and I_0 , but good agreement is obtained using C_1 and I_1 . Which single ‘effective oscillator’ describes a multi-level system well at high- v depends thus on the observable of interest.

6.3.3 Straggling: multiple components

In the same way we obtain for straggling for valence band plus core levels:

$$\frac{d\Omega^2}{dx} = \sum_i a_i \frac{U_i^2}{v^2} \left[U_i \ln \left(\frac{q_{\max}^i}{q_{\min}^i} \right) + \frac{1}{4} ((q_{\max}^i)^2 - (q_{\min}^i)^2) \right] \quad (6.27)$$

This is shown in the lower right panel of fig. 6.7. For this example the straggling approaches with increasing v first the Bohr limit for the valence band density and then, above 300 eV, rises again sharply. At very large projectile velocity the straggling is again fairly constant and one has reached the Bohr limit for the total electron density. For larger v values (using $U_i^2 = 4\pi n_i$):

$$\begin{aligned} \frac{d\Omega^2}{dx} &= \sum_i a_i \frac{U_i^3}{v^2} \ln \left(\frac{Bv^2}{U_i} \right) + \sum_i a_i \frac{B^2 U_i^2}{4} \\ &= \frac{C_2 I_2^3}{v^2} \ln \left(\frac{Bv^2}{I_2} \right) + \pi B^2 n_{\text{av}} \end{aligned} \quad (6.28)$$

with

$$\begin{aligned} I_2 &= \frac{\sum_i a_i U_i^3 \ln U_i}{\sum_i a_i U_i^3}, \\ C_2 &= \frac{\sum_i a_i U_i^3}{I_2^3}. \end{aligned}$$

The deeper level affects the straggling more than even the stopping case, and thus $I_0 \leq I_1 \leq I_2$ and $C_2 \leq C_1 \leq C_0 \leq 1$. Note that the average electron density calculated for this oscillator representing the straggling at higher energy, $C_2 I_2^2 / (4\pi)$, is different from n_{av} and can thus not be used to obtain the second term in eq. 6.28.

6.4 Deriving parameters for the core levels from appropriate GOS calculations

In the previous we found an approximate expression for the IMFP, stopping and straggling in terms of the plasmon energy and the effective energy representing core electrons. As the core level contribution to the ELF is generally not concentrated at a single energy but distributed over a large range of ω values we have to find a way to get the most appropriate choice of U_i (and a_i) of each core level.

One way to obtain the contribution of a core level to the ELF in the optical limit is based on (atomic) Generalised Oscillator Strength (GOS) calculations based on hydrogenic wave functions

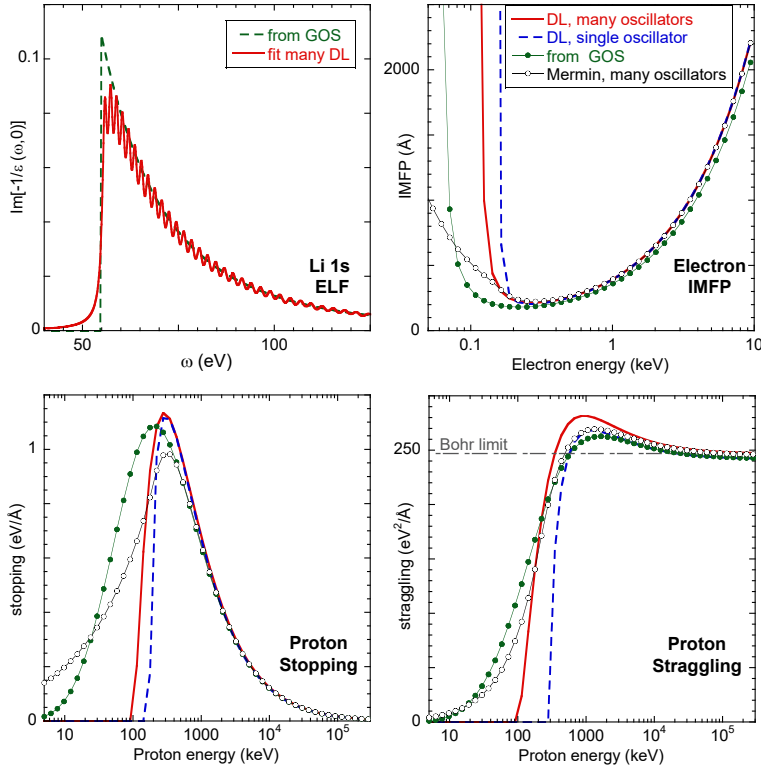


Figure 6.8: Top left: The ELF for the Li 1s level as calculated based on the GOS (dashed line) and a fit using many narrow DL oscillators (full line). The top right shows the IMFP as calculated for electrons using this set of DL oscillators (full line) or a single oscillator with the parameter from table 6.1, as well as the IMFP as calculated by integrating the GOS loss function (dots) and interpreting this set of oscillators as Mermin oscillators (circles). The bottom panels show the same for proton stopping and straggling, using now for the single oscillator the parameters of table 6.3 and 6.4 respectively

[16]. An example of this is shown in fig. 6.8 for the case of the Li 1s core level. One can approximate this ELF as a sum of many narrow DL loss functions in a very similar way as the method Penn described to obtain the IMFP based on Lindhard dielectric functions [17]. The Lindhard dielectric function at $q = 0$ is identical to the Drude-Lindhard dielectric function with width $\Gamma \rightarrow 0$ at $q = 0$. The ELF at ω integrated over $d\omega$ corresponds to an electron density $\frac{\omega d\omega}{2\pi^2} \text{Im} \left[\frac{-1}{\epsilon(\omega)} \right]$ (i.e. its contribution to the Bethe sum, eq. 6.5). If the whole unit cell would be filled with a free electron gas with $\omega_p = \omega$ then this would correspond to an electron density of $\omega^2/(4\pi)$. The volume fraction $G(\omega)d\omega$ filled with an electron gas with plasmon frequency between ω and $\omega + d\omega$ is thus given by $G(\omega) = \frac{2}{\pi\omega} \text{Im} \left[\frac{-1}{\epsilon(\omega)} \right] d\omega$. Thus, similar to what described by Penn, we can write any measured ELF at $q = 0$ as an integral over Drude-Lindhard dielectric functions:

$$\text{Im} \left[\frac{-1}{\epsilon(\omega, 0)} \right] = \int_0^\infty d\omega_p G(\omega_p) \text{Im} \left[\frac{-1}{\epsilon_{\text{DL}}(\omega, 0; \omega_p)} \right]. \quad (6.29)$$

The observed loss function can thus be described as an infinite sum of DL loss function with a_i being replaced by $G(\omega)$. Eq. 6.23 can then be written as an integral representing the familiar equation for the mean excitation energy:

$$\ln I_1 = \frac{\int_0^\infty \omega' \log \omega' \text{Im}[-1/\epsilon(\omega', 0)] d\omega'}{\int_0^\infty \omega' \text{Im}[-1/\epsilon(\omega', 0)] d\omega'} \quad (6.30)$$

Here the integral in the denominator corresponds to the Bethe sum rule (eq. 6.5) and gives simply 4π times the electron density. The fraction occupied by the oscillator (energy I_1) that has the same stopping in the high-energy limit is then $C_1 = \int_0^\infty \omega' \text{Im}[-1/\epsilon(\omega', q)] d\omega' / I_1^2$.

By the same token the expression for the IMFP (eq. 6.26) becomes simply:

$$\ln I_0 = \frac{\int_0^\infty \log \omega' \text{Im}[-1/\epsilon(\omega', 0)] d\omega'}{\int_0^\infty \text{Im}[-1/\epsilon(\omega', 0)] d\omega'} \quad (6.31)$$

with $C_0 = \int_0^\infty \text{Im}[-1/\epsilon(q, \omega')] d\omega' / I_0$.

Z	valence band		1s		2s		2p	
	C_p	ω_p (eV)	a_1	U_1 (eV)	a_2	U_2 (eV)	a_3	U_3 (eV)
Li	0.98	8.1	1.89E-2	79.1	-	-	-	-
Be	0.99	18.5	1.21E-2	161	-	-	-	-
C	0.84	34	2.69E-3	410	-	-	-	-
Na	0.97	6.0	2.74E-5	1541	5.79E-3	103	9.14E-2	45.1
Mg	0.97	11.05	3.15E-5	1874	5.13E-3	143	6.35E-2	71.5
Al	0.97	15.9	3.08E-5	2241	4.05E-3	190	4.21E-2	104.2
Si	0.93	17.2	1.85E-5	2642	2.11E-3	240	1.95E-2	141

Table 6.1: Values for the plasmon and outer core DL oscillators as used for the calculation of the IMFP. Plasmon energies are based on the valence band electron densities of the elemental solids. The core hole parameters a_i , U_i were calculated from the GOS for each subshell using eq. 6.31.

For straggling eq. 6.28 becomes for a continuous distribution:

$$\ln I_2 = \lim_{\omega_{\max} \rightarrow \infty} \frac{\int_0^{\omega_{\max}} \omega'^2 \log \omega' \operatorname{Im}[-1/\epsilon(\omega', 0)] d\omega'}{\int_0^{\omega_{\max}} \omega'^2 \operatorname{Im}[-1/\epsilon(\omega', 0)] d\omega'} \quad (6.32)$$

with $C_2 = \int_0^{\infty} \omega'^2 \operatorname{Im}[-1/\epsilon(\omega', q)] d\omega' / I_2^3$. For a GOS-derived ELF I_2 converges (slowly) to a constant value for $\omega_{\max} \rightarrow \infty$.

Thus if one wants to replace the GOS by a single oscillator to simplify the description of the interaction of charged particles with matter, then the parameters that reproduce the right behaviour in the high-energy limit are different for the IMFP, stopping and straggling. This is a consequence of the fact that the contribution of collisions with different energy losses are weighted differently in these three processes.

6.5 Comparing with experiment

We used a very simple dielectric function and further assumed that the target can be separated in valence band and core levels, each represented by DL oscillators. This made it possible to express the experimental observables of IMFP stopping and straggling by simple analytical expressions, for both electrons and protons. A method was described how to obtain the optimum set of parameters for this simplified model, using as a guide that the model should give the correct results in the high-energy limit. Now we want to compare these results with measurements of (electron) IMFP, (proton and electron) stopping as well as proton straggling. We start with the IMFP, as the model works best here. Subsequently, briefly give some examples for stopping and straggling, as for these cases the limitation of the model becomes progressively more obvious. We restrict ourselves somewhat arbitrarily to the light elements (up to $Z = 14$). Extension to e.g. the transition metals with their more complicated ELF at low ω values requires a more extensive discussion, beyond the scope of the present paper.

6.5.1 IMFP

Ideally one would compare the IMFP calculated with our simple model with those obtained from experimental data. However, highly accurate measurements of the IMFP over a large energy range are scarce. The general consensus is that the IMFP calculated from optical data, using the method of Penn [17] represents the state-of-the-art of our knowledge of this quantity. Hence we will use the IMFP as calculated, based on this theory by Tanuma et al as our benchmark [5]. For the IMFP the contribution of the core levels is less significant, compared to stopping and straggling. So the first comparison we make uses eq. 6.15. For this we use the plasmon energies given in table 6.1. These are very close to the ones used in [5], except for diamond where we use a larger ω_p (in better agreement with the experiment [18]) in combination with a C_p value significantly smaller than 1, such that the static refractive index of diamond is reproduced [15].

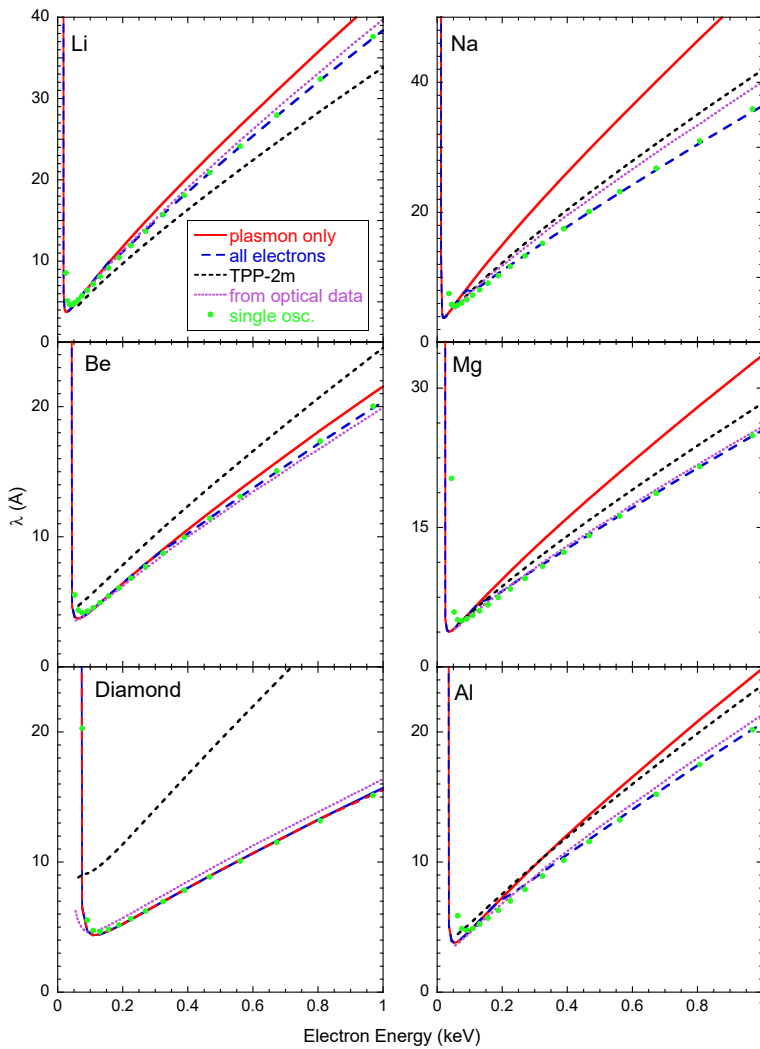


Figure 6.9: IMFP as calculated for electrons based on the valence band (plasmon) only (eq. 6.15, solid line) and for the valence and core electrons (eq. 6.25, long dashed line). Also shown are the estimates of the IMFP based on optical data [5] (dotted line) and the TPP-2m formula [5] (short dashed line). Also shown (dots) is the description based on a single oscillator with a weighted average ionization energy I_{av}^0 as obtained from eq. 6.26.

In figure 6.9 we compare the IMFP of a single component (VB only), based on the plasmon density with the IMFP obtained by Tanuma et al [5] calculated from optical measurements (which we consider the best estimate available of this quantity). Agreement is quite good at low E but, except for diamond, the agreement deteriorates at larger E values. This deterioration starts at higher E values when the outer core level binding energy increases (and hence not visible for carbon for the energy range plotted).

Thus we added the core levels to the IMFP calculation using eq. 6.25 and the parameters a_i , U_i as given in table 6.1. This indeed reduces the IMFP at large electron energies by a modest amount and the agreement with the optical-derived IMFP values is now very good, for energies above 100 eV. Only for Na does the deviation between the present data and the literature ones exceed 1 Å. That Na shows the largest deviation is not completely surprising. Here the contribution to the IMFP of the six 2p shallow core electrons is almost comparable to that of the single valence electron, and hence the approximate nature of the 2p core electron parameters is the likely cause of the somewhat larger deviation.

Using the values of table 6.1 to calculate I_0 and C_0 we obtain the corresponding approximate IMFP which is shown in fig. 6.9 as well. The description of the IMFP obtained using this single oscillator is of similar quality as the description obtained using multiple oscillators, except at very low energies. The IMFP calculated based on multiple oscillators often show a slight ‘bump’ at the E value where the outer core starts contributing (e.g. at 0.2 keV in the case of Al) This is not present in the curve for the average oscillator, which is closer to the optical values near such an offset.

Often the IMFP is described by the TPP-2m equation:

$$\frac{1}{\lambda(E)} = \frac{\omega_p^2 [\beta \ln \gamma E - C/E + D/E^2]}{E}. \quad (6.33)$$

with:

$$\beta = -0.10 + 0.994/(\omega_p^2 + E_g^2)^{0.5} + 0.069\rho^{0.1} \quad (6.34a)$$

$$\gamma = 0.191\rho^{-0.5} \quad (6.34b)$$

$$C = 1.97 - 0.97U \quad (6.34c)$$

$$D = 53.4 - 20.8U \quad (6.34d)$$

$$U = N_v\rho/M \quad (6.34e)$$

with λ in Å, ρ the density g/cm³, ω_p and E_g (bandgap) in eV, N_v the number of valence electrons per atom that contribute to the plasmon, and M the atomic mass (in a.m.u.) with E the beam energy ($2v^2$ in a.u.) and C , D , β and γ parameters. In the TPP-2M description the parameters tend to depend on the density (g/cm³), a dependence that is completely absent in the description given here. This equation is not derived but based on an analogy with the cross section of atoms for inelastic scattering [19]. ω_p is well-defined in terms of the valence band electron density, but β , γ , C and D are parameters that are related to physical quantity (e.g. density) in a phenomenological way, not easily understood on physical grounds.

The TPP-2m IMFP values are shown in fig. 6.9 as well. Generally the formula derived here describe the IMFP better. Diamond and to a lesser extent Be are one of the few cases where the TPP-2m formula does not work well [20]. It is noted that the TPP-2m equation uses the same parameters to describe a wide range materials, whereas in the approach described here, one has to calculate, for each element, C_0 , and I_0 from the valence band electron density and the GOS of the outer core levels.

deriving I_0 and C_0 when the IMFP is known

In case the IMFP is know (e.g. from a full calculation based on the optical ELF) One can use that eq. 6.15 as an alternative to eq. 6.33 and fit I_0 and C_0 and parameterize the energy

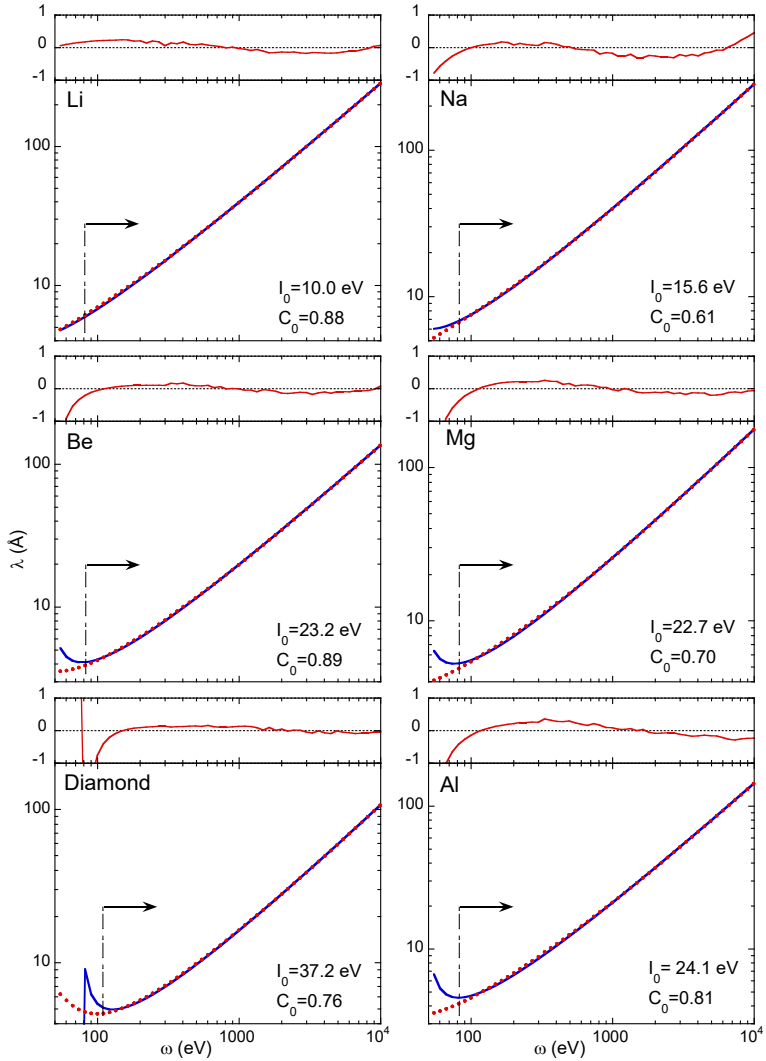


Figure 6.10: Fits of the IMFP as derived from optical data in ref. [5] to formula 6.15 for some low-Z elements. Only the optical IMFP values above a minimum, as indicated by the arrow, are used in the fit. The residuals of each fit is shown above the graph, and is less than 1 Å for the energies considered in the fit. The values of I_0 and C_0 obtained from the fit are given as well.

	from model		from fit		prefactor x (eV/Å)				logfactor y (eV $^{-1}$)			
	C_{av}	I_{av}^0	C_{av}	I_{av}^0	$\omega_p^2 \beta$ [5]	$\omega_p^2 \beta$ [5]	$\frac{C_p \omega_p}{4a_0}$	$\frac{C_{\text{av}} I_{\text{av}}^0}{4a_0}$	γ [5]	γ [5]	$\frac{4}{\omega_p}$	$\frac{4}{I_{\text{av}}^0}$
Li	0.794	11.9	0.88	10.0	4.17	5.32	3.74	4.46	0.434	0.261	0.494	0.338
Be	0.880	22.8	0.89	23.2	9.81	8.35	8.65	9.51	0.167	0.141	0.216	0.178
C	0.792	37.3	0.76	37.2	13.5	6.94	13.5	14.0	0.102	0.102	0.118	0.108
Na	0.656	15.9	0.61	15.6	4.41	4.54	2.75	4.15	0.303	0.194	0.666	0.262
Mg	0.639	21.6	0.70	22.7	7.61	7.12	5.06	6.80	0.165	0.144	0.362	0.192
Al	0.774	26.5	0.81	24.1	9.69	8.99	7.30	9.05	0.126	0.116	0.252	0.156
Si	0.75	25.3	0.77	22.1	8.55	8.86	7.58	8.80	0.119	0.125	0.233	0.165

Table 6.2: Analysis of the IMFP of some low- Z elements. The first 2 columns show C_{av} and I_{av}^0 using the values of table 6.1. The next 2 columns are the same quantities but obtained by fitting ω_p and C_p of eq. 6.15 against the IMFP derived from optical data as published in ref. [5] from 100 eV onwards. All theories predict at high E IMFP in the form of $1/\lambda = (x/E) \log yE$. Estimates of the prefactor x are given, based on the fit of the IMFP from optical data, the TPP-2m formula, the present theory based only on the plasmon energy, the present theory based on I_{av}^0 . The last 4 columns give estimates of y based on the same 4 approaches.

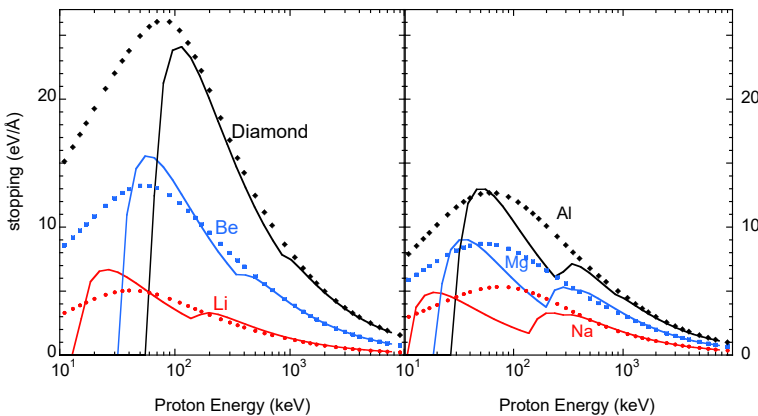


Figure 6.11: Proton stopping as calculated using eq.6.21 (lines) and the values of table 6.3 compared to the stopping from the SRIM program symbols, for the elements as indicated.

dependence of the IMFP. The accuracy of the fit for energies larger than 100 eV is $\approx 0.5 - 1\%$. This is shown in fig. 6.10. The values obtained are shown in table 6.2 as well, and resemble those obtained from the estimated ionization energies closely, validating the present approach. Compared to the TPP-2m type-formula, the advantage is that it has only two parameters, and that the parameters have a more well-defined physical meaning. The disadvantage is that the model works only for energies above $\approx 3I_0$ (80 eV in most case, 110 eV for diamond) rather than 50 eV.

6.5.2 Stopping

In fig. 6.11 we show the stopping obtained for protons using this simple model for the same low- Z elements as the IMFP calculation, using now the parameters from table 6.3. A comparison is made to the SRIM stopping values [21] a widely used database of stopping values. The SRIM stopping for these elements differ greatly and the same trend is seen in these simple model calculations. Above 1 MeV there is good agreement between the model and SRIM, but in this energy range the simple Bethe formula works quite well too. At lower energy the onset of the contribution of each level to the stopping is too sudden, making the model calculations of limited practical use.

Results for Si for both proton and electron stopping are shown in fig. 6.12. For protons the results are compared to SRIM [21] results, which are supported by many experimental measurements. For electrons we compare with the electron stopping as obtained from optical data by Shinotsuka et al [22]. Electron stopping, although important for e.g. materials science and

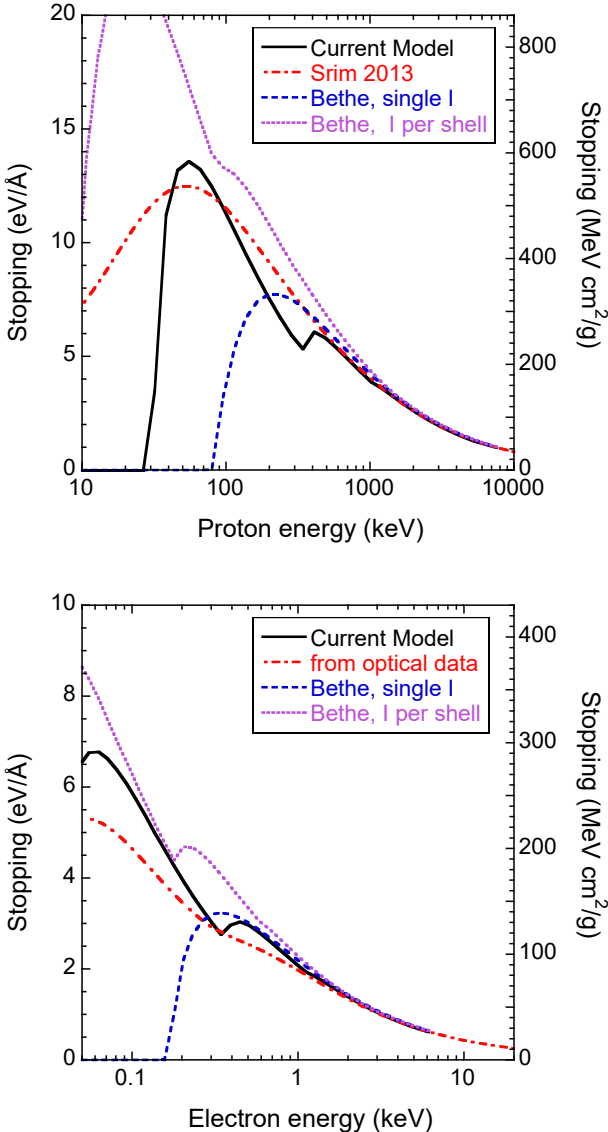


Figure 6.12: The stopping for protons (top panel) and electrons (lower panel) in Si as calculated using eq. 6.21, as obtained from optical data and from the Bethe formula, using a single mean excitation energy, and a mean excitation energy per subshell, as given in table 6.3, as well as SRIM values (protons) and stopping calculated based on optical data by Shinotsuka et al [22].

medical physics application, is hard to measure directly, and what is presented as experimental data of electron stopping in this energy range, are in reality values obtained from a measured electron energy loss spectrum, interpreted as a loss function, using an approximate formula [23]. Clearly the agreement is not very good, as can be expected for such a rough approximation of the dielectric function. It is, however a better approximation that the Bethe approximation using either a single I value or different I values per shell. The assumption of zero-width causes a sudden sharp increase in stopping for both the valence band, and at larger energy also for the 2p contribution, whereas in the SRIM stopping or other, more realistic, approaches this behaviour is smoothed out. We get, of course, good agreement at large energy of all theories, justifying the I values used. Hence the stopping calculation can be used to check if the I values are reasonable, as the ion stopping is relatively well known. The fact that for electron stopping the present theory predicts overall larger values than Shinotsuka's calculation, is at least in part due to the neglect of exchange in the simple model.

6.5.3 Straggling

Finally a single example for straggling is given for the case of protons on Silicon in figure 6.13. Here we use a single component for the valence band and the 3 core levels components using the parameters of table 6.4. The model predicts a sudden onset of the contribution for each level

Z	1s				2s				2p			
	from GOS		from Lit.		from GOS		from Lit.		from GOS		from Lit.	
	a_1	U_1	a_1	U_1	a_2	U_2	a_2	U_2	a_3	U_3	a_3	U_3
Li	1.40E-2	95.9	1.8E-2	85 ⁺	-	-	-	-	-	-	-	-
Be	9.02E-3	194	8.0E-3	209*	-	-	-	-	-	-	-	-
C	2.01E-3	494	2.0E-3	486*	-	-	-	-	-	-	-	-
Na	2.06E-5	1853	8.8E-6	2824 ⁺	3.48E-3	142	2.5E-3	168 ⁺	6.88E-2	54.1	3.1E-1	82 ⁺
Mg	2.36E-5	2252	1.3E-5	3035 ⁺	3.11E-3	196	2.8E-3	206 ⁺	4.86E-2	84.9	2.7E-2	115 ⁺
Al	2.31E-5	2964	2.3E-5	2701*	2.47E-3	260	7.3E-4	476*	3.26E-2	123	2.2E-2	150*
Si	1.39E-5	3173	1.3E-5	3206*	1.29E-3	328	4.0E-4	586*	1.52E-2	165	1.2E-2	186*

Table 6.3: Values of the energy U (in eV) of the oscillators representing the core levels and the fraction of the volume occupied by this core level as calculated from the GOS using Eq.6.30. Also shown are the 'mean ionization energies taken from the literature, either [24] (indicated by a *) or, if these are not available as calculated from the binding energy and a scaling factor as determined by Sternheimer [25] (indicated by +). The factors a_i are chosen such that the sum rule for these oscillators correspond to the nominal number of core electrons (e.g. 2 for s levels) for the elemental solids (diamond in the case of C).

Z	1s		2s		2p	
	C_2	I_2 (eV)	C_2	I_2 (eV)	C_2	I_2 (eV)
Li	3.77E-3	159.1	-	-	-	-
Be	2.49E-3	320	-	-	-	-
C	5.7E-4	802	-	-	-	-
Na	5.91E-6	\approx 3650	3.26E-4	354	2.36E-2	82.0
Mg	6.86E-6	\approx 3700	3.05E-4	480	1.79E-2	125
Al	6.77E-6	\approx 4400	2.51E-4	627	1.26E-2	178
Si	4.09E-6	\approx 5200	1.34E-4	786	6.02E-3	237

Table 6.4: Values for DL oscillators as used for the calculation of the straggling. For 1s core level uncertainties of I_2 for element from Na are due to the slow convergence of eq. 6.32

reaching quite quickly after a small overshooting a constant value, corresponding to the Bohr straggling of the density of the electrons contributing. If we calculate the straggling using a large number of DL oscillators for each core level, as described in fig. 6.8 then the sudden onsets are smeared out. If one uses the GOS itself to calculate the dielectric function then the straggling increases even more gradual, in agreement with other calculations e.g. by Chu [26]. Thus for straggling the simplification of using a single DL oscillator for each core level can only be used as a very rough approximation. Comparison with experiment, which themselves show considerable spread as these are difficult measurements, is further complicated due to the influence of the inhomogeneity of the electron density ('bunching' [27, 28]) that is not present in the current calculation, or in the theory by Chu.

6.6 Conclusion

We worked out the IMFP, stopping and straggling for electrons and protons for a simple model dielectric function (single DL oscillator with vanishing width). We have seen that (at equal particle speed v) differences between the proton and electron case are due to the different maximum momentum transfer to the system that is possible for either projectile. This has only a minor impact on the IMFP, has significant impact on stopping and changes the straggling greatly.

More complicated systems can be described by the sum of DL oscillators. For high-enough projectile velocities the sum of DL oscillators can be replaced by a single effective oscillator. However the parameters of this effective oscillator depend on the observable, and has lowest energy for the IMFP, and highest for straggling. This is a consequence of the different weighting with ω that each process has. This is a significant set-back, as ideally the dielectric function one

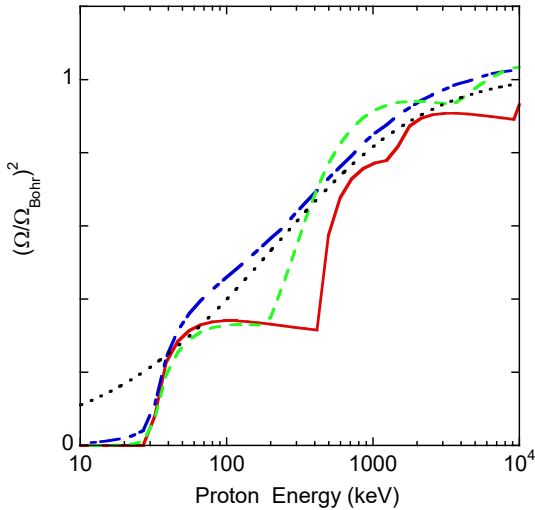


Figure 6.13: Straggling of protons in silicon. Full red line: based on DL oscillator for valence band and 3 oscillators from table 6.4. Dashed-dotted blue line: Based on a DL oscillator of the valence band and GOS-derived dielectric function. dashed green line: Based on fits of the GOS with many DL oscillators using procedure as illustrated in fig. 6.10. The dotted black line is the (atomic) calculation by Chu [26] usually used to estimate the straggling.

uses should be the basis of the description of a wide range of phenomena.

At least for low- Z elements the method described here gives a good description of the IMFP for energies over 100 eV. For these elements the formula derived here describes the IMFP better than the widely used TPP-2m formula. The parameters used in the present method are easily understood on physical grounds whereas for the TPP-2m formula interpretation of the corresponding parameters is not straightforward.

The description of stopping and straggling gives the right trend but is hampered by a too sudden onset of the contribution of each shell and hence the model use here is too simple for real practical use.

For electrons the main shortcoming is the neglecting of exchange effects. In that sense the theory described here is more appropriate to positrons.

Bibliography

- [1] N. Bohr, On the theory of the decrease of velocity of moving electrified particles on passing through matter, *Philos. Mag.* 25 (1913) 10. doi:/10.1080/14786440108634305.
- [2] H. Bethe, Zur Theorie des Durchgangs schneller Korpuskularstrahlen durch Materie, *Ann. Phys.* 397 (3) (1930) 325–400. doi:10.1002/andp.19303970303.
URL <http://dx.doi.org/10.1002/andp.19303970303>
- [3] J. Lindhard, On the properties of a gas of charged particles, *K. Dan. Vidensk. Selsk. Mat.-Fys. Medd.* 28 (8) (1954) 1–57.
- [4] M. Nastasi, J. Mayer, J. K. Hirvonen, *Ion–solid Interactions*, Cambridge University Press, 1996. doi:10.1017/cbo9780511565007.
- [5] S. Tanuma, C. J. Powell, D. R. Penn, Calculations of electron inelastic mean free paths. IX. Data for 41 elemental solids over the 50 eV to 30 keV range, *Surf. Interface Anal.* 43 (2011) 689. doi:10.1002/sia.3522.
- [6] H. Nikjoo, D. Emfietzoglou, T. Liamsuwan, R. Taleei, D. Liljequist, S. Uehara, Radiation track, DNA damage and response—a review, *Rep. Prog. Phys.* 79 (2016) 116601. doi:10.1088/0034-4885/79/11/116601.
- [7] M. Vos, P. Grande, Model dielectric functions for ion stopping: The relation between their shell corrections, plasmon dispersion and Compton profiles, in: *Advances in Quantum Chemistry*, Elsevier, 2022, pp. 267 –301. doi:10.1016/bs.aiq.2022.07.001.
- [8] H. T. Nguyen-Truong, Analytical formula for high-energy electron inelastic mean free path, *The Journal of Physical Chemistry C* 119 (41) (2015) 23627–23631. doi:10.1021/acs.jpcc.5b09048.
- [9] P. Sigmund, *Particle Penetration and Radiation Effects*, Vol. 151 of Springer Series in Solid-State Sciences, Springer, Berlin, 2006.
- [10] C. D. Archubi, N. R. Arista, General formulation of interactions and energy loss of particles in plasmas: Quantum-wave-packet model versus a semiclassical approach, *Phys. Rev. A* 105 (2022) 032806. doi:10.1103/physreva.105.032806.
- [11] R. H. Ritchie, A. Howie, Electron excitation and the optical potential in electron microscopy, *Philos. Mag.* 36 (1977) 463. doi:10.1080/14786437708244948.
- [12] N. Mermin, Lindhard dielectric function in the relaxation-time approximation, *Phys. Rev. B* 1 (1970) 2362 –2363. doi:10.1103/physrevb.1.2362.
- [13] U. Fano, Ionizing collisions of very fast particles and the dipole strength of optical transitions, *Phys. Rev.* 95 (1954) 1198–1200. doi:10.1103/physrev.95.1198.
- [14] M. S. Livingston, H. A. Bethe, Nuclear physics c. nuclear dynamics, experimental, *Rev. Mod. Phys.* 9 (3) (1937) 245–390. doi:10.1103/revmodphys.9.245.

- [15] M. Vos, P. Grande, Simple model dielectric functions for insulators, *J. Phys. Chem. Solids* 104 (2017) 192. doi:10.1016/j.jpcs.2016.12.015.
- [16] S. Heredia-Avalos, R. Garcia-Molina, J. M. Fernández-Varea, I. Abril, Calculated energy loss of swift He, Li, B, and N ions in SiO₂, Al₂O₃, and ZrO₂, *Phys. Rev. A* 72 (2005) 052902. doi:10.1103/physreva.72.052902.
- [17] D. Penn, Electron mean-free-path calculations using a model dielectric function, *Phys. Rev. B* 35 (1987) 482. doi:10.1103/PhysRevB.35.482.
- [18] H. Raether, Excitation of plasmons and interband transitions by electrons, Springer tracts in modern physics ; v.88, Springer Verlag, Berlin, 1979.
- [19] M. Inokuti, Inelastic Collisions of Fast Charged Particles with Atoms and Molecules—The Bethe Theory Revisited, *Rev. Mod. Phys.* 43 (1971) 297. doi:10.1103/RevModPhys.43.297.
- [20] S. Tanuma, C. J. Powell, D. R. Penn, Calculations of electron inelastic mean free paths, *Surf. Interface Anal.* 36 (1) (2004) 1–14. doi:10.1002/sia.1997.
- [21] J. Ziegler, M. Ziegler, J. Biersack, SRIM – the stopping and range of ions in matter (2010), *Nucl. Instrum. Methods Phys. Res., Sect. B* 268 (11-12) (2010) 1818–1823. doi:10.1016/j.nimb.2010.02.091.
- [22] H. Shinotsuka, S. Tanuma, C. Powell, D. Penn, Calculations of electron stopping powers for 41 elemental solids over the 50ev to 30kev range with the full penn algorithm, *Nucl. Instrum. Methods Phys. Res., Sect. B* 270 (2012) 75–92. doi:10.1016/j.nimb.2011.09.016.
- [23] S. Luo, X. Zhang, D. Joy, Experimental determinations of electron stopping power at low energies, *Radiat. Eff. Defects Solids* 117 (1-3) (1991) 235–242. doi:10.1080/10420159108220619.
- [24] P. Sigmund, P. Deluca, A. Wambersie, Stopping of ions heavier than helium, *Journal of the International Commission on Radiation Units and Measurements* 5 (1) (2005) 0–0. doi:10.1093/jicru/ndi001.
- [25] R. Sternheimer, M. Berger, S. Seltzer, Density effect for the ionization loss of charged particles in various substances, *At. Data Nucl. Data Tables* 30 (1984) 261–271. doi:10.1016/0092-640X(84)90002-0.
- [26] W. K. Chu, Backscattering spectrometry, Academic Press, New York, 1978.
- [27] Q. Yang, D. O'Connor, Z. Wang, Empirical formulae for energy loss straggling of ions in matter, *Nucl. Instrum. Methods Phys. Res., Sect. B* 61 (1991) 149. doi:10.1016/0168-583X(91)95454-1.
- [28] F. Selau, H. Trombini, R. Fadanelli, M. Vos, P. Grande, On the energy-loss straggling of protons in elemental solids: The importance of electron bunching, *Nucl. Instrum. Methods Phys. Res., Sect. B* 497 (2021) 70. doi:10.1016/j.nimb.2021.03.006.